Universidad Politécnica de Madrid
Escuela Técnica Superior de Ingenieros de Telecomunicaciones

Doctoral Thesis

INVESTIGATIONS ON III-NITRIDES NANOSTRUCTURES: APPLICATION TO RENEWABLE ENERGIES AND BIO-SENSING

Paul Eduardo David Soto Rodriguez
Msc. In Applied Physics

Instituto de sistemas Optoelectrónicos y Microtecnología
Departamento de Ingeniería Electrónica
Universidad Politécnica de Madrid
2016

Universidad Politécnica de Madrid
Escuela Técnica Superior de Ingenieros de Telecomunicaciones

Doctoral Thesis

INVESTIGATIONS ON III-NITRIDES NANOSTRUCTURES: APPLICATION TO RENEWABLE ENERGIES AND BIO-SENSING

Presented by
Paul E. D. Soto Rodriguez
Msc. in Science in Applied Physics

Supervisor
Dr. Enrique Calleja Pardo
Professor
Co-supervisor
Dr. Zarko Gačević
Assistant professor

This dissertation is submitted for the degree of Doctor of Philosophy
At Instituto de sistemas Optoelectrónicos y Microtecnología
March 2016

Doctoral Thesis: INVESTIGATIONS ON III-NITRIDES NANOSTRUCTURES: APPLICATION TO RENEWABLE ENERGIES AND BIO-SENSING

Author: Paul Eduardo David Soto Rodriguez

Thesis Supervisors: Prof.

El tribunal nombrado por el Mgfco. y Excmo. Sr. Rector de la Universidad Politécnica de Madrid, el día ……… de ………. de 2016 para juzgar la tesis arriba indicada, compuesto por los siguientes doctores:

Dr. ………………………………………………………………………... (Presidente)
Dr. ………………………………………………………………………….. (Vocal)
Dr. ………………………………………………………………………….. (Vocal)
Dr. ………………………………………………………………………….. (Vocal)
Dr. ………………………………………………………………………. (Secretario)

Realizando al acta de lectura y defensa de la Tesis el día ……… de…………………….
De 2016 en Madrid, acuerda otorgarle la calificación de ………………………………..

El Presidente:

El Secretario:

Los Vocales:

Dedication

This thesis is dedicated to my beloved wife Veronica Irina Calderon Nash. Without your support and encouragement I would not be able to reach this point. By your side this journey has been possible and I am sure it will be a tipping point in our future, a future which I embrace with hope and love. No words I can write which would describe my gratitude and feelings towards you. Nevertheless I want to thank you for being by my side and just say "Te amo", "ik hou van je schatje".

Acknowledgement

This thesis work is an effort of years and involves many people for which I am very grateful and would express my sincere gratitude and give special mention in this acknowledgement.

First I would like to thank to all group members with whom we shared the office:

Victor Jésus Goméz Hernandez, you were the only “native” Spanish in the group and always very willing to help with the bureaucracy. We shared the same passion for soccer and thanks to you we were able to maintain periodically very good matches at the ETSIT fields. Mine time at ISOM was as enjoyable as it has been also thanks to your lively spirit, during lectures and work in the lab. Thank you and hope you may finish your Phd also soon, wish you the best of luck.

Praveen Kumar, coming from such a distant place as India to a complete new environment as Spain would have been difficult to cope with I would imagine. However, from day one your positive and hard working spirit prevailed. Thank you for sharing your lab experience and good willingness to help with any problem we encountered. Many of the achievements presented in current thesis would not have been possible without your input, starting with the revival of the MECA MBE system. I wish you and your family (Pooja and little Parth) all the best.

Naveed ul Hassan Alvi, you had the previous experience of Sweden from your Phd and suffered the radical change to the Southern Europe part as I did. Despite all obstacles you managed to accomplish your needs and I am happy that everything worked out for you. Thank you for sharing you expertise on biosensors and water-splitting. The work done on these fields were made possible due to your presence. I am sure that back in Pakistan you and your wife Gul have had a new air and wish both of you the very best.

Pavel Aseev, your enthusiasm for science and hardworking spirit are admirable. We spend a lot of time doing growth and characterization together, sample after sample and always enjoyed our conversations and discussions. I am sure you have a great career ahead of you and wish you and Kate all the best.

I would like to thank all the members of ISOM from technicians, to students, researchers and administrative workers. In special I would like to thank Ana Bengoechea and Steven Albert for their advice and always enjoyable talks as Javier Martinez, José María Ulloa Herrero y Antonio Utrilla. Also I want to thank Elias Muñoz, the conversations we had were always of great value for me. During my stay at ISOM many also left whom I would like to thank as is the case of Noemi García Lepetit, we coincide during the first years and was very helpful specially with my incorporation into the Spanish society clarifying habits and language usage. Dong Joo Choi whom joined our Friday soccer sessions. All the guys from the Master courses MISE who also were part of the soccer games, Francisco, Alejandro Clemotte, Juan

Diego, Miguel Maldonado, Rodolfo Campués, Carlos David Amalla, Jesus Cernicharo, Calos Benito, Javier Villena y Leonel Vazquez.

I would like to thank all the groups with whom we started and enjoyed collaboration, the group of prof. Magnus Willander in Sweden, specialized in potentiometric biosensors, the TEM group of prof. Francisco Morales from Universidad de Cadiz, special thanks to José Manuel, the chemical analytical group from Universidad Complutense of prof. José Pingarrón my highly thanks go to Reynaldo Villalonga and Alfredo Sánchez. I would like to thank both Alexander Senichev from Max Planck Institute of Microstructure Physics and Christoph Lienau from Oldenburg University for the SNOM measurements. In addition, I would like to thank Ameed ul Hassan Alvi member of the department of Physics at the University of Agriculture in Pakistan and M. Phil. Waheed ul Hassan member of the department of Chemistry at the Bahauddin Zakariya University in Pakistan for the Hydrogen quantifications measurements.

My deepest thanks to Stefano Sanguinetti who allowed me to be part of his lab in L-Ness for the Phd internship, I learned a lot during my short stay. My thanks also go for the members of the group: Sergio Bietti, David Scarpellini, Giorgio Benedetti and Alexey Federov.

I want to thank my current supervisor Zarko Gacevic with whom I was able to work with at his final stage of his Phd (coinciding with my start), learning whatever I could during this short period of time. Thank you for your critical review on the current thesis and comments. My thanks also go to my other supervisor Enrique Calleja, who also spend his valuable time in revising current thesis and discussing presented results. Both contributed in the final layout of the thesis and made possible to reach this final stage.

I want to thank the familiy, both mines as my wife’s for despite the distance always being present. Thank you Mom for having always the right words to say, Dad for the unforgettable trip to Brasil, Negrita and the kids Nico and Milla just for being there and sharing your moments of joy.

And finally I would like to thank Richard Nötzel my mentor and supervisor during the initial course of this thesis. His ideas and insight are carried along the work presented. It was him who convinced me to come to Spain and start this journey. The time we spent discussing results at the office or repairing the MBE/CBE have been invaluable learning experiences. I hope we may once more coincide in a future and wish you all the best.

INDEX

RESUMEN

Esta tesis, titulada "Investigaciones sobre Nanoestructuras de nitruros del grupo III: Aplicaciones en Energías Renovables y Bio-Sensores" presenta el trabajo realizado en el "Instituto de Sistemas Optoelectrónicos y Microtecnología" (ISOM).

El principal objetivo del trabajo presentado es:

> Investigar el potencial de los nitruros del grupo III (In(Ga)N), en particular películas delgadas/nano-estructuras para bio-sensores y foto-electrólisis. Las estructuras investigadas contienen variados contenidos de indio (de medio a alto) así como morfologías diversas, tales son: películas delgadas compactas de InGaN, redes de nano-paredes de InGaN, nano-columnas de InGaN y puntos cuánticos de InN.

La Tesis trata los siguientes puntos:

> El crecimiento epitaxial por haces moleculares de películas delgadas/nano-estructuras sobre sustratos de GaN/zafiro (0001) ó Si(111), así como su detallada caracterización morfológica, estructural, óptica y electroquímica.
>
> Comprender y evaluar sistemáticamente su comportamiento electroquímico, para su uso final en aplicaciones de bio-sensores y de foto-electrólisis.

El trabajo se presenta como sigue:

Capítulo I: Son expuestos la motivación para realizar el trabajo (incluyendo el estado de arte) y los objetivos principales de la tesis.

Capítulo II: Son dadas las propiedades fundamentales de los materiales utilizados (nitruros del grupo III) así como de las nano-estructuras utilizadas (nano-columnas y puntos cuánticos (QDs)). Debido a su importancia en el desarrollo de la tesis, las propiedades fundamentales que afectan de forma directa la actividad electroquímica de los materiales utilizados (nitruros del grupo III), también serán descritas.

Capítulo III: Se presentan detalles sobres las técnicas experimentales utilizadas en la presente tesis: técnicas de crecimiento epitaxial (MBE), caracterización morfológica (SEM y AFM), estructural (difracción de rayos-X y TEM), caracterización óptica (PL, CL y SNOM), así como caracterización química (GC)

Capítulo IV: se presenta un resumen de electroquímica para la caracterización de las estructuras, y relacionados con la aplicaciones propuestas. Se describe la electroquímica de electrodos metálicos y semiconductores (tipo n no-degenerados) y luego se discutirá sobre el caso particular de electrodos de InGaN de alto contenido de In (semiconductor tipo n degenerado). Se introduce el concepto de bio-sensor así como los parámetros que caracterizan el funcionamiento de los mismos. Se dará una introducción general de electrólisis, inducida tanto mediante batería así como utilizando un (foto)-electrodo semiconductor no-degenerado. Se destacarán parámetros que cuantifican y describen el mecanismo de electrólisis.

Capítulo V: Especificaciones respecto al crecimiento de películas delgadas/nano-estructuras. Las muestras fabricadas y estudiadas a lo largo de esta tesis contienen las siguientes estructuras:

(a) Crecimientos sobre sustratos de plantillas GaN-sobre-zafiro(0001):
  (i) Capas individuales de InGaN de alto contenido de indio (In).
  (ii) QDs de InN sobre (las antes mencionadas) capas individuales de InGaN.
(b) Crecimientos sobre sustratos de Si(111).
  (iii) Capas individuales de InGaN de alto contenido de In.
  (iv) Redes de nano-paredes de InGaN.
  (v) QDs de InN sobre capas individuales de InGaN (antes mencionadas), nano-paredes de InGaN, así como directamente sobre el substrato.
  (vi) Nano-columnas de InGaN.

Este capítulo provee un análisis sistemático, en relación al manejo de la morfología de películas delgadas/ nano-estructuras por medio de la relación de flujo de materiales de grupos III y V (III/V). A medida que la relación III/V varíe desde valores casi estequiométricos (III/V~1), a rico en nitrógeno (III/V<1), y más aun a, altamente rico en nitrógeno (III/V<<1), la morfología evoluciona desde: película compacta a redes de nano-paredes y en una morfología de columnas (nano-columna). Este capítulo también entrega una visión en cuanto a las propiedades morfológicas y estructurales de las películas delgadas/nano-estructuras crecidas, que son relevantes para el desarrollo de la tesis.

Capítulo VI (dividido en 3 partes): La primera presenta los resultados de las medidas potenciométricas de las estructuras crecidas sobre plantillas de GaN, para el uso en aplicaciones de bio-sensor. En específico, se presenta la respuesta de las muestras con QDs de InN en la superficie de una capa de InGaN sola y se compara con capas individuales de In(Ga)N sola. Las medidas realizadas revelan que la muestra que contiene los QDs de InN se comporta de manera más estable (en tiempo) y tiene mayor sensibilidad (de hecho, la respuesta de las capas individuales de In(Ga)N sola es inestable en el tiempo). En consecuencia, se demuestra que el uso de QDs de InN (sobre la superficie de la capa de InGaN) lleva a una mejora significativa de funcionamiento del bio-sensor de glucosa y colesterol. Un comportamiento no-nernstiano ha sido observado, que indica un efecto catalítico inducido por la presencia de los puntos cuánticos incrementando la actividad redox en la superficie. Todas las figuras de mérito son presentadas y discutidas.

La segunda parte presenta dos estudios comparativos relacionados a aplicaciones de separación de agua. El primero involucra dos estructuras (i) una capa de InGaN sola crecida sobre una plantilla de GaN y (ii) red de nano-paredes crecida sobre Si(111). Mientras que se observa una muy buena fotocorriente y eficiencia de generación de hidrógeno en ambos casos (esto sin alimentación externa), la última estructura (ii) presenta una mejora en los valores observados. El segundo estudio involucra dos estructuras diferentes crecidas sobre plantillas de GaN: (i) una capa individual de InGaN y (ii) puntos cuánticos de InN sobre una capa de InGaN. Son discutidos extensamente los resultados así como las tendencias observadas.

La tercera y última parte consiste en estudiar las propiedades electroquímicas mediante experimentos en base de medidas de ciclo voltametría. El estudio consiste en un análisis electroquímico extenso de la reacción redox que sucede en la superficie las películas delgadas/estructuras crecidas sobre Si(111) y cuáles son los parámetros en una exploración típica de voltametría cíclica (CV) modificados a causa de: 1) contenido de In, 2) área superficial y 3) inclusión de puntos de cuánticos de InN. Para realizar los experimentos se empleó una sonda redox de hexacianoferrato(II) potásico/ hexacianoferrato(III) potásico. Los resultados demuestran que es necesario encontrar un equilibrio óptimo entre eficiencia catalítica (incrementado mediante la adición de puntos cuánticos de InN) y área (activa) superficial (identificado como el plano c) para incrementar aún más la eficiencia de un bio-sensor, o foto-electrodo para foto-electrólisis, estructurado a base de QDs de InN sobre capa de InGaN. En este sentido el incremento del área activa electroquímica superficial (plano c) y catalítico (puntos cuánticos) son esenciales.

La caracterización en AFM, SEM, PL, CL, estación de puntas y HRXRD se realizó en las instalaciones de ISOM, mientras que el análisis TEM fue realizado externamente en la “Universidad de Cádiz” (España) por el grupo del Prof. Dr. *Francisco Miguel Morales Sánchez*; la caracterización de bio-sensor, y fotocatalítica fue realizada en la “Linköping University” (Suecia) por el grupo del Prof. Dr. *Marcus Willander*; la microscopía de barrido campo óptico cercano (SNOM) se realizó en el “Max Planck Institute of Microstructure Physics” (Alemania) por el Dr. *Alexander Schenichev* bajo la supervisión de *Christoph Lienau* de la “Carl von Ossietzky Universität Oldenburg”; la caracterización electrocatalítica se realizó en las instalaciones del grupo de Química Analítica en la “Universidad Complutense de Madrid” (España) por el grupo del Prof. Dr. *José Manuel Pingarrón*, las mediciones cuantitativas de producción de hidrógeno y oxígeno fueron realizadas por M. Phil. *Ameed ul Hassan Alvi* miembro del departmento de Física en la Universidad de Agricultura en Pakistan y M. Phil. *Waheed ul Hassan* miembro del departamento de Química en la Universidad Bahauddin Zakariya en Pakistan.

ABSTRACT

This thesis, entitled “Investigations on III-Nitrides Nanostructures: Application to Renewable Energies and Bio-Sensing”, presents the work done at the “Instituto de Sistemas Optoelectrónicos y Microtecnología” (ISOM).

The main objective of the presented work is:

> To investigate the potential of III-nitride (In(Ga)N, in particular) thin films/nanostructures for biosensors and water-splitting. The investigated structures have varying In contents (from medium to high) and varying morphologies, that are: thin compact InGaN films, InGaN nanowall networks, InGaN nanocolumns and InN quantum dots

The thesis addresses:

> The molecular beam epitaxy growth of the mentioned thin films/nanostructures, on either GaN templates or Si(111) substrates, and their detailed morphological, structural, optical and electrochemical characterization.
>
> The insight and systematic evaluation of their electrochemical performance, for their final employment in bio-sensing and water-splitting applications.

The work is presented as follows:

Chapter I: The motivation for the work (including state of the art) and main goals of the thesis are explained.

Chapter II: The fundamental properties of the employed material (III-nitrides) and employed nanostructures (nanocolumns and quantum dots (QDs)) are given. Due to their importance for the thesis development, the fundamental properties having a direct impact on the electrochemical activity of the employed material (III-nitrides).

Chapter III: Details about experimental techniques used for the thesis realization are presented: epitaxial growth technique (MBE), morphological characterization (SEM and AFM), structural characterization (X-ray diffraction and TEM), optical characterization (PL, CL and SNOM), as well as chemical (GC) characterization.

Chapter IV: Application related characterization of the structures, grown on both GaN templates and on Si(111), is addressed. For this, a general overview of electrochemistry for metals and (non degenerated n-type) semiconductors electrodes is

provided after which a discussion on the (degenerated n-type semiconductor) high In-content InGaN electrode is given. The biosensor concept is introduced as are the parameters that characterize its performance. A general introduction to water-splitting is given (both induced by electrolysis or with the aid of a non-degenerated semiconductor (photo)-electrode). Important parameters needed to fully characterize the water-splitting process/device will be highlighted.

Chapter V: Specifications concerning the thin film/nanostructures growth. The samples fabricated and studied throughout this thesis, contain the following structures:

(a) Grown on GaN templates:
  (i) high Indium (In) content InGaN single layers
  (ii) InN QDs on the top of (previously addressed) InGaN single layers
(b) Grown on Si(111) substrate:
  (iii) high In-content InGaN single layers
  (iv) InGaN nanowall networks
  (v) InN QDs directly on top of the substrate, and also on the top of (previously addressed) InGaN single layers and nanowall networks
  (vi) InGaN nanocolumns

This chapter provides a systematic analysis, regarding the control of the thin film/nanostructure morphology by the means of III/V flux ratio. As the III/V ratio changes from nearly stoichiometric (~1), to nitrogen rich (<1), and further, to highly nitrogen rich (<<1) one, the layer morphology evolves from compact to a nanowall-network morphology and further to a fully columnar morphology (nanocolumns). This chapter also provides insight into those morphological and structural properties of the grown thin films/nanostructures, which are relevant for the further development of the thesis.

Chapter VI (divided in three parts): In the first part it presents results of potentiometric measurements of the structures grown on GaN templates, targeted for biosensing applications. Specifically, the response of the samples containing surface InN QDs on single InGaN layers is compared to their counterpart samples, consisting of bare single In(Ga)N layers. The measurements reveal that the sample containing surface QDs show higher and more stable (in time) responsivity (actually, the response of bare In(Ga)N films is found highly decreasing over time). We consequently show that the employment of surface InN QDs (on the top of thin InGaN layers) leads to a significantly improved performance of glucose and cholesterol biosensors. Non-nernstian behaviour is observed indicating that the InN QDs have a catalytic effect enhancing the redox reaction at the surface. All figures of merits are addressed and thoroughly discussed.

In the second part it presents two comparative studies related to water-splitting applications. The first study involves two different structures (i) a thin InGaN single layer grown on GaN template substrate: and (ii) InGaN nanowall network grown on (a nitridated) Si(111). While excellent photocurrent and Hydrogen production efficiency are observed in both cases (with zero bias applied), somewhat better results are obtained for the latter structure. The second study involves two different structures grown on GaN templates: (i) a single InGaN layer and its (ii) InN QDs on InGaN layer counterpart. In this case, a considerable efficiency increase is observed by the inclusion of InN QDs. The background results for the observed tendencies are thoroughly discussed.

The third and last part includes electrochemical analysis of the grown samples by cyclic voltammetry measurements. An extensive analysis of the redox reaction occurring at the interface of all the layers/nanostructures grown on Si(111) and, on the other hand, an analysis determining which parameters (redox potentials, shape, etc) in a typical CV scan are influenced by: (i) In content, (ii) surface area and (iii) presence of surface InN QDs. To conduct experiments, a redox potassium hexacyanoferrate (II) / potassium hexacyanoferrate (III) probe was used. The results show that an optimum balance between catalytic efficiency (which is increased by the addition of surface InN QDs),and (active) surface area (the free c- crystal plane (0001) is identified as the crystal plane inducing surface electrochemical activity), needs to be found, to further boost the efficiency of InN-QDs-on-InGaN-layer based biosensors and water-splitting electrodes. In this sense, the enhancement of catalytic efficiency and increase of electrochemically active surface area (that is, increase of free c-plane surface) are essential.

The characterization by AFM, SEM, PL, CL, probe station and HRXRD was performed at ISOM´s facilities whereas the TEM analysis was performed externally at the “Universidad de Cádiz” (Spain) by the group of Prof. Dr. *Francisco Miguel Morales Sánchez*; bio-sensing, photocatalytic characterization done at “Linköping University” (Sweden) by the group of Prof. Dr. *Marcus Willander*; scanning near field optical microscopy (SNOM) measurements were performed at the “Max Planck Institute of Microstructure Physics” (Germany) by Dr. *Alexander Schenichev* under the supervision of *Christoph Lienau* from “Carl von Ossietzky Universität Oldenburg”; the electrocatalytic characterization was done at the facilities of Chemical Analytical group at “Universidad Complutense de Madrid” (Spain) by the group of Prof. Dr. *José Manuel Pingarrón*, the quantitative measurements for Hydrogen and Oxygen production were carried out by M. Phil. *Ameed ul Hassan Alvi* member of the department of Physics at the University of Agriculture in Pakistan and M. Phil. *Waheed ul Hassan* member of the department of Chemistry at the Bahauddin Zakariya University in Pakistan.

ACRONYMS

Acronyms listed in alphabetical order.

2 DEG	Two-dimensional electron gas
λ_B	Broglie wavelength of electron
A^0X	Acceptor-bound excitons
AC	Alternating current
AFM	Atomic force microscopy
Al_2O_3	Sapphire
AlN	Aluminium nitride
APD	Avalanche photo diode
As	Arsenide
BEP	Beam equivalent pressure
BF	Bright-field
BSF	Base stacking fault
$CaCl_2$	Calcium chloride
CBM	Conduction band minimum
CCD	Charge-coupled device
CdS	Cadmium sulfide
CdSe	Cadmium selenide
CE	Counter electrode
CHox	Cholesterol oxidase
CL	Cathodoluminescence
Co	Cobalt
CV	Cyclic voltammetry
D^0X	Donor-bound excitons
DC	Direct current
DF	Dark-field
EBL	Electron beam lithography
E_c	Conduction band energy position
EC	Electrochemical cell
ECD	Electron capture detector
EDS	Energy dispersive X-ray spectroscopy
E_f	Fermi energy
E_g	Bandgap energy
EMF	Electromotive force
E_v	Valance Band Energy position
Fe	Iron
FE-SEM	Field emission SEM
FIBL	Focused ion beam lithography
FID	Flame Ionization detector
FvdM	Frank van der Merwe
FWHM	Full width at half maximum
FX_A	A-exciton
FX_B	B-exciton
FX_C	C-exciton
Ga	Gallium
GaAs	Gallium arsenide
GaN	Gallium nitride
GaP	Gallium phospide
GC model	Gouy-Chapman model
GC	Gas chromatography
Ge	Germanium
GOD	Glucose oxidase
HAADF	High-angle annular dark-field

He	Helium
He-Cd	Helium-cadmium
HEMT	High-electron-mobility transistor
HH	Heavy hole
HRTEM	High-resolution TEM
HRXRD	High resolution X-ray diffraction
HVPE	Hydride vapour phase epitaxy
IHP	Inner Helmholtz plane
InGaN	Indium gallium nitride
InP	Indium phosphide
IPCE	Incident power density efficiency
IR	Infrared
ISOM	Instituto de Sistemas Optoelectrónicos y Microtecnología
I-V	Current-voltage
K-Cells	Knudsen cells
LD	Laser diode
LEDs	Light emitting diodes
LEEBi	Low energy electron beam
LEED	Low energy electron diffraction
LFM	Lateral force microscopy
LH	Light holes
LPE	Liquid phase epitaxy
LT	Low temperature
MBE	Molecular beam epitaxy
Mg	Magnesium
MLs	Monolayers
Mn	Manganesium
MOVPE	Metal organic vapour phase epitaxy
NaCl	Sodium chloride
NaOH	Sodium hydroxide
NCs	Nanocolumns
NWM	Nanowall matrix
NWN	Nanowall network
OED	Optical emission detector
OHP	Outer Helmholtz plane
PA	Parameter analyzer
PAMBE	Plasma assisted MBE
PBS	phosphate buffered saline
PEC	Photo-electrochemical
PL	Photoluminescence
PMT	Photomultiplier tube
QCSE	Quantum confined Stark effect
QDs	Quantum dots
QMS	Quadrupole mass spectrometer
QSE	Quantum Stark effect
QWs	Quantum wells
RE	Reference electrode
RF	Radio frequency
RHEED	Reflection high-energy electron diffraction
RMS	Root-mean-square
RSM	Reciprocal space map
RT	Room-temperature
SAD	Selected area diffraction

Sb	Antimony
SEM	Scanning electron microscopy
SFs	Stacking faults
SHE	Standard hydrogen electrode
Si	Silicon
SiC	Silicon carbide
SiNx	Silicon nitride
SK	Stranski-Krastanov
SNOM	Scanning near-field optical microscopy
SQDs	Surface quantum dots
STEM	Scanning TEM
TCD	Thermal conductivity detector
TDs	Threading dislocations
TEM	Transmission electron microscopy
TES	Two-electron satellite
TM	Transition metal
TOF	Time of flight
TSRs	Tetrahedral-shaped recesses
UHV	Ultra high vacuum
UV	Ultaviolet
VBM	Valence band maximum
VDW	Van der Waals
VW	Volmer-Weber
WE	Working electrode
WL	Wetting layer
Wz	Wurtzite
YB	Yellow band
ZB	Zinc blend
ZnO	Zinc oxide

We live searching answers on all possible scales, from macro to nano and around the world to ourselves. Science is our transport and devoted i am; to maintain myself on track and go so far as possible as I can, and my quest starts and hopefully prevails, satisfied only by the journey of life itself.

CHAPTER 1

INTRODUCTION AND GOALS

1.1 A historical perspective

1.1.1 Gallium Nitride (GaN) Research

In terms of research, GaN had its breakthrough around the 1970´s when the first GaN single crystals growth was obtained and its optically pumped stimulated emission was observed [Dingle 1971]. The main problems were due to the absence of a native substrate. The large lattice-mismatch between substrate and the grown epilayers results in bad quality of the latter. The best results were obtained after introducing an AlN (later a GaN) buffer layer on sapphire [Akasaki 1989, Nakamura 1991a]. Growth was mainly performed by Metal Organic Vapour Phase Epitaxy (MOVPE) at quite high growth temperature and low pressure, which was a real technological bottleneck at that time, so that, a change in reactor design or growth technique was required [Amano 1986, Nakamura 1991b, Kung 1995]. Then, an increase in crystal quality was attained, but still having high threading dislocations densities (TDs) in the range of 7×10^8 to 10^{10} cm^{-2} [Lester 1995, Kapolnek 1995, Heying 1996].

Another critical issue was to accomplish an efficient p-type doping and hole conductivity in GaN. It was not until 1989 that p-type GaN was achieved by Amano et al. using Mg as dopant and an ex-situ low energy electron beam (LEEBI) treatment [Amano 1989]. However, the explanation and solution for the poor conducting properties of p-type attempts of GaN was given later by Nakamura[1] [Nakamura 1992a,b] together with a cheap and easy process to solve it (thermal annealing), what opened the way to commercialise the premier efficient blue Light Emitting Diodes (LEDs). On the other hand, the strong internal electric fields induced by the lack of inversion symmetry in the wurtzite (Wz) structure causes a separation of electron and hole wavefunctions leading to a reduction in radiative efficiency [Chichibu 1996] and emission energy shifts due to quantum confined Stark effect (QSE). This phenomenon limits the maximum width of quantum wells (QWs) in the device active regions in order to reduce the separation of electron and hole wavefunctions. In addition, polarization-induced electric fields produce a red shift of emission wavelength at

---

[1] Nakamura showed that H radicals from NH_3 or H_2 present in the growth environment passivate the Mg dopant. Other research showed that LEEBI or a simple thermal annealing in an NH_3 free environment was able to facilitate out-diffusion of the passivating H radicals.

low carrier density by QSE and a further blue shift with increasing carrier density by screening effect [Bernardini 1997].

Developments in crystal growth and doping led to the demonstration of GaN p-n LEDs in 1991, and with further epitaxial growth improvements, the first AlInGaN based laser diode (LD) in 1996 [Akasaki 1991, Nakamura 1991c, 1996]. For these results, mainly the efficient generation of blue and white light, the authors were awarded the Nobel Prize in 2014 [Nobel Media]. Since then several improvements were made to enhance crystal quality by using different growth techniques to grow on different crystal orientations and substrates and so increasing recombination life times [Miyajima 2001] and reducing polarization-induced electric fields and threading dislocations (TD) densities [Kucharski 2009].

Nowadays, violet and blue c-plane laser diodes reached maturity with very high output powers and long lifetimes, leading to commercialization of ultraviolet LDs for Blue-ray discs, high power projectors and pico-projectors. Meanwhile, the struggle keeps on achieving efficient, long-lived ultraviolet (UV) and green LDs. Also III-Nitrides represent a breakthrough for High Electron Mobility Transistors (HEMT) technology due to high saturation velocity and heat transfer, making GaN the second largest material used in semiconductor industry [Web 2014].

1.1.2 Indium Nitride (InN) Research

A large part of the history of research on InN goes in line with GaN. The premier synthesized InN powder was obtained in 1934 by Juza and Hahn [Juza 1938] giving the initial values for lattice parameters[2]. Later on and up to 1990 a sporadic research was performed, concerning mainly studies of basic properties. The dissociation of InN under nitrogen overpressure and the determination of its direct bandgap nature was studied along the 1970s [MacChesney 1970, Hovel 1972]. Growth of InN material by Hydride Vapour Phase Epitaxy (HVPE), presented a very high “residual” electron concentration, in the order

---

[2] InN was obtained from decomposition of $InF_6(NH_4)_3$ at 600 ºC. Juza and Hahn reported the crystal structure of InN to be wurtzite having lattice parameters a=3.533±0.004 Å, and c=5.698±0.004 Å. Surprisingly very close to today’s reported values. In the same article they also studied GaN crystals; however we only highlight InN results as it was, more precisely its bandgap, origin of controversy on a later timescale.

of 10^{20} cm^{-3} [Marasina 1977] compared to 10^{18} cm^{-3} [Hovel 1972] from material grown by sputtering. Therefore, the sputtering was for a long time the preferred growth technique.

Until the end of the 80's the InN bandgap was thought to be around 1.89 eV considering absorption properties of sputtered material [Tansley 1986]. In the last two decades MOVPE and MBE (molecular beam epitaxy) techniques allowed producing films of significantly higher quality [Davydov 2002, Lu H. 2000, Saito 2002]. Nevertheless, a controversy persisted on determining the InN direct bandgap value. An interesting discussion and overview was given by Butcher and Tansley [Butcher 2005], pointing to a spread on reported bandgap values from 1.1 eV [Inushima 2001], 0.9 eV [Davydov 2002], 0.8-0.7 eV [Wu 2002, Nanishi 2003] down to 0.65-0.6 eV [Higashiwaki 2004, Haddad 2003]. The origin of this discrepancy was attributed to several possible reasons, most of them providing only partial explanations. Suggestions for observations of a higher band-gap included degeneracy effects due to the features of small effective electron mass and high carrier concentrations (a strong Moss–Burstein effect), oxygen inclusion. Smaller energy band-gap values were explained by defects, non-stoichiometry, film non-uniformity and Mie resonances.

J. Wu et. al. [Wu 2003] reported the most recent and accepted value of InN bandgap to be 0.65 eV by photoluminescence measurements on an InN sample grown by MBE. The finding of the new bandgap value allowed considering the ternary indium gallium nitride (InGaN) as a wide bandgap material being able to cover the light spectrum from near ultra violet (360 nm, GaN) to near infrared (1.7 μm, InN).

In 2004, H. Lu et al. [Lu H. 2004] reported a strong and fast electrical response (i.e. large increase in surface carrier density) of the InN surface, when it was exposed to certain chemical solvents. This property was found highly appealing InN application in both chemical and biological sensors. An extremely important property of high In-content In(Ga)N is its high positive (donor-like) density of surface states. Several groups have demonstrated the downwards bending of the conduction and valence bands of InGaN with In-content above 40% as a consequence of surface electron accumulation generated by the mentioned positive surface states to compensate the charge [Bailey 2008, Linhart 2012]. The crucial role of surface states in chemical sensing performance, for the case of arsenide systems [Milla 2014a,b], has been shown recently. This fact shows that active sites promoting redox reactions are directly related to the presence of donor states. Therefore, the contribution of high donor state densities (at In(Ga)N surfaces) in combination with quantum dot (QD) properties, opens the door for novel sensor designs. This work will, on one hand, provide experimental evidence that demonstrates potential of high In content In(Ga)N nanostructures (in particular InN QDs) for chemical and biological sensors, and on the other hand, will propose models for better insight into underlying mechanisms which drive the sensing applications. Therefore, the material properties responsible for high electron accumulation will be addressed in more detail in the next chapter. Proof of concept on biosensors performance will be presented for two widely studied analites as are glucose and cholesterol. Glucose is an important analyte for clinical usage sampling for which its concentration levels in blood are vital to be monitored. The same is valid for food-industry, where a good control on the glucose concentration levels is eessential. As an example, consider standard range levels in blood: Normal blood glucose level for non-diabetics lies below the 6.9 mmol/L (too low levels is also harmful because below 2.2 mmol/L extreme hypoglycaemia is determined) and according to the American national institute of health (NIH) values above on the longterm leads to hyperglycaemia which may cause heart disease, eye, kidney and nerve damage. The most common cause of hyperglycaemia is diabetes and for diabetics, according to the American diabetes association, the recommended glucose levels are between 5-7.2 mmol/L before meals and 10 mmol/L after meals. For the case of Cholesterol, it can be harmful (leading to narrowing of arteries in the body that cause heart attacks, strokes and peripheral artery disease) when present in large quantities in the bloodstream, therefore its analysis and supervision is critical. Several regulation standards hold which are established by local health departments of each nation; for example in UK the standard from the national institute for health and care excellence (NICE) recommends a cholesterol level below 7.5 mmol/l on the other hand in USA according to the national cholesterol education program (NCEP) a division of the national heart, lung and blood institute (NHLBI) the total cholesterol level is recommended to be below 240 mg/dl (13.33 mmol/L).

Full potential of InGaN alloys cannot be explored unless the complete composition span is achieved with a proper substrate which is yet to be found. The observed properties of InN also implied that the ternary InGaN could present thus a high electron mobility [Polyakov 2006] that together with a tunable bandgap would become a unique material choice for near-infrared high-speed optoelectronic devices (such as terahertz emitters) [Kryliouk 2005, Lu 2007, Cimalla 2007, Wilke 2008, Lim 2008, Lu 2009, Sofikiti 2009a].

The rising increase of interest in InGaN alloys is depicted in figure 1.1. The research trend measured by the yearly amount of publications is presented over the last two decades.

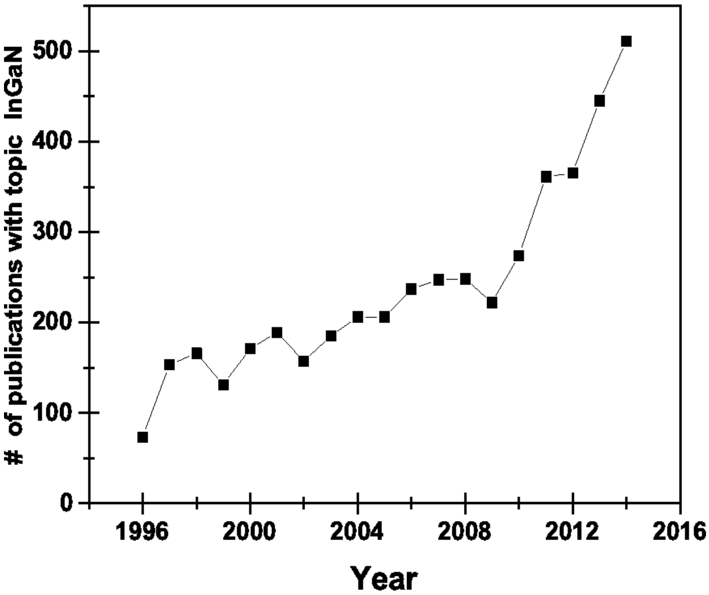

Figure 1.1: Research trend on InGaN, as measured from the number of publications in the last 2 decades. Source of information: *Sciencedirect.*

The search of renewable energy sources is currently one of the most investigated fields to alleviate the need of energy consumption in the world with environment-friendly solutions. The limited availability of oil and gas [Tverberg 2012, Web Earth] together with the increase of air and water pollution [Fenger 2009] demands an urgent reaction to search clean and "unlimited" energy sources. A huge effort has already been made on photovoltaics (PV) where new materials, structures and designs have been proposed.

Hydrogen generation is of great interest even considering small scale systems for specific applications, and nowadays the needed technology is available [Coelho 2010]. In terms of fuel, hydrogen generation by water splitting is one of the most interesting areas of the research to overcome or ease potential energy shortage from other classical sources.

Different new materials have been investigated for electrochemical electrodes to enhance water splitting and to mimic the process observed in nature. High electron surface accumulation and high chemical stability of high-In-content In(Ga)N, make it one of the most promising materials for investigation towards water splitting and biosensing applications.

1.2 Goals and structure

The main goals of the present research are the following ones:

- To study the growth of high In-content InGaN layers on GaN templates.
- To use the above high In-content InGaN layers as buffers to grow InN QDs on top.
- To investigate and compare the high In-content InGaN layers, grown on GaN templates, with and without InN QDs, as glucose and cholesterol biosensors and water-splitting applications.

Once the initial results have been obtained on GaN templates, the next goal is to extend these achievements on cheap Si(111) substrates and where lower crystalline quality is expected, fact non critical for final device performance in envisaged applications (biosensing and water splitting). More specifically, the goals are:

- To study the growth of high In-content InGaN layers and nanostructures on nitrided Si(111) substrates:
    - InGaN thin films (single layers)
    - InGaN nanowall-network (NWN), which refers to an InGaN matrix (typically faceted) formed in the early stage of 3D InGaN growth on Si(111).
    - InGaN nanocolumns (NCs).
    - InN QDs on the top of the above mentioned (high In-content) InGaN thin films and NWNs .
    - InN QDs on nitrided Si(111) (no InGaN buffers)
- To test the InGaN NWNs as photoanodes for water-splitting applications.
- To evaluate the surface electrochemical performance of InGaN thin films/nanostructures (grown on nitrided Si(111)).

1.2.1 Structure

In order to accomplish these goals, the work is organized in four blocks all of which are considered as results and discussions:

1. Characterization:
   In this chapter the most relevant parameters and properties, related to electrochemistry of semiconductor materials is introduced. First, the concept of "water-splitting" and its relevant hallmarks (hydrogen generation, stability, operation mode, etc.) are discussed. Second, the full description of the concept "bio-sensor" as well as its (desired) features (fast and stable response, selectivity and

sensitivity) is given. Third, the parameters (and/or properties), such as: redox potential, shape and symmetry of CV curve, peak current, nernstian behaviour are explained together with the experimental procedures to assess these parameters.

2. Epitaxial Growth and basic characterization:

- ❖ Growth by plasma assisted molecular beam epitaxy (PA-MBE) of III-nitrides on GaN templates is rather well known, being the most common substrate of choice. However, growing high In-content InGaN good-quality layers is still challenging due to the poor crystalline quality arising from high mismatch (between In(Ga)N and GaN) and the low growth temperatures needed to incorporate enough In. To overcome the before mentioned issues, the growth conditions are varied to seek for the best quality (that, in addition, should allow the grown thin film to be used as a template for InN QDs growth). Evisaged applications (biosensing and water splitting) do not rely on extremely high crystalline quality as is the case for optoelectronic applications. Evenmore, the lower crystalline quality introduces more surface states which on the other hand are important factors for final improved device performance.

  Although InGaN NCs directly grown on Si(111) keep an excellent crystal quality (mainly due to their small footprint and early relaxation), the growth of uniform, high crystal quality flat 2D InGaN layers is found more difficult. This work addresses the optimal growth conditions to grow InGaN layers on Si(111) with the best structural and optical properties. InN QDs have been also grown on both high In-content 2D InGaN layers and InGaN NWNs. All characterizations displaying that the realized growth complies with the optimal conditions (morphological, structural and optical), are presented.

3. Applications: Bio-sensing and water-splitting

- ❖ All optimized InGaN layers grown on GaNtemplates were considered and studied as glucose and cholesterol biosensors. The high In-content InGaN layers, with and without InN QDs, as well as thin InN films, were compared in terms of sensor performances. Potentiometric measurements were used to fully characterize the biosensor looking at response time, selectivity, durability and sensitivity as most remarkable hallmarks.
- ❖ InGaN NWNs grown on Si(111) and high In-content InGaN layers grown on GaNtemplates were characterized as water-splitting devices. The study of the optical properties of InGaN NWNs revealed that the material band gap energy is above the energy required for efficient water splitting (1.23 eV). This property qualifies these structures as potential ones for water-splitting application. Similar performance was found in high In-content InGaN layers grown on GaN templates. Both structures were (comparatively) tested as photoanodes with zero external applied bias for water-splitting.
- ❖ The role (and background mechanisms) of InN QDs in water-splitting devices was addressed. This was done by comparing the hydrogen production efficiency of bare

InGaN layers, grown on GaN templates, with their counterparts, covered with surface InN QDs.

4. Electrochemical performance analysis:

- To evaluate the electrochemical performance of the InGaN samples grown on Si(111) substrates. In this study the idea is to evaluate the contribution of: (i) In content (ii) surface-to-volume ratio (optimum amount of electrochemical active area is searched playing thus the crystal planes a critical role) and (iii) the presence of surface QDs to the electrochemical performance of InGaN layers (regarding increase of peak current, shift of redox potential as shape of the curve). For this analysis a well-known potassium hexacyanoferrate (II) / potassium hexacyanoferrate (III) redox probe is used.

  To understand the influence of **In-content** on the surface electrochemical activity, four different InGaN single layers with In-contents of 6%, 35%, 73% and 88% (grown on Si(111)) were analysed by cyclic voltammetry.
  To understand the influence of different **crystal planes** on electrochemical activity, nanostructures with different morphologies were studied. It is well-known that for nanocolumns the surface to volume ratio is larger than for compact films. Bearing in mind that the electrochemical activity is driven by free-surface, this fact should favour the NCs for chemical sensing. However, in compact film the free-surface is mainly composed by c- crystal plane, whereas in nanocolumns it is mainly composed by nonpolar m-planes (NC side walls), being the amount of polar c-planes (NC tops) typically very low (roughly estimating, few percent or less) This means that the change of the surface-to-volume ratio is inevitably linked to the amount and type of surface crystal plane. The study of different morphologies, containing different surface-to-volume ratios, provides a way to distinguish the electrochemical activity on different crystal planes. Generally speaking, the idea that increased surface-to-volume ratio leads to enhanced electrochemical activity is widely accepted; to check the validity of this assumption, different crystal planes were intentionally involved into electrochemical response, via employment of bulk layers, NWNs and NCs (grown directly on nitridated Si(111)).
  Finally, to evaluate the influence of surface InN QDs, the electrochmecal response of (i) bare InGaN layer and InGaN layer with InN QDs on top as well as (ii) bare NWN and NWN with InN QDs on top have been compared.

CHAPTER 2

FUNDAMENTAL PROPERTIES OF III-NITRIDES

This chapter provides a review of the III-nitride films basic properties, more specifically of gallium nitride (GaN), indium nitride (InN) and indium gallium nitride (InGaN), that will be of interest to understand their epitaxial growth and applications for bio-sensing and water-splitting. In addition, an overview of the properties of III-nitride nanostructures like nanocolumns (NCs) and quantum dots (QDs) is given. Finally, a small survey on found chemical sensing properties for InN will be delivered.

2.1 Crystalline structure of III-nitrides

In general, materials properties are determined by their crystallographic structure. Group III nitrides may have wurtzite (Wz), zincblend (ZB), or rock salt structure. The last one can only be obtained under extremely high pressure [Xia 1993] conditions but not by epitaxial growth, hence only Wz and ZB structures will be discussed in the following. These structures are very well known and a wide amount of work and details can be found in the literature [Kittel 1956]. In the case of ZB[3] the cubic unit cell has four group III atoms and four nitrogen atoms. The position of the atoms within the unit cells is identical to that in the diamond crystal structure. The stacking sequence for the (111) closed-packed planes in this structure is the AaBbCc. Small and large letters stand for the two different constituents. A scheme of this sequence is shown in figure 2.1.

In the case of Wz[4], its unit cell has a hexagonal structure and thus two lattice constants c and a. As can be seen from figure 2.2 (a), the Wz structure consists of two interpenetrating hexagonal close-packed (hcp) sub-lattices, each with one type of atom, and offset of 5/8 of the cell height (5c/8). There are alternating bi-atomic close-packed (0001) planes of gallium (Ga) and nitrogen (N) pairs, thus giving a stacking sequence of AaBb in the (0001) direction. The most commonly used planes in Wz are presented in figure 2.2 (b), corresponding to the (0001) c-plane, the (11-20) a-plane, (11-22) r-plane, and (1-100) m-plane.

---

[3] In terms of crystallographic notations crystal structures are denoted in space groups, the ZB is the F43m in the Hermann-Mauguin notation and T2D in the Schoenflies notation.

[4] Wz structure belongs to the space grouping P63mc in the Hermann-Mauguin notation and C46v in the Schoenflies notation. The point group symmetry is 6mm in the Hermann-Mauguin notation and C6v in the Schoenflies notation.

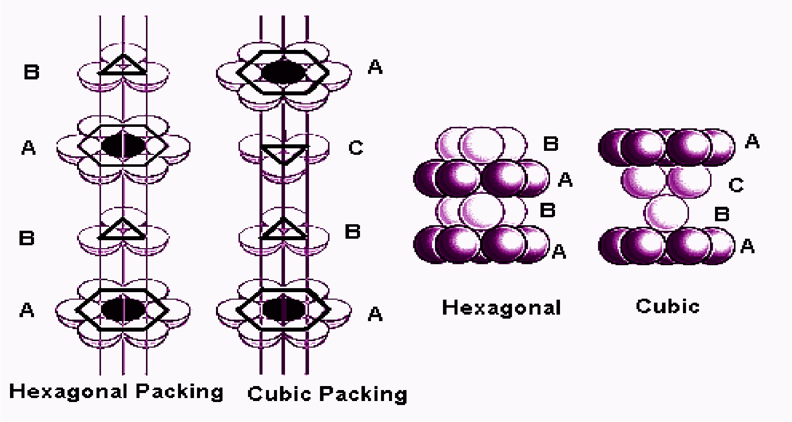

Figure 2.1: Stacking sequence for the (111) closed-packed planes in ZB structure is AaBbCc. Small and large letters stand for the two difference constituents.

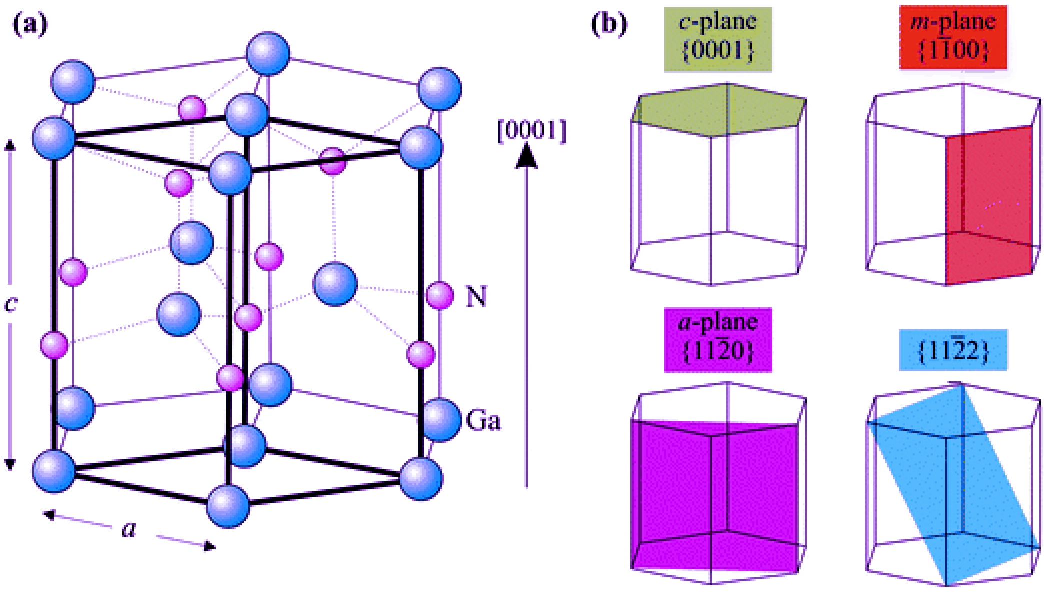

Figure 2.2: (a) Scheme of the wurtzite structure; (b) Most common used planes in wurtzite.

Between Wz and ZB structures the only difference is the bond angle, the ZB shows a 60° bond angle along the (111) rotation in contrast to the Wz (0001) direction giving the difference in stacking sequence. The Wz III-nitride group lacks an inversion plane perpendicular to the c-axis. This fact is responsible for nitride surfaces to have either a group III element (Al, Ga or In) polarity with a designation of (0001)A plane or a N-polarity with a designation of (0001)B plane, the so-called spontaneous polarization (P_{sp}). This P_{sp} has been found to increase from GaN over InN to AlN and it also has a negative sign. However, mechanical stress also results in polarization, which is then called piezoelectric polarization (P_{pz}). As both polarization are 'on the same plane', the total polarization is just the sum of both, see figure 2.3.

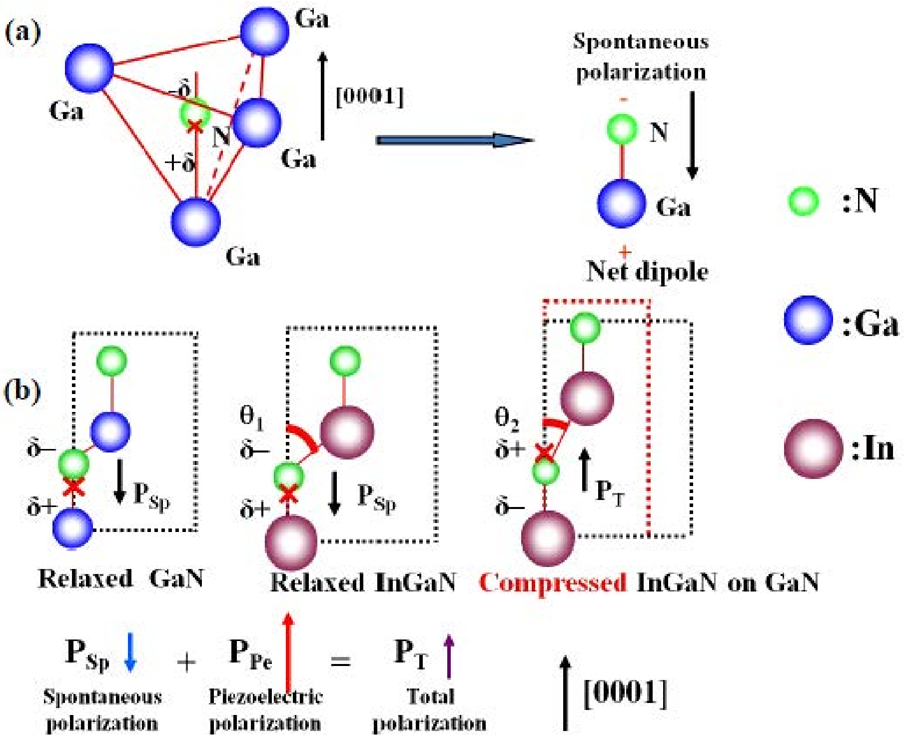

Figure 2.3: Schematic diagrams of (a) spontaneous and (b) piezoelectric polarization. Taken from [Sun, 2011]

	Parameter	InN	GaN
Lattice constant	a^{*}	3.5377 Å	3.1884 Å
Lattice constant	c^{*}	5.7037 Å	5.1850 Å
Elastic coefficient	C_{13}^{*}	85 GPa	101 GPa
Elastic coefficient	C_{33}^{*}	236 GPa	395 GPa
Electron mobility	μ_e^{**}	2050 cm^2 /V s	900 cm^2 /V s
Density	ρ^{**}	6.81 g/cm^3	6.15 g/cm^3
Effective electron mass	m^{*}_{e}/m_0^{**}	0.07	0.20
Bandgap	E_g^{**}	0.64-0.7 eV	3.45 eV

Table 2.1: Material properties for InN and GaN ** [Wu 2009];* [Morales 2009]

The crystalline structure can be considered to be the equivalent of the material's 'DNA', as it defines all optical, thermal, and electrical properties. Any modification on the crystal structure variable (such as atom, lattice parameter, angle bond, etc.) changes therefore the before mentioned properties. In this thesis, the GaN, InN and the ternary alloy InGaN are of most importance, therefore, a summary of these materials structural parameters concerning stress/strain, lattice constant, and effective mass is given in table 2.1.

Vegard´s law [Vegard 1921, 1928] states that the crystallographic parameters of a continuous substitutional solid solution vary linearly with its concentration (at constant temperature) when the nature of the bonding in the constituent phases remains unchanged. It is understood in this context that the substituting atoms are statistically distributed. The lattice parameter is controlled by the relative size of the atoms or species exchanged.

However, there are several parameters that do not follow (experimentally) this law, but present a deviation, as is the case of the bandgap, which follows a “modified” quadratic version of Vegard’s law (2.1):

$$E_{In_xGa_{1-x}N} = E_{InN} \bullet x + E_{GaN} \bullet (1-x) - b \bullet x \bullet (1-x) \tag{2.1}$$

where ‘$E_{In_xGa_{1-x}N}$’ corresponds to the bandgap of the ternary $In_xGa_{1-x}N$ and ‘E_{InN}’, ‘E_{GaN}’ are the bandgaps of InN and GaN respectively. The parameter ‘b’, called bowing parameter, is to be considered as a constant characteristic of an alloy system at constant temperature and pressure. The deviation term is similar to the expression for enthalpy or excess Gibbs energy of mixing for a regular solution.

For most semiconductors the above equation (Eqn. 2.1) holds, however there are indications that the deviation could be of higher symmetry (as can be seen the deviation in Eqn. 2.1 is quadratic). A complete study on this can be found in the work done by K.T Jacob, Shubra Raj and L. Rannesh [Jacob 2007]. Most interesting is the controversy on the bowing parameter of InGaN. The presence of strain, phase separation and inhomogeneities in InGaN layers, as well as the techniques used to measure the indium composition and band gap energy of InGaN, could lead to an inaccurate determination of the bowing parameter. Indeed, values ranging from 1 to 6 eV have been reported for the InGaN bowing parameter. The dispersion of the published values indicates that it is difficult to get a universal agreement on the bowing parameter, due to the fact that InGaN samples were grown by different techniques and under different conditions. Therefore the used bowing parameters in this thesis are estimated from photoluminescence (PL) measurements at room temperature and verified by high resolution X-ray diffraction (HRXRD) measurements.

2.2 Electronic properties and bandgap

The relevant electronic properties for both bio-sensing and water-splitting applications are found in high In-content InGaN and InN films. High quality MBE grown InN films have been achieved for some time now and a growth diagram for plasma assisted MBE (PAMBE) was presented by C. S. Gallinat et al. [Gallinat 2007] which permits growth of high quality InN films. The InN has therefore been studied more in detail and a review of its main attributes of interest will be presented for discussed applications.

2.2.1 Effect of Native Defects on the Intrinsic N-type Doping

Doping is of extreme importance for optoelectronic applications. However, in early development stages GaN has shown rather difficult to be p-type doped, until better growth quality and unintentionally n-type residual doping was optimized. The p-doping problem is even more pronounced for InN because it presents a very strong n-type “residual”. In the case of InN the origin of the observed n-type conduction is still a topic of debate and investigation. Before deepening in all possible and plausible causes, a closer look to the InN bandgap is given as it originates several interesting debates with direct consequences towards the observed n-type nature.

The energy-eigenvalue problem of a semiconductor crystal yields mathematical solutions that form what is known as the band-structure of the semiconductor (also known as the dispersion relation of the material, the function of energy (E) with the wave vector k, E(k)). The majority of physical phenomena (electronic, optical, and/or magnetic) in semiconductors can be interpreted by the material band-structure, the most critical points being the local maxima in the valence band (the highest valence band points) and the local minima in the conduction band (the lowest conduction band points). The highest point of the valence band is designated as Γ-point, and it constitutes the origin point ($k_x = 0$, $k_y = 0$, $k_z = 0$) in the k-space. In the so-called direct semiconductors (the case of a huge majority of III-V semiconductors, such as GaAs, GaP and GaN), the maximum of the valence band and the minimum of the conduction band coincide in the k-space, that is, at the Γ-point. Such semiconductors nowadays form the core of most optical devices. If the minimum of the conduction band is displaced (with respect to the maximum of the valence band) and reached at another point of the k-space, the semiconductor is said to have an indirect-gap character (the case of group IV elemental semiconductors, such as Si and Ge).

A better understanding of the band-structure is obtained when looking at the energy eigenvalues of the individual atoms that constitute the semiconductor crystal. All semiconductors have tetrahedral bonds that have sp^3 hybridization. However, the individual atoms have the outermost (valence) electrons in s- and p-type orbital. The spherical s-state and the p-type lobes are depicted in figure 2.4. Let the states be denoted by $|S\rangle$, $|X\rangle$, $|Y\rangle$, $|Z\rangle$

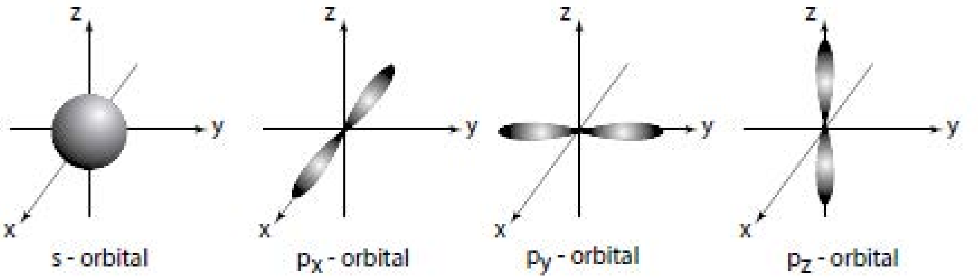

Figure 2.4: Schematic s- and p- orbitals of atomic systems. The s-orbital has spherical symmetry; the p-orbital are odd along the direction they are oriented (i.e., being anti-symmetric: the p_x orbital has two lobes, one positive, and the other negative).

When the atoms are placed in a crystal, the valence electrons hybridize (change) into sp^3 orbital that leads to a tetrahedral bonding geometry. The crystal develops its own band-structure with prohibited bands (gaps) and allowed bands. For semiconductors, the allowed bands in the band-structure can be reduced to the conduction and valence bands only. Let us mention that it has been observed that the states near the conduction band minimum behave very much like the $|S\rangle$ states, whereas the states near the valence band maximum behave very much as the linear combination of the three p states ($|X\rangle, |Y\rangle, |Z\rangle$). In that sense, the allowed states in the formed semiconductor keep a tight relation with the states of the constituent individual atoms. Figure 2.5 depicts these properties.

Dispersion at bottom of the conduction band, in narrow bandgap semiconductors, takes a non-parabolic form as was shown, e.g., by E. O. Kane for InSb and InAs [Kane 1957]. The origin of this non-parabolicity is "the $k{\cdot}p$ repulsion" across the semiconductor (narrow) bandgap. Therefore, the problem can be treated analytically with an 8x8 $k{\cdot}p$ Hamiltonian matrix, describing the electron wave function as the linear combination of p-like valence band and s-like conduction band states.

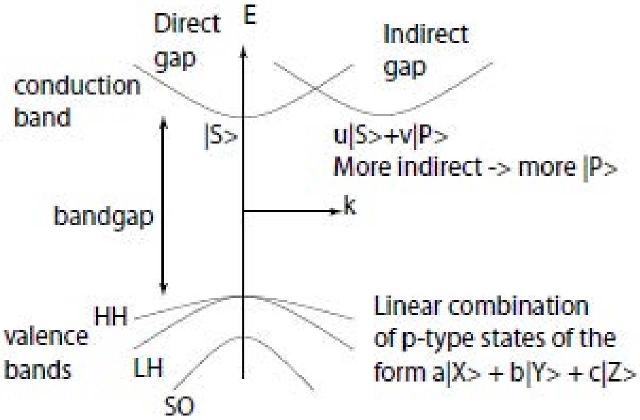

Figure 2.5: The typical band-structure of semiconductors. For direct-gap semiconductors, the conduction band state at k = 0 is s-like. The valence band states are linear combinations of p-like orbitals. For indirect-gap semiconductors on the other hand, even the conduction band minima states have some amount of p-like nature mixed into the s-like state.

For III-nitrides the crystal splitting Δ_{crys} as well as the spin-orbit coupling Δ_{so} are very small; for InN, for example, Δ_{crys} is 40 meV [Vurgaftman 2003] whereas Δ_{so} is 5 meV [Rinke 2008]. In a first approximation, these values can be neglected, allowing thus the 8x8 *k·p* Hamiltonian matrix simplification. The 8x8 *k·p* Hamiltonian matrix can be represented as the sum of two separate 4x4 matrices, one containing the pure *k·p* interaction and the other one containing the interaction of all remote bands.

Considering the electronic wave functions $|iS\rangle, \left|-X+iY/\sqrt{2}\right\rangle, \left|X-iY/\sqrt{2}\right\rangle$ and taking $|Z\rangle$ as basis:

$$H = \frac{\hbar^2 k^2}{2m_0} + \begin{pmatrix} E_g & iP_{xy}k_x & iP_{xy}k_y & iP_z k_z \\ -iP_{xy}k_x & 0 & 0 & 0 \\ -iP_{xy}k_y & 0 & 0 & 0 \\ -iP_z k_z & 0 & 0 & 0 \end{pmatrix} + H_{remote} \tag{2.2}$$

where P_{xy} and P_z are the momentum matrix elements:

$$P_{xy} = \frac{\hbar}{2m_0}\langle S|\frac{\hbar}{i}\frac{\partial}{\partial x}|X\rangle = \frac{\hbar}{2m_0}\langle S|\frac{\hbar}{i}\frac{\partial}{\partial y}|Y\rangle \tag{2.3}$$

$$P_z = \frac{\hbar}{2m_0}\langle S|\frac{\hbar}{i}\frac{\partial}{\partial z}|Z\rangle \tag{2.4}$$

If at low k isotropic band structure is assumed $P_{xy} \sim P_z$, the Hamiltonian can be diagonalized as was done by J. Wu et al. [Wu 2002] obtaining the following eigenvalue for the conduction band dispersion:

$$E_C(k) = E_g + \frac{\hbar^2 k^2}{2m_0} + \frac{1}{2}\left(\sqrt{E_g{}^2 + 4E_p \cdot \frac{\hbar^2 k^2}{2m_0}} - E_g\right) \tag{2.5}$$

where E_g is the intrinsic bandgap, m_0 is the electron mass in vacuum, and $E_p=(2m_0/\hbar^2)|P_z|^2$ is the $k \cdot p$ interaction energy ($E_C(0)$ is referred to the conduction band minimum). This equation (Eqn. 2.5) shows that the non-parabolicity is more pronounced for materials with small E_g (i.e. small bandgap) and/or with high E_p (i.e. strong $k \cdot p$ interaction). Near the Γ point, i.e. at very small k, the equation indicates the parabolic $E_C(k)$ dispersion relation. In figure 2.6 both parabolic and non-parabolic $E_C(k)$ dispersion are shown for InN. As can be observed, the parabolic approximation deviates significantly from the non-parabolic dispersion relation when k >~0.05/Å, that is, when the electron concentration is n>~10^{19} cm^{-3} so that the Fermi level (E_F) moves deep into the conduction band (resonant).

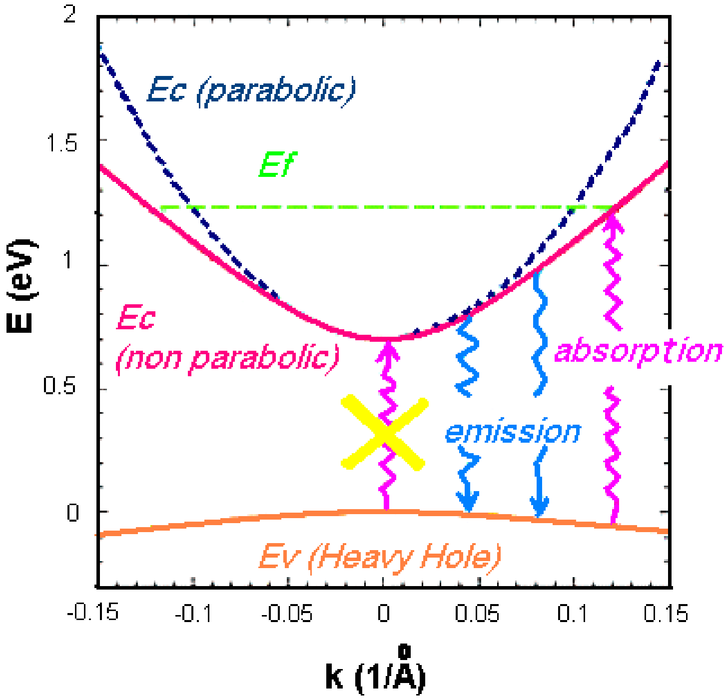

Figure 2.6: Calculated conduction and valence band dispersion of InN using the k·p model. The Fermi level for n=10^{20} cm^{-3} is shown. Taken from [Wu 2002].

This simple calculation gives a possible explanation, first, for exceptionally high dispersion of the values reported for the InN bandgap; the specific case of the high n–type doping, placing the Fermi level inside the conduction band (degenerate doping), implies that the energy onset of the optical absorption overestimates the actual intrinsic bandgap (in the case of degenerate doping, the optical absorption is forbidden for below-Fermi-level transitions) leading to the so-called Burstein–Moss effect. Second, another important feature can be extracted from the previous analysis; the effective mass can be obtained from Eqn. 2.5 as it is defined as:

$$m_e^*(k) = \frac{\hbar^2 k}{dE_C(k)/dk} \tag{2.6}$$

When k tends to 0:

$$\frac{m_e^*(0)}{m_0} = \left(1 + \frac{E_p}{E_g}\right)^{-1} \tag{2.7}$$

Many groups have measured electron effective mass of InN, by various techniques. Similarly to the case of the band gap, the high dispersion of values, varying from 0.039 to 0.24 has been reported [Hofmann 2006, Wu 2002] (note that the small effective mass leads to a high electron mobility; in best samples (grown by MBE) the electron mobility currently exhibits values of ~2000 cm^2/Vs [King 2009]).

The *high free electron concentration* originates from unintentional dopants, such as chemical impurities (mainly oxygen) and native defects (mainly nitrogen vacancies). Therefore, its value strongly depends on the growth method used; a higher (chemical/crystal) quality film (as grown by MBE) yields a lower free electron density (compared to the values obtained in highly defective films (as those grown by sputtering).

The high dispersion on InN bandgap value, and its established low value, caused confusion because it ruptured a common trend seen in semiconductors, commonly referred to as the empirical “common-cation” rule. This rule states that for isovalent, common-cation (anion) semiconductors, the direct bandgap increases at the Γ point upon decrease of the anion (cation) atomic number. The established InN bandgap of 0.64 eV is much smaller with respect to the bandgap of indium phosphide [EG (InP) = 1.46 eV].

Wei et al. [Wei 2003] showed that this can be understood when considering chemical trends (figure 2.7 (b)) and atomic size contributions. According to the tight-binding model [Yu 1999], the valence band maximum (VBM) comes from bonding anion and cation *p* orbitals (InN: In 5p, N 2p). Because of an increase of the anion *p* orbital energy from elements N to Sb and its enhanced spin-orbit coupling, the energetic position of the VBM in group V compounds (InN, InP, InAs, InSb) increases with increasing anion atomic number (figure 2.7 (a)).

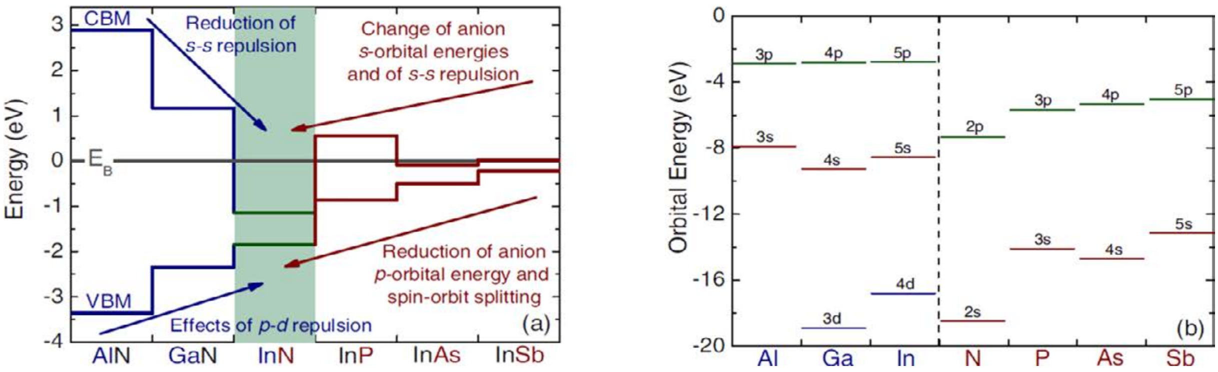

Figure 2.7: (a) Conduction and valence band edges of related group III-V semiconductors w/r to E_{FS}. (b) Atomic orbital energies of group III and V elements. Taken from [Wei 2003].

The conduction band minimum (CBM) in InN is formed by anti-bonding cation and anion *s*-states, i.e., In *5s* and N *2s*. The observed energy of the N *2s* orbital (E_{N2s} = -18.5 eV) is of very low value in comparison to other group V anion *s* orbital energies (e.g., E_{P3s} = -14.09 eV). Combined with the effect of a weak volume deformation potential [aV(InN) = -4.2 eV, aV(InP) = -5.9 eV], defined as the change in semiconductor bandgap resulting from a local deformation in the lattice crystal (relative change in volume), which fails to open the bandgap for the case of InN [Wei 2003], this leads to the exceptionally low position of the CBM with an exceptionally high electron affinity of 5.8 eV [Li 2005], and small bandgap.

When a semiconductor is doped above a certain level, the amount of free carriers measured becomes constant. A universal charge neutrality level, on an absolute energy scale, for a given semiconductor is represented by the so called branch point energy [Van de Walle 2003]. This branch point energy marks the energy where surface states change their character from predominantly donor type (below) to predominantly acceptor type (above).

In addition, within the amphoteric defect model (ADM) [Walukiewicz 1987, 1989] it represents the energy at which the formation of donor (below) or acceptor (above) native defects becomes favourable. More precisely, the branch point determines the favourable charge state of all gap states (including surface states, metal- and interface-induced gap states, and defect-induced gap states). Therefore, its position relative to the band edges in the material is essential in determining fundamental bulk and surface electronic properties such as surface space charge features, doping limits, and metal/semiconductor contact characteristics.

Another interesting concept is the Fermi stabilization energy (E_{FS}). The E_{FS} is not correlated to the position of the conduction or valence band edges of a material but is universally located ~4.9 eV below the vacuum level [Walukiewicz 2001]. It marks the Fermi level position at which (at same rate) donor and acceptor type defects are formed, and at which the Fermi energy will stabilize as a consequence of a large introduction of native defects as, e.g., with particle irradiation. These native defects are called “amphoteric” native defects and are, strictly speaking, defects that possess both positive and negative charge states depending on the position of the Fermi energy.

A direct result of the low CBM in InN is the extremely high position of the E_{FS} [Walukiewicz 2001, King 2008a, Schleife 2009] of the branch point or Fermi stabilization energy [Walukiewicz 1989, 2001], which is located 1.83 eV above the VBM, i.e., ~1.2 eV above the CBM (figure 2.7 (a)). This indicates that for Fermi levels lower than 1.83 eV above the VBM, defects preferentially display donor-like behavior, which explains the strong propensity of InN toward n-type conductivity.

Opposite to most semiconductors where high electron concentrations are commonly achieved via doping with donor impurities (or high-energy particle irradiation), InN is very difficult to dope p-type. Furthermore, characterizing the p-type InN material is extremely complicated due to the fact that an electron accumulation layer is present at InN surfaces [Mahboob 2004a]. When measured by Hall Effect, the electrical properties are determined by this surface layer (high mobility) rather than in the bulk of the sample. As previously mentioned, in as-grown InN samples the surface Fermi energy is located well below the branch point energy. Therefore, unoccupied surface states will preferentially be donor-type and a positively charged surface state area forms. To compensate the resulting charge, and in order to maintain charge neutrality, a downward bending of the conduction band and an increase in the surface electron concentration, i.e., the formation of a surface electron accumulation area, takes place. A pinning of the surface Fermi energy at the branch point energy has been observed in slightly n-type samples [King 2008a]. With increasing free electron concentration in the bulk, the surface Fermi energy moves significantly closer to the branch point energy to help balance out the surface state charge, and fewer surface states are occupied.

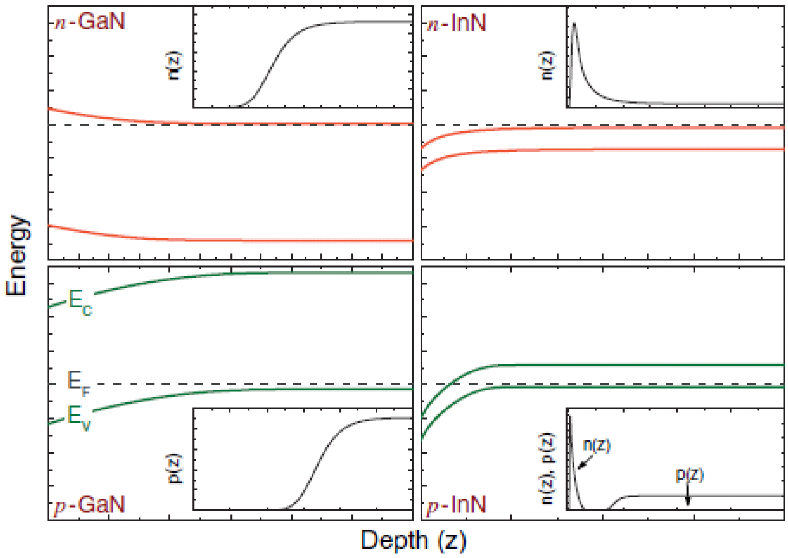

Figure 2.8: Schematic representation of band bending relative to the Fermi energy (E_F) for both n and p- type GaN as n and p- type InN. In addition, the electron (n(z)) and hole (p(z)) concentration variation in the near-surface region of each case is shown. Taken from [King 2008b].

For the case of $In_{1-x}Ga_xN$ the E_{FS} crosses the CBM at $x \approx 0.6$. Therefore, a surface electron accumulation is expected for In content exceeding 40%, while a surface depletion is expected for the rest of the composition values. This effect has been experimentally confirmed by King et al. using X-ray photoemission spectroscopy [Veal 2006, King 2008b]. They found that the transition from surface accumulation to depletion occurs at In content 43% for n-type InGaN, and from surface inversion to hole depletion at In content of 59% for p-type InGaN. A deviation of surface Fermi level pinning from E_{FS} was measured across the composition range. Another study done by A. Knübel et al. [Knübel 2010] also showed similar results by means of electrolyte capacitance-voltage profiling. The expected band bending is represented in figure 2.8. By means of density functional theory calculations, Van de Walle et al. [Van de Walle 2007] explained the surface Fermi level pinning above the CBM in InN. In addition, they predicted the absence of such an electron accumulation on non-polar InN planes ((1-100) and (11-20)) and on polar surfaces if only In-N dimmers are present. In this study results were presented in terms of two stoichiometry regimes: moderate and high cation/anion (III/V) ratios. Although King [King 2007] reported the universality of electron accumulation on both polar and non-polar InN surfaces, C. L. Wu et al. [Wu C. 2009] presented a study where clear evidence for the absence of accumulation layer on in situ cleaved non-polar InN surfaces was shown. Several posterior studies have reported reduced positive donor density or even absence of electron accumulation [Van de Walle 2007, Chang 2010, Linhart 2010, Sofikiti 2009b, 2010]. The dispersion observed on the behaviour is linked, most likely, to the quality of the non-polar surface. Nevertheless in before mentioned studies the found electron accumulation at the non-polar surface is always, relative to the polar surface, very low.

2.3 Optical properties

The radiative properties in a semiconductor can be studied by exposing it to light (e.g. from a laser) with a higher energy than its bandgap, in an experiment called photoluminescence (PL). The emitted photons from the light source are absorbed and as a result an electron is usually raised from a lower-energy filled state to a higher-energy empty state, and in general the energy difference between the two states is equal to the energy of the absorbed photon. If this higher-energy state is not an equilibrium state, then the electrons will lose energy to the lower energy empty state and emit electromagnetic radiation in the process. The released radiation energy is very close to the energy difference between the higher and lower energy states. These are called radiative transitions and are of extreme importance for optoelectronic applications.

In general there are several possible radiative recombination processes, namely:

- *Band-to-band*: Direct transition from conduction band towards the valence band.
- *Free exciton*: The excited electron may pair a hole to form a so-called exciton. Recombination of the electron-hole pair results in a narrow and sharp peak in the emission spectra.
- *Deep level*: Native defects in the lattice, such as vacancies, interstitial or substitutional impurities, or impurity-vacancy complexes can give rise to deep levels in semiconductors. Normally these produce non-radiative recombination; however, there exist defects which generate radiative transitions (stacking faults (SFs), yellow band (YB), etc).
- *Donor/acceptor pair*: Transitions between intentional and unintentional donor and acceptor levels in semiconductors give rise to radiative recombination.
- *Bound to free (Free to bound)*: In this transition the energy of the higher level electron state is unbound (bound) or lies in the continuum.
- *Phonon replicas*: The spatial lattice that defines the electronic bands in a particular semiconductor has its own optical properties. Semiconductor crystals, like any other, are composed of a three-dimensional array of atoms linked by spring-like restoring

forces. This lattice supports characteristic normal vibrational modes whose dispersion relation can be derived from classical solutions for the atomic equations of motion. The modes are either optical, where atoms of opposite charge vibrate out of phase to give an oscillating dipole moment which couples to light; or acoustical, which means they oscillate in phase which each other and propagates light at constant (sound) speed (for long wave-lengths, small wave vector).

- *(Aceptor/Donor) Bound Exciton*: A bound exciton is formed by binding a free exciton to a chemical impurity atom (ion), complex, or a host lattice defect. The binding energy of the exciton to the defect or impurity is generally weak compared to the free-exciton binding energy. These bound excitons are extrinsic properties of the semiconductor; the free excitons may be bound to either neutral donors/acceptors or ionized donors/acceptors. They feature sharp-line (width <0.1 meV) optical transitions in both absorption and photoluminescence spectra. The absorption or emission energies of these bound-exciton transitions always appear below those of the corresponding free-exciton transitions.
- UX instead of TES in NCs and films (donor close to surfaces)

A schematic overview of the possible recombination processes is presented in figure 2.9.

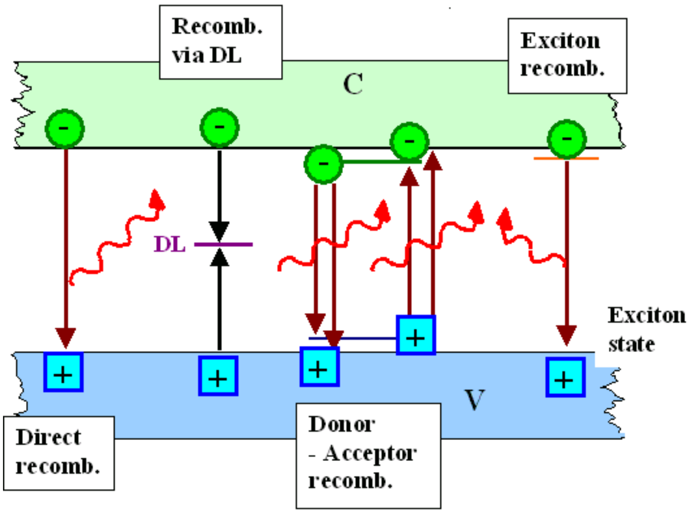

Figure 2.9: Schematic of recombination processes. Adapted from [Föll]

The best quality III-nitride films are GaN because of a long standing experience and growth optimization and also not suffering from alloy problems. Therefore, the GaN photoluminescence spectrum is the most studied and known. In the following some highlights are given about GaN optical properties which are indicative of the materials crystal quality needed for optoelectronic applications.

An interesting feature of radiative transitions which have been observed in GaP, CdS, CdSe, ZnO , InP as in high quality GaN is the so-called two-electron satellite (TES) transition. TES occurs when an exciton bound to a neutral donor (D^0X) recombines and leaves the donor in an excited state. The TES energy is therefore lower than that of the D^0X peak by the difference in the ground and excited state energies of the neutral donor. A schematic of this process is shown in figure 2.10.

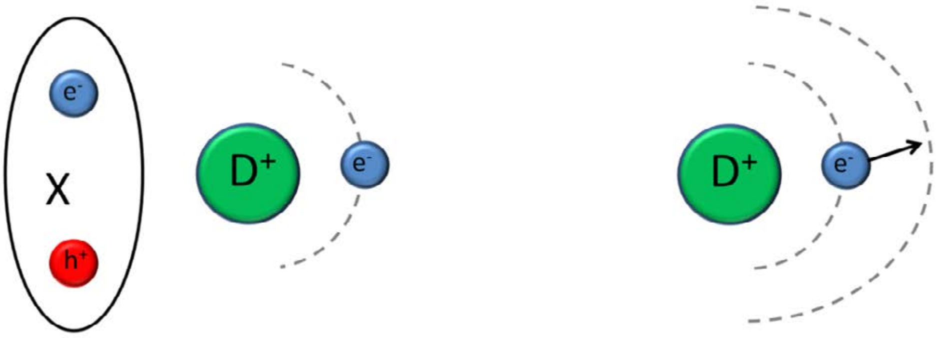

Intial state: (D^o, X) Final state: D^o

Figure 2.10: Recombination scheme for a donor-bound exciton. Left: Initial state incorporation of an electron-hole pair (exciton "X") bound to the neutral donor (positive core D^+ with an electron e^-). Right: Final state incorporation of the core D^+ and electron e^- . In the normal (D^0X) recombination, the donor electron remains in the ground state *1s*. In the TES transition, an excited state *2s*, *2p*, *3s* etc. is produced**.**

Since nominally undoped GaN is usually n-type ($n \approx 10^{16}$-10^{17} cm^{-3}) PL spectra at low temperature is dominated by donor-bound excitons (D^0X) lines located at ≈3.47 eV. The full width at half maximum (FWHM) of individual lines in the best samples reported is lower than 100 μeV and governed by lifetime broadening. Acceptor-bound excitons energy transitions (A^0X) are observed at ~5 meV lower energy in respect to D^0X.

Wurtzite GaN has its valence band split into three sub-bands caused by the axial crystal field and the spin-orbit interaction. This fact yields up to 3 free exciton transitions. An exciton created by an electron and a heavy hole (HH) is referred to as A-exciton (FX_A); the one corresponding to light holes (LH) is labeled as B-exciton (FX_B), whereas the C-exciton (FX_C) relates to a hole in the next valence band below. The exact energy of these three excitonic transitions was obtained from studies performed on thick GaN epilayers and homoepitaxial epilayers where full strain relaxation happens. The most accurate measurements were carried out in homoepitaxial GaN samples, where very sharp PL lines are observed, with linewidths below 1 meV [Leszczynski 1999, Prystawko 1999]. Values of exciton energies of 3.478 eV for A- free exciton (FX_A), 3.484 eV (FX_B) and 3.502 eV (FX_C) have been obtained with an accuracy of about 2 meV [Monemar 1997]. Finally, the binding energy of all three (A, B, C) free excitons in GaN is determined to be about 25-27 meV [Hoffmann 1998].

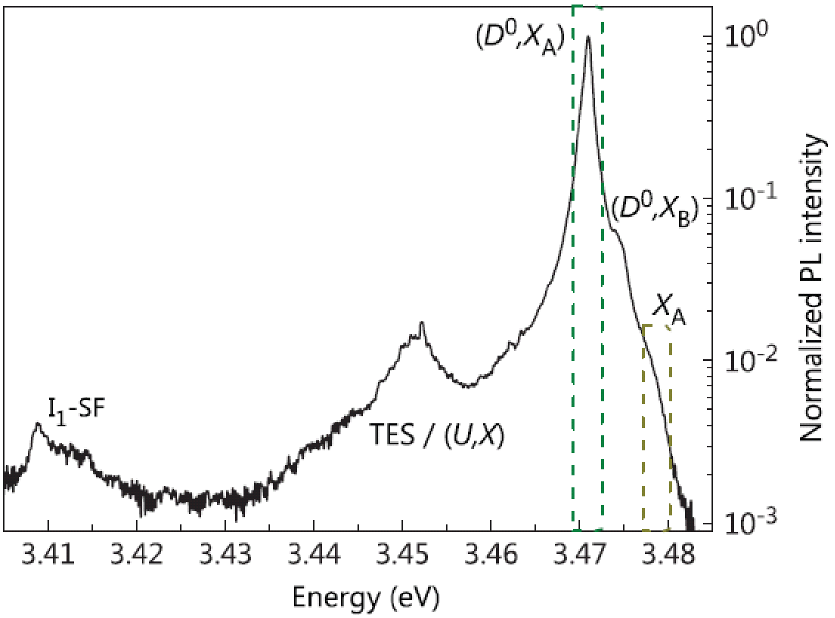

Figure 2.11: Typical Low-temperature (10 K) PL spectrum for a GaN NC. The spectrum is dominated by the recombination of A excitons bound to neutral donors [(D^0, X_A)] at 3.471 eV. Transitions attributed to the recombination of B-excitons bound to neutral donors [(D^0, X_B)] at 3.475 eV and free A-excitons (X_A) at 3.478 eV are also detected. The TES/(U,X) band at 3.45 eV (see text). The I_1-SF is attributed to the recombination of excitons bound to I_1 basal-plane stacking faults (SF) at 3.41 eV. The dashed boxes indicate a 3-meV wide spectral window centred around the (D^0, X_A) and X_A transitions used for time-resolved photoluminescence analysis in [Hauswald 2014]**.**

A typical PL spectrum of GaN nanocolumns (NCs), in which a very low density of defects is present, as compared to thin film, is shown in figure 2.11, taken from [Hauswald 2014]. Aside from the intrinsic two-electron satellite (TES) of the (D^0X_A) transition in GaN, additional transitions related to excitons bound to as yet unknown defects [(U,X)] are shown at 3.45 eV. These unknown defects are possibly related to the NC lateral surface as was suggested by Lefebvre et al. [Lefebvre 2011]. They studied NCs with different diameters and observed the corresponding low temperature (8 K) PL spectra, as by lowering Ga flux during growth the NCs average diameter (thus density) was reduced and the corresponding UX line peak intensity became increased in value (dominant together with typical observed DBE); suggesting thus a surface related defect contribution. Additionally, lines originating from the recombination of excitons bound to I_1 basal-plane stacking faults (BSF) are observed at 3.41

eV. This emission corresponds to localized excitons generated by BSF corresponding to local changes in the stacking sequence.

In the specific case for Wz GaN, BSFs constitute ZB segments in a Wz matrix more precisely it corresponds to a local deviation from the 2H stacking of the Wz matrix to a 3C zinc-blende stacking (see Appendix 1 for more detail). This change in stacking sequence induces a bound state in the semiconductor bandgap and being planar defects, having thus a two-dimensional nature, these stacking faults act as quantum wells, giving rise to radiative transitions of excitons with characteristic energies.

For very high quality GaN thin films it is possible to observe fine structures (e.g. polariton longitudinal transverse splitting and the singlet-triplet exchange splitting) in the excitonic transitions. The fine structure of the A-exciton was determined by Hoffmann and co-workers [Hoffmann 1996, 1998]. Hoffmann et al. [Hoffmann 1998] have identified the PL peaks at 3.47904 eV and 3.47892 eV with the lower transverse branch of the spin singlet state and with the spin triplet state of the A-exciton, respectively. Such identification gives the value of the exchange splitting of about 120 µeV with an accuracy of about 100 µeV. The PL peak at 3.48000 eV was identified as the longitudinal branch of the spin singlet state of the A-exciton [Hoffmann 1998]. This identification yields the value of the longitudinal-transverse splitting of the A-exciton to be about 1.0 meV with an uncertainty of 0.1 meV [Hoffmann 1996, 1998].

2.4 III-nitride nanostructures

Nanostructures are very appealing due their unique properties. In particular semiconductor quantum dots (QDs) are very small three-dimensional systems whose dimensions ranges from nanometers to tens of nanometers. Their size is smaller than the Broglie wavelength of electron (λ_B), therefore quantum effects take place in these dots. Since quantum confinement takes place, the energy spectra of electrons and holes (and consequently excitons) are composed of discrete series (like those of atoms, see figure 2.12). The discrete energy levels depend on the size of the dot, which determines the magnitude of the quantum effect (quantum size effect). Figure 2.12 summarizes the density of states as the semiconductor dimension is scaled down: bulk semiconductor (3-D), quantum wells (2-D), quantum wires (1-D) and quantum dots (0-D).

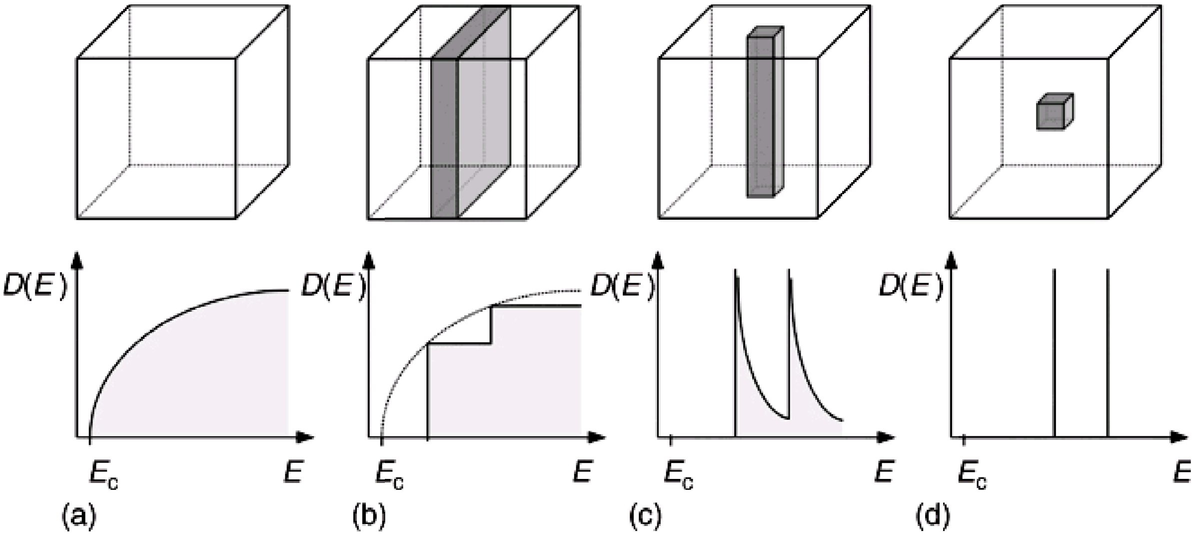

Figure 2.12: Density of states for a) Bulk (3-D), b) Quantum well (2-D), c) Quantum wire (1D) and d) Quantum dot (0-D) [Scholz 2009].

The discrete energy levels for the QDs make them behave as “artificial atoms”. This feature is responsible for a wide range of applications in various research fields such as optoelectronics [Suris 1996], biomedicine [Jamieson 2007], microscopy [Deerinck 2008] and advanced solar cells (as in the case of intermediate band solar cells proposed by Luque et al [Luque 1997]). However the problem with QDs is that they are randomly distributed (upon the growth) with random sizes and shapes; thus it is not possible to take a full advantage of their employment, as needed in, for example, optoelectronic applications. This is not the case for chemical sensors for which there is a strong belief, in the chemical sensor community, that QDs, in particular, will become a leading nanostructure for chemical sensing [Korotcenkov 2011]. Same is valid for hydrogen generation, where it is shown that QDs enhance electron-hole (e-h) pair generation, stimulating the hydrogen generation [Tian J. 2013]. For the purpose of the present study, it is thus not critical to obtain an exceptionally ordered growth. On the other hand, a proof of concept will be shown for bio-sensing and water-splitting applications, in where the QDs role is not related to fine-tuned optical properties but to act as a catalyst for electrochemical reactions occurring at the surface of a specific electrode. This facilitates considerably the selection of the growth method to be used, which nevertheless needs to be controlled and repeatable.

In general there are two basic technological approaches to control size of nanostructures. The two approaches, commonly referred to as “top-down” and “bottom-up” techniques, have been systematically implemented over the last decades to create repetitive surface patterns which allow controlled (and repetitive) device fabrication. The “top-down” techniques refer to producing nanoscale structures by machining and (dry) etching, whereas “bottom-up” techniques refer to building organic and/or inorganic structures atom-by-atom or molecule-by-molecule. In the present thesis, the focus will lay on the latter case, in particular on self-organization (self-assembled) growth of QDs. In the following, comments on QDs fabrication by substrate patterning are given for completeness.

Over a long period of time (and especially in III-Arsenide growth) the most straightforward way to fabricate QDs was to pattern a quantum well (QW). Up to date, patterning is widely used to control QDs size and spatial arrangement in a precise way. The patterning is done by lithographic techniques, comprising many kinds of methods. The most common one is optical lithography, based on excimer lasers, which holds a resolution below 0.2 µm and ultraviolet optics and resists with steep sensitivity curves, with a resolution below 0.1 µm. X-ray lithography has the advantage of a much shorter wavelength and is thus suitable for smaller nanostructures fabrication. However there are still some problems to be solved here, for example high resolution x-ray lenses are not available and an additional process is required to fabricate mask.

For lateral patterning, the most developed approaches are the electron beam lithography (EBL) and the focused ion beam lithography (FIBL). These techniques achieve a resolution below the 50 nm. QDs formation by this approach is accomplished by the use of patterned substrates, for example, by growing in tetrahedral-shaped recesses (TSRs). The main disadvantage of lithographic techniques is that they often lead to chemical contamination and crystal structure degradation (defects formation).

Self organization growth of QDs will happen during epitaxial growth on a lattice mismatched substrate. An overview of the three growth modes of a pseudo-morphic layer is given below. They depend on the interplay between surface, interface and strain energy.

- *Volmer-Weber (VW)*: Direct 3-D growth by island formation on the substrate. In this case, atoms are more strongly bound to each other than to the substrate.
- *Frank van der Merwe (FvdM)*: Growth proceeds layer by layer in a two dimensional way. Here film atoms are more strongly bound to the substrate than to each other.
- *Stranski–Krastanov (SK)*: A mixture of FvdM and VW modes, i.e layer + island formation. The initial monolayers grow under compressive strain; beyond a “critical thicknes”, that is usually few monolayers, the layer relaxation is initiated, by formation of islands (more free surface facilitates strain relaxation).

The main difference between the VW and SK is the plastic vs. elastic strain relaxation, respectively; this means that the excess strain is relaxed mainly through defect formation in the VW mode vs. an extra-free-surface creation in the SK mode. This typically implies higher crystal quality of QDs formed by SK [Simmonds 2012].

The growth of InN QDs on high In-content layers which will be studied in the present thesis is justified by the following fact: the lattice mismatch between InN and InGaN can be reduced (and tuned) by increasing the In amount, considering the linear approximation given by Vegard´s law. As seen for the case of InAs on GaAs, with lattice mismatch of ~7%, the formation of InAs QDs is seen to follow the SK growth mode. Therefore a similar behaviour is expected for InN on InGaN for which the lattice mismatch is in the same range; as this implies that the strain will be comparable and island (QDs) formation may proceed by the same growth mode.

2.4.1 Optical Properties of Nanostructures

Self-assembled QDs by SK growth are formed in a 2-step process. A few monolayers (2D, wetting layer) are grown until, above a certain threshold (critical thickness), typically around 2 monolayers; the 3-D island formation occurs then, to release efficiently the accumulated energy. As previously discussed, the electronic structure of QDs resembles electronic structure of atoms; three-dimensional confinement of carriers in QDs leads to localized states both for conduction- and valence-band carriers (the so-called shells), and consequent discrete inter-band transitions. In SK self-assembled QDs the discrete states appear energetically close to a quasi-continuum of delocalized states corresponding to the 2-D motion of carriers in the wetting layer (WL). A schematic representation of the corresponding energy levels of conduction and valence band states in the region close to the optical band gap is shown in figure 2.13.

The finite height of the confinement potential restricts the number of confined shells. On one hand, by the proper compositional tuning of barriers (and/or QDs) one can control the QD/barrier band offsets. On the other hand, by tuning the QD size, one can control the energy separation between successive shells, leading, finally, to the control of the number of confined shells. Due to a relatively small height (few nanometers) and a relatively big diameter (of the order of tens of nanometers), the confinement in self-assembled QDs is, in general, much stronger in the vertical than in the lateral direction. Only the lowest confined state is usually relevant for the QD optoelectronic properties.

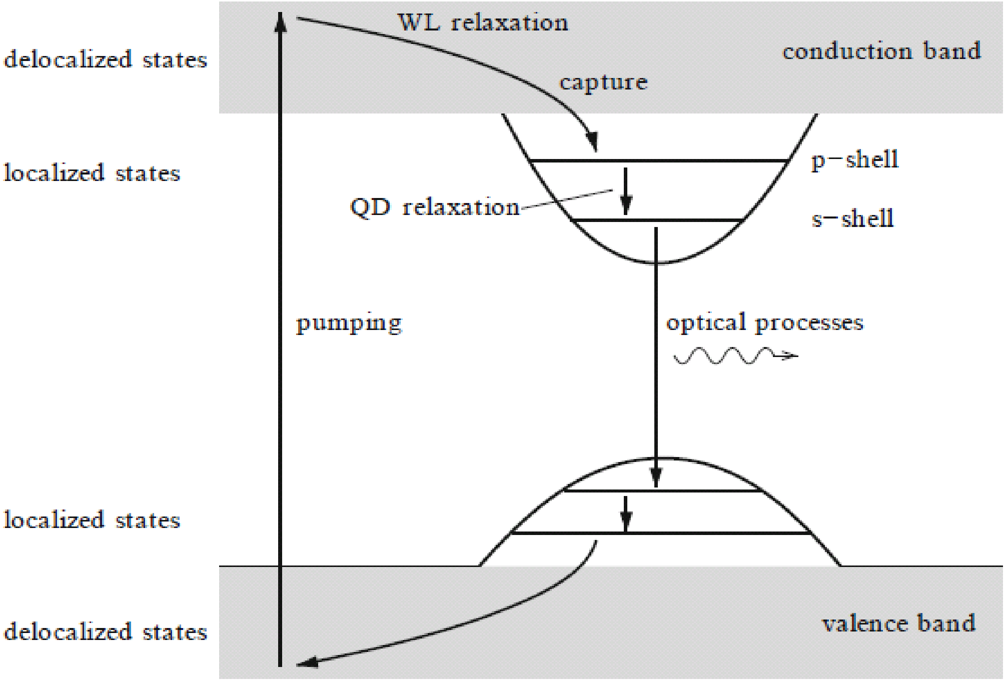

Figure 2.13: Schematic representation of energy levels in a quantum dot (QD) with two shells for carriers in the conduction and valence band, respectively. The quasi-continuum of the wetting layer (WL) is shown as shaded areas. Taken from [Michler 2009].

The band-offsets for III-N QDs are much larger than those in their III-P and III-As counterparts (with the exception of InN QDs in high In-content InGaN matrix). This enables “higher robustness” of excitons that may survive up to room temperature.

Apart from the typically high band offsets in III-N QDs, another feature strongly determines their energy spectra. The lack of central symmetry of Wz crystal structure leads to the formation of uncompensated static charge at the III-N polar and semi-polar interfaces. This charge leads to additional Coulomb potential, leading to a strong band curving. Due to its high impact on QD energy spectra, this phenomenon is separately addressed in the following chapter.

2.4.1.1 Remark on Polarization Effects

The unscreened dipoles at the crystal’s boundaries produce an internal electric field through in the material. When a charge is placed in an electric field, it experiences an electric force. This electric force is proportional to the strength of the electric field multiplied by the charge. As electron and hole have opposite charge, the built in electric field spatially separate electrons and holes. The impact of the spatial separation of the electrons and holes can be explained in the case of nanostructures. Let´s consider a (0001) oriented single quantum well (QW). The mobile electrons and holes inside the QW are confined and cannot leave the QW since they do not have enough energy to overcome the surrounding energy barriers (see appendix 2, figure A2.1). However, the polarization induced electric force spatially separate the electrons and holes in opposite directions inside the QW, leading to reduced electron and hole wave function overlap [Scholz 2012]. Reduced overlap leads to lower interband oscillator strength [Grandjean 2007]. The radiative recombination lifetime is approximately proportional to the inverse square of the wavefunction overlap [Ludwig 2006] leading to a dramatically decreased probability of radiative recombination, that is, an increased probability of non-radiative recombination. Apart from heavily changed recombination dynamics, the strong electric field leads to a CB/VB energy curving, producing eventually red-shifts of the QW transition energies [Waltereit 2000]. The perturbation of the confined energy spectra caused by electric field is commonly denoted as the quantum confined Stark effect (QCSE) [Ryou 2009].

By means of perturbation theory, considering the case of an infinite QW centred in x=0 as the unperturbed case and the perturbed system the tilted QW, it is possible to obtain an equation describing how the ground state energy of the tilted QW is modified by the application of an electric field, this equation presents the main features for the QCSE. Calculations are shown explicitly in the appendix 2 and the obtained equation is:

$$\Delta E = -24\left(\frac{2}{3\pi}\right)^6 \frac{e^2 m^* d^4}{\hbar^2} E_z{}^2 \tag{2.8}$$

In here E_z is the component of the electric field along the z direction and d is the well-width. This shows that the levels shift to lower energy in proportion to $-E_z^2$ a redshift in energy is thus expected due to the application of an electric field.

2.4.1.2 Excitons in QDs

Excitons in QDs vary from those in bulk materials. The main difference lays in the origin of the binding energy; whereas in the bulk material the binding is almost exclusively due to Coulomb potential, in the QDs the confinement potential (originating from the QD small size) is commonly the dominant binding mechanism. Actually, in the regime of strong confinement, the Coulomb potential can be treated as a mere perturbation of the confinement potential. The perturbation can be either positive or negative; consequently QD excitons may have positive and negative binding energies. In the weak confinement regime, the QD excitons resemble more to the bulk-like ones, as the Coulomb potential starts to play the dominant role in the exciton binding. QDs can be populated with one or several electrons and holes simultaneously, forming a single exciton or forming exciton complexes. As the occupation of the QD shells follows Pauli's principle, the ground state of the QD may be occupied by maximally two electrons and two holes with opposite spins. This configuration is often referred to as the biexciton (see figure 2.14 (c)), of which the emission energy is usually shifted by coulomb and exchange interaction with respect to the exciton emission energy. On the other hand, configurations with a single unpaired spin carrier are usually referred to as trions or charged excitons. This collection of excitonic complexes is indicated in figure 2.14 (a–c). If more charges are filled into the QD, higher shells are occupied with emission bands at notably higher energies.

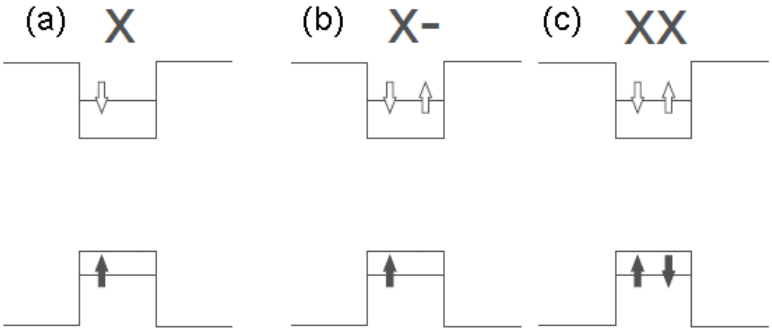

Figure 2.14: Selected charge and spin configurations in the s-shell, often referred to as exciton X, trion X− (X+ analogous) and biexciton (XX). Adapted from [Tartakovskii 2012].

2.4.1.3 Surface States

The reader should notice that for most optoelectronic applications the QDs should be embedded in a functional structure and for this the QDs need to be covered by a capping layer. Although the capping is an important topic on its own, as it can modify the QD electronic structure (via strain or uncompensated static charge at the QD interface) and therefore be directly used to tune QD transition energies/wavelengths (such as in arsenide systems), this topic is out of the scope of this thesis (but definitively an interesting issue for future research). Therefore, the studied QDs in this thesis are exclusively surface QDs (SQDs). This implies that surface states, heavily influence by the dangling bonds and surface defects, play an essential role for the QD optical properties. In general, nonradiative recombination states may lower the overall optical efficiency. Indeed, in arsenide systems it has been shown that the surface potential strongly influences the PL properties [Shen 1990, Moison 1990, Dreybrodt 1993, Liu 1997, Miao 2000, Chen 2001]. The PL linewidth is broadened due to coupling of QD and surface states and the intensity decreases as a result of nonradiative recombination at the surface [Miao 2010, Selçuk 2010].

2.4.2 InN QDs

Like other semiconductor nanostructures, the optical bandgap of InN QDs increases in the presence of quantum confinement. For InN the quantum confinement is thought to become important (in the order of the excitonic Bohr radius) for a characteristic length of 10 nm as pointed out by Chao et al. [Chao 2006]. In this work, a clear blue-shift as a function of decreasing nanorods size was observed (not related to the Moss-Burnstein effect), and (correctly) attributed to the quantum size effect. The same was observed by W.C. Ke et al. [Ke 2006] for the case of a GaN matrix with embedded InN QDs grown by MOCVD. In figure 2.15 the main results are shown. The QD height, measured by atomic force microscopy (AFM), determines the degree of confinement in the vertical direction. The PL peak shifts coherently from 0.78 to 1.07 eV, as the the reduction of the average QD height decreases from 32.4 to 6.5 nm. The inset in this figure shows how a model based on the effective mass approximation explains the observed PL peak shifts.

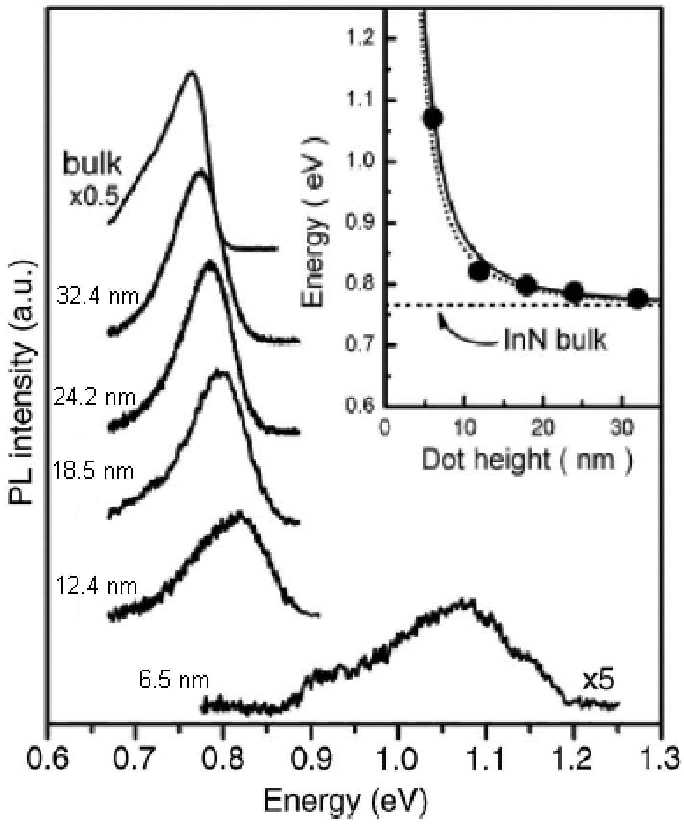

Figure 2.15: PL spectra measured at 17K in InN QDs with different heights. The insert shows the peak energy as a function of QD height. The solid line is calculated by the effective mass approximation using $0.042m_0$ ($0.07m_0$ for the dotted line) as the electron effective mass. Taken from [Ke 2006].

2.5 Chemical sensors

The interest in the current thesis lies in the properties of high In-content InGaN and InN QDs and will focus on the In(Ga)N chemical sensing properties. The unusual surface band bending (and electron accumulation) present in InN, are exploited for chemical sensing. Just after the discovery of the narrow bandgap of InN, Lu et al. [Lu H. 2004] reported a fast response of sheet carrier concentration and mobility to solvent exposure, such as methanol and water. Pt-coated InN nanorods were found to change resistance upon exposure to H_2 (but not to N_2 and O_2) [Kryliouk 2005]. InN surface functionalization by aminosilane molecules has been accomplished and used to bind negatively charged Au colloids [Chen C. 2006]. Anion sensing with InN , characterized with a remarkable selectivity, stability, response time and repeatability, was shown by Lu et al. [Lu 2007, 2008] In all these experiments, it was shown that InN is sensitive to anions, but not to cations. This strongly suggests that the sensing mechanism is based on positively charged InN surface states, which, by Coulomb force, attract the negatively charged ions in aqueous solutions.

CHAPTER 3

EXPERIMENTAL SET-UP

In this chapter the experimental tools used during the Thesis are reviewed. Molecular beam epitaxy (MBE) is the choice for growth and for characterization the tools were scanning electron microscopy (SEM), atomic force microscopy (AFM), high–resolution X-ray diffraction (HRXRD), tunnelling electron microscopy (TEM), photoluminescence (PL), cathodoluminescence (CL), scanning near field optical microscopy (SNOM), and gas chromatograph (GC).

For an easier overview the chapter organization will follow the categories:

- Epitaxial growth set-ups
- Morphological characterization set-ups
- Structural characterization set-ups
- Optical characterization set-ups
- Electrochemical characterization set-up

3.1 Epitaxial Growth: Molecular Beam Epitaxy

The samples used in this Thesis were grown in two different MBE systems: a RIBER Compact 21 and a MECA 2000. The first one to grow most samples on GaN templates, while those on Si(111) were grown in the second system. The basics for both systems follow the same general scheme, as shown in figure 3.1, where the MBE growth chamber is shown.

The system comprises a loading chamber, where samples are loaded and outgassed at 200ºC to remove mainly water, and a growth chamber where samples are transferred to proceed to the growth. The transfer between chambers is done by means of a mechanical/magnetic push rod through a gate valve. Both chambers are independently pumped to achieve the working pressure under ultra high vacuum (UHV) conditions. UHV conditions are even more important in the growth chamber to ensure a long mean path of atoms and molecules, so that a molecular beam regime is maintained (no dispersion). UHV is achieved by a combination of vacuum pumps, namely, a rough pumping with a rotary pump (down to ~10^{-3} Torr) that also backs a turbo molecular pump to achieve a pressure of 10^{-7} - 10^{-8} Torr. An ion pump (based on gettering effect of titanium sublimation) pushes the pressure down to 10^{-9} - 10^{-10} Torr. The ultimate UHV is reached by means of a cryogenic pump reaching a pressure of 10^{-10} - 10^{-11} Torr, which is considered the base pressure set point to allow growth processes. Cryogenic pumps have a high pumping speed for nitrogen (not so the ion ones) what makes them quite efficient to pump out the nitrogen needed to grow nitrides. Finally, in order to keep UHV conditions during growth, liquid nitrogen runs continuously through a cryogenic panel inside the growth chamber.

Pure molecular nitrogen (7 to 8N) is fed from a high pressure cylinder (through pressure reductors, filters, purifiers, valves and a Mass Flow Controller) into a radio frequency (RF)-Plasma source that breaks the molecules and provides the so called "active nitrogen", most likely atomic nitrogen, which is extremely reactive. Therefore, the growth technique is known as plasma-assisted (PA-MBE) or radio frequency (RF-MBE) molecular beam epitaxy. The active nitrogen flux is kept constant at a given source power by a feedback loop of the emission signal from atomic nitrogen species by means of an optical emission detector (OED).

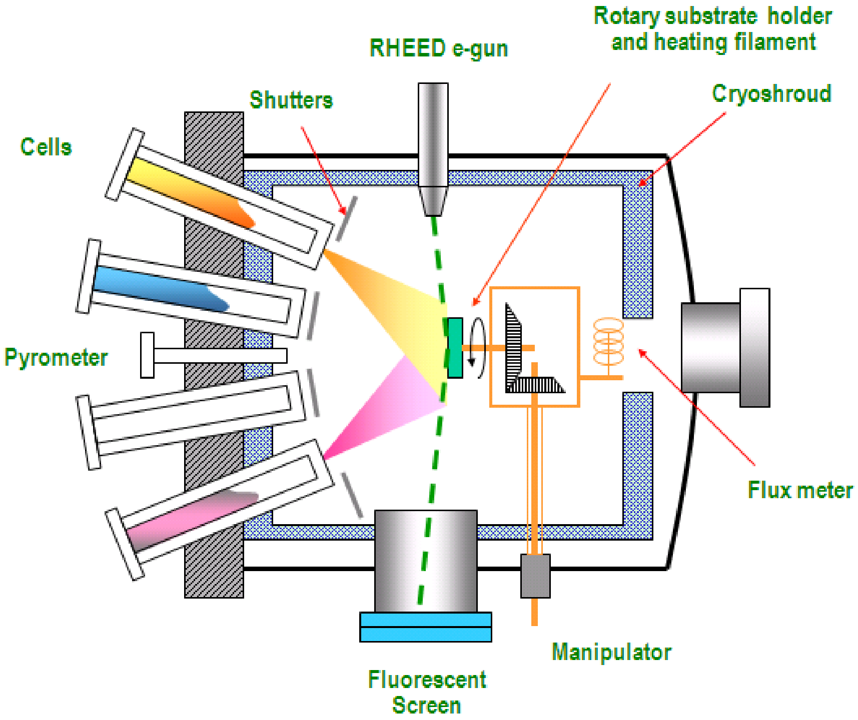

Figure 3.1: Scheme of an MBE system.

Within the growth chamber the substrate is placed in a holder with a heating filament. This holder can rotate to achieve a homogeneous growth, considering that the molecular beams have different impinging angles in respect to the substrate. The molecular beams are obtained from small furnaces charged with the material constituents (Ga, In, Al) as well as dopant species (Si, Mg), called Knudsen cells (K-Cells), from where the beams are formed by material sublimation that creates a given vapour pressure. The geometry arrangement of the different cells is such that all beams merge at the substrate surface. Knudsen cells are furnaces that have a Boron Nitride crucible, a heating filament, several metal (tantalum) shields and a thermocouple mechanically attached to the crucible bottom. Every Knudsen cell has a mechanically (typical) driven molybdenum shutter to stop the beam in a very short time fraction, what is essential to achieve sharp interfaces in heterostructures.

Growth proceeds under a kinetic regime, far from thermodynamic equilibrium, in contrast to other epitaxial methods, for instance liquid phase epitaxy (LPE) or metal-organic vapor phase epitaxy (MOVPE). The molecules/atoms from the impinging beams that reach the substrate surface can diffuse, decompose (molecules), incorporate into the crystal (substrate) or desorb. A schematic representation of possible adatoms behaviour on the surface during the growth process is shown in figure 3.2.

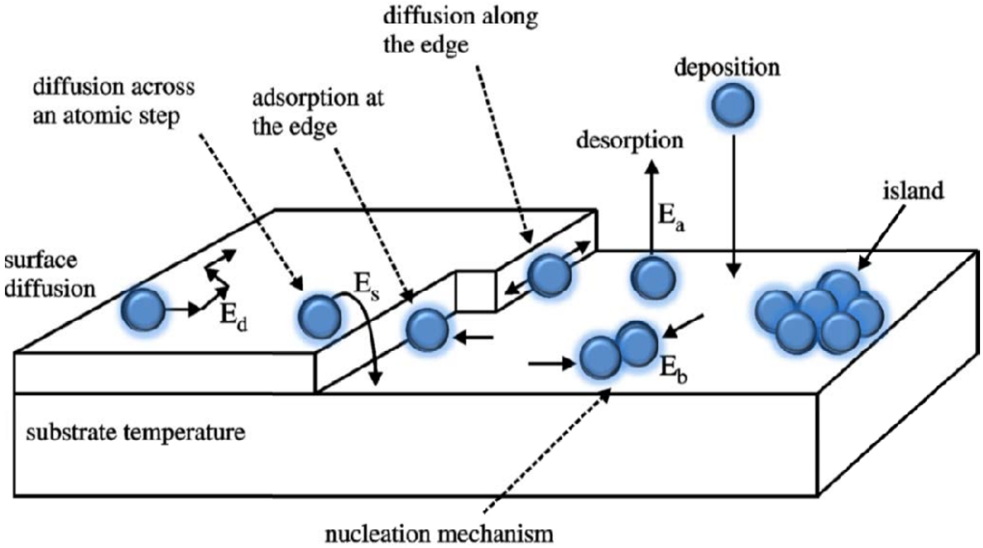

Figure 3.2: Behaviour of adatoms in the surface deposition process (diffusion until nucleation with other adatoms; deposition on edges). Adapted from [Web TUK].

The control of these kinetic processes can be precisely achieved by means of the substrate temperature, the K-cell temperatures (beams density), and active nitrogen flux. Reproducibility will depend on the accuracy to keep these parameters fixed.

3.1.1 Bayard-Alpert Gauge

To monitorize the fluxes and pressure a Bayard-Alpert ionization Gauge is used. A UHV Bayard-Alpert gauge together with the schematic representation of filament and grid is shown in figure 3.3. The Bayard-Alpert vacuum gauge ionizes the gas molecules within the gauge volume by the means of a heated filament (cathode) which emits electrons towards a grid (anode). By maintaining a constant flow of electrons, which pass into the space enclosed by the grid and collide with the gas molecules present, producing positive ions. These ions are collected by the thin ion collector wire, located along the axis of the grid, which is maintained at almost ground potential, being negative with respect to the grid. At constant filament to grid voltage and constant electron emission current the rate at which positive ions are formed is directly proportional to the amount (density) of molecules (pressure) present in the gauge. This relation is valid and most accurate for pressures below 1×10^{-3} Torr. The strength of the ion current is then calibrated in an electrometer that is adjusted in units of pressure.

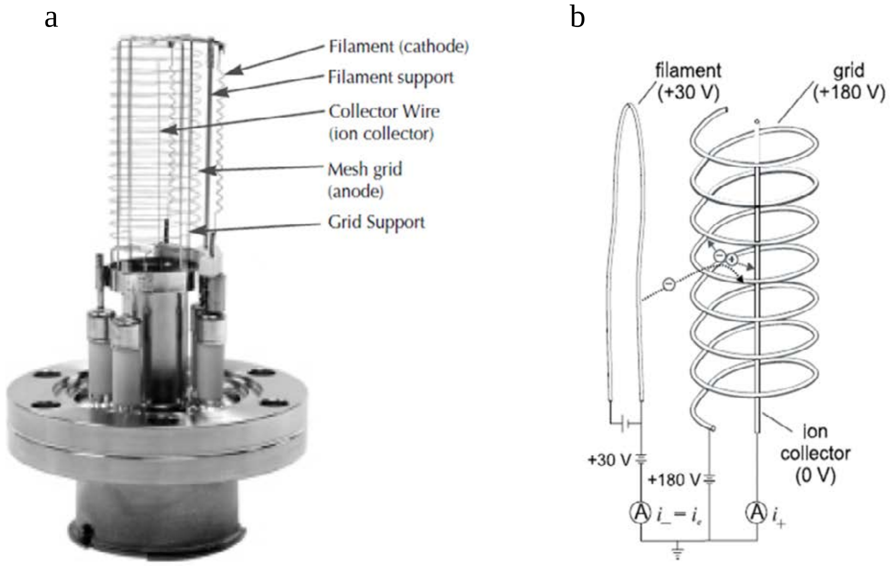

Figure 3.3: (a) Bayard-Alpert filament UHV gauge, (b) schematic representation of filament (cathode) and grid (anode).

3.1.2 Quadrupole Mass Spectrometer

To identify the molecules present in the chamber a quadrupole mass spectrometer (QMS) is used. Many different types of mass spectrometers exist where electric and magnetic fields are used either separately or in combination. For the case of static fields different ions are distinguished in space through their different trajectories (static mass analysers) or in time through their different flight times (time-of-flight -TOF, mass analysers).

The QMS makes use of a quadrupole radio-frequency electric field (dynamic mass analyser) which forces ions of a particular mass onto stable oscillatory trajectories. A typical feature present in a mass spectrometer, independently of the type, is that mass separation is established according to the ratio $\frac{M}{z \cdot e}$ (*M*: molecular mass, *e*: elementary charge and *z*: number of elementary charges). A doubly charged ion hence appears on the scale of a mass spectrometer (which refers to z=1) at half the value of its true mass.

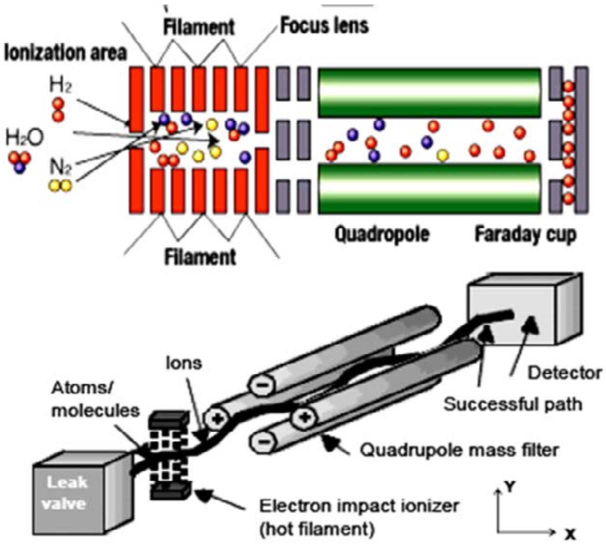

Figure 3.4: Schematic representation, complete system, of the quadrupole mass spectrometer.

A QMS consists of an ionizer (similar to the Bayard Alpert, i.e bombardment by electrons from a hot filament), an ion accelerator, and a mass filter consisting of four parallel metal rods arranged as shown in figure 3.4. Of these four rods, two (opposite) rods have an applied potential of (U+Vcos(ωt)) and the other two rods have a potential of -(U+Vcos(ωt)), where U is a DC voltage and Vcos(ωt) is an AC voltage. The applied voltages change the trajectory of ions traveling down the flight path located between the four rods. For given DC and AC voltages, only ions of a certain mass-to-charge ratio pass through the quadrupole filter while all other ions are expelled of their original path. In this way, a mass spectrum is obtained by monitoring the ions passing through the quadrupole filter as the voltages on the rods are varied.

The QMS is thus a powerful tool that allows determining the type and amount (partial pressure) of molecules and therefore is used to determine the residual gas species within the growth chamber before growth. This QMS is also used quite effectively to detect leaks (from outside in) blowing tiny amounts of He to the outer walls and joints and detecting it inside the chamber.

Another application of the QMS is desorption rate measurements. When a solid with a surface free of adsorbed particles is placed in a gas medium, the process of adsorption will commence. Under static conditions, the adsorption will continue until an equilibrium concentration of adsorbed particles is reached. For a better picture, consider the solid surface being placed inside in a chamber of volume (**V**), which is under a constant pumping (evacuation) at speed (**S**), and the gas inside the chamber is leaked at a constant rate (**L**), the above equilibrium concentration can be described in terms of the steady-state pressure ($\mathbf{p_{eq}}$) inside the chamber:

$$L = KSp_{eq} \tag{3.1}$$

Here K is a proportionality constant (K=3.27×10^{19} molecules^{-1} at p= 1 Torr and T=295K). If the sample surface is heated at a constant rate, the gas pressure inside the chamber increases due to the flux of desorbing particles. Assuming no re-adsorption of the desorbing particles and disregarding adsorption on the walls of the system, the mass balance of particles leaving and entering the chamber is given by adsorption and desorption processes:

$$A\frac{dN}{dt} + L = KSp + KV\frac{dp}{dt} \tag{3.2}$$

Here A is the surface area of the adsorbent, dN/dt is the rate of desorption and p is the instantaneous pressure inside the chamber. This can be rewritten in terms of the beam equivalent pressure (BEP) defined as $\Delta p = p - p_{eq}$:

$$\frac{d\Delta p}{dt} + \frac{\Delta p}{\tau} = a\frac{dN}{dt} \tag{3.3}$$

Where $a = A/K \cdot V$ and $\tau = V/s$. T is the characteristic pumping time. The desorption rate depends thus on the pumping speed. At small pumping speed ($\tau \rightarrow \infty$), the desorption rate is proportional to the variation of pressure in time ($dN/dt \propto d\Delta p/dt$). On the other hand, at high pumping speed ($\tau \rightarrow 0$), the desorption rate is proportional to the pressure ($\Delta p = a \cdot \tau \cdot dN/dt$) and can thus be determined by the QMS. To simplify the process the surface temperature is varied linearly ($T = T0 + (dT/dt) \cdot t$). This method allows determining various adsorptions and desorption parameters, such as: (i) number and population of various desorbing phases, (ii) activation energy of desorption, (iii) order of the desorption and (iv) the pre-exponential frequency factor for the desorption.

This becomes clearer if we analyze the equilibrium state of surfaces species in contact whit its gas phase as:

$$[A]_S \rightleftarrows [A]_G \tag{3.4}$$

Where $[A]_S$ and $[A]_G$ are the surface and the gas phase concentrations of an adsorbate molecule, A. The rate of desorption of adsorbed molecules from the surface is then given by:

$$-\frac{dA}{dt} = k[A]^n \tag{3.5}$$

Where n is the order of the desorption and k is the rate constant for the desorption. The rate constant k has a temperature dependence given by the Arrhenius equation:

$$k = \nu \exp\left(-\frac{E_d}{k_B T}\right) \tag{3.6}$$

Here, ν is the pre-exponential frequency factor, E_d is the activation energy of desorption and k_B is the Boltzmann constant. Replacing in above equation (Eq. 3.6):

$$-\frac{dA}{dt} = \nu \exp\left(-\frac{E_d}{k_B T}\right)[A]^n \tag{3.7}$$

3.1.3 Reflection High-Energy Electron Diffraction (RHEED)

Reflection high-energy electron diffraction (RHEED) is an important technique for studying surface structures (reconstructions) on flat surfaces, as well as surface phase transitions. It is extremely sensitive to surface changes, either by structural changes or due to chemicals adsorption. The set-up consists of an electron gun, a phosphor screen and a clean surface. A schematic of the experimental setup for RHEED can be seen in figure 3.5.

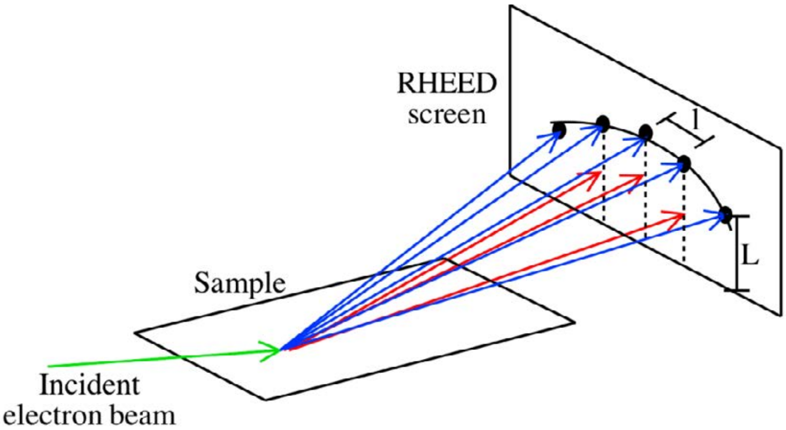

Figure 3.5: Schematic of RHEED.

Since electrons hit the sample surface under a glancing angle the set up does not interfere with the growth process (see figure 3.1). This feature makes of RHEED an ideal in situ probe to monitor the growth of thin films However, due to the glancing angle, the electron-atom interaction is limited to the surface, that is, the penetration depth of RHEED is extremely small limiting its sensitivity to the atomic structure of the first few planes of the crystal lattice. In kinematic theory it is assumed that the electrons are all scattered elastically from the surface and that only the incident beam produces diffracted beams. Elastic scattering reveal the symmetry as geometric arrangements of atoms near the surface. On the contrary, inelastic scattering processes where energy quanta are transferred to or from the topmost atomic layers of a solid, yield information about possible excitations of the surface or interface. Before deepening on the topic, the basis of the measurement will be set by giving an overview of electron diffraction.

3.1.3.1 Relating 'Real' and 'Reciprocal' Space

A set of crystal planes that are separated by a distance *'d'* in real space are represented in the reciprocal space by dots separated by a distance of 2π/d as represented in figure 3.6 (a). Considering another set of planes, closer to each other, a spot appears and which is also modified in distance, as seen in figure 3.6 (b). Notice that the closer the planes are to each other the further away the spots are in the reciprocal map, and viceversa, the further the planes are of each other the closer the spots are in the reciprocal map.

When non parallel planes are considered the dot in the reciprocal space will not be vertically aligned as in the previous cases (figure 3.6 (c)).

The distance between adjacent points in a reciprocal lattice is thus inversely proportional to the distance between points in the corresponding direction of the direct lattice. For a purely planar lattice mesh the periodic repeat distance (**d**) is infinite in the perpendicular (**z**) direction (In 2-D **c***, of the 3-D reciprocal vector **G=ha*+kb*+lc***, in the reciprocal space is any vector perpendicular to the surface). The reciprocal lattice 'points' along the surface normal are therefore infinitely dense - one speaks of a rod in reciprocal space (see figure 3.6 (c)).

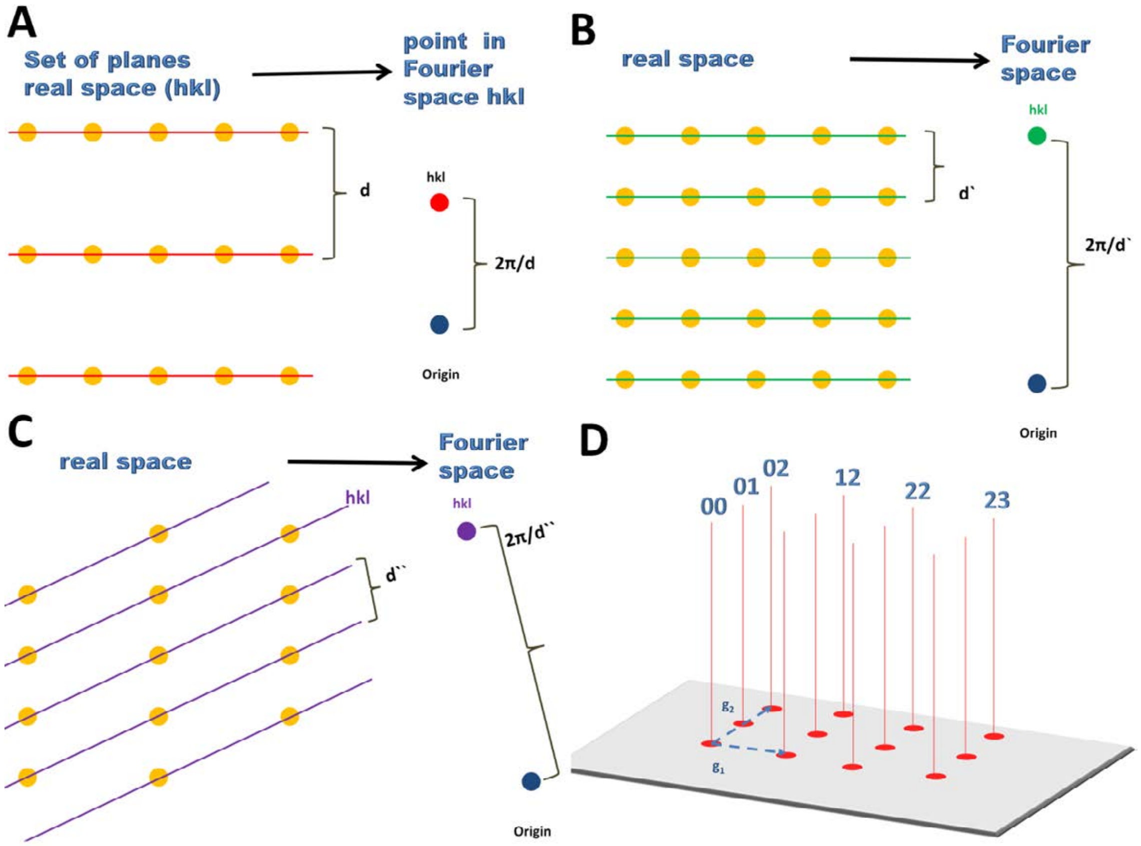

Figure 3.6: (a) Relation between a set of planes in real space and Fourier space. (b) Effect of a narrower distance parallel set of planes in real space and Fourier space. (c) Effect of non parallel set of planes in real space and Fourier space (d) reciprocal rods from a planar lattice mesh.

The diffraction conditions in real space correspond to Bragg's law as illustrated in figure 3.7, it states that the difference in the optical pathway of impinging and diffracted beams corresponds to a multiple number of the wavelength of the incoming beam: $2d_{hkl} \sin \theta = n \lambda$.

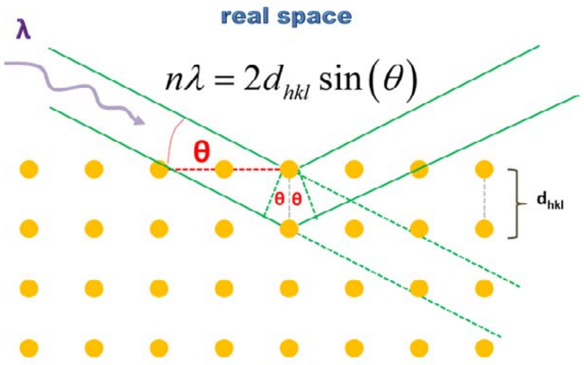

Figure 3.7: Bragg model shows the diffraction conditions in real space 'd_{hkl}' is the distance between planes and λ the wavelength of incoming beam, θ is the angle of the beam with respect to the surface.

On the contrary to the real space, where the diffraction occurs on a single set of planes, in the reciprocal space the diffraction yields a given spot and the incoming and diffracted beams will form vectors ***'k₀'***, ***'k₁'*** centred at this spot. The incoming beam gives rise to a vector from the spot to the origin of the reciprocal space, defined by a length of (1/ λ). This vector can be taken as a radius of a sphere, using the Ewald method. All possible directions for the diffracted beam are determined by the intersection of the sphere with available spots, therefore a set of planes in real space. The scattering vector '**q**' ($q= k_1 - k_0 = 4 \pi \lambda \sin \theta$) can be defined, as is shown in figure 3.8 (a).

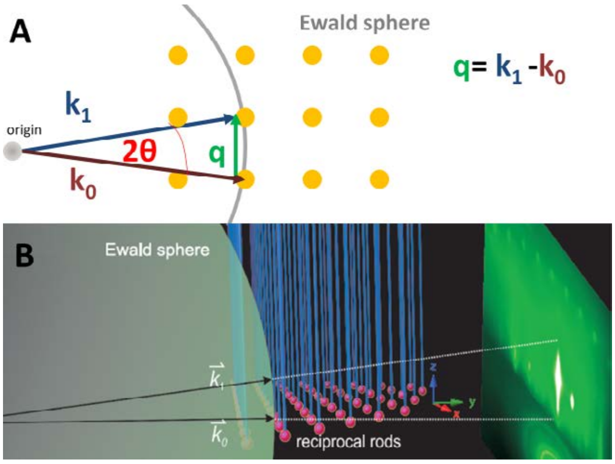

Figure 3.8: (a) Ewald sphere shows the equivalent diffraction condition in the reciprocal space. Here 'q' is the reciprocal space vector. (b) The electron diffraction shown by the intersection of the Ewald sphere with reciprocal rods on a phosporous screen.

Returning to the RHEED discussion, the dots observed on the phosphourus screen correspond to electron diffraction on the substrate surface (see figure 3.5). As mentioned, electrons strike onto the sample under a very low incident angle with respect to the growing surface and with a high energy. Therefore, they will only be scattered from the top layers of atoms of the sample. The atomic arrangement is hence a two-dimensional array of the surface atoms. As discussed before, the reciprocal space image of this lattice can be seen as vertical lines, commonly known as reciprocal rods. The points at the crossing between the Ewald sphere and the reciprocal rods will satisfy the Bragg condition of diffraction and will be displayed on the RHEED screen (see figure 3.8 (b)). An example of the practical usage of RHEED in determining the lattice spacing in real space is shown in figure 3.9, which is direct consequence of relating real with reciprocal space.

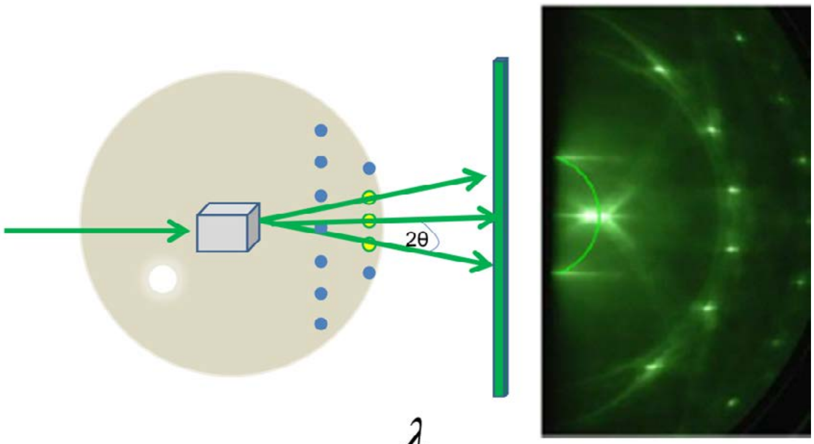

$$\sin(2\theta) = \frac{\lambda}{a}$$

Figure 3.9: Example of RHEED pattern from which the lattice parameter can be determined**.**

Although a perfect crystal should present dots as diffraction pattern, it is due to the (on a large scale) intrinsic imperfection (e.g. defects and mosaicity) that causes streaky reciprocal lattice features. In terms of the reciprocal lattice rods, these will be uniform only if the surface is perfectly flat. Multilevel surfaces will lead to lattice rods that have texture, and the shape of each diffraction spot will be that cross-section of the corresponding rod which intersects the Ewald sphere. Reciprocal lattice rods of multiple level surfaces will have modulations in their diameters with periods of 2π times the inverse of the layer separation. The diffraction conditions for a given spot are met when the Ewald sphere intersects the rods. Surfaces with a larger number of exposed levels will have rods that more closely resemble bulk reciprocal lattices.

But also another fact should be considered as responsible for the streaking feature namely compared to techniques as low energy electron diffraction (LEED) where all electrons are backscattered, RHEED shows long streaks normal to the surface which may occur due to the large radius of the Ewald sphere at high energies, as essentially all electrons are forward scattered.

In RHEED the streaking is thus caused by the grazing angle (and high energy) at which the Ewald sphere intersects the reciprocal lattice rods. If the reciprocal rods are broad enough (which will depend on the crystal quality), streaking will result. The resulting diffraction pattern is thus indicative of the film smoothness at nanometer scale and the patterns are due solely to reflection/diffraction. However, if the reciprocal lattice features appear spotty then it indicates there is roughness (3-D features have thin enough reciprocal lattice rod to appear spotty) at nanometer scale. Some typical RHEED patterns are shown in figure 3.11 (a). The reader can find an extensive analysis on material structure by electron diffraction in in the book by B.K. Vainshtein [Vainshtein 1964].

Free surfaces tend to reconstruct themselves to minimize energy, and this fact will provide very significant information, by RHEED analysis, on the actual processes taking place on the surface (real time) during growth. As it can be seen, this reconstruction provides a different "plane" periodicity as that from "bulk", and different periodicity means extra features in the diffraction pattern. Since typically the surface periodicity is larger than the "bulk", the effect is the introduction of a "faint" line in between the "bulk" ones in the diffraction pattern.

One example of these surface reconstructions is shown in figure 3.10 where periodicity can also be different depending on the orientation (0 and 90º). This different periodicity is labelled according to the repetition after a number of "bulk" planes, like "2x1" in the example of figure 3.10(b). The reconstructions give information about the growth regime, for example, if it proceeds under metal or nitrogen rich conditions in GaN, or metal/ arsenic stabilized in GaAs.

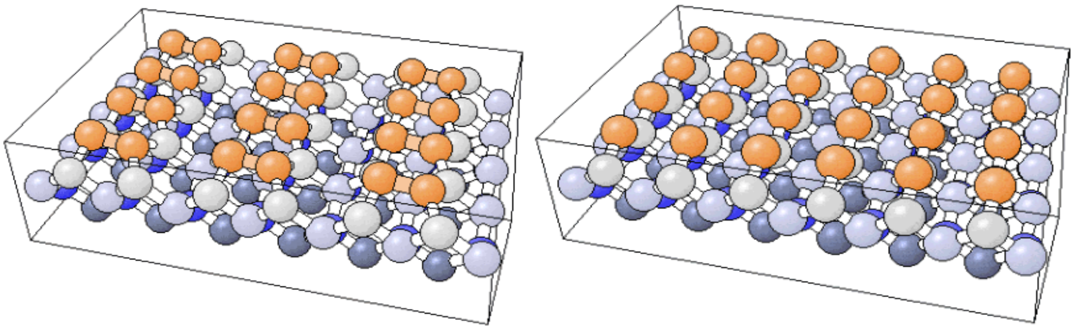

Figure 3.10: (a) Unreconstructed Si(100)-(1x1) surface. Si atoms of the topmost layer (orange) are bonded to only 2 other Si atoms in the second layer (clear grey). (b) Reconstructed Si(100)-(2x1) surface. Si atoms of the topmost layer form a covalent bond with an adjacent surface atom, thus drawn together as pairs called "*dimers*".

One of the most well known configurations is the 7x7 observed on Si(111) (figure 3.11 (b)) at high temperatures that converts into a 2x1 at lower temperatures. The change between both reconstructions occurs at a very precise temperature (827ºC), what helps to determine quite accurately the substrate temperature.

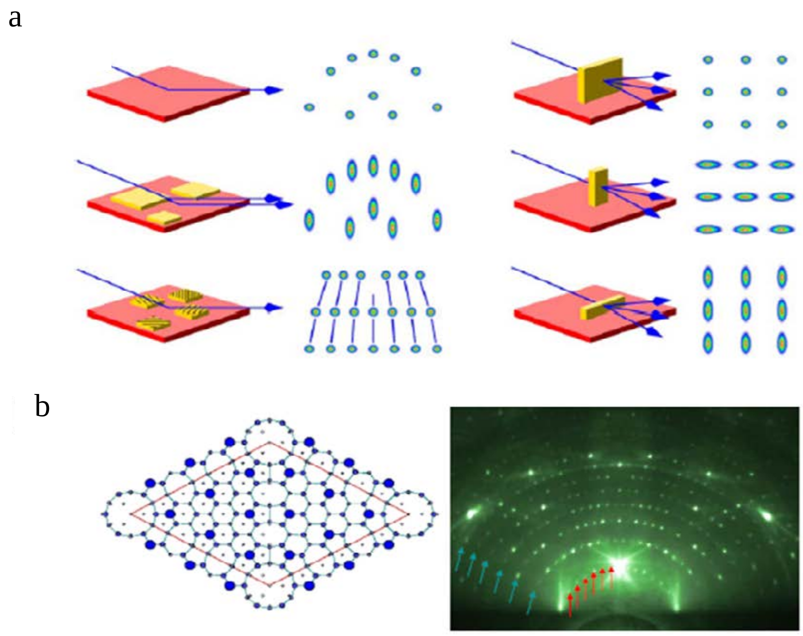

Figure 3.11: (a) Different RHEED signatures. (b) 7x7 surface reconstruction of Si(111).

The spot intensity variation during growth also gives important information, as its oscillation period is directly related to the deposition rate. The basic of this estimation is given in figure 3.12 where oscillations generate upon completion of atomic monolayers: maximum signal for complete layers (specular) and minimum for 50% layer coverage.

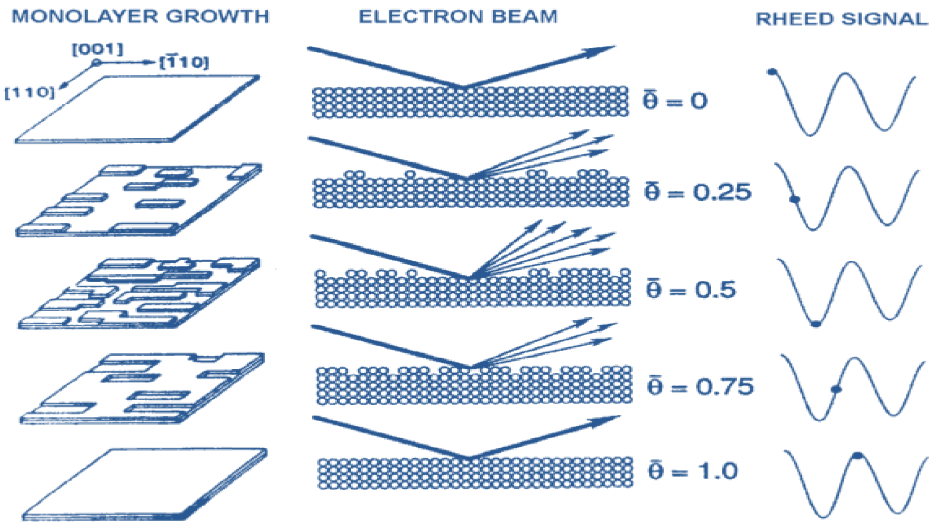

Figure 3.12: Schematics of RHEED oscillation generation upon monolayer completion**.**

Thus in summary, RHEED may be used for the following:

- In situ analysis of surface morphology (surface flatness and islands sizes)
- Identifying surface reconstructions by analysing diffraction patterns.
- Real time monitoring of atomic-layer growth by RHEED oscillations.

- Determination of binary growth rates and thus, ternary alloy composition.
- Temperature calibration by desorption times of specific constituents (e.g Ga).
- Extract information about lattice types and constants.

3.2 Morphology Characterization

3.2.1 Atomic Force Microscopy (AFM)

The atomic force microscopy (AFM) is a technique that measures local properties -such as vertical and lateral dimensions, or magnetism and current when provided with an adequate probe tip. In case of morphological properties, a very sharp tip made of Si_3N_4 or Si is placed at the edge of cantilever that has a spring constant varying in the 0.01-50 N/m range, as shown in figure 3.13. The spring constant '*k*' of a rectangular cantilever is expressed as:

$$k = \frac{E\,t^3 w}{4\,L^3} \tag{3.8}$$

where 'E' is the elasticity modulus, and 'w', 'L', and 't' are the width, length, and thickness of the cantilever, respectively. The spring constant strongly depends on the thickness of the cantilever which is more difficult to measure than its width and length. In practice, for a particular cantilever the thickness can be determined by measuring its resonance frequency 'F_r' which is given by:

$$F_r = 0.163\left(\frac{E}{\rho}\right)^{\frac{1}{2}} \frac{t}{L^2} \tag{3.9}$$

where 'ρ' is the density of the cantilever material. Cantilevers of small spring force constant are most suitable for imaging soft materials, while rigid cantilevers are needed for probing the nanomechanical properties of sample surfaces and also for dynamic-mode AFM measurements. The AFM uses the repulsive force between the tip and sample, very close to each other, that is measured by the cantilever deflection to estimate local properties.

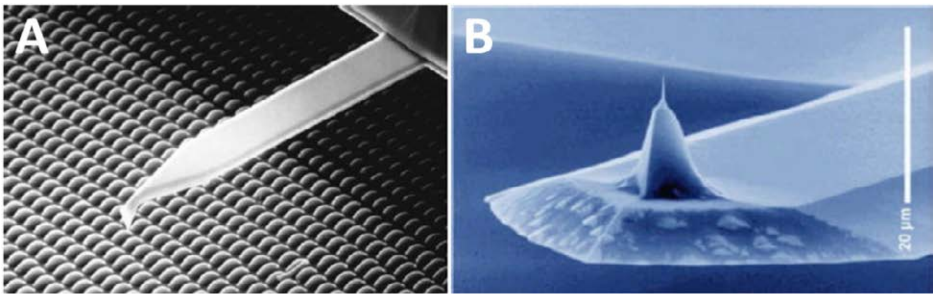

Figure 3.13: Electron microscopy images of (a) Cantilever and (b) Tip of an AFM probe. [Warwick]

The tip is scanned over the surface while a feedback system maintains the tip at a constant "force" on the surface (to obtain height information), or distance (to obtain force information) above the sample surface. As the tip scans the surface of the sample, the cantilever bends when the tip moves up and down depending on the sample surface contour. The cantilever bending is measured by means of an attached mirror where a laser beam is deflected and detected by a photodetector (usually a split diode photodetector) as shown in figure 3.14. The photodetector measures the difference in light intensities between the upper and lower elements and the resulting signal is feedback to piezo-mechanical actuators that keep the tip at constant force or distance to the sample surface.

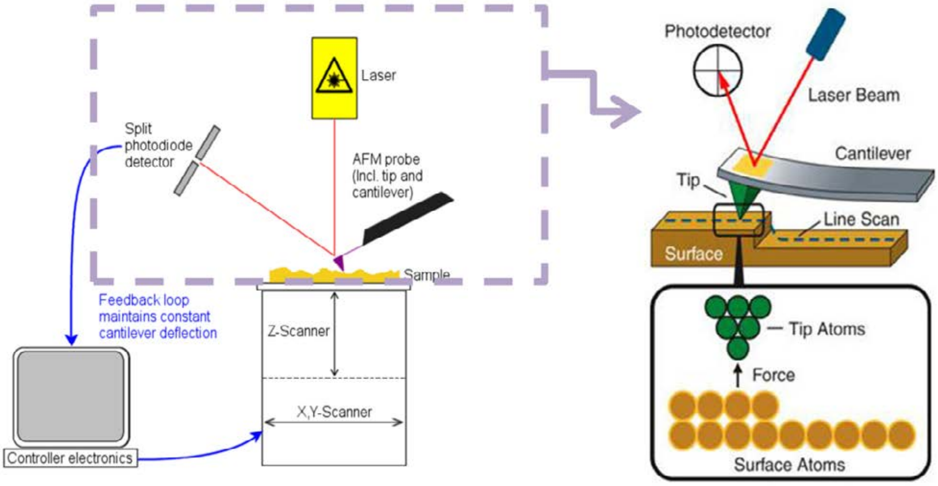

Figure 3.14: Schematic setup of an AFM. Taken from [Jones (2011)]

Operation modes

The AFM system can be used in three different operation modes: contact mode, non-contact mode and the tapping mode, each one used for a different purpose that will be explained in detail.

3.2.1.2 Contact mode

This is the most common mode for AFM operation, in which the tip is placed close to the surface (close enough for the tip to feel interaction from surface atoms, typically between 0.1–100 nm) during the measurement. The repulsive force is kept constant while scanning, what means that the tip must be pushed up or down correlated to the surface profile by means of a piezoelectric positioning element (force values are typically $\sim 10^{-9}$ N). The voltage needed to move the tip, that correlates with the height of the features on the sample surface is displayed as a function of the scan (lateral) position on the sample.

It is also possible to perform lateral force microscopy (LFM) in which in the lateral force applied to the tip causes buckling or torsion of the cantilever depending on whether the fast-scanning direction is along or perpendicular to the cantilever beam, respectively. The twisting of the cantilever gives rise to a differential signal at the horizontal photodetector row, as shown in figure 3.15. The spatial variation of this signal is converted into a lateral force microscopy image. On flat surfaces the torsion is caused by the friction between the tip and the sample and so the LFM is also referred to as frictional force microscopy. For corrugated surfaces the situation is different because the differential signal is not directly related to the lateral force, hence some additional information is obtained from combining lateral and height profiles.

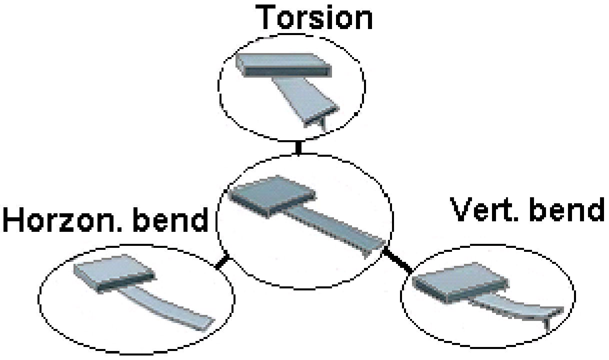

Figure 3.15: Torsion and deflection of the cantilever. Taken from [West].

The risk with the contact mode is that an excessive lateral force by the probe to the sample may produce damage. In an ambient environment the sample surface is covered by a layer of absorbed gases (mainly water vapour and nitrogen) of about 10-30 monolayers thick. When the probe touches this gas layer a meniscus is formed and the cantilever is pulled towards the sample surface by surface tension. The force depends on the tip size, typically of the order of a 100 nm. A solution to minimize this force is to change the environment, for instance immersing the sample in a liquid as the drag force opposes the attractive force towards the sample surface. In addition, the presence of electrostatic charges on the sample may contribute to additional attractive forces between tip and sample. All these forces combine to define a normal force controlled by the feedback system. This normal force creates a frictional force as the tip scans on the sample. In practice, the frictional forces are far more destructive than the normal force and can damage the sample, dull the cantilever probe and distort the resulting data.

3.2.1.3 Non-contact mode

In this mode, either the cantilever vibrates at its resonance frequency, or the vertical sample position is modulated. The attractive forces here are weaker than in the contact mode, thus the tip is given a small oscillation (amplitude typically <5 nm) so that AC detection methods can be used to detect small forces between the tip and the sample by measuring the change in amplitude, phase or frequency of the oscillating cantilever in response to force gradients from the sample. The dominant force between the tip and sample at short range is the Van Der Waals (VDW) force, and limits the distance for the tip over the sample surface as this VDW force decreases fast with increasing separation distance [West]. Therefore a narrow spatial region exists over which the VDW force acts and where the oscillation amplitude is modified by the short-range VDW interaction before the tip becomes abruptly captured by the surface (liquid) layer. Once the tip is captured it has to be set free again to resume its "free" oscillation, so that the feedback system can respond correctly to changes in the surface topography. In general, whenever a fluid layer (contaminant) is present, it is usually thicker than the range of the VDW force gradient, causing the tip to get trapped in this layer and yielding a non real image. The same effect is observed if the tip hovers beyond the effective range of the forces it attempts to measure. Performing the measurements in UHV on cleaved/baked surfaces can solve these problems.

3.2.1.4 Tapping mode

This mode was introduced to overcome the problem of the tip getting trapped in the surface liquid layer. Here the tip oscillates at much higher amplitude (10-100 nm) that requires rigid cantilevers with resonance frequencies of about 300-400 kHz. The resolution, however, is not as high as that of the non-contact mode since the very sharp tip is very fragile and becomes blunt instantaneously when it makes aggressive contact with the sample. During measurements, the tip oscillation is reduced by the energy loss caused by the interaction with the surface, reduction that gives a measure of surface features. The tip-sample impact force here is far greater than in the other two modes previously discussed, so it can be destructive for the tip, even if the lateral friction force is eliminated. An overview of the tip movement for all three modes discussed is shown in figure 3.16.

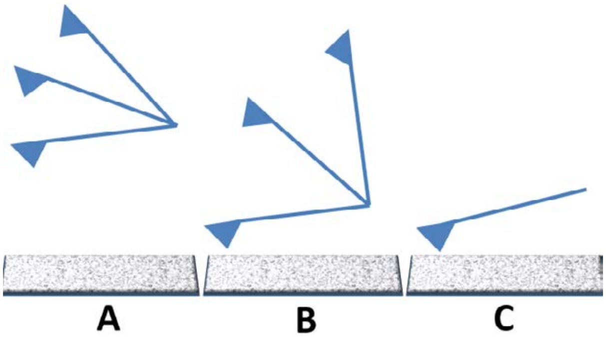

Figure 3.16: The three operation modes of the AFM: (a) Non-contact mode, (b) Tapping mode, (c) Contact mode [Magonov 1996].

3.2.2 Scanning Electron Microscopy (SEM)

In scanning electron microscopy (SEM) technique an electron beam, with an energy ranging from 1 to 30 keV, is focused and scanned on a sample by means of electromagnetic lenses. From this interaction, a detector counts (primarily) the number of low energy secondary electrons. In the SEM system at the ISOM Institute, a FEI Inspect F50, the column is under high vacuum by means of two ion-pumps and the filament is placed in a high electric field that accelerates electrons towards the sample through a focussing system as indicated in figure 3.17.

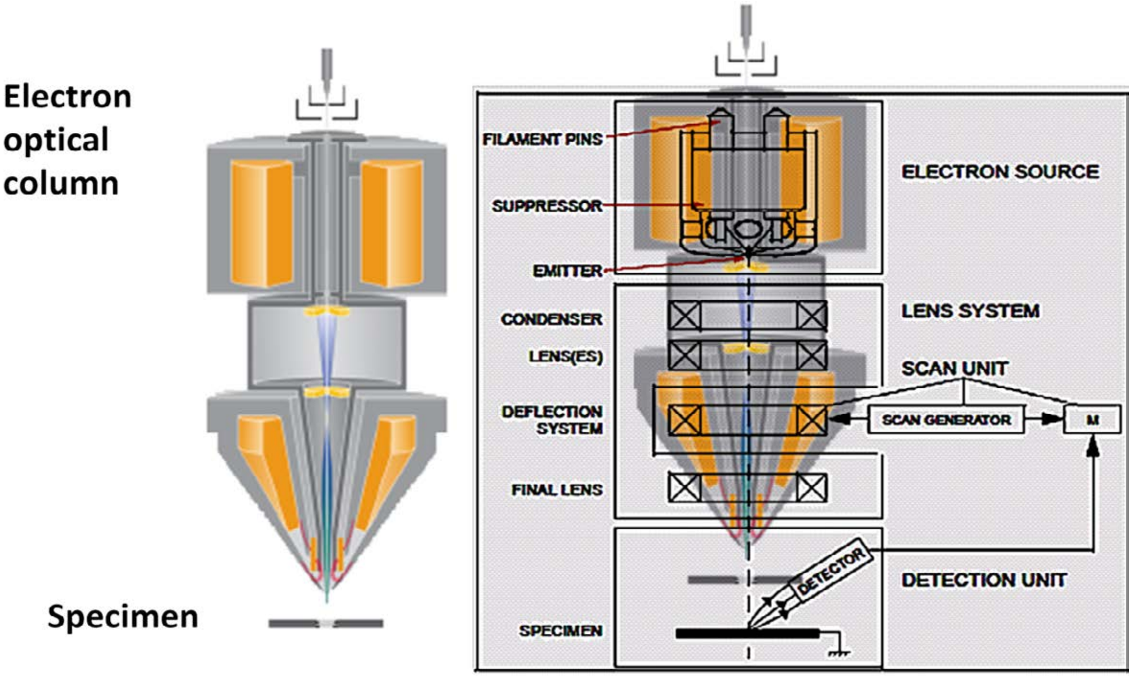

Figure 3.17: Schematic of FE-SEM.

This type of microscope, where electrons are generated by field emission and accelerated, is called field emission SEM (FE-SEM) and provides images of very high quality at high magnification. SEM based on thermionic emission also exists and these were the first to be used, being called plainly SEM. The difference lies on how electrons are ejected from the cathode to the vacuum. A schematic drawing is presented in figure 3.18 where it can be seen that for bare SEM electrons from the Fermi level $\mathbf{E_F}$ of the cathode material overcome the work function Φ by thermionic emission. The acceleration of the emitted electrons by the electric field between the cathode and anode can be described by the potential energy shown in the figure $\mathbf{V}=-|\mathbf{E}|x$. For the field emission case (FE-SEM) this potential energy is much higher than the one at which emission starts above 10^7 $\mathrm{Vcm^{-2}}$. Such field strengths decrease the width **b** of the potential wall in front of the cathode to a few tens of nanometres so that electrons from the Fermi level $\mathbf{E_F}$ can penetrate the potential barrier by the wave-mechanical tunnelling effect. Field-effect cathodes need to work in UHV better than 10^{-6} Pa because otherwise the tip radius (usually made of tungsten and r~0.1µm) is destroyed by ion bombardment from the residual gas.

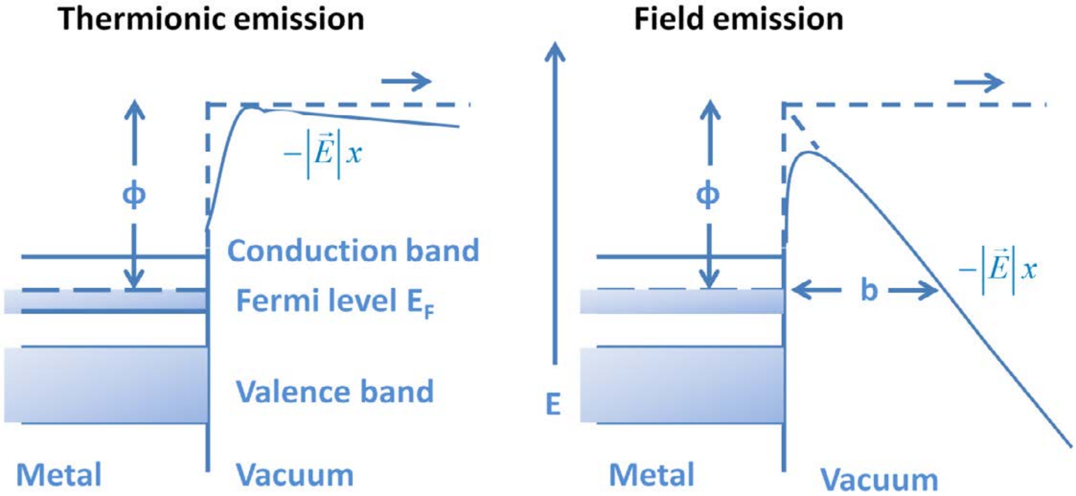

Figure 3.18: (left) Thermionic emission at the potential barrier (work function Φ) of the metal-vacuum boundary in the presence of a small electric field E. (right) Field emission by wave-mechanical tunnelling through the potential barrier of width b produced by a high electric field E. In both figures$=-|E|x$ is the decrease of potential energy caused by the external field E.

SEM/FE-SEM images allow the analysis of the sample morphology and topography in great detail. The resolution is determined mainly by the effective electron beam spot size, the detector sensitivity and the working distance. The main advantages of FE-SEM over the SEM are that its filament has a longer lifetime and gives a much higher resolution due to the following facts:

- Crossover diameter is much smaller. This is the point at which the electrons are focused when leaving the electron gun (considered as the virtual electron source).
- Effective spot diameter much smaller since electrons are emitted from a much smaller area.
- Emitted electron beam is more coherent and the energy spread is very low.
- Higher brightness can be obtained.

The FE-SEM system at ISOM has a theoretical resolution of 1.2 nm at 30 keV. The detected secondary electrons provide an image with a grey distribution from black (low amount of secondary electrons) to white (high amount of secondary electrons). Care has to be taken when working with semi- insulating materials as very few conduction electrons are present in an insulator, and therefore secondary electrons lose energy primarily through the excitation of valence electrons into the conduction band. The secondary electron emission from insulators depends strongly on the surface barrier, unlike the case of metals. In addition, charging the insulator surface by the electron beam may blur the images. To overcome this, metal sputtering of a few nanometres is used or contacting the surface with conducting materials (by means of e.g. conducting silverpaste).

One of the main advantages of these microscopes is that the accelerated electrons interact with matter in various ways allowing several characterization techniques to be realized (if the right characterization tools are installed). An overview of the possible interactions is presented in figure 3.19, the electron interaction with matter is seen to be limited to the penetration regime, the so-called excitation volume. Hence, it depends on the acceleration voltage of the electrons and material density. The excitation volume may be estimated from Monte Carlo simulations. Since some time, Monte Carlo software are used to understand the capabilities of electron microscopes at higher energy (> 10 keV) [Newbury 1976] or at lower energy (< 5 keV) [Hovington 1997]. The updated version of CASINO (acronym derived from “Monte Carlo simulation of electron trajectory in solids) based on the simulations done for the lower energy, allows an efficient use for all acceleration voltages typical of a FE-SEM (0.1 to 30 KeV).

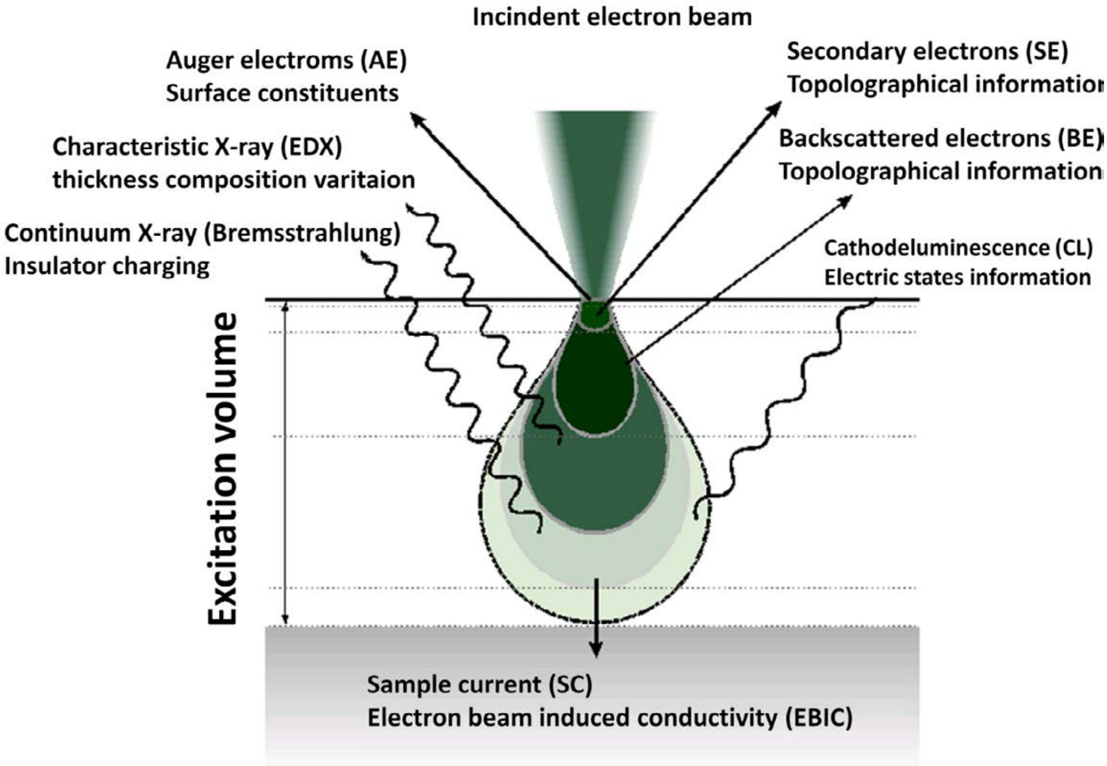

Figure 3.19: Main interactions suffered by electrons when penetrating matter.

As an example, to see the excitation volume in a 450 nm thick InGaN layer on a Si substrate, Casino simulated the electron trajectories considering 5, 10, 15 and 20 keV. The results are shown in figure 3.20. For the simulation 200 electron were considered and a beam diameter of 1 nm. Notice that the scales are different, the maximum depth scales are:

- 5keV: 225 nm
- 10 k eV: 800 nm
- 15 keV: 2200 nm
- 20keV: 4200 nm

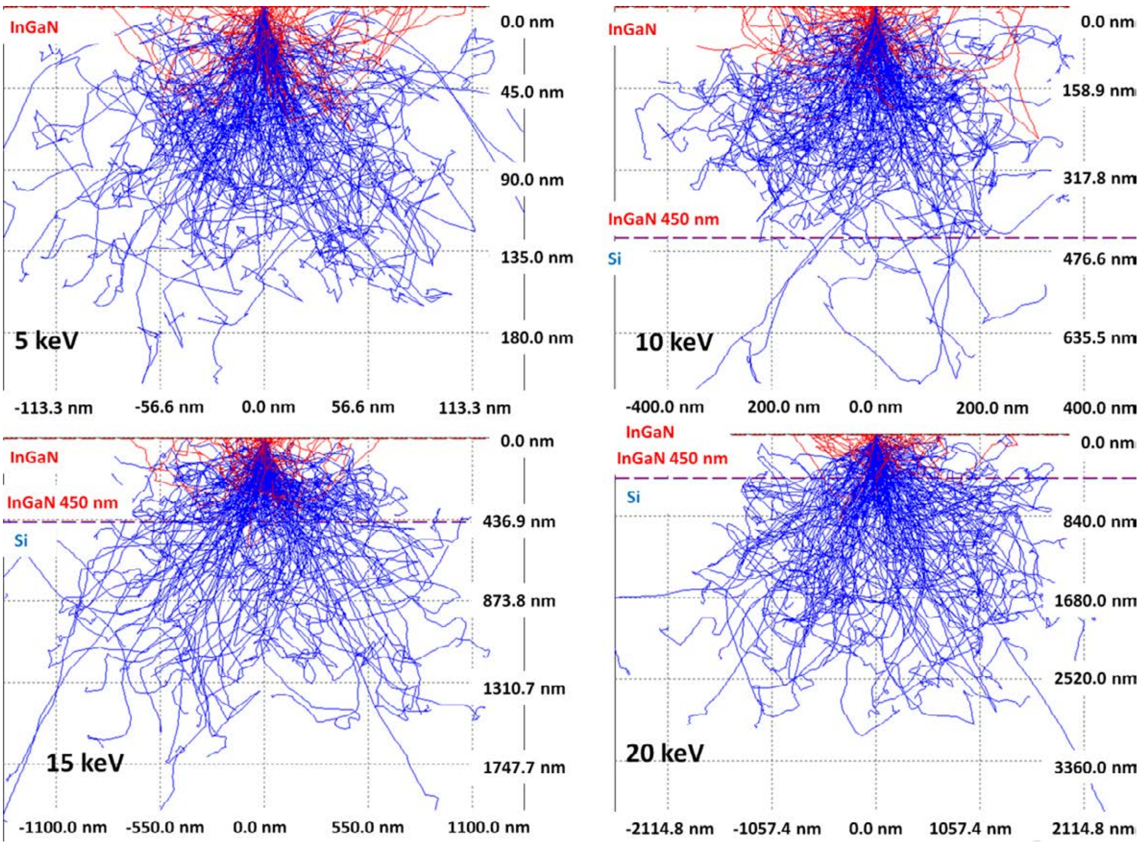

Figure 3.20: Electron trajectories calculations done by the CASINO software (www.gel.usherbrooke.ca/casino/download.html) for 5, 10, 15 and 20 keV. A 450 nm thick InGaN layer (indicated by the red dotted line) on Si substrate was considered.

Nevertherless, the maximum interaction volume is dependent on the highest density of electrons and can be expressed in terms of energy per depth, a profile as shown in figure 3.21 for 5 and 20 keV. In here, the light blue area is where the least interaction occurs to 5% of total interaction, red indicates 10%, green 25%, yellow 50%, dark blue 75% and purple 90%. Taking this into account, the majority of secondary electrons captured by the SEM detector will come solely from InGaN (with a depth of about 45nm) when 5 keV is applied, whereas 20 keV will excite completely the InGaN and part of Si as it probes 500 nm. Depending thus on the region of interest we need to adjust the applied energy accordingly.

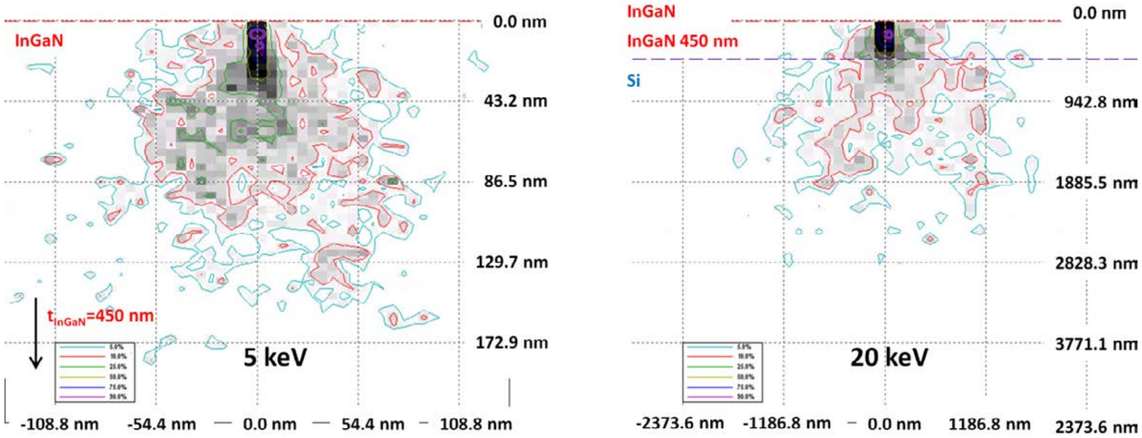

Figure 3.21: Energy per depth profile displayed for 5 and 20 keV. Results calculated by the Casino software considering a 450 nm thick InGaN layer on Si substrate.

3.3 Structural Characterization

3.3.1 High Resolution X-ray Diffraction (HRXRD)

A powerful technique to characterize strain state of epitaxial layers, either from thermal or lattice mismatch, as well as their composition (in special for alloys) is the high resolution x-ray diffraction. X-rays from a quasi point source are sent to the crystal surface under a given angle. After being reflected by different crystal planes, the resulting rays are detected as a function of the sample (or detector) rotation angle. The high resolution X-ray diffraction (HRXRD) analysis in the current thesis was performed by a Panalytical X´Pert Pro MRD system. A picture with the main coordinates used (measuring parameters) is indicated in figure 3.22.

The measure is based on the Bragg's law that determines the angles for constructive and destructive interference between rays emerging from the crystal:

$$2\, d_{hkl} \cdot \sin\, \theta_{B} = n\, \lambda \tag{3.10}$$

Equation 3.3 represents the Bragg's law for constructive interference, where “n” is an integer, ‘λ’ is the wavelength of monochromatic X-rays impinging under an angle ‘θ_B’ on a set of planes with lattice spacing ‘dhkl’ where (hkl) are the Miller indexes (see figure 3.7 (a)). In some simple cases (relaxed layers) it is possible to determine the lattice constant value, the layer thickness and composition by just applying the Bragg's law to each peak in the spectrum.

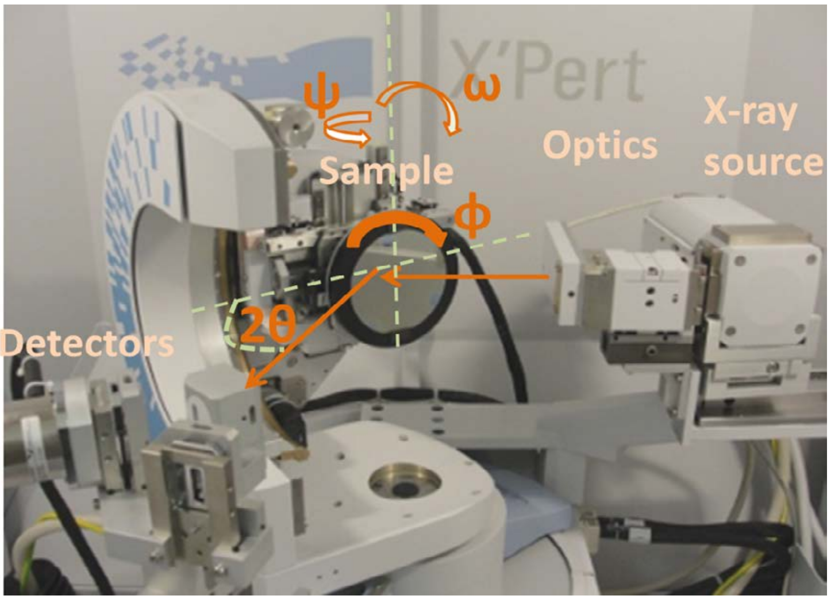

Figure 3.22: Panalytical X´Pert MRD HRXRD set-up with the main coordinates and elements indicated.

From the X-ray source two wavelengths emerge, corresponding to the Cu-$K_{\alpha 1}$ and Cu-$K_{\alpha 2}$ transitions. High resolution needs a monochromatic beam with a small angle distribution and to accomplish this, a collimator is used. The reflection of the Cu-$K_{\alpha 1}$ transition is selected to impinge on the sample at an angle θ to the crystal plane being studied. The first order Bragg condition for constructive interference happens for n=1 at an angle θ_B (equation (3.3)) and the signal is detected with a scintillation detector. This spectrometer is very sensitive and can measure linewidths typically as small as 10 arcsec. During the data acquisition to obtain the *rocking curve*, the detector is rotated with twice the speed of that of the sample, so that the angle between the incident and diffracted beams is twice the angle of incidence as shown in figure 3.22. The plane of reflection must be selected accordingly to the growth orientation of the crystal, that is, for a crystal grown along the (100) or (002) directions, the (400) reflection is preferred when doing the measurement. These planes alternate group-III and group-V atoms, that implies that this reflection reveals details about the smallest crystallographic spacing along the growth direction.

Typical diffraction patterns in the reciprocal space are presented in figure 3.23 (a) for the following cases: a single crystal, a random poly-crystal and a textured poly-crystal. Real measurements are shown in figure 3.23 (b) for the case of a single Si crystal, a polycrystalline Si and textured Al on Si.

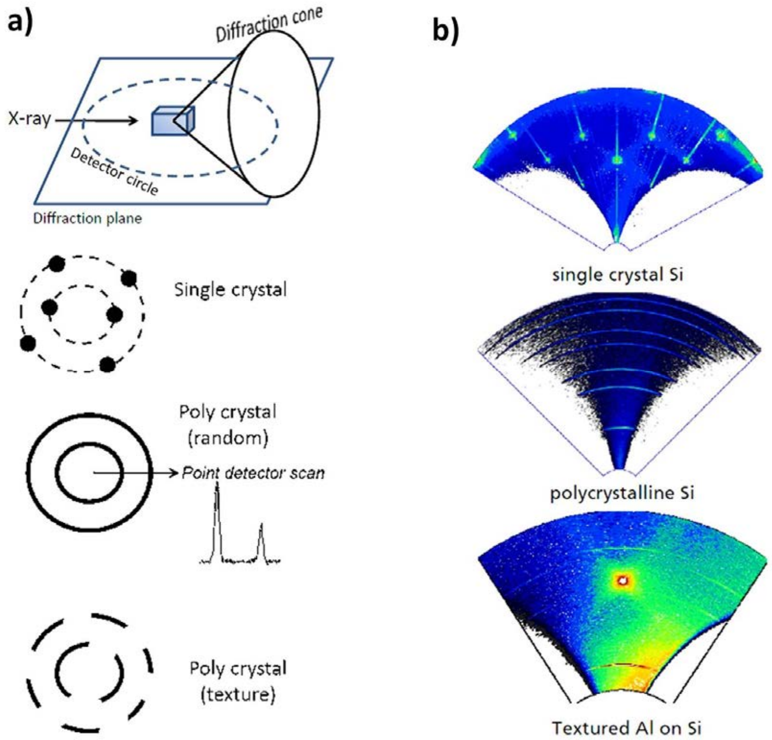

Figure 3.23: (a) Typical diffraction pattern for single crystal and both random and textured Poly crystal. (b) Diffraction pattern for single crystal Si, polycrystalline Si and textured Al on Si.

In the following, the XRD measurements are described in each measurement mode with the previously defined parameters. For the case of the so-called "2θ-ω" or "ω-2θ" scan the X-ray source moves in an angle of ω and 2θ is the angle of the detector movement just as we showed in the previous discussions. The movement in the reciprocal space will be along the **q** scattering vector direction (as defined in figure 3.7), moving thus in the radial direction during sample scan and will show a clear peak when scanning over the diffraction pattern, as shown in the schematic of figure 3.24 for a symmetric 2θ-ω scan in the case of a poly-crystal. From these kinds of measurements and considering relaxed (unstrained) material, the out of plane component can be obtained for any allowed (00l) reflection by:

$$c = \frac{l \bullet \lambda}{2 \bullet \sin \theta_B} \tag{3.11}$$

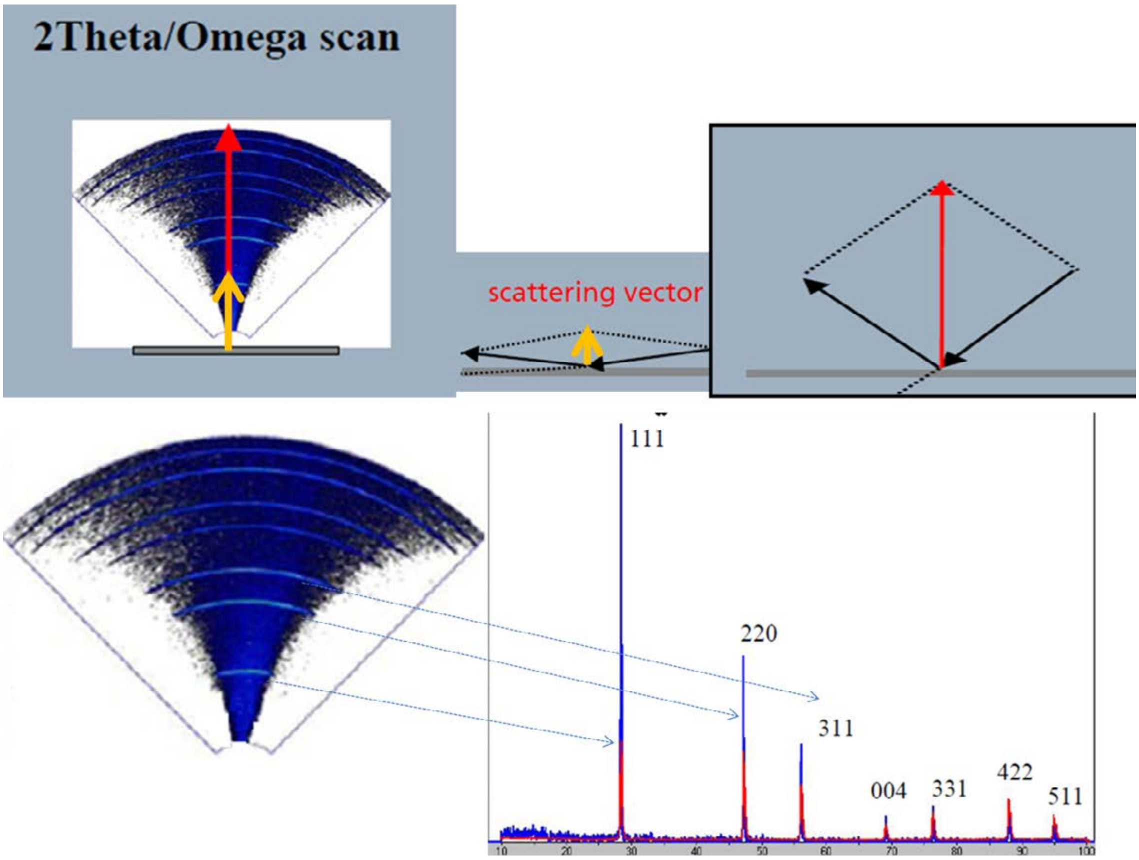

Figure 3.24: Step by step descriptions of the 2θ-ω scan. The scan direction is described by the initial orange (final red) vector representing the reciprocal scattering vector q. The corresponding measured spectrum is shown alongside. The first diffraction streaks are shown explicitly linked to the XRD spectra.

For offset in ω (non-symmetric scan) the scattering vector's direction changes as shown in figure 3.25 (a). By changing thus ω and at the same time performing a 2θ-ω scan for each value of ω, it is possible to explore/map the complete reciprocal space. Such kind of measurements, illustrated in figure 3.25 (b), which involves 2 axis of the reciprocal space map are called 2 axis scan and in the particular case of the 2θ-ω scan for each value of ω the performed measurement is called a reciprocal space map (RSM).

After having introduced 2θ-ω scan and observed the movements for solely ω, it is straight forward to imagine a scan solely around ω, called rocking curve. A scan over asymmetric planes, different to the (00l) planes, gives additional information as not only the '***c***' parameter defines the peaks in the spectra but also the '***a***' (in plane) lattice parameter contributes. The same is valid for the RSM and even more, the actual lattice parameters can be extracted for these scans as information on composition, strain and mosaicity can be obtained.

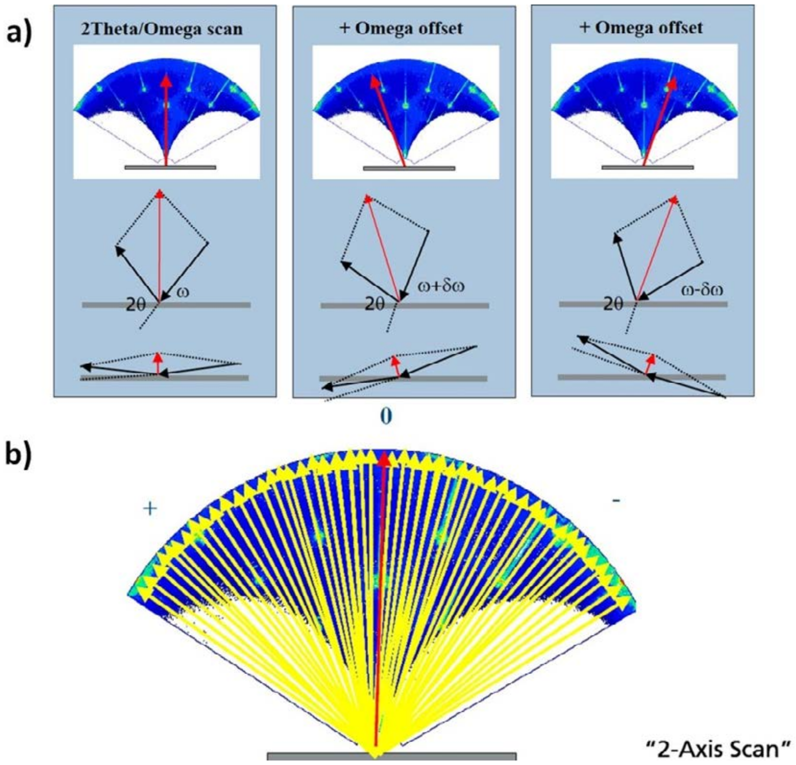

Figure 3.25: (a) Change of direction by in the reciprocal space by applying an offset for ω. (b) Illustration for the 2 axis scan.

An example for a RSM around an asymmetric axis and where we have strain is presented in figure 3.26 (a) for a sample with strained Si layer on top a Si_{1-x} Ge_x layer grown on a Si substrate. In addition, all the properties that can be extracted are summarized in the figure. The schematic of how it would be seen in for the symmetric (002) next to the (224) is presented in figure 3.26 (b). As can be seen in case of the presence of a strained layer vertical aligned peaks are observed and if the layers are relaxed we will have an offset in the horizontal direction.

To extract the information the values obtained of ω, 2θ from the HRXRD scan are used and the corresponding scatter directions are calculated by the following equations [Morales 2009]:

$$\begin{aligned} q_x &= \frac{1}{\lambda}\left(\cos(\omega) - \cos(2\theta - \omega) \right) \\ q_y &= \frac{1}{\lambda}\left(\sin(\omega) + \sin(2\theta - \omega) \right) \end{aligned} \tag{3.12}$$

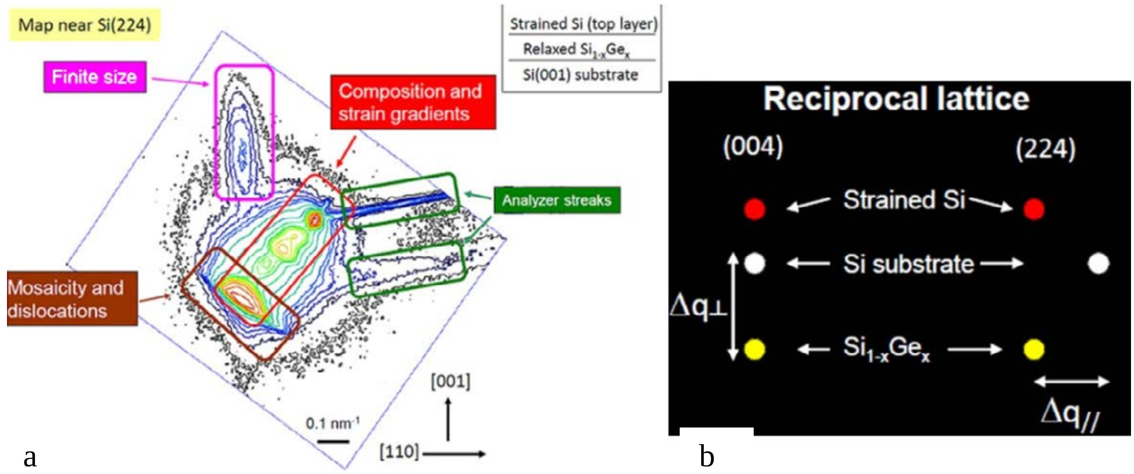

Figure 3.26: (a) RSM of sample with strained Si layer on top a Si_{1-x} Ge_x layer grown on a Si substrate, in addition all the properties that can be extracted are summarized in the figure. (b) Schematic of RSM symmetric diffraction around 002 and 224 directions of Si.

To calculate the in- and out-of-plane misfit strain the following equation can be used:

$$f_{//} = \frac{(q_{m//} - q_{r//})}{q_{r//}}$$
$$f_{\perp} = \frac{(q_{m\perp} - q_{r\perp})}{q_{r\perp}} \tag{3.13}$$

Here the ‘$\mathbf{q_m}$’ corresponds to the measured value and ‘$\mathbf{q_r}$’ corresponds to the relaxed layer in- and out-of-plane reciprocal vectors. The composition is calculated from bi-axial strain equation:

$$f_{\perp} = -2\frac{C_{13}}{C_{33}} f_{//} \tag{3.14}$$

Here ‘$\mathbf{C_{13}}$’ and ‘$\mathbf{C_{33}}$’ are the distortion (elastic) coefficients which in case of ternaries as InGaN are calculated as a linear dependence (modified Vegard's law) on the composition same for ‘$q_{r//}$’ and ‘$q_{r\perp}$’:

$$\begin{aligned} C^{InGaN}{}_{13} &= x \cdot C^{InN}{}_{13} + (1-x) \cdot C^{GaN}{}_{13} \\ C^{InGaN}{}_{33} &= x \cdot C^{InN}{}_{33} + (1-x) \cdot C^{GaN}{}_{33} \\ q_{r//}{}^{InGaN} &= x \cdot q_{//}{}^{InN} + (1-x) \cdot q_{//}{}^{GaN} \\ q_{r\perp}{}^{InGaN} &= x \cdot q_{r\perp}{}^{InN} + (1-x) \cdot q_{r\perp}{}^{GaN} \end{aligned} \tag{3.15}$$

For the case of InGaN on GaN template the reciprocal maps are taken around the (10-15) plane and by decomposing the plane in its equivalent orthogonal plane components (10-10) and (0005) the projection (the scattering vectors) as a function of the lattice parameters are obtained. For this, the formula for the distance between planes in the hexagonal case is used:

$$\frac{1}{d^2_{hkl}} = \frac{4}{3}\cdot\{(h^2 + h\cdot k + k^2)\cdot a^2\} + l^2\cdot c^2 \tag{3.16}$$

Together with Bragg´s law both lattice parameters ‘a’ and ‘c’ can be obtained:

$$a = q_{m//} = \frac{\sqrt{3}\cdot\lambda}{3\cdot q_x}$$
$$c = q_{m\perp} = \frac{5\cdot\lambda}{2\cdot q_y} \tag{3.17}$$

For the case of Si the scan measurements needs to be performed around the (224) plane.

3.3.2 Transmission Electron Microscopy (TEM).

In the case of SEM the interaction of electron with matter was discussed and summarized in figure 3.16 showing several possible interactions. When the electron beam has even higher energy and the sample is very thin, an additional interaction is possible due to the electron wave-like behaviour, namely, the transmission of electrons through the sample. The wave-like behaviour of the electron was first introduced by Broglie, and the electron wavelength (ignoring relativistic effects and units inconsistency) can be approximated as:

$$\lambda = \frac{1.22}{\sqrt{E}} \tag{3.18}$$

In this equation E is the energy in electron volts (eV) and λ the associated wavelength in nm. Equation 3.18 says that a 100 keV electron behaves as a wave with λ~0.004 nm, which is much smaller than the diameter of an atom. Though there exist many limitations to reach such “spatial” resolution (for example, lack of good quality of electron lenses), nevertheless the point resolution of modern TEMs lies in the 0.1 nm range. In addition to the excellent spatial resolution, the strong interaction of the electrons with matter allows the interaction volume to be extremely small, but still being one of the reasons for limited resolution in practice.

TEM incorporate a similar electron generation and focusing system as those in SEM systems, i.e. an objective lens, intermediate and projector lens are placed after the sample and before a screen where the image is formed (figure 3.27). Depending on the plane that is chosen as objective plane for the intermediate and projector lenses, either a diffraction mode (where the back focus plane is taken as objective plane), or an image mode (where the image plane is taken as objective plane) are possible.

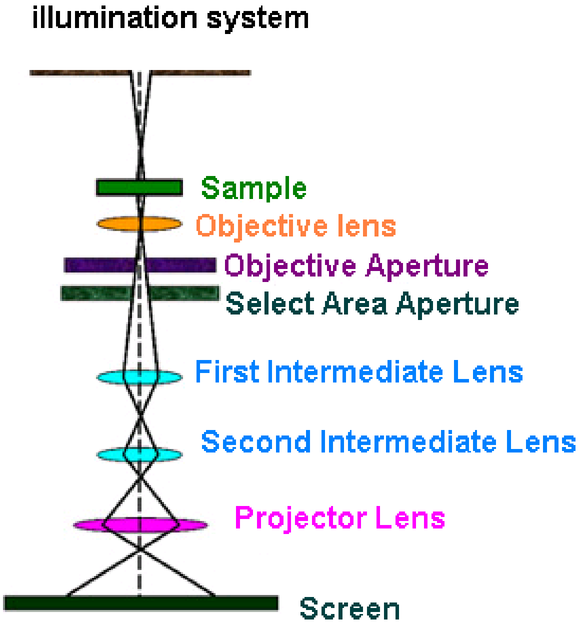

Figure 3.27: TEM schematic.

There are two basic modes of TEM operation: i) bright-field (BF) mode, where the (000) transmitted beam contributes to the image; and ii) dark-field (DF) imaging mode, in which the (000) beam is excluded. The size of the objective aperture in bright-field mode directly determines the information to be emphasized in the final image. If the size is chosen as to exclude the diffracted beams, the configuration then corresponds to the one used for low-resolution defect studies, so-called diffraction contrast. In this case, a crystalline sample is oriented to excite a particular diffracted beam, or a systematic row of reflections, and the image is sensitive to the differences in sample thickness, distortion of crystal lattices due to defects, strain and bending.

Several imaging modes are available, depending on how images are formed by using the objective aperture and the diffraction/imaging mode to select electrons that have been scattered through particular angles:

- Selected area diffraction (SAD): An aperture is inserted above the sample which only permits electrons that pass through the aperture to hit the sample. BF and DF imaging are done together with SAD the direct beam is selected to form a BF image. To form a DF image only electrons that are not in the direct beam are selected
- Annular Dark-Field: By using an annular aperture (or by software: controlling scanning coils to spin the direct beam around the optic axis.), conical diffraction is used. The direct beam is always off axis but electrons diffracted at the cone angle are

always scattered on (parallel-) axis. An annular dark field image formed only by very high angle, incoherently scattered electrons (as opposed to Bragg scattered electrons) is highly sensitive to variations in the atomic number of atoms in the sample (Z-contrast images). This technique is also known as high-angle annular dark-field imaging (HAADF).

- Scanning TEM (STEM): Similar to SEM, electrons are captured directly by a detector during the scanning. Serial recording is used. The signal is generated at a point on the sample, detected, amplified, and a corresponding signal displayed at an equivalent point on the computer display. The image builds up over several seconds or even minutes

3.3.2.1 High Resolution Transmission Electron Microscopy (HRTEM)

The high-resolution transmission electron microscopy (HRTEM) uses both the transmitted and the scattered beams to create an interference image. It is a phase contrast image and can be as small as the unit cell of the crystal. Here, outgoing modulated electron waves, being at very low angles, interfere with themselves during propagation through the objective lens. All electrons emerging from the specimen are combined at a point in the image plane. HRTEM has been extensively and successfully used for analyzing crystal structures and lattice imperfections of various kinds in advanced materials at atomic resolution. It can be used to characterize point defects, stacking faults, dislocations, precipitates, grain boundaries, and surface structures.

3.3.2.2 Energy Dispersive X-ray Spectroscopy (EDS/EDX)

A stationary atom within the sample has ground state (or unexcited) electrons sorted in discrete energy levels or electron shells bound to the nucleus. The incident beam may excite an electron from an inner shell, expelling the electron from the shell and at the same time create an electron hole at the previous location of the expelled electron. An electron from an outer (higher-energy) shell is then able to fill the hole, and the difference in energy between the higher-energy shell and the lower energy shell may be released in the form of an X-ray. The energies of these X-rays are characteristic of the difference in energy between the two shells as of the atomic structure of the emitting element. The intensity and energy of the X-rays emitted from a specimen can be measured by an energy-dispersive spectrometer. EDS allows thus the elemental composition of the specimen to be measured.

The TEM measurements were all carried out by the group of Francisco Morales in Cádiz.

For the samples presented in current thesis where this technique was used their crystal structure and composition were accessed by selected-area electron diffraction (SAED), and EDX spectroscopy using a 5x5 nm^2 punctual scanning TEM (STEM) probe. The cross section and layers interface were studied by conventional TEM (CTEM), high angle annular dark field (HAADF) imaging, and high-resolution TEM (HRTEM) performed in JEOL 1200EX and JEOL-FEG 2011 microscopes. For TEM, the samples were thinned to electron-transparency by mechanical grinding, polishing, and ion milling at 3 KeV with GATAN’s low voltage precision ion polish system.

3.4 Optical Characterization

3.4.1 Photoluminescence (PL)

For optoelectronic applications the optical characterization of the grown samples is needed. There exist a variety of techniques however the concentration will be focused on the so called photoluminescence spectroscopy (PL). This technique uses the fact that electrons can be excited to jump over the energy bandgap of the material by optical radiation at high enough frequencies. The excited electrons and holes relax to energies near the band edge by interactions with phonons (lattice vibrations) and recombining radiantly with energy characteristic for the material and structure [Gfroerer 2000].

In the experiment itself the use of pump laser is to create electron-hole pairs. The electrons are collected at the lowest energy level in the conduction band, whereas the holes accumulate at the highest energy state in the valence band. If these two energy levels are at the same position in k-space, typically at k=0 then the semiconductor is called a *direct semiconductor*, otherwise an *indirect semiconductor* (see figure 3.28). In case of the direct semiconductor, the electron recombines with the hole emitting a photon with a wavelength corresponding to the bandgap. The light that is emitted this way, the luminescence, is emitted

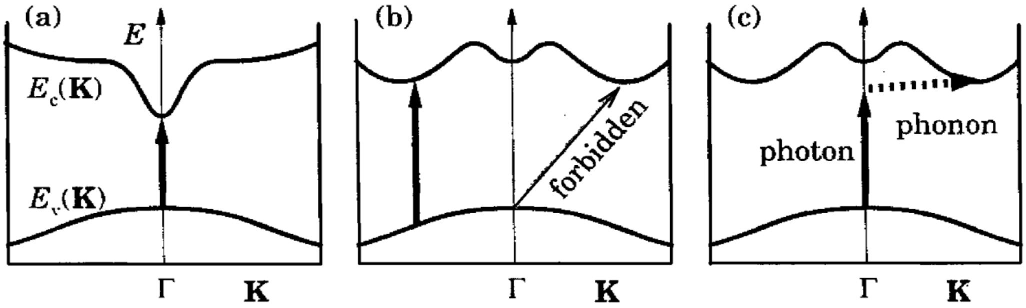

Figure 3.28: Optical absorption across the bandgap in different types of semiconductors (a) Absorption across a direct bandgap at Γ. (b) Absorption across an indirect bandgap is forbidden but vertical transitions occur for all K. (c) Transition across an indirect bandgap with absorption of both a phonon and a photon. Taken from [Davies 1998]

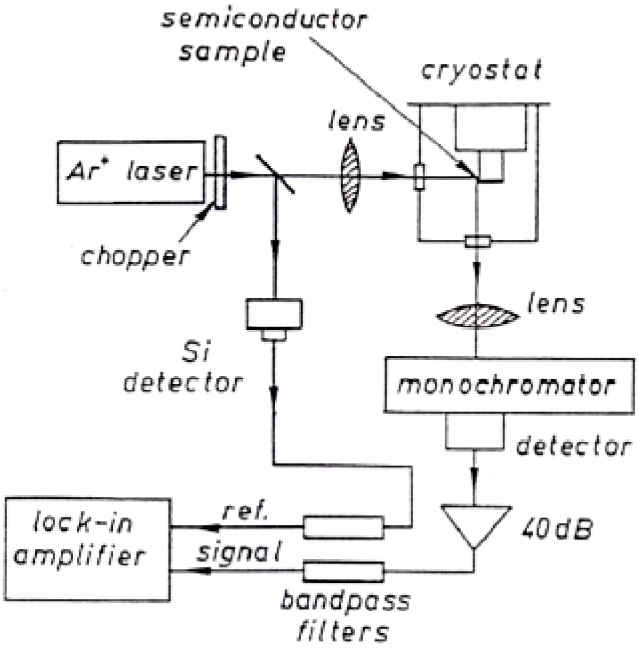

Figure 3.29: A schematic setup for the PL measurements.

in all directions from the sample surface. Lenses are used to collect and focus the light into a monochromator that let only one wavelength of the light pass through to the detector as the configuration is shown in figure 3.29. The wavelength of the monochromator is controlled by a computer. To remove noise as for example light bulbs the use of a lock-in technique is presented. It consists in modulating the light from the pump laser with a chopper. The chopper is a rotating metallic disk with holes that periodically blocks the laser beam. The signal from the detector (sum of the noise and the modulated sample signal) is multiplied with a reference signal of the same frequency and rectified, thus the noise part is averaged out. Usually the light from the pump laser is filtered out before entering the spectrum analyzing equipment.

At room temperature (300K) the PL peak is usually broadened and red-shifted compared to the low temperature (4K) due to thermal expansion of the lattice and broadening of the Fermi-Dirac distributions, respectively. Yet some vital information can be gathered, such as bandgap energy and crystal quality. In the case of ternaries, it is essential as the bandgap is directly related to the composition and therefore it can be calculated by the modified Vergard´s law which states as shown by Eq. 2.1 of chapter 2.

In addition, another very important hallmark that can be extracted by PL is the activation energy. The activation energy is defined as the energy a carrier needs to overcome before being able to recombine. The mechanism is governed by an Arrhenius law, stating that emission that occurs is directly proportional to the probability of the activation energy to overcome the thermal energy ‘k_BT’.

For films with excellent crystalline quality and where no or low non radiative recombination centres are present, such as defects, even exciton emission can be distinguished as discussed in detail in chapter 2.

3.4.2 Cathodoluminescence (CL)

In a FE-SEM, the electron beam interaction with specimen may generate not only secondary electrons but depending on the applied accelerating voltage also backscattered electron, X-rays (used for energy dispersive spectroscopy, EDS) or cathodoluminsecence (CL) as was shown in figure 3.19.

CL is the emission of light from a material under e-beam irradiation. Compared with light, electron excitation is rather strong. The incident electrons generate a high density of electron–hole (e–h) pairs due to inelastic scattering—it is commonly accepted that an incident electron of energy ‘E’ can generate $\sim E/3E_g$ pairs. Those e–h pairs can recombine and emit photons. The energy of these photons depends on the energy difference between the electrons and holes, which is related to the bandgap ‘E_g’ or to the energy levels of the impurities and defects. Consequently, CL can reveal most of the luminescence processes in the materials. Development of the electron microscopes improved control of the size and the position of the electron beam, allows acquiring luminescence from nanoscale regions.

CL is a powerful method to correlate luminescence with the sample structure and to clarify the origin of the luminescence by combination with other electron beam (e-beam) techniques. With CL, one can also map the luminescence distribution both laterally and along the sample depth that can provide precious information on the growth mechanisms, especially in ternary materials where obtained luminescence is directly correlated with its composition.

Using the CASINO software previously introduced an estimation can be given for the region in where CL takes place upon a certain electron acceleration voltage applied by the microscope. As an example, the cases for 5 and 20 keV for a 450 nm InGaN layer on a Si substrate are presented in figure 3.30. From here it is clear that a 5 keV acceleration voltage will generate CL signal mostly coming from a region between 5-90 nm from the sample surface and 10 keV on the other hand will come mostly from 92-270 nm from the surface sample.

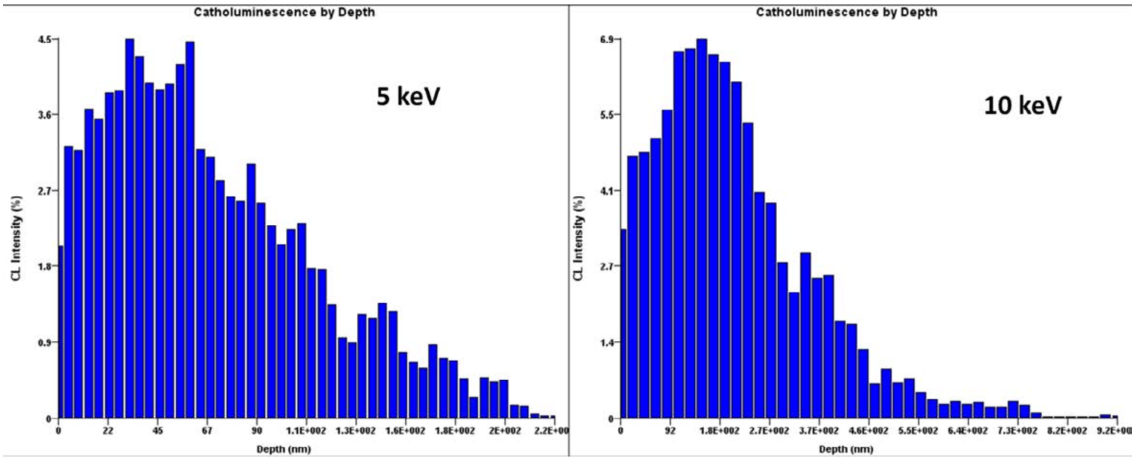

Figure 3.30: Results of the CASINO simulation software for 200 electrons. The CL by depth for a simulated sample of 450 nm thick InGaN on Si.

3.4.3 Scanning Near Field Optical Microscopy (SNOM)

In 1873 the German physicist Ernst Abbe [Lauterbach 2012] observed that the resolution of optical imaging instruments is fundamentally limited by the diffraction of light. His investigation revealed that ultimately the resolution of an imaging instrument is not constrained by the quality of the instrument, but by the wavelength of light used and the aperture of its optics. This meant that a microscope could not resolve two objects located closer than $\lambda/2N_A$, where ‘λ’ is the wavelength of light and ‘N_A’ is the numerical aperture of the imaging lens.

In 1928 E.H. Synge [Synge 1928] proposed a method to overcome the diffraction limit by measuring the evanescent waves of a certain sample. Evanescent waves are formed when waves travelling in a medium undergo total internal reflection at its boundary when striking at an angle greater than the so-called critical angle. An example is presented in figure 3.31 (a) with the regions of emission around a QD illuminated by a laser. Where evanescent waves are being emitted is called the near-field, the distance is typically below λ, and where propagative waves are being emitted is called far-field, distances above λ. SNOM, as its name states, measures the near field by the use of a feedback nanoprobe (figure 3.31 (b)). In the same way as in AFM a constant distance is maintained by tapering the nanoprobe. Therefore it is possible to obtain morphological information beyond optical diffraction limitations. An optical fibre located along (coaxial) the nanoprobe is collecting or guiding light towards the sample. The size of the point light source (aperture at optical fiber´s tip) defines the resolution of the SNOM experiment (typically 50-100 nm). However, notice that this resolution is the effective emission capture area thus emitters of smaller dimension still will be detected as the emission will be entering from the conical distribution with the emitter as central point. Nevertheless the exact location of smaller emitters is now difficult to determine.

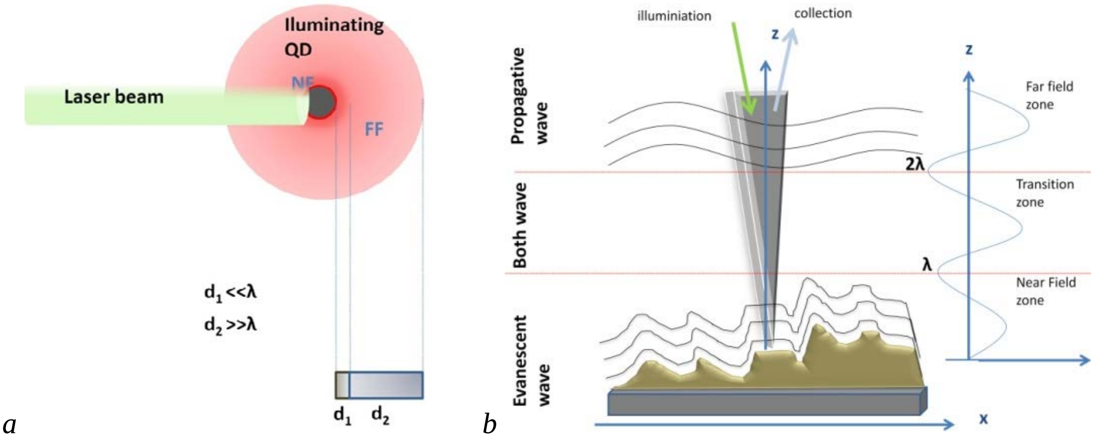

Figure 3.31: (a) Defined emission regions around a laser illuminated QD (b) Measuring near field by use of a feedback nanoprobe.

There exist four operation modes (illustrated in figure 3.32):

Transmission mode imaging: The sample is illuminated through the probe, and the light passes through the sample is collected and detected.

Reflection mode imaging: The sample is illuminated through the probe, and the light reflected from the surface is collected and detected.

Collection mode imaging. The sample is illuminated with a macroscopic light source from the top to bottom, and the probe is used to collect the light from the sample surface.

Illumination/collection mode imaging: The probe is used both for the illumination of the sample as for the collection of the reflected signal.

The detection of the collected light can be achieved by several instruments as for example: avalanche photo diode (APD), a photomultiplier tube (PMT) a CCD or a spectrometer.

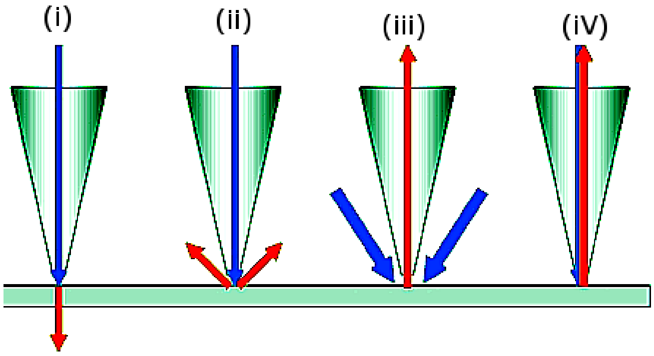

Figure 3.32: Schematic representation of the four SNOM operation modes.

3.5 Chemical Characterization

3.5.1 Gas Chromatography

In early 1900´s, gas chromatography (GC) was discovered by Mikhail Semenovich Tsvett as a technique to separate compounds [Berezkin 1989]. The underlying principle is the movement of material in one physical state (gas) through another, fixed material, being in a different physical state (solid, liquid). The fixed material is generally located in a column of very small width (10^{-3}-10^{-6} m) and rather long (2-60 m). As the material in motion, being in a mobile phase, passes through the material that is fixed, the former is adsorbed at different rates depending on the materials compound properties. In this way, expelled from the column the mobile material is separated into its several compounds which can be measured and so identified by a mass spectrometer. To increase the efficiency of separation, the column is placed in a kind of furnace to secure a high enough temperature for the mobile material to keep its gas phase. Large surface areas are desired for the fixed material to increase adsorption of the mobile phase one. The material to be analyzed may be injected, whether an injector evaporates the material into the column, or desired gases produced from some reaction may be introduced directly through some inlet towards the GC.

The carrier gas plays an important role, and varies in the GC used. Carrier gas must be dry, free of oxygen and chemically inert mobile-phase. Helium is most commonly used because it is one of safest elements and at the same time, it has good efficiency. It also offers larger range of flow rates what makes it compatible with many detectors. Nitrogen, argon, and hydrogen are also used depending upon the desired performance and detector to be used. Both hydrogen and helium, which are commonly used on most traditional detectors such as flame ionization (FID), thermal conductivity (TCD) and electron capture (ECD), provide a shorter analysis time and lower elution temperatures, temperature needed to extract one material from another by the use of a solvent, of the sample due to higher flow rates and low molecular weight. For instance, hydrogen or helium as the carrier gas gives the highest sensitivity with TCD because the difference in thermal conductivity between the organic vapour and hydrogen/helium is greater than other carrier gases. Other detectors, such as mass spectroscopy, use nitrogen or argon which has a much better advantage than hydrogen or helium due to their higher molecular weights, which improve vacuum pump efficiency.

The carrier gas system contains, in general, a molecular sieve to remove water and other impurities. A two stage pressure regulation is required to minimize the pressure surges and to monitor the flow rate of the gas. Monitoring the flow rate of gas, requires a flow or pressure regulator on both tank and chromatograph gas inlet; different gas types will use different type of regulator.

In this Thesis the GC system used had a TCD detector that works by measuring the change in carrier gas thermal conductivity (see figure 3.33) caused by the presence of the sample (mobile-phase material indicated as blue triangle in figure 3.33 (b)) which has a different thermal conductivity from that of the carrier gas (indicated as orange sphere in figure 3.33 (a)). Their working principle consists of an electrically heated source that is maintained at constant power. The temperature of the source depends upon the thermal conductivities of the surrounding gases. The source is usually a thin wire made of platinum or gold. The resistance of the wire depends upon temperature, which is dependent upon the thermal conductivity of the gas (A scheme of the circuit is shown in figure 3.33 (c)).

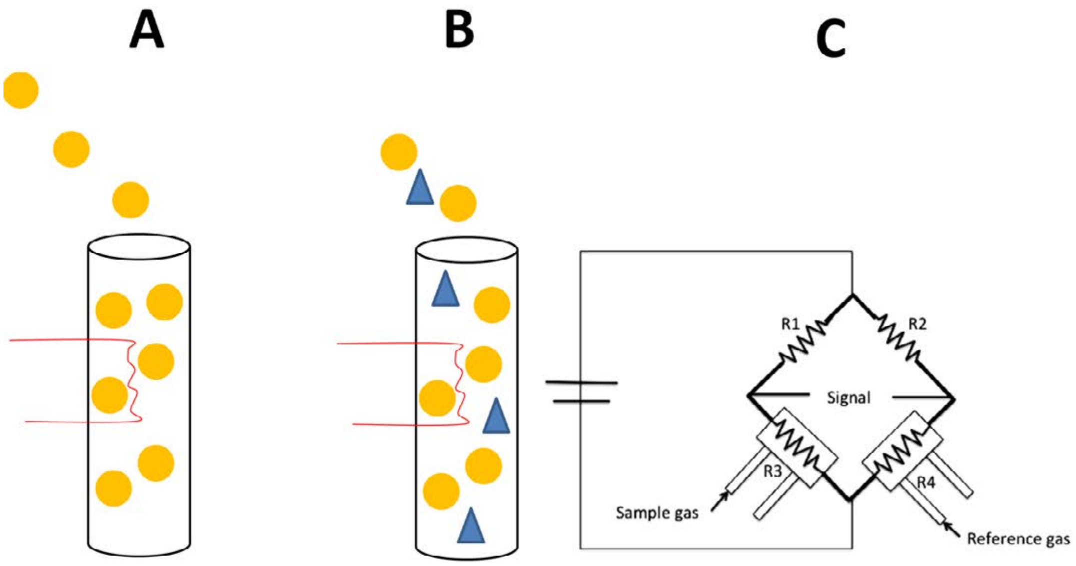

Figure 3.33: TCD detector working principle. (a) A heated filament is cooled by the flow of carrier gas (orange spheres). (b) When the carrier is contaminated by a sample of interest (blue triangle), the cooling effect of the gas changes. The difference in the cooling is used to generate the detector signal. (c) A wheastone bridge configuration is used to detect the signal.

Usually two detectors are employed, one of which is used as the reference for the carrier gas and the other which monitors the thermal conductivity of the carrier gas and sample mixture. Carrier gases such as helium and hydrogen have very high thermal conductivities so the addition of even a small amount of sample is readily detected. A scheme of the GC setup is illustrated in figure 3.34 in where the complete column is represented by the orange line.

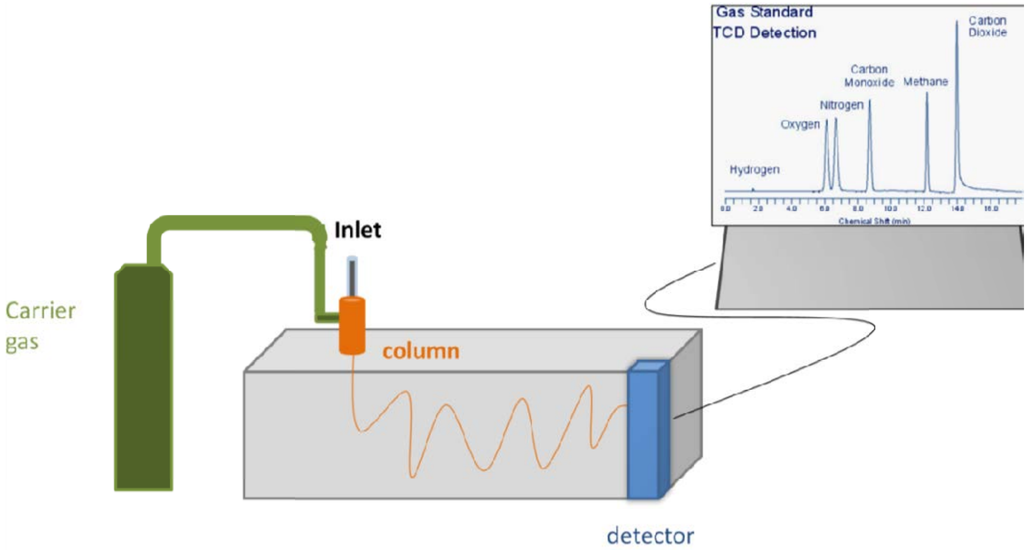

Figure 3.34: Scheme of GC operating principle. Notice that the orange line displays a continues column.

CHAPTER 4

ELECTROCHEMISTRY: THEORETICAL BACKGROUND

In this chapter the main parameters (hallmarks) describing the device performance for both water splitting and bio-sensing applications are established. Due to the unique properties of both high In-content InGaN and InN materials, nontraditional features are expected to drive the devices hallmarks. For completeness, the typical mechanisms behind both applications (water splitting and bio sensing) are presented as an introduction to electrochemistry, being the basis to explain the observed device performance.

4.1 Water Splitting (Hydrogen generation)

The principal components relevant for the water splitting process can be easily identified by considering the simple electrolysis process, where water molecules are split by means of an external electrical power source. The complete water splitting system consists of (at least) two electrodes, a recipient, an external power source, and water with salts. The recipient that contains the water and salts is called electrochemical cell (EC). The water and salt are in this case the electrolyte. The salts are mainly added to the water to increase its conductivity.

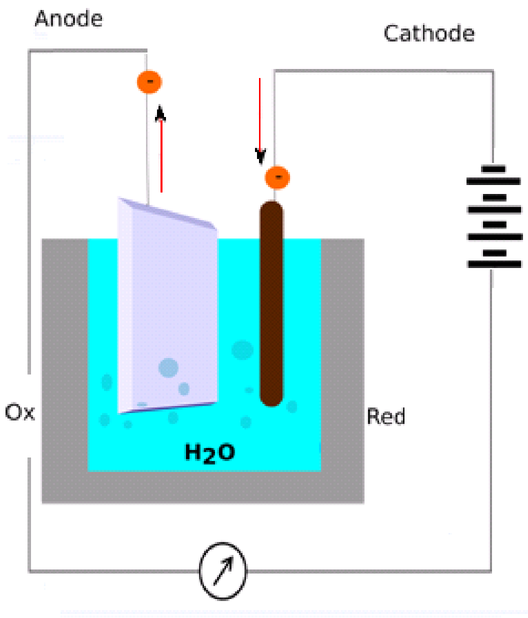

Figure 4.1: Schematic of a typical Electrochemical Cell. The electrode where electrons enter the circuit is called cathode whereas the exit electrode is called anode.

For an electrolytic process an electric current circulating through a circuit is needed. Here, instead of a classical wire circuit, chemical reactions and charge exchange in the solution being electrolyzed provide both the electric current and the circuit loop. Figure 4.1

shows an EC where electrons, represented by orange spheres, enter, from the power source, into a conductive material (cathode electrode) submerged in a liquid, in this example, water. The current is maintained by chemical reactions until electrons reach the opposite electrode (anode electrode) closing the circuit when reaching the power source.

An electro-chemical process involves electron-transfer as part of the reactions that take place at the electrodes surface. Defining “oxidation number” as the net positive charge in a species, oxidation means the process of losing one electron, which means increasing the oxidation number, while reduction is the process of gaining an electron, which means decreasing the oxidation number. Then, a redox reaction is that involving oxidation of one or more species and a simultaneous reduction of others.

Regarding the electrochemical process in the EC, the loss (oxidation) or gain (reduction) of electrons may take place involving species in i) the electrolyte, or ii) at the electrodes. In this way in i) by oxidation the species loses an electron and consequently in ii) the electrode gains (accepts) by reduction the electron expelled by the species. The electrode that accepts electrons and where the species are being oxidized is the anode. On the other hand, the electrode where the species are being reduced is the cathode.

The agents that promote the oxidation (reduction) are called oxidizing (reducing), or oxidant (reductant) agents. The oxidation agent thus gains electrons and is reduced in the chemical reaction. Commonly known as the electron acceptor, the oxidizing agent is normally in one of its higher possible oxidation states, because it will gain electrons and be reduced.

In the present example of water electrolysis the anode electrode accepting electrons and conducting them through the closed circuit towards the cathode may be regarded as the oxidizing agent. Similarly, the cathode will be the reducing agent. Notice that in the EC the closed circuit ensures that both reactions at the electrodes are linked, i.e when oxidation occurs at the anode a likewise reduction occurs at the cathode. The chemical reaction starts at the electrodes once the current is “on”, and this corresponds to the case when at least 1.23 eV is applied between electrodes, as the energy needed to break the water molecule bond. In the case of water plus salt as electrolyte, the oxidation, proceeds when electrons are expelled from ions/analyte and enter the electrode.

Observing the case of water (H_2O) in more detail, where O_2 is formed at the anode, hydrogen protons (H^+) at cathode and the electrons follow the half reaction (unbalanced):

$$H_2O \rightarrow O_2(g) + H^+ + e^- \tag{4.1}$$

that after balancing, becomes:

$$2H_2O \rightarrow O_2(g) + 4H^+ + 4e^- \tag{4.2}$$

The formation of H_2 and hydroxide ions at the cathode follows the half reaction (unbalanced):

$$H_2O + e^- \rightarrow H_2(g) + OH^- \tag{4.3}$$

and after balancing becomes:

$$4H_2O + 4e^- \rightarrow 2H_2(g) + 4OH^- \tag{4.4}$$

The overall reaction is obtained by adding both half reactions:

$$6H_2O + 4e^- \rightarrow O_2(g) + 2H_2(g) + 4H^+ + 4OH^- + 4e^- \tag{4.5}$$

From here, electrons can be eliminated on both equation sides obtaining:

$$6H_2O \rightarrow O_2(g) + 2H_2(g) + 4H^+ + 4OH^- \tag{4.6}$$

Now the hydroxide and protons will react to form water $4H^+ + 4OH^- \rightarrow 4H_2O$ and therefore we finally obtain:

$$2H_2O \rightarrow O_2(g) + 2H_2(g) \tag{4.7}$$

Above reactions suggest that with this setup only Hydrogen and Oxygen gas will be produced. Notice that, as done by the balancing, one can always add OH^- or H^+ to balance the charge. Recalling that pH is defined as the negative of the logarithm to base 10 of the activity of the hydrogen ion, there is always presence of such ions due to the pH of the electrolyte (water plus salts), so pH is determined by the salts.

From this simple example of water splitting by electrolysis, several crucial key points affecting the water splitting process in a EC can be extracted. First of all, it is clear that the amount of products (Hydrogen and oxygen) generated depends on the efficiency of the redox reactions. Being the electrodes the oxidizing and reducing agents, they need to be optimized to increase this redox reaction as much as possible. The ***electrochemical activity*** of electrodes is thus essential. On the other hand, the ***transport of species*** towards the place (electrodes in this case) where the redox reaction occurs must be optimized in terms of ***selectivity*** of this transport, as only the species desired should take part of the redox reactions, thus the only being transported (notice this implies that elements used for the transport must not react with the electrode, or only to a minimum extent); and in terms of ***speed of reaction*** since this will also enhance efficiency. Considering these key points, the electrolysis of water can be optimized by:

- Improving the oxidation process (for anode) or the reduction process (for cathode) at the interface between electrolyte and surface electrode.
- Choosing an adequate electrolyte, salt in this case, as the water is to be split. The salt, being the main responsible for the transport, must be chosen so not to react with the electrodes while providing a good conductivity.
- Adding a catalyst which is a chemical agent that increases the reaction speed. The modification of surfaces by attaching an external chemical agent on them, such as a catalyst, is called surface functionalization. This process is not always straightforward and needs to be optimized.

One of the most sustainable methods of producing H_2 is photo-electrochemical (PEC) water-splitting, which is essentially an electrolysis process, but using sunlight as power source providing the current. Solar energy is used to break water molecules into H_2 and O_2 through a process called "hydrogen evolution reaction." This implies an additional requirement which is that the process of sunlight absorption needs to generate enough potential to start the redox reaction, i.e. at least 1.23 eV.

Unluckily, due to the slowness of reactions, there exist several potential losses in an electrochemical process such as the redox reaction. The difference between the resulting potential in a EC (let it be E) and each individual reaction equilibrium potential (E_{eq}) is called polarization and is quantified in terms of an overpotential (η). This overpotential is called anodic when positive and cathodic when negative in value. There are three types of polarization and these are additive, as expressed in equation:

$$\eta_{total} = E - E_{eq} = \eta_{act} + \eta_{conc} + iR \tag{4.8}$$

Here η_{act} is the activation potential which is a function describing the charge transfer kinetics of an electrochemical reaction; η_{conc} is the concentration overpotential which corresponds to a function describing the mass transport limitations associated with electrochemical processes; iR is the ohmic drop which takes into account the electrolytic resistivity in the closed circuit.

From the above definitions it is easy to relate the iR, in case of the PEC, to the potential loss due to the contacts connecting the wires to the electrodes. The η_{conc} can be related to the electrolyte (salts) as it describes the mass transport limitations, whereas the η_{act} will be the key to start the redox process and therefore the water splitting/ Hydrogen generation. It is clear from this that the actual potential needed to be provided to the electrode, for most efficient performance, must be undoubtedly higher than 1.23 eV.

One of the main attributes of considering In(Ga)N as an electrode is its high stability in aqueous solution as an example R. Kirste et al. [Adapted from Kirste 2015] shows that for both Ga and N-polar surfaces if GaN only an extremely low amount of Ga particles (0.3 and 50 parts per billion (ppb) respectively) are measured by inductively coupled plasma spectrometry (ICP-MS) over a weeks period. The effect of surface polarity on photoelectrochemical properties is very recently been studied for GaN in a variety of electrolytes (H_2SO_4, Na_2SO_4 and NaOH) showing higher efficiency from the polar surfaces [Bae 2016]. For InGaN several electrolytes have been tested with success KOH, H_2SO_4 (with scarifying agents), HBr and HCl are the most common used [Juodkazytė 2014] [Li J 2008]. Higher stability of n-type InGaN towards etching (photo-corrosion) is expected when used with co-catalysts and HBr shows most stable results [Finken 2015][Luo 2008].

In this thesis the aim is to demonstrate that InN QDs grown on InGaN layers can act as catalysts for efficient PEC action, reducing the overpotential needed to start the redox reaction. Both 0.5M HBr (pH3) and H_2SO_4 (pH3) and the latter with scarifying agents 0.5M Na_2SO_4 will be used as electrolytes.

4.2 Biosensors and Electrochemical sensing

Biosensors are systems capable of detecting an analyte of interest by changing the properties of a biological sensitive element (bio-receptor, molecular recognizers, etc) and converting this change (pH, fluorescence, heat, mass charge, electro-catalytical behavior, etc) into a measurable electrical signal. A scheme of its operational flow is shown in figure 4.2. Each part of these systems should be optimized independently for a specific analyte of interest.

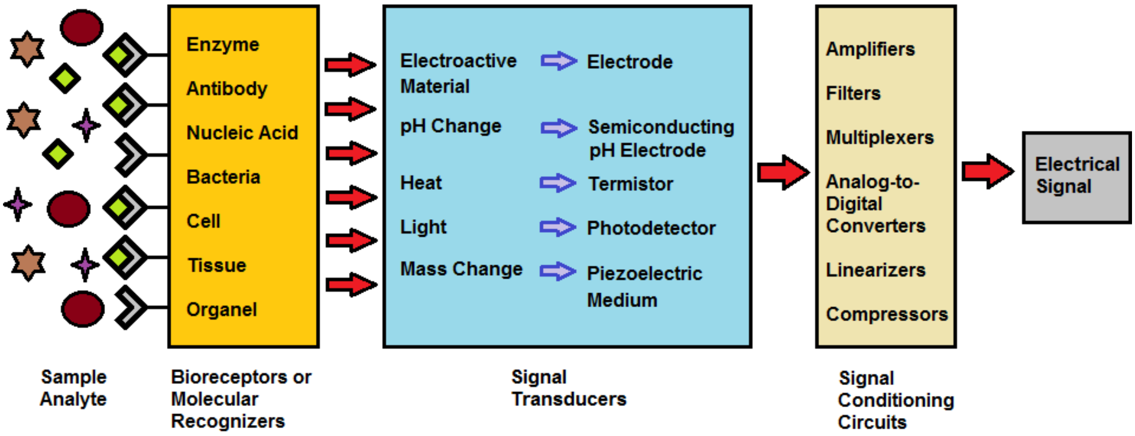

Figure 4.2: Definition and components description of a biosensor.

When the conversion mechanism is electrochemical the biosensor is said to be an electrochemical biosensor which is the case presented in current thesis. In this case the bioreceptor and electrode should be chosen considering its affinity towards the analyte of interest, that is, how easy the bioreceptor functionalization on the electrode is and how the attachment of the analyte of interest to the functionalized bioreceptor promotes a detectable electrochemical reaction on the electrode. As will be shown, InGaN can act as an electrochemical anode (accepting electrons) and the bioreceptor chosen is an enzyme acting as a catalyst for the anodic reaction occurring at the electrode. Two different enzymes will be used namely glucose oxidase (GOD) for the case of the glucose biosensor and cholesterol oxidase (CHox) for the cholesterol biosensor. Notice that when no bioreceptor is involved in the signal production then the device is called plain “electrochemical sensor”.

The main parameters characterizing a biosensor are:

- **Sensitivity:** The output signal (S) should be as high as possible for the lowest variation in analyte concentration ($\Delta c_{analyte}$). High value of $\frac{\Delta S}{\Delta c_{analyte}}$ is thus desired.
- **Simple Calibration:** Conventional standards (mV/decade or mV/mM) should define the calibration.
- **Linear Response:** The value of $\frac{\Delta S}{\Delta c_{analyte}}$ needs to be constant over a large concentration range.
- **Background Noise:** The noise should be kept to a minimum and being able to cancel (as an example, the possibility of electrode cleaning without loss of performance)
- **No Hysteresis:** The obtained output signal should be independent of prior history of measurements.

- **Selectivity:** The obtained output signal should be originated solely from interaction with those species of interest, i.e. target analyte concentration.
- **Long-term Stability:** It should maintain its overall properties over a long period of time, e.g. not to be subjected to fouling, poisoning, or oxide formation that interfere with signal.
- **Dynamic Response:** The response to any variation in analyte concentration should occur as fast as possible.
- **Biocompatibility:** Essential for its consideration in clinical trials: it should minimize clotting, platelet interactions, activation of complement when in direct contact with bloodstream.

The basic setup for electrochemical measurements has already been discussed for the case of water splitting. For electrochemical (bio-)sensing, depending on the measuring techniques, the system has to be modified accordingly. The two main types of electro-analytical measurements are voltammetric and potentiometric, which require at least two electrodes (conductors) and a contacting element (electrolyte) solution, constituting the electrochemical cell.

The electrode surface can be considered as a junction between an ionic conductor and an electronic conductor. One of the two electrodes responds to the target analyte(s) and is thus labelled as “indicator” (or working) electrode. The second one, called the reference electrode, is set at constant potential (*i.e.* independent of the properties of the solution). ECs can be classified as electrolytic (when they consume electricity from an external source), or galvanic (if they are used to produce electrical energy).

Several available electrochemical characterization techniques exist such as:

- **Potentiometry** is a static technique where information about the electrochemical activity is obtained by measuring the electromotive (EMF) cell value, in this experiment at the working electrode no current flows. Changes observed in EMF are caused either by (i) ionic concentration changes altering the surface potential, (ii) the intrinsic charge of the analyte molecule, or (iii) changes in the electrolyte potential.
- **Voltammetry** which is based on the measurement of current when a potential is applied across the electrochemical cell. Different measurement configurations are available including AC and DC polarography, linear scan voltammetry, anodic and

cathodic stripping analysis, amperommetry, differential pulse voltammetry, and the most widely used technique along this work, cyclic voltammetry.

The role of the potential is analogous to that of the wavelength in optical measurements. It can force the chemical species to gain or lose an electron (reduction or oxidation, respectively). Therefore, the resulting current in voltammetric measurements is directly related to the rate at which electrons move across the electrode–solution interface.

4.3 Electrochemical Characterization

In this section the electrochemical characterization techniques used are described, as is the special case of electron transfer by redox reaction at (degenerated) semiconductor interfaces. This is essential to be understood, since, on one-side, both envisaged applications (water splitting and bio-sensing) are based on redox reactions occurring at the electrodes interface. Secondly because the material system considered (high In% InGaN) is a degenerated semiconductor above ~40% In, as shown in chapter 2

A typical measurement setup has several electrodes, the analyte of interest and the electrolyte. Depending on the physical quantity to be measured there are different configurations, including 2 or 3 electrodes. For voltage measurements only two electrodes are needed, while for current measurements a three electrode system is used. These two types of measurements are independently known as potentiometry and voltammetry or amperometric techniques [Bard 2001].

The electrodes can be distinguished as following:

- Having a known fixed potential that is not involved in the chemical reaction directly, called reference electrode.
- In case current is needed to be measured, an additional electrode always involved in the chemical reaction, called counter electrode, is used. This electrode is only present in a 3 electrode configuration.
- The most important one is the working electrode where the electrochemical activity occurs.

The electrolyte is the solution in which the analytes of interest are immersed. A term that will be used and needs to be defined at this point is *solvation* which is the process by which solvent molecules surround and interact with solute ions or molecules. This corresponds thus to the ability of solvent molecules to stabilize ions by surrounding and enclosing them in a sheath of weakly bonded solvent molecules, this allows to disperse the electrical charge. Anions are best solvated by hydrogen-bonding solvents; cations are generally solvated by binding to nucleophilic sites on a solvent molecule. In figure 4.3, two-dimensional diagrams illustrating the primary solvation shell about Na^+ and Cl^- are shown in case of NaCl in water. The water dipoles are drawn as red arrows, and partial charges are noted. Due to the electrical field surrounding each ion, a certain number of water dipoles tend to reorient their directions along the electric field lines. These molecules are forming the so called first solvation level and follow the ion during its movement through solution. Additional water molecules are oriented in secondary and tertiary layers about the ions. As the further they are located from the ion the electric field becomes weaker, these water dipoles are not strictly oriented along the electrical field lines anymore. Finally, at even larger distances from the ion, the water is not disturbed. Forming thus in total a surrounding shell around the ion. The energy needed to re-form (upon perturbation) this salvation shell is generally referred as the *reorganization energy* of the solvation shell and is represented by λ. We may consider thus that presented electrolyte has the same structure as pure water, except the disturbances around the ions contained in it.

In general we may state then that in an electrolyte solvated ions are formed and (if analytes are part of the salvation shell) that these are the main responsible for transporting the analytes towards the working electrode as the conductivity of the electrolyte is determined by the ion concentration as so the pH of the solution is determined by the pH of the electrolyte.

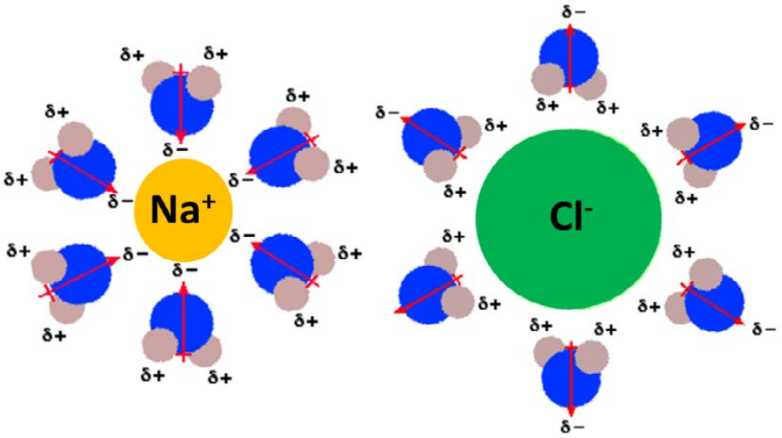

Figure 4.3: Two-dimensional diagrams illustrating the primary solvation shell about Na^+ and Cl^- dissolved in water. Adapted from [Diels-Alder].

In the case of potentiometry, the potential between the reference and working electrodes is probed. This potential is that of the EC, also called electromotive force (EMF). The biosensor is calibrated by plotting the EMF as a function of concentration. The response time, selectivity and long term storage stability are the factors of interest to be determined. The principal mechanism behind these measurements is normally strictly related to the amount of reducing and oxidizing agents concentrations present and therefore obeys the Nernst equation. For the following reaction $Ox + z \cdot e^{-} \rightleftharpoons \mathrm{Re}\,d$ for example the EMF will state:

$$EMF = E_0 + \frac{0.05916}{z} \ln_{10} \left(\frac{[Red]}{[Ox]} \right) \tag{4.9}$$

Here ‘E_0’ is the standard cell potential, ‘z’ is the amount of electrons involved in the redox process and [Red] and [Ox] are the concentration of oxidized and reduced species in the solution. By means of this expression a biosensor can be easily calibrated, as the addition of a specific amount of analyte of interest will give a unique EMF value. Notice that this potentiometric measurement technique is *independent of the area in contact* with the electrolyte and *no external potential* is needed to be applied.

In the case of amperometric measurements, the measured current is related to the migration and diffusion of the analytes available in the electrolyte towards the electrode, driven by the external potential and concentration gradients respect. Therefore all electrochemical reaction is unequivocally and solely related to the electrode.

Before going more in detail to the redox reactions occurring at the electrode, several concepts need to be introduced. For both, physicists or electrochemists it is quite clarifying to introduce at this point some definitions and underlying theory, as many terms are taken from one field and used on another one, being the way to derive them somehow different. In applied electrochemistry a Fermi energy is introduced for the redox system $E_{F,redox}$. In terms of solid-state physics, the electronic states in the electrolyte are discrete states localized at the electro-active species of the redox system, being the oxidized form the empty state and the reduced form the occupied state (see figure 4.4 (c)). Bear in mind that the band diagram in figure 4.4 (c) is an energy representation of the electrolyte and therefore the abscissa axis represents the probability of the energy level occupancy. Filled area means occupied states. The terms E_{Ox} and E_{Red} (also used to be denotes as E_O and E_R) correspond to the oxidation and reduction potential and λ is the previously introduced reorganization energy of the solvents.

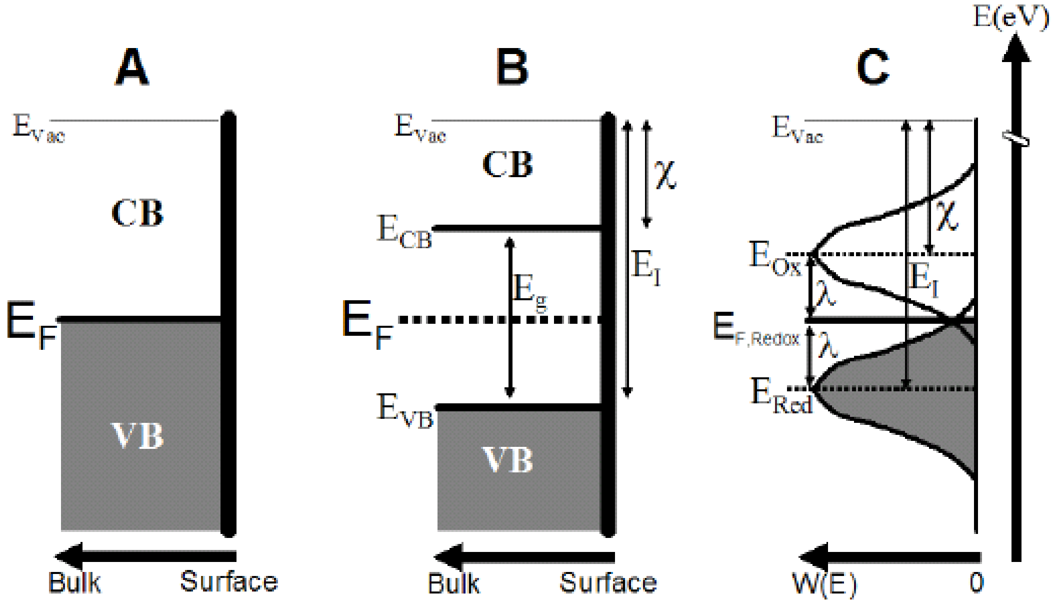

Figure 4.4: Simplified schematic band diagrams for (a) metal; (b) semiconductor with the conduction (CB) and valence (VB) bands, Fermi level (E_F), bandgap (E_g), electron affinity (χ) and ionization energy (E_I). The vacuum energy level, E_{vac}, is taken as reference (zero value). In (c) the distribution of the energy levels in the electrolyte is represented as electronic energy states in analogy to the standard representation of the solid electrode. Here λ represents the reorganization energy of the solvation shell. As the band diagram in (c) is an energy representation of the electrolyte, the abscissa axis represents the probability of the energy level occupancy. Filled area means occupied states.

In addition it is common to use a relative energy scale versus the widely used standard hydrogen electrode (SHE), which lies 4.5 eV [Gerrischer 1983] under the vacuum level, that is taken as the zero value (see figure 4.5). With this qualitative reasoning, the Fermi energy (given in eV) of the redox system can be expressed as:

$$E_{\mathrm{F},redox} = -e \cdot U_{Ox/\mathrm{Re}d}(SHE) - 4.5 \qquad (4.10)$$

where $U_{Ox/Red}$ represents the redox potential and *e* the electron elementary charge.

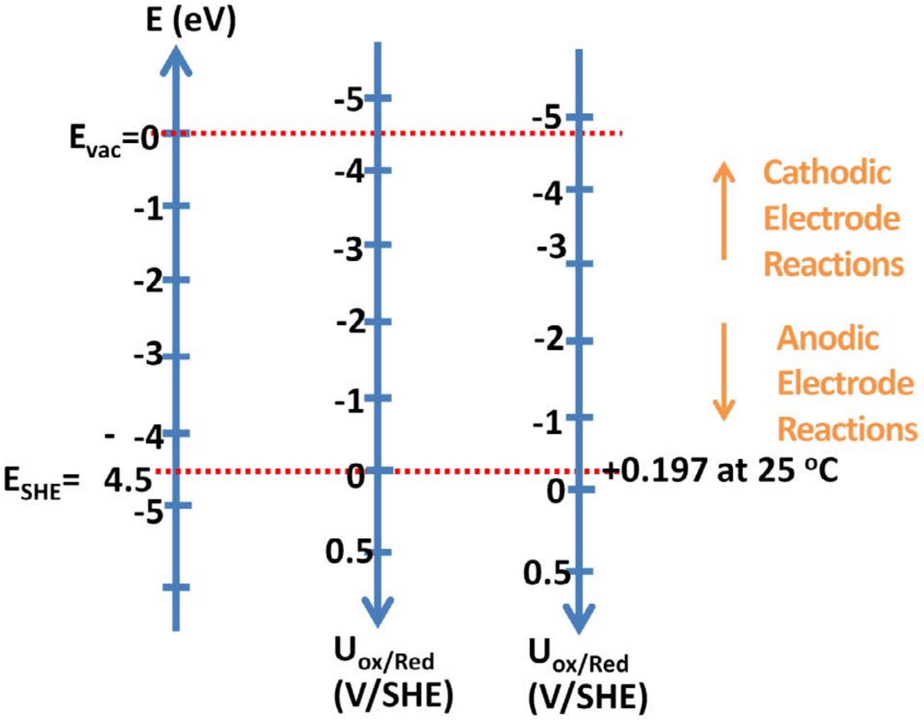

Figure 4.5: Correspondence between the absolute electronic energy scale in the solid (vacuum level reference) and the electrochemical energy scale in the electrolyte (standard hydrogen electrode (SHE) and the most common used silver chloride electrode (for sat. KCl it corresponds to 0.197 eV at 25 ºC) scales. These are the energy scales of the references electrodes.

The $E_{F,redox}$ level represents the average of the actual electronic states in the oxidized (E_{ox}) and reduced (E_{red}) forms;

$$E_{F,redox} = \frac{E_{Ox} + E_{\mathrm{Re}d}}{2} \tag{4.11}$$

The density of energy states in a solid can be obtained by solving the Schrödinger’s equation over a three-dimensional periodic lattice of atoms (a common simplistic way to represent this is by the simplified energy band structure represented in figure 4.4 (a)). However, in the case of redox species the difference between empty (E_{Ox}) and occupied (E_{Red}) energy states is determined by the rearrangement or relaxation energy shift of the ion solvation shell; when an electron is transferred from the solid to the available unoccupied level of a redox ion in the electrolyte, the polar solvent molecules surrounding the ion will rearrange in order to accommodate the new charge excess. This process involves a reorganization energy λ described by the Franck-Condon electron energy shift which stems from semiconductor physics usage [Franck 1925, Condon 1928]. Taking same rearrangement energy values for both oxidized and reduced species as a first approximation, λ yields:

$$\lambda = \frac{E_{Ox} - E_{\mathrm{Red}}}{2} \tag{4.12}$$

From Dogonadze and Marcus approaches [Dogonadze 1965, Marcus 1965], λ is approximately equal to 1 eV. Since thermal fluctuations in the solvent result in fluctuations in the polarization of the ion, E_{Ox} and E_{Red} levels are better represented by probability distributions (see figure 4.4 (c)).

Despite the analogy among the different energy distributions of figure 4.4, the direct comparison of the band energy model in the electrolytic ion with that in the semiconductor is limited. Notice for example that the X-axis in the redox species case represents the probability distribution of the energy levels occupancy while in the semiconductor it refers to the distance coordinate within the crystal lattice. The different nature of both systems implies a different behavior during the electronic transitions; when an electronic transition takes place in a solid semiconductor, it represents the total energy change of the system, and the spatial distribution of the resulting energy levels at the surface will basically give only information on its electronic behavior. However, the energy levels distribution in the electrolyte case is localized at the ion core, where each state represents a different energetic configuration of the system (eventually accompanied with a chemical change). This band model representation nevertheless is ideal to provide a general picture of the thermodynamically available energy levels for electrons and thus, useful to describe the electrochemical transport occurring at the electrode/electrolyte interface.

As stated at the beginning, three components determine the system, namely: electrodes, electrolyte and ions/analyte of interest. The presence of the analytes produces redox reactions to happen at the electrodes, generating a voltage drop which can be either in the electrolyte, which is the case for a metal working electrode, or in the case of a moderated doped semiconductor working electrode, the space charge layer. An overview of metal electrodes is given in figure 4.6, where the redox states are represented by a density of states displayed accordingly to the Marcus-Gerischer model, as described below.

The total current density, ‘j’, at a metal-solution interface is the sum of the anodic current density, ‘j_a’, and the cathodic density, ‘j_c’. By convention, the cathodic current is negative.

$$j = j_a + j_c \tag{4.13}$$

Anodic current flows when oxidation occurs at the electrode surface:

$$R \rightarrow O + e^{-} \qquad \text{(e.g. } Fe^{2+}(aq) \rightarrow Fe^{3+}(aq) + e^{-}\text{)} \qquad (4.14)$$

Notice that in this case the electrode accepts the generated electron, the amount of oxidized species increments. However in literature the oxidized species are also called reducing agents, as in the case of the example given, Fe^{3+} is created which could be reduced to form Fe^{2+}. It is for this reason that it is equivalent to talk about an increment in oxidized species or reducing agents.

Cathodic current flows when reduction occurs at the electrode surface:

$$O + e^{-} \rightarrow R \qquad \text{(e.g. } Fe^{3+}(aq) + e^{-} \rightarrow Fe^{2+}(aq)\text{)} \qquad (4.15)$$

The Marcus-Gerischer approach of electron transfer assumes that the Born-Oppenheimer approximation applies, i.e., the nuclei, being so much heavier than the electron, move relatively slowly and may be treated as stationary during electron transfer. Hence electrons are transferred to energy levels at or near the Fermi level in the metal (notice that if the nuclei would move faster than the electrons there would not be enough time for the electrons to interact and no solvation shell would be formed therefore no electron transfer would occur as resulting reaction products would be in an unstable environment).

4.3.1 Electron Transport between Electrode and Electrolyte

A change in the applied potential in the metal electrode results in charging it, which leads to a change in the potential at its surface. As the energy of the surface electrons is altered, the position of the Fermi level changes. However, the occupation probability of states at about the Fermi level remains constant. As a result the current densities are simply proportional to the overlap integral of the Fermi function in the metal and the density of states function for the solution species:

$Ja \propto$ (overlap of E_F and E_{Red})

$Jc \propto$ -(overlap of E_F and E_{Ox})

In above equation E_R and E_O are the reduction and oxidation respectively.

At the equilibrium potential, the overlap integrals are equal. The values of 'j_a' and 'j_c' are therefore equal and opposite and the net current density is zero. This situation is shown in figure 4.6 (a). At a positive overpotential the Fermi level of the metal is shifted down in the electron energy level diagram, thus the overlap integral for the reduced species is greater than that for the oxidized species. The net current density is therefore positive. An anodic current flows and oxidation of the reduced species occurs. This situation is shown in the upper right diagram in figure 4.6 (a). At a negative overpotential, the overlap integral for the oxidized species is greater than that for the reduced species. The net current density is therefore negative. A cathodic current flows and reduction of the oxidized species occurs. This situation is shown in the lower right diagram in figure 4.6 (a).

For a metal/electrolyte interface, upon overpotential change, it is possible to observe both oxidation as reduction. The total current is the sum of both cathodic and anodic currents, as displayed in the graph of figure 4.6 (b).

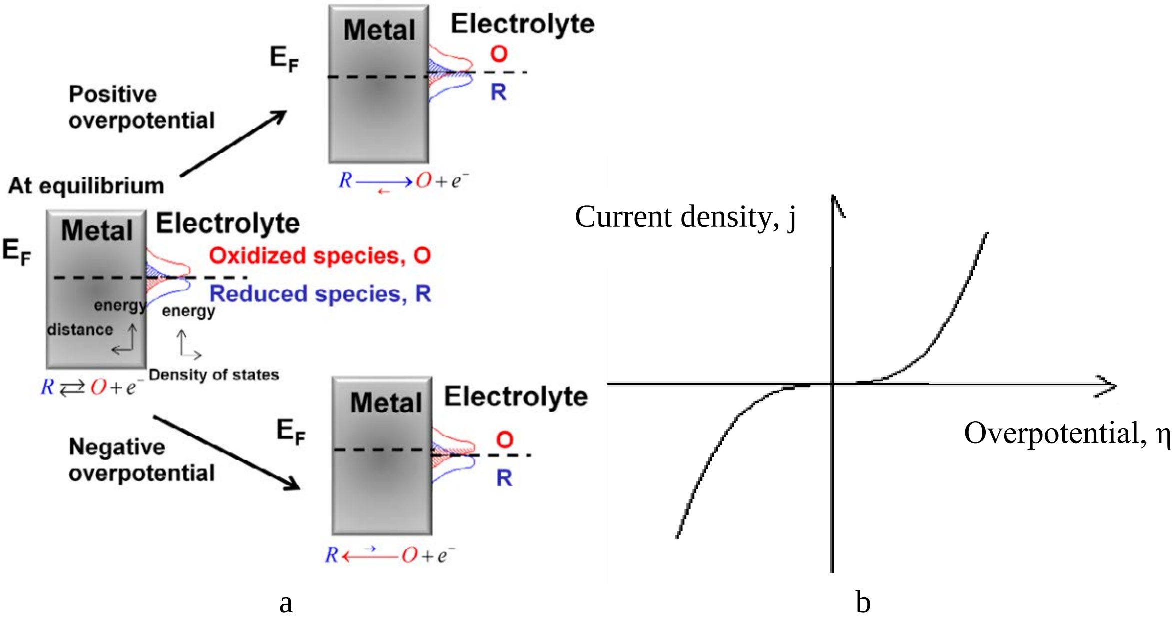

Figure 4.6: (a) Redox process in a metal/electrolyte is described by the Gerisher model considering overpotential. (b) The expected output I-V curve. Adapted from [Pastor-Moreno 2002]

4.3.2 Electron Transport between n-type Electrode and Electrolyte

The case of an n-type semiconductor (always moderately doped) is slightly different. Inside the semiconductor a depletion region develops, the difference between the semiconductor Fermi level, which for a non degenerate case lies inside its energy gap, and the energy difference compared to the Fermi level of the highly conductive electrolyte are balanced by a band bending at the interface after placing the electrode in contact with electrolyte. In figure 4.7, the simplistic energy diagram is shown for the case after contacting electrode and electrolyte and under different applied bias. The size of the arrows denotes the magnitude of the current in the two (i.e. anodic and cathodic) directions.

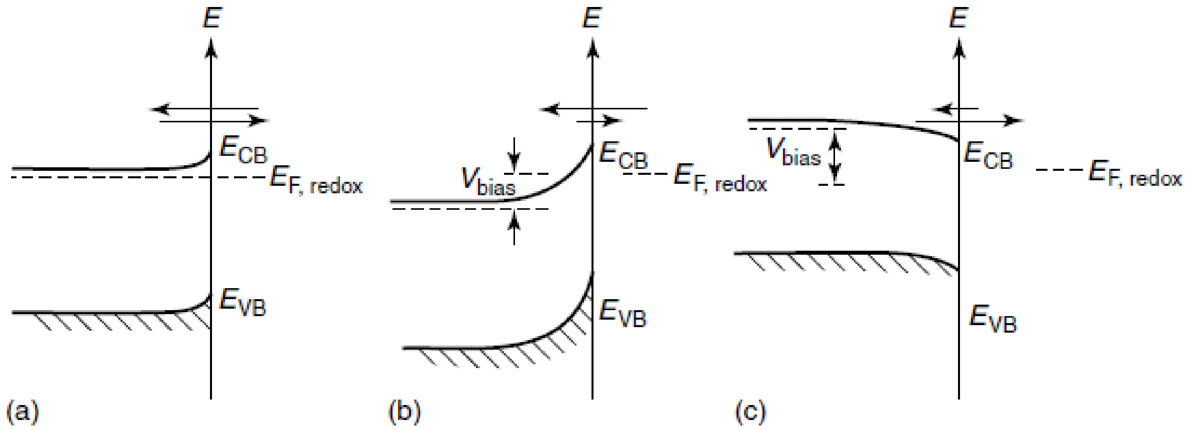

Figure 4.7: Three different situations for an n-type semiconductor-electrolyte interface: (a) at equilibrium; (b) under reverse bias (connected with the positive terminal); and (c) under forward bias (connected to the negative terminal). The size of the arrows denotes the magnitude of the current in the two (i.e. anodic and cathodic) directions.

As for a metal electrode, the total current density ‘j’ is the sum of the anodic and cathodic current densities (j_a & j_c). The Born-Oppenheimer approximation still applies for the presented case, semiconductor electrode, but unlike the case of a metal electrode, charge transfer cannot occur at the Fermi level if the density of states is zero at that energy (i.e. it is in the bandgap of the semiconductor). Charge transfer will occur at the surface energy of the conduction band, ‘$E_{CB,S}$’. Current flow at a semiconductor electrode is dependent on the surface concentration of majority charge carriers. For a n-type semiconductor, the concentration of electrons at the surface is a significant factor in the rate of charge flow in the cathodic reaction:

$j_{c\ \mu} \propto$ -(overlap of $E_{CB,S}$ and E_{Ox}) ([e-]surface)

Whilst for the anodic reaction the availability of electrons in the conduction band is essentially constant:

$j_{a\ \mu}$ - $\propto$-(overlap of $E_{CB,S}$ and E_{Red})

The overlap at the conduction band (CB) edge will not change by potential and therefore the anodic current will be constant. In contrast to the case of the metal presented in figure 4.6 (b) this will make the relation between overpotential and current more diode like.

At negative overpotential (forward bias) there exists a higher electron surface concentration and therefore a higher cathodic current (figure 4.7 (c)). There is an exponential relationship between the concentration of electrons and the overpotential. At positive overpotential the concentration of surface electrons is reduced (tending to zero closer to the equilibrium condition shown in figure 4.7 (a) and the anodic current (figure 4.7 (b)).

At sufficiently *large positive* potentials, inversion can occur if the band bending at the surface of the semiconductor is sufficiently high that the Fermi level enters the valence band (VB). There will be then a finite probability of finding a valence band hole at the surface of the semiconductor. A cathodic current can flow and the total current density will be reduced in magnitude.

At very high doping levels the semiconductor becomes degenerated (i.e.semiconductor Fermi level resonant to the CB). The Fermi level lies within the CB and electrons are able to tunnel (or thermionic field assisted) since now there are enough states in the CB occupied by electrons.

In the following some electrochemical characterization techniques are reviewed, as well as the electron transfer model at a semiconductor/electrolyte interface.

4.3.3 Linear Sweep Voltammetry

Measurements are done in a three electrode configuration, with a Reference electrode (RE), a Counter (auxiliary) electrode (CE) and a Working electrode (WE). A potentiostat controls the voltage between WE and CE and keeps the voltage between WE and RE constant. The output is the current (i) measured between WE and CE (see figure 4.8). Full information on the electrochemical behavior can thus be obtained by sweeping the potential with time and reading out the i-E curve.

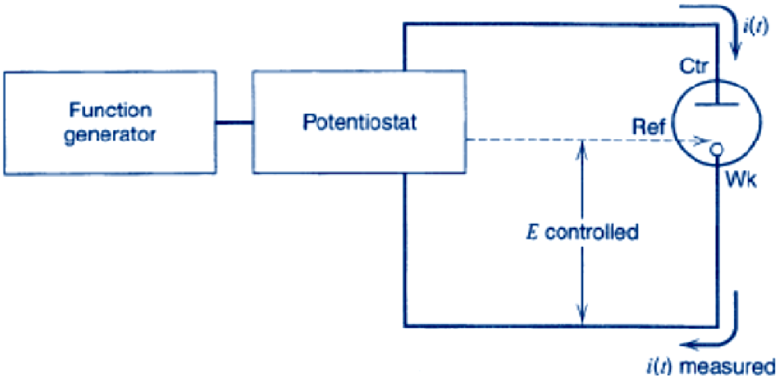

Figure 4.8: Scheme of a Potentiostat.

Let´s consider a reversible system with an oxidation process occurring at an oxidation potential ‘E_0’. If a inear potential ramp is then applied (see figure 4.9 (a)) the concentration will change where the oxidation converts the electro active analyte A^- into a stable A as:

$$A^{-} - e \longrightarrow A \tag{4.16}$$

In electrochemistry it is possible to distinguish between two types of current:

- Faradaic current: Which provide from charge that is transferred across the electrified interface as a result of an electrochemical reaction.
- Non-faradaic currents: Which provides from charge associated with the movement of electrolyte ions, reorientation of solvent dipoles, adsorption/desorption, etc. at the electrode-electrolyte interface. This is the background current in voltammetric measurements.

Having defined these current, it is possible to see from figure 4.9 (b) that initially non faradic currents flow and only when the potential reaches the vicinity of E_0 the oxidation starts to occur and Faradaic current starts to flow. The more positive the applied potential becomes, the less surface concentration of analyte will be available (as it is being oxidized). This change of surface analyte concentration causes a flux of analytes (as there will be a region of high analyte concentration and region of higher analyte concentration and therefore a gradient exists and diffusion starts to play a role) to appear towards the electrode surface that increases the faradaic current. When the potential value goes beyond the oxidation potential (E_0), the analyte concentration almost drops to zero, the mass transfer rate of the analyte reaches its maximum and then it declines as the depletion effects sets in. This occurs as all analytes are oxidized the ions left at the boundary will form a layer of ions compensating the surface charge giving rise to the before mentioned depletion. The resulting curve is a peaked current-potential curve as shown in figure 4.9 (b). The observed peak related to the oxidation of analytes is called anodic peak.

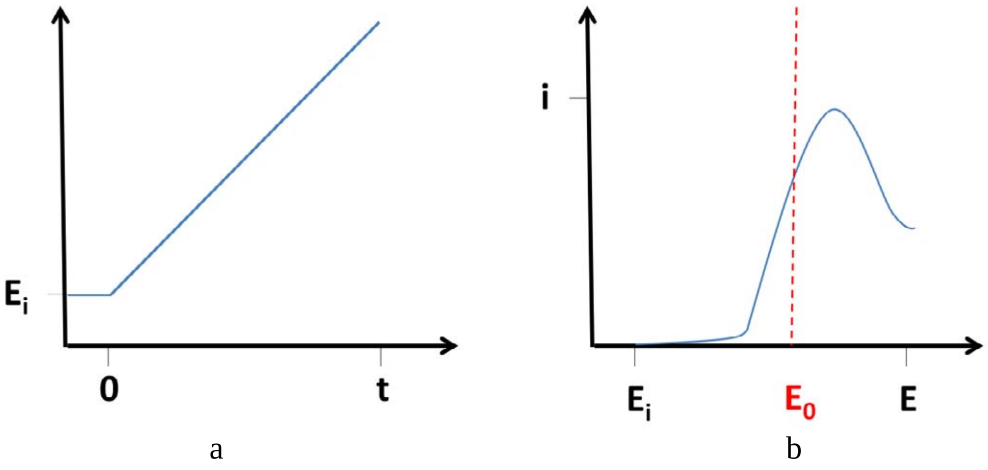

a b

Figure 4.9: (a) Linear potential sweep over time ‘t’; (b) Observed current output ‘i’ reading for the redox process upon potential sweep (E).

4.3.4 Cyclic voltammetry (CV)

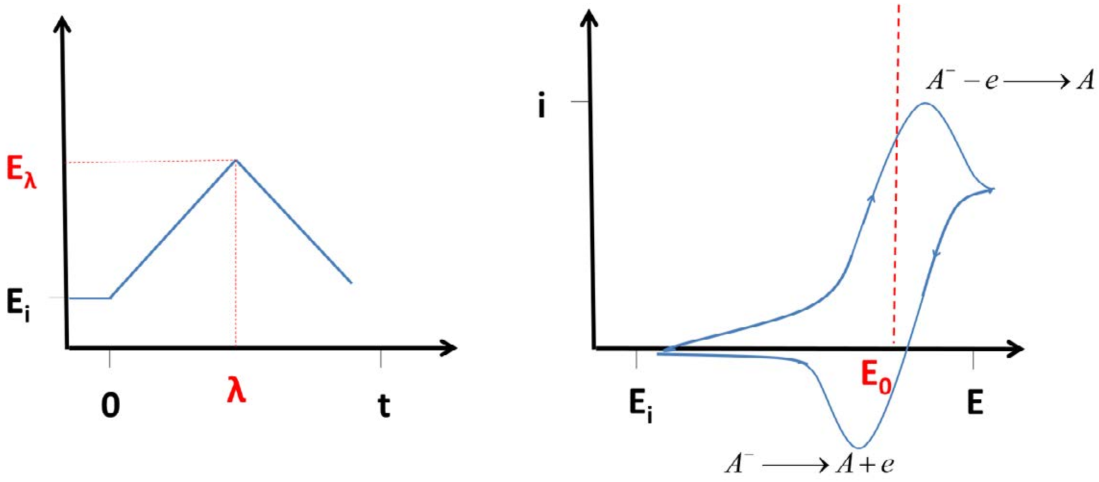

a b

Figure 4.10: (a) Potential sweep over time with reversal point at time λ. (b) CV curve obtained with the forward-reverse cycle shown in (a). The corresponding oxidation and reduction processes for analyte *A* are shown.

When there is a potential sweep, like in the case of the linear sweep voltammetry, if the potential is reversed (backwards) at the end of the forward sweep the electrochemical measurement technique is called cyclic voltammetry (CV). The reversing point, E_λ in figure 4.10 is the point where potential starts sweeping in a negative direction and in the electrode’s vicinity there is a large concentration of analytes *A*. As the potential approaches and passes, E°’, more analytes are being reduced and a cathodic current flows. This reversal current has a shape much like that of the forward peak, as explained in the linear sweep for essentially the same reasons (mass limited transfer). The observed peak in the reversed case corresponding to the reduction of the analytes is called cathodic peak.

In the case of a biosensor the anodic peaks will change upon addition of the analyte of interest to the solution, increasing the species being reduced. The CV results can be plotted as current versus potential or current density versus potential.

4.3.5 Electron Transfer Model

When a metal or semiconductor is placed in contact with an electrolyte the ions in the electrolyte attach to the electrode charging the interface at the electrolyte side. To maintain the electrical neutrality of the system the same process occurs with opposite charge at the other electrode. Different regimes are possible in the electrolyte depending on where and how ions are accumulating, and the potential drops differently in each regime. Different models describing the potential behavior are summarized here.

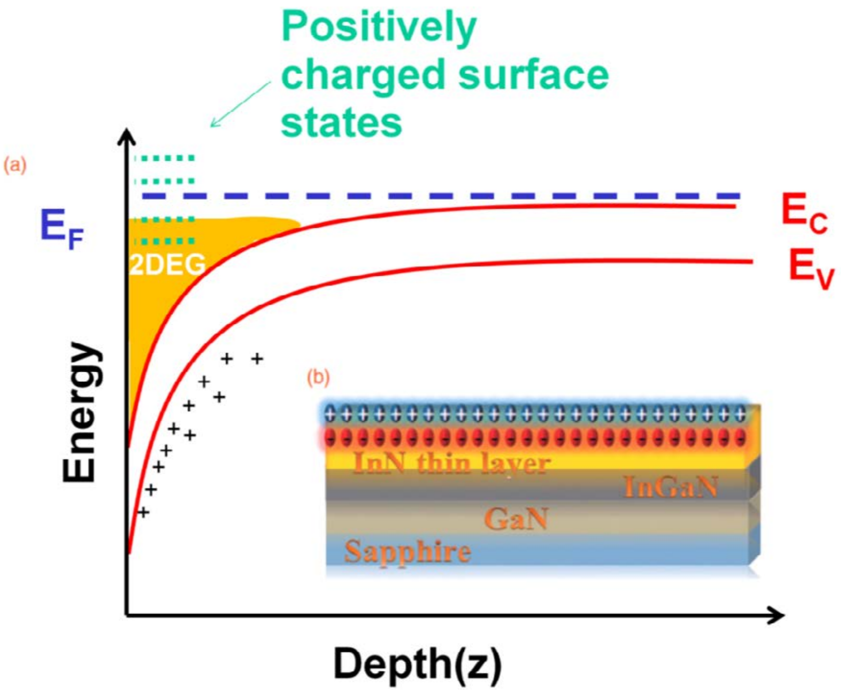

Figure 4.11: (a) Simplified Energy diagram for InGaN with In content above 40%. E_F is the Fermi energy level, $E_{C,V}$ is the conduction and valence band respectively.Inset: (b) Schematic showing the positive surface charge on a InN thin layer surface.

The behavior of an anode of InGaN with In content above 40%, with the simplest model for the spatial charge distribution at a metal/semiconductor-electrolyte interface, proposed in 1879 by Helmholtz, is schematically depicted in figure 4.13. Let´s recall the main properties (a schematic of the simplistic band diagram is presented in figure 4.11): above 40% In-content, as proposed by Van der Walle and explained in chapter 2 a large density of positive donors are present and surfaces states are located inside the conduction which may take part of the electron transfer acting as positive donors. A downwards bending of its energy bands is present and it is also seen that above this In-content (40%) the InGaN is highly doped and that the surface charge accumulation forms a natural two-dimensional electron gas (2 DEG) channel located immediately under the surface. Adsorbates on the surface could effectively affect the surface band bending, thereby modulating the electron density in the surface electron accumulation layer. This effect can give rise to a significant surface conductance change, which is an excellent attribute for sensing applications. In addition, the increase in electron accumulation reduces the width of this 2DEG channel which also separates the positive donors located in the bulk effectively (although still weakly) increasing the attraction of anions towards the electrode surface. Keep in mind that the positive donor states present directly beneath the surface will have a more essential role in attracting anions as it effectively screens the 2DEG giving rise to a net positive charge on the surface able to attract efficiently anions, as depicted in figure 4.11 (b).

As a reminder as it takes crucial part in the Helmholtz model, in figure 4.12 the form of a solvated anion in water based electrolyte is shown explicitly indicating the several solvation layers.

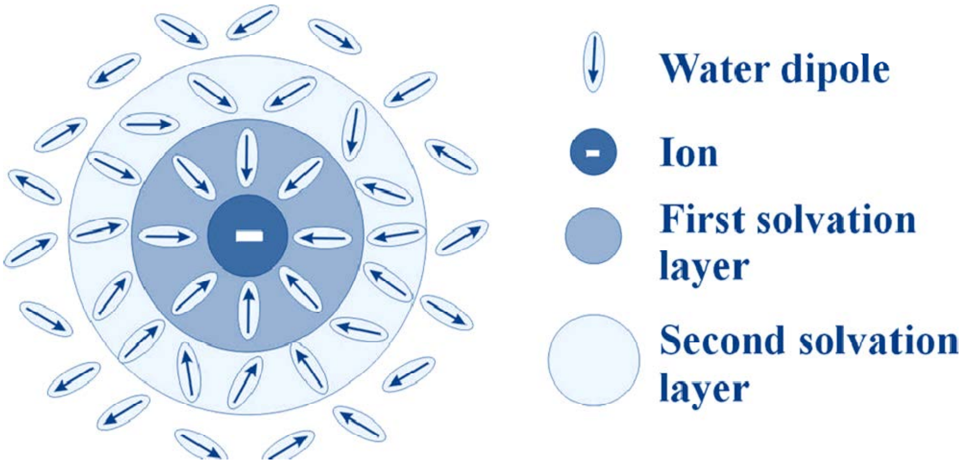

Figure 4.12: Schematic drawing of a salvation shell surrounding the anion in water based solvent.

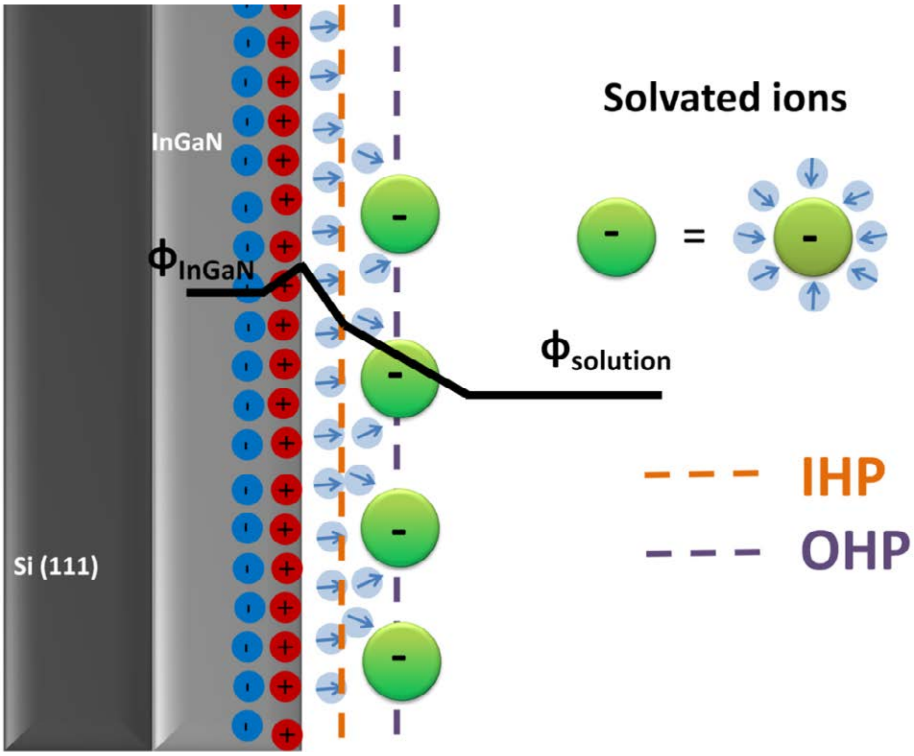

Figure 4.13: Schematic of the Helmholtz model. Indicated only the region close to the InGaN electrode, for simplicity the interaction is considered to be strong enough to only have "anions " (negatively charged solvated ion) in the nearby regime. The orange line denotes the inner Helmholtz (IHP) plane and the purple line the outer Helmholtz plane (OHP). The blue circles with arrow represent water dipoles.

It is because above mentioned reasons that in figure 4.13 the attraction of anions and the net (weak) positive charge on the surface of the InGaN electrode is considered. Please remember that a closed system consisting of two electrodes in an EC cell plus the electrolyte is considered. The InGaN electrode here is the working electrode and acts as an anode. In general there would be 3 distributions of solvated ions present in the electrolyte namely nearby both electrodes and far from the electrodes, in the following we focus on the regime nearby the InGaN electrode.

The Helmholtz model assumes that no reactions occur near the electrode which could transfer electrons, and consider only Van der Waals interactions to be present between the ions in solution and the electrode. These interactions are solely due to the charge density present at the electrode originated from either an excess or deficiency of electrons at the electrode's surface. The charge neutrality at the electrode is balanced by a redistribution of ions close to its surface. These attracted ions form a layer balancing the electrode's charge (called inner Helmholtz plane, IHP). The closest distance an ion can come to the electrode will be limited to the radius of the ion plus a single solvation sphere around an individual ion. Overall, two layers of charge and a potential drop from the electrode to the edge of the outer layer (called outer Helmholtz Plane, OHP) are observed.

If a potential Φ_{InGaN} is considered at the InGaN electrode/electrolyte interface and far from the electrode, in the electrolyte, a potential U = Φ_{Solution} is assumed. This established a potential difference:

$$\Phi_{InGaN} - \Phi_{Solution} = Q / C \tag{4.17}$$

Where Q is the net charge stored between both charged ion layers and C is the corresponding capacitance.

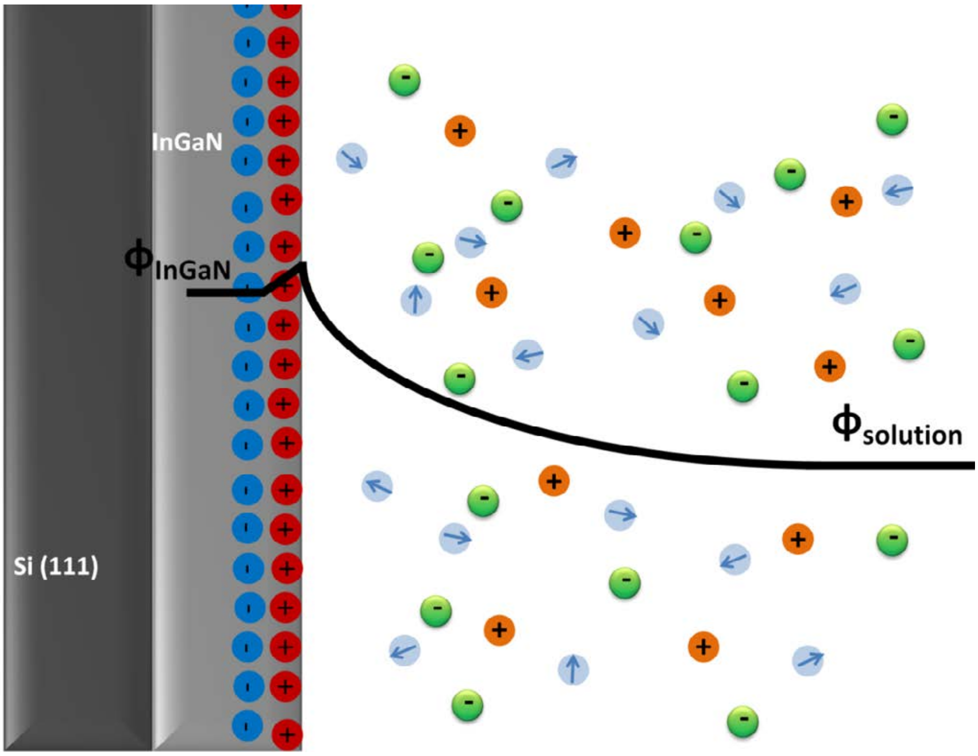

Figure 4.14: Schematic of the Gouy-Chapmann model.

In the special case of solutions with low ionic concentrations, the charge of the electrode is not completly counterbalanced. Therefore, a diffuse layer of charge extending into the solution is needed to be introduced in which an excess of ions of one charge exists. This new charge distribution model was proposed by Gouy-Chapman based in 1916 considering a diffusing layer of point-charges (GC model), as depicted in figure 4.14. Notice that here only the distribution of solvated ions (both cations as anions) further away (compared to figure 4.13) of the electrode is displayed. This model assumes the charges decay rapidly and continuously from electrode to electrolyte without distinct layer separation. Current model is far more complete than the previous one and takes into account crucial physical phenomena left out by Helmholtz. For instance, it includes thermal fluctuations (obeying a Boltzmann distribution law), as Poisson´s electrostatic law to be valid (i.e. the potential gradient is directly related to the distribution of charged ions and dielectric constant of the medium, electrolyte). The ions are also assumed to follow Fick’s law of diffusion, meaning they diffuse from regions of high concentration to low concentration across a concentration gradient.

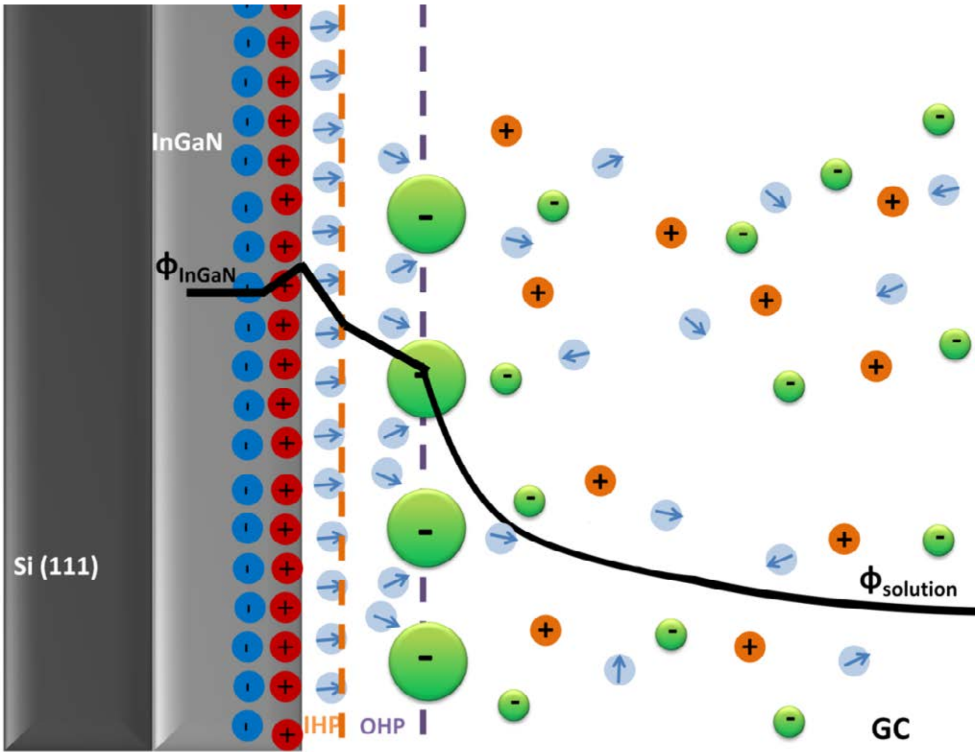

Figure 4.15: Schematic of the Stern model.

However in later years, it was determined that the GC model overestimates the interface charge accumulated between the two ion layers and thus the capacitance for high-concentration electrolytes. Stern [Gileadi 1975] recognized that the ions in the electrolyte exhibit a certain ionic radius and, therefore, cannot approach the electrode surface closer than this radius. Actually Stern´s first concepts were introduced when the Helmholtz model was considered. Here the Stern model will be considered as a combination of both Helmholtz and GC model, illustrated in figure 4.15, where the distance of ions closest approach is called the Outer Helmholtz Plane (OHP). The shell covering the solvated ions also contributes to the distance of the closest approach creating an additional inner Helmholtz plane (IHP). Out of these planes the GC model is valid.

Above definition implies that in this model, the amount of charge in the electrode is matched by the magnitude of counter-charges in the outer Helmholtz plane (OHP). This corresponds to the area close to the IHP in where the polarized electrolyte ions are collected. This separation of two layers of polarized solvated ions through the double-layer phenomena store electrical charges as in a conventional capacitor as the introduced by equation 4.16. The double-layer charge produces a static electric field in the molecular IHP layer of the solvent molecules which is directly related to the strength of the applied voltage.

The ‘thickness’ of a charged layer in for example a metallic electrode, i.e., the average extension perpendicular to the surface, is about 0.1 nm. This value mainly depends on the electron density due to the fact that the atoms in solid electrodes are stationary. However in the electrolyte, the thickness depends on the size of the solvent molecules and of the movement and concentration of ions in the solvent. It ranges from 0.1 to 10 nm as described by the Debye length. The sum of the thicknesses is the total thickness of a double layer.

Having introduced the models for the InGaN layer it would be possible to give a prediction on the role of InN QDs. It is observed, and discussed in chapter 2, that InN posses the largest amount of positive surface donor states and that nanostructures have a confined nature obeying Pauli´s principle allowing thus a fixed number of positive donors to be present in the surface position where QDs are present. At the QDs positions the amount of electrons available would be insufficient to screen the positive charge leaving each QD with a positively charged surface. All together this would lead to an uncompensated surface charge for the case where InN QDs are grown on a high In-content InGaN surface leaving a net positive charge on the surface, as is shown in figure 4.16. The role of the InN QDs from this interpretation would be thus to enhance the attraction of anions, this implies them to have a catalytic behavior towards the oxidation process. The Increase of In-content will also enhance the oxidation as it would increase the 2DEG.

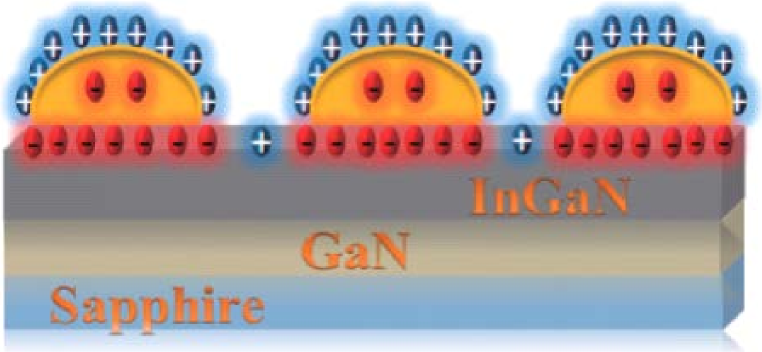

Figure 4.16: Schematic of expected charge distribution on a High In-content (>40%) sample with InN QDs.

4.3.6 Analysis by Potassium hexacyanoferrate (II) / Potassium hexacyanoferrate (III)

The special case of potassium hexacyanoferrate (II) / potassium hexacyanoferrate (III) is widely used to study and calibrate electrodes. With these redox species the rate of electron transfer is faster and a single electron is involved in the process. This eases the method application and the study of the electrochemical properties of a certain electrode, since the electron rate is faster than the rate at which the salts anions hexacyanoferrate (III) are transported (diffuses) from the solution volume (bulk) towards the anion selective electrode surface. In this case, as hexacyanoferrate (III) is reduced to hexacyanoferrate (II), the reaction is:

$$Fe^{III}\left(CN\right)_6^{3-} + e^- \rightarrow Fe^{II}\left(CN\right)_6^{4-} \tag{4.18}$$

In such a case the peak current, Ip, is governed by the Randle-Sevcik relationship

$$I_p = k \cdot n^{3/2} \cdot A \cdot D^{1/2} \cdot v^{1/2} \tag{4.19}$$

where the constant ‘k’= 2.72×10^5; ‘*n*’ is the number of moles of electrons transferred per mole of electroactive species (e.g., hexacyanoferrate); ‘A’ is the area of the electrode in cm^2; ‘D’ is the diffusion coefficient in cm^2s^{-1}; ‘C^b’ is the solution concentration in mole per litre; and ‘υ’ is the scan rate of the potential in volt·s^{-1}.

In general most theories found in the literature are valid for cyclic voltammetry at metal/electrolyte interfaces, and for moderately doped ($N_{D,A}$ ~10^{15}-10^{19} cm^{-3}) semiconductors/electrolyte where it can be considered that the redox potential is fixed at the surface. In addition, surface states are neglected, as these for moderate doped semiconductor are located inside the bandgap, and can give rise to additional active states which may allow electron transfer towards /from the electrolyte and cause additional band bending. But for a first approximation and to introduce main concepts it is sufficient.

4.3.7 Effect of Illuminating the Semiconductor Electrode

Shinning a semiconductor electrode with light having photons energy larger than the bandgap results in the generation of electron-hole pairs in the region close to the surface within the absorption length α^{-1}. In the case of a Schottky-barrier, the electrons and holes generated upon illumination in the depletion region are separated by the internal electric field that yield a photocurrent dependent on the depletion layer width W (see figure 4.17). If the photo-generation rate is constant throughout the space charge layer, which is the case for $\alpha W << 1$, a linear relation between the photocurrent (j_{ph}) and the depletion width (W) is derived. Depending thus on the incoming photon energy, enough carriers can be generated to start a redox reaction when the electrode is put in contact with the electrolyte. Remember that, when in such a contact, the bands will re-align/accommodate energetically depending on the redox

Fermi energy of the electrolyte. Therefore a similar analysis of the electron transfer model is essential to characterize the photoelectrochemical behavior and thus, the PEC water splitting process. One can define an *incident-photon-to-current-conversion efficiency (IPCE)* as the percentage of electrons taking part in the redox reaction with respect to the number of incident monochromatic photons:

$$IPCE = 1240 \cdot \rho_I \cdot \lambda_i^{-1} \cdot I^{-1} \cdot 100 \tag{4.20}$$

Where ρ_I is the photo-current-density (mA·cm^{-2}), λ_i is the incident-light wavelength (nm) and I the light intensity (mW·cm^{-2})

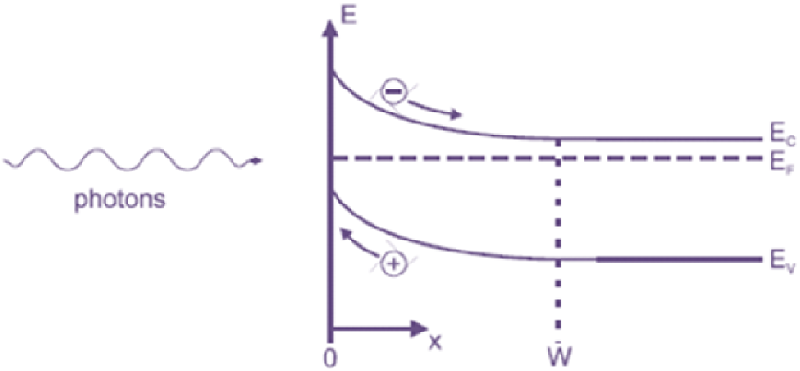

Figure 4.17: Illumination of an n-type Schottky barrier results in the generation of electron-hole pairs. Free charge carriers generated within the space charge region (depletion layer), that is, at x ≤ W, are separated by the electric field and contribute to the photocurrent. The contribution of carriers generated outside of the depletion region (x > W) is neglected because they would recombine before reaching the contacts.

This value will tell how efficient the illumination of the semiconductor electrodes is in terms of the redox reaction taking place at the surface. For water splitting this would mean an increase of oxygen generation taking place at the anode and hydrogen generation at the cathode.

The hydrogen production can be estimated by the first Faraday's law of electrolysis relating the reaction stoichiometry (referring to the amount of substances needed to fulfill the reaction) to electrical measurements, stating that the mass of any substance deposited or dissolved at any electrode during electrolysis is directly proportional to the quantity of electricity that passes through the solution. More precisely, the deposited mass on the electrode is proportional to the measured charge. Mathematically it can be described in terms of current, for example, for the hydrogen generation:

$$H_2\left(Mole\right) = \frac{1}{2}\frac{\int_0^t I d\tau}{F} \tag{4.21}$$

where ‘F’ is the Faraday constant (the quantity of charge in Coulomb carried by one mol of electrons), ‘I’ is the measured current, and ‘τ’ is the time variable.

Evidently our case of high In content InGaN differs for the case presented in figure 4.17. Firstly there is the downwards bending and secondly the Fermi energy is located inside the conduction band. Still e-h pair will be generated and enough carriers can be generated to start a redox reaction. Photogenerated holes may tunnel through the thin barrier generated by the downwards bending and electrons have enough available states to access as it is a degenerated semiconductor with Fermi level inside the conduction band as will be discussed in detail when presenting the application results.

CHAPTER 5

EPITAXIAL GROWTH AND BASIC CHARACTERIZATION

Optical, structural and electrical characteristics of InGaN alloys are affected by the growth conditions. Indeed, the variation of the growth parameters leads to a large spread in InGaN thin films quality (crystalline, optical, etc.). This makes the understanding of InGaN growth kinetics one of the key issues for further growth improvement. In this chapter a review on the main aspects affecting the InGaN growth kinetics is presented, the choice of substrate is discussed, as well as growth conditions for the InGaN nanostructures (on both GaN template and Si(111)) grown particularly for the development of this thesis. Moreover, the growth of InGaN alloys as nanostructures on both GaN template and Si(111) substrates is described. As many of these growths are important results on their own, extensive basic material characterization is presented for those less conventional growths.

5.1 InGaN Growth Kinetics

Growing InGaN alloys with high In content and quality remains a challenging task. The main drawbacks when growing high-quality InGaN alloys are the following:

- The inter-atomic spacing difference between InN and GaN is large and typically results in a solid phase miscibility gap [Popovici 2000, Ho 1996]
- The relatively high nitrogen vapour pressure needed to avoid the decomposition of InN ($InN \rightarrow In^0 + \frac{1}{2}N_2$) as compared to that needed for GaN limits the indium incorporation in the InGaN alloy [Nagatomo 1989]. The low vapour pressure for GaN means that almost all the input Ga is incorporated to the film. Therefore for a fixed V/III ratio, at fixed nitrogen input, Ga is preferentially incorporated.
- The formation enthalpies for InN and GaN differ and cause a strong indium surface segregation to the growth front [Yoshimoto 1991].
- The fact that the threshold temperature for InN decomposition is lower than for In desorption (opposite from GaN) leads to a permanent problem of In metal droplets formation, on the growth front (surface). [Shimizu 1994, Lu H. 1997]

The above mentioned problems, however, can be minimized by careful optimization of the growth parameters, such as: (i) the use of relatively low growth temperatures, (ii) stoichiometric or N-rich growth conditions (III/V ≤ 1), (iii) a relatively low growth rate and (iv) a low growth pressure. Growth parameters were thoroughly studied and finally established in order to optimize the grown layers.

5.2 Choice of Adequate Substrate

The search for an appropriate substrate to grow, homoepitaxially if possible, is another important issue. The substrates should comply with some minimal requirements in order to achieve better epitaxial quality. These requirements include:

- ***Epitaxial relationship:*** provides a “pattern” for epitaxial growth.
- ***Low lattice mismatch:*** as it prevents high strain in the grown layer (in the opposite case, the layers can relax by defect generation having a detrimental impact on the device performance).
- ***Low thermal mismatch:*** prevents defects (in particular crack) formation during cooling upon the growth termination.
- ***Chemical stability***: necessary for the epitaxial growth and posterior processing into device.
- ***Low cost***: enables device production at industrial scale.

Good electrical conductivity: this requirement is mostly for applications which include back contacts.

Good thermal conductivity: this requirement applies when power devices are envisaged

Even tough no substrate is available complying all abovementioned requirements, the most common substrates and meeting partially above requirements used to grow III-nitrides are Al_2O_3, SiC, and Si, all having large thermal and lattice mismatches with InGaN alloys. More detail for each substrate will be provide in upfollowing sections. An overview of the choices used as substrate for GaN film growth is given in table 4.1 reproduced from [Kane 2014]. Notice that nitrides will be deposited on the hexagonal side facet of Si(111) and the lattice parameter on the surface to take into account would be 0.3823nm.

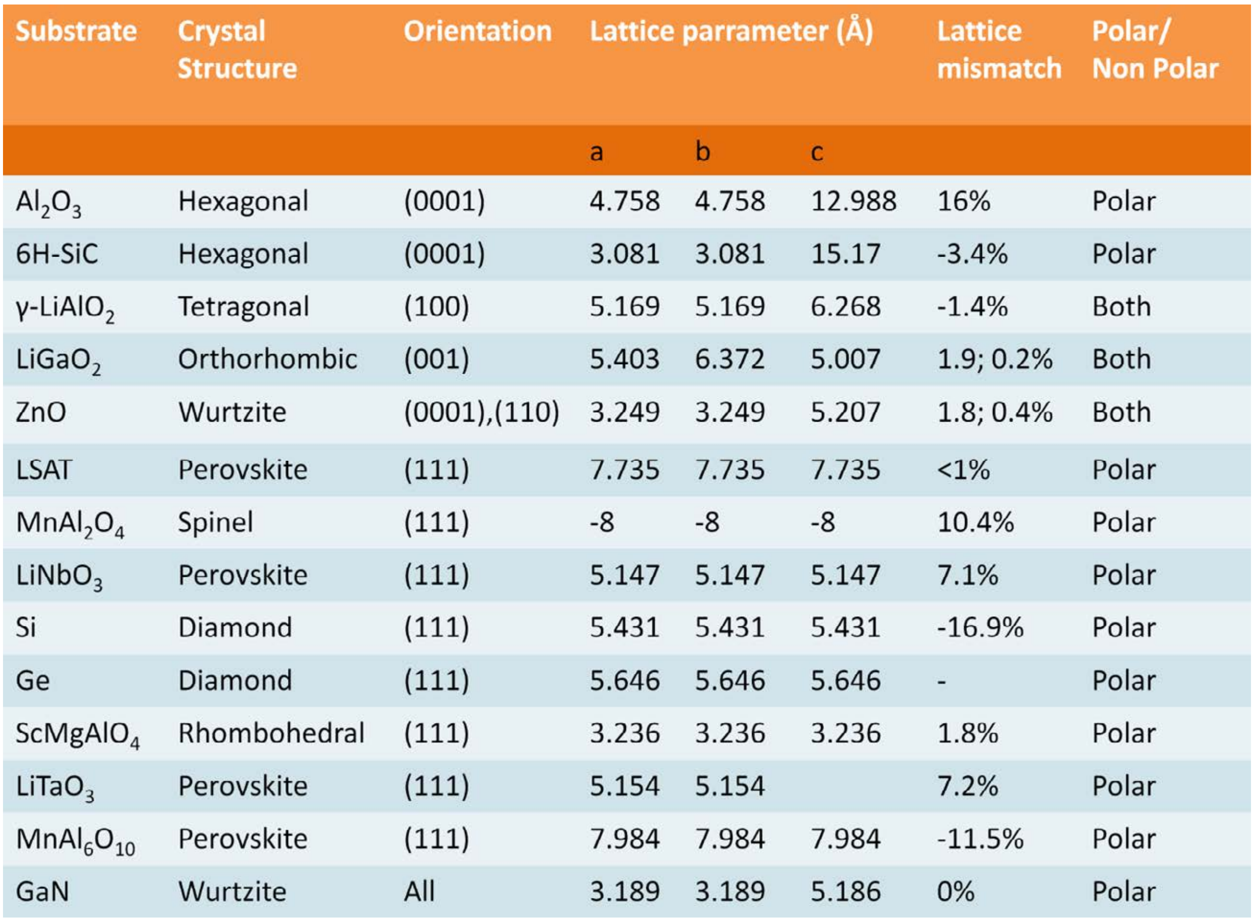

Substrate	Crystal Structure	Orientation	Lattice parrameter (Å)			Lattice mismatch	Polar/ Non Polar
			a	b	c		
Al_2O_3	Hexagonal	(0001)	4.758	4.758	12.988	16%	Polar
6H-SiC	Hexagonal	(0001)	3.081	3.081	15.17	-3.4%	Polar
γ-$LiAlO_2$	Tetragonal	(100)	5.169	5.169	6.268	-1.4%	Both
$LiGaO_2$	Orthorhombic	(001)	5.403	6.372	5.007	1.9; 0.2%	Both
ZnO	Wurtzite	(0001),(110)	3.249	3.249	5.207	1.8; 0.4%	Both
LSAT	Perovskite	(111)	7.735	7.735	7.735	<1%	Polar
$MnAl_2O_4$	Spinel	(111)	-8	-8	-8	10.4%	Polar
$LiNbO_3$	Perovskite	(111)	5.147	5.147	5.147	7.1%	Polar
Si	Diamond	(111)	5.431	5.431	5.431	-16.9%	Polar
Ge	Diamond	(111)	5.646	5.646	5.646	-	Polar
$ScMgAlO_4$	Rhombohedral	(111)	3.236	3.236	3.236	1.8%	Polar
$LiTaO_3$	Perovskite	(111)	5.154	5.154		7.2%	Polar
$MnAl_6O_{10}$	Perovskite	(111)	7.984	7.984	7.984	-11.5%	Polar
GaN	Wurtzite	All	3.189	3.189	5.186	0%	Polar

Table 5.1: Summary of most common used materials as substrate to grow GaN films and their main properties. Reproduced from [Kane 2014].

The most common material choices as substrates were SiC and sapphire, mainly due to the need of thermal and chemical stability which is required during the growth of III-nitrides. Also lattice mismatch is an issue that will be discussed later. In Figure 5.1 an overview is given by the graph presenting lattice constant versus bandgap and wavelength for most important semiconductors as Si, 6H-SiC, 3C-SiC and sapphire commonly used as substrates.

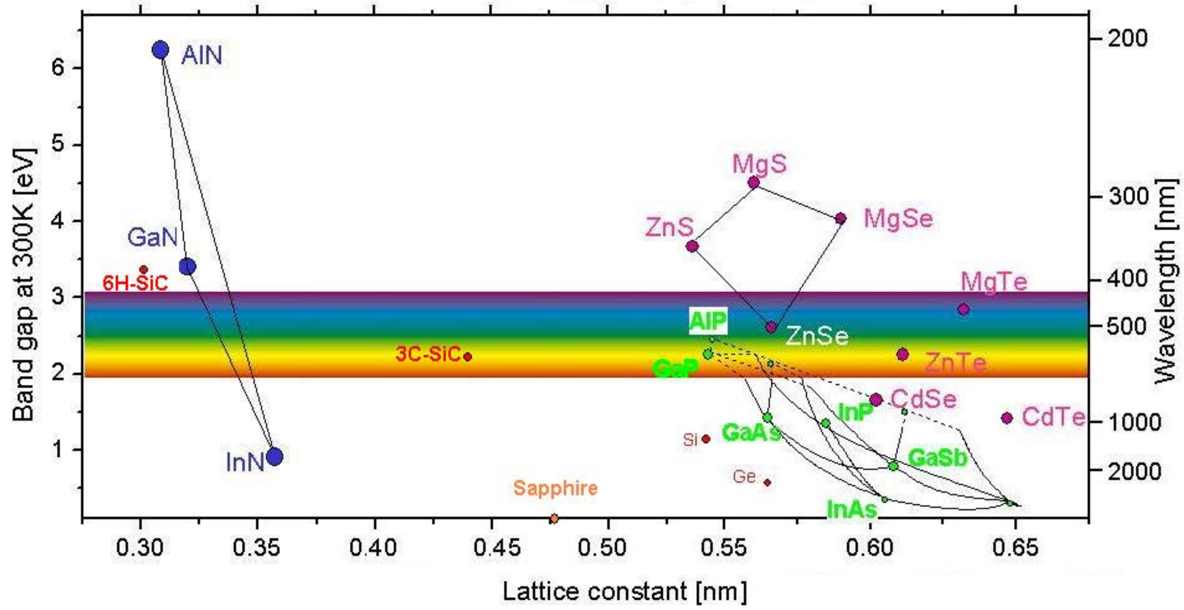

Figure 5.1: Graph of lattice constant versus bandgap and wavelength for most important semiconductors as Si, 6H-SiC, 3C-SiC and sapphire commonly used as substrates.

5.2.1 SiC Substrates

Although expensive, SiC has good properties in terms of both thermal and electrical conductivity; this makes it a very adequate substrate for III-nitride epitaxy aiming to both optical and electronic devices.

The basic unit of crystalline SiC is a covalently bonded tetrahedron of C atoms, with a Si atom at its centre, or vice versa, that is, either SiC_4 or CSi_4, as shown in figure 5.2.

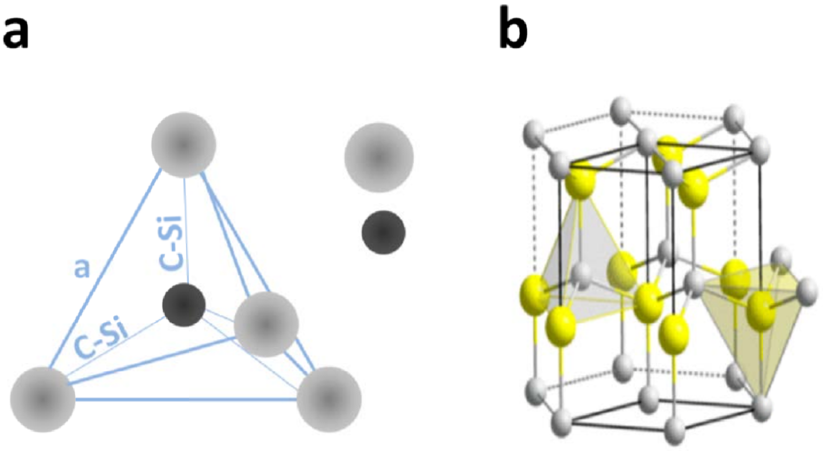

Figure 5.2: (a) Tetragonal bonding of a carbon atom with the four nearest silicon neighbours. The distances a and C-Si are about 3.08 Å and 1.89 Å respectively. (b) The SiC unit cell.

A variation in the stacking order of SiC along the c-direction leads to more than 250 polytypes, of which a few prominent ones are shown in figure 5.3. Despite the fact that all

SiC polytypes chemically consist of 50% carbon atoms covalently bonded with 50% silicon atoms, each SiC polytype has its own distinct set of electrical properties. Different polytypes of SiC are actually composed of different stacking sequences of Si-C bilayers (also called Si-C double layers), where each single Si-C bilayer can simplistically be viewed as a planar sheet of silicon atoms coupled with a planar sheet of carbon atoms. The plane formed by a bilayer sheet of Si and C atoms is known as the basal plane, while the crystallographic c-axis direction, also known as the stacking direction or the [0001] direction, is defined normal to the Si-C bilayer plane.

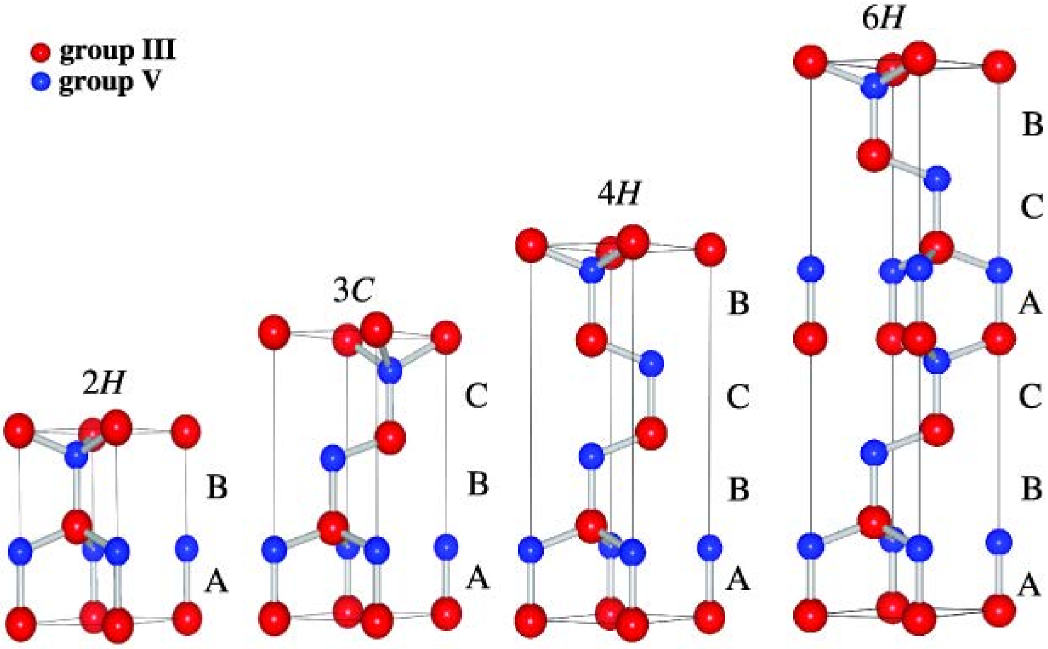

Figure 5.3: Stacking sequence of double layers of the four most common SiC polytypes.

5.2.2 Sapphire Substrates

Large area and good crystal quality are easily available for sapphire substrates, at a relatively low cost. They are transparent (to UV and visible light), stable at high temperature, and the III-nitrides-on-sapphire technology is quite mature, now. However, it has some disadvantages as well, such as a large lattice mismatch (16%) with GaN, which inevitably leads to a high threading dislocation density in the epitaxial layer grown on the top. The large differences of both, thermal expansion coefficient and lattice parameter between sapphire and III-nitrides generate biaxial compressive strain in the grown epitaxial layers. In general, crystal orientations of sapphire and GaN (grown on c-plane [0001] sapphire) are parallel (GaN[0001]||sapphire[0001]), but the unit cell of GaN is rotated by 30° around the c axis with respect to the sapphire unit cell (GaN[10-10]||sapphire[11-20]), thus minimizing the lattice mismatch (that otherwise would be of 30%, see figure 5.4). As sapphire is an insulator, backside electrical contacts for optoelectronic devices cannot be made. Sapphire has also a rather poor thermal conductivity that makes heat dissipation more difficult in power devices (LD, HEMT).

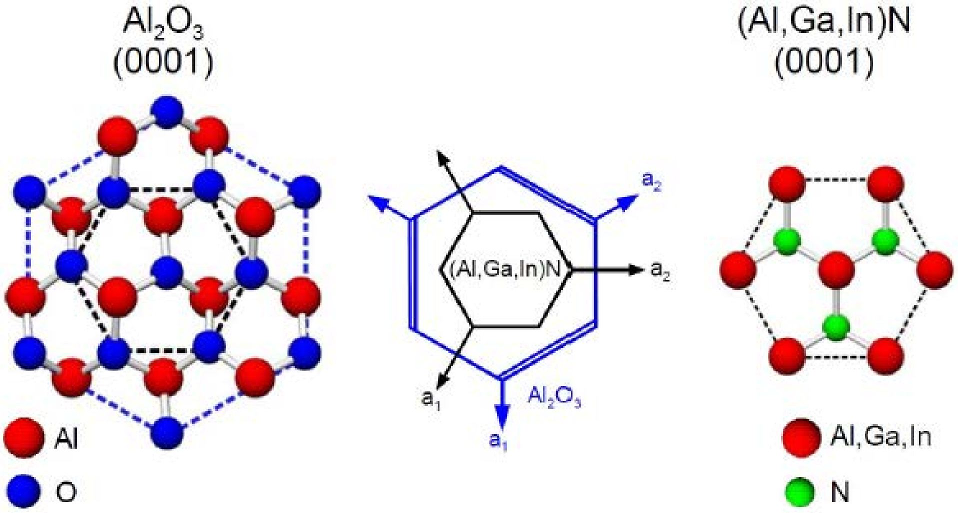

Figure 5.4: Sapphire (Al_2O_3) and (Al,Ga,In)N orientation symmetry

Even though sapphire has a rhombohedral structure, it can be described by a hexagonal cell that is larger than the basic rhombohedral unit cell. For various commercially available sapphire orientations, the relationship of orientation and crystallographic symmetry with a GaN epitaxial film are given in figure 5.5. Taking into account lattice mismatch and crystal symmetry, (10-10) sapphire (m-plane) seems the most suitable for GaN growth. Nevertheless, the c-axis of a GaN film grown on a (10-10) sapphire substrate is not parallel to the c-axis of the sapphire substrate. This means that twins may be generated. This is a big disadvantage of a (10-10) plane compared to a (0001) plane. Several planes (other than the c-plane) have been used for growth leading to non-polar III-nitride films. It is necessary to emphasize that growth presented in current thesis is performed on commercial GaN tem plate where 3.3 μM thick GaN is grown by MOCVD on top of a Sapphire substrate. Therefore prior to the InGAN growth a 80 nm GaN thick buffer layer will be grown establishing a transition between MOCVD and MBE growth.

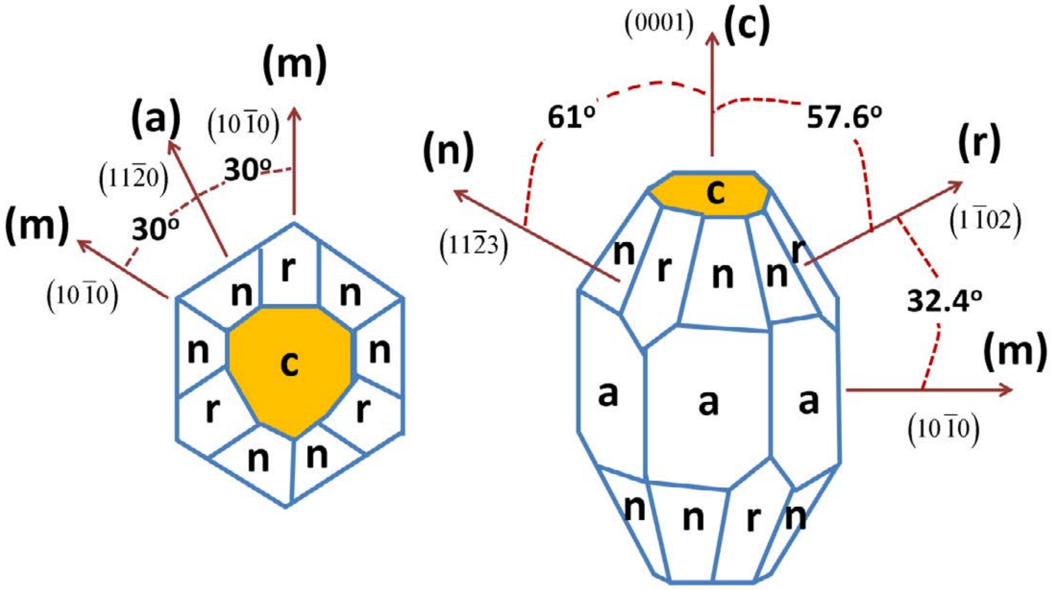

Figure 5.5: Rhombohedral structure and crystal planes of sapphire. Adapted from [Ambacher 1998]

5.2.3 Silicon Substrate

The third most common material of choice is silicon. Si is much cheaper than SiC and sapphire, it has an excellent crystal quality and a reasonable thermal conductivity. Silicon wafers can be grown with sizes up to 12-inch (whereas SiC and sapphire substrates are typically limited to 2 to 4-inch sizes). For these reasons, there is an increasing interest and effort to grow GaN on silicon; this would lead to a massive fabrication of low-cost LEDs. In this case, Si wafers oriented towards the (111), are the crystal direction of choice, to achieve hexagonal III-nitrides. Being silicon the leading material for microelectronic applications, the growth of III-nitrides on it would, in principle, offer the possibility to monolithically integrate III-nitride devices with silicon microelectronics. This would yield highly efficient direct band gap optical devices on cheap and technologically mature substrates. Another advantage of silicon substrates is the possibility to process (i.e. “shape”) devices by wet etching (cheap and fast); sapphire and SiC, on the other hand, require dry etching (to obtain, for instance, vertical LEDs). An important drawback when using silicon substrates, particularly when growing by MOVPE at high temperatures, is the melt-back etching of the substrate, which results in a significant increase in the surface roughness and consequently, additional difficulty for epitaxial layers nucleation. On the other hand, Si is a fast diffuser, which may lead to unintentional doping (Si is a shallow donor in GaN) of the grown layers.

The large thermal mismatch that in the case of GaN on Si can be as large as 54% represents a strong challenge to overpass. When cooling down, upon growth termination, GaN layers will be subjected, in this case, to biaxial tensile strain which may result in cracking.

Si has a diamond-lattice structure with the space group of $Fd\bar{3}m$ (No. 227) and can be thought of as two interpenetrating face centred cubic (fcc) sub-lattices with one sub-lattice displaced from the other by one quarter of the distance along a body diagonal of the cube (i.e., a displacement of $a\frac{\sqrt{3}}{4}$ where a = 5.43102 Å is the lattice constant). Each atom in the lattice is surrounded by four equidistant nearest neighbours that lie at the corners of a tetrahedron. Figure 5.6 illustrates the unit cell and 2-D surface along the [0 0 1] and [1 1 1] directions of the Si unit cell. For growth the best crystal plane would be the “hexagonal” one, namely the (111); it has same symmetry as [0001] nitrides crystal planes thus allowing a better epitaxial relationship.

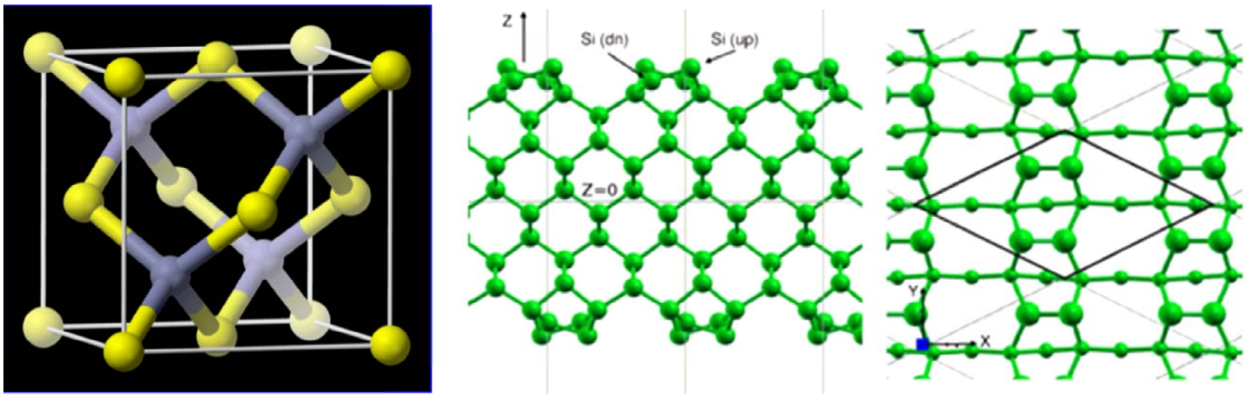

Figure 5.6: Unit cell and 2-D surface along the [1 1 1] and [0 0 1] directions of the Si cell.

Considering all previous particularities, this thesis has been developed using sapphire and Si(111) substrates. The differences in surface kinetics (diffusivity), lattice mismatch, and residual thermal strain, between the two substrates, will allow a good comparison of the III-nitride layers properties and device performance made on them. In both cases commercial substrates were used, particularly GaN templates grown on sapphire (0001). The know-how, acquired in the growth on GaN templates, will be later transferred to the Si(111) substrates.

5.3 Growth Techniques

Metal organic vapour phase epitaxy (MOVPE) was the typical method used at early stages of III-nitrides development. Molecular beam epitaxy (MBE) was not considered in early times, although it has many advantages to grow various compound semiconductors and quantum structures, including the achievement of abrupt interfaces, sharp doping profiles and superior in situ growth monitoring. However it was not considered an alternative to MOVPE to grow III-nitride films until the last 2 decades and for devices when S.E Hooper et al. demonstrated [Hooper 2004] the first pulsed laser diodes (LDs) emitting at 400 nm grown by MBE. Since then, many improvements in nitride devices were accomplished using either ammonia (NH_3), or a plasma-assisted (PA) MBE. Ammonia has a rather high pyrolysis temperature, setting thus a lower limit for growth temperature relatively high; the growth of high In content InGaN by this technique, is thus quite challenging. On the other hand, radio frequency plasma sources break the nitrogen molecule, thus providing very reactive atomic species, though the cracking efficiency is rather low. In chapter 3 a detailed description of the MBE system was presented.

As mentioned before, significant progress in MBE-grown nitride devices has been demonstrated, though many challenges still exist, particularly to grow high quality InGaN layers with high In composition. Significant part of this thesis will focus on the methods to overcome these issues. In the following, the growth on GaN templates will be analysed first. The knowledge will then be transferred to Si(111) substrates.

5.4 Growth on GaN Templates

This section presents and discusses the growth conditions used to grow InGaN layers by PA-MBE. Slightly N-rich growth conditions, together with relatively low growth temperatures, lead to the best morphological and optical properties of grown layers. The growth of InN QDs, by deposition of few InN monolayers (MLs) (on previously optimized InGaN layers) revealed 3MLs as a critical coverage; 3MLs of InN already leads to full InN coalescence. Bimodal QDs sizes are distinguished. Best optical results were found for a 2ML InN coverage where an increase of bigger sized QDs density is found to dominate the radiative recombination.

5.4.1 High-In content single InGaN layers

The quality of III-nitride materials depends, among other factors, on the relation between impinging metal and nitrogen fluxes during growth (III/N ratio). In a first approximation, stoichiometry is reached when the fluxes are nominally equal. However, common growth temperatures, used to produce metal desorption, lead to effectively N-rich conditions. Thus, the metal flux has to be increased (depending on the growth temperature) to achieve actual stoichiometry. High (effective) metal-rich (M-rich) conditions generate metal droplets on the surface, whereas high (effective) nitrogen-rich (N-rich) growth conditions lead to rough 3D surfaces[5], neither of the two being desired for applications.

In general high quality GaN films are grown at relatively high temperatures, typically above 650°C. When talking about temperature in MBE growth it is perhaps necessary highlight that dispersion in values may be observed, as each researcher calibrates his system not necessary in the same way, and thermocouple read-out may fluctuate more or less from one system to other. In the case of InN (also InGaN) the In-N bond is weaker so that the onset of InN decomposition is observed at temperatures as low as 500°C (for In-polar layers, and some 100°C higher for N-polar layers). On the other hand, the onset of In desorption is observed at a significantly higher temperature (significant In desorption occurs already at 520°C as stated in “Molecular Beam Epitaxy: Applications to Key Materials” by Robin F.C. Farrow [Farrow 1996]). As a result, as the In composition in InGaN layers is to be increased, the growth temperature must be decreased, the key question lies in how much it should be reduced in order to obtain the best quality InGaN alloy. Most reports concentrate on the top temperature limit for InGaN, as this allows a reasonable quality when GaN layers must be subsequently grown on top or before the InGaN as buffer layers to accommodate the (lattice) mismatch strain between film and substrate. Buffer layers have been an essential to increase the quality in the III-nitride MBE growth, but for some applications their use introduces an additional barrier to take into account. A more detailed analysis on the buffer implications will be given when the growth on Si(111) substrates is addressed.

It has been well established in the literature [Heying 2000b] that the optimal growth regime for GaN by PAMBE is the so called “intermediate regime” that consists on slightly metal rich conditions providing a surface metal bi-layer. This regime works quite well for GaN but may raise some limitations for InGaN layers in terms of In incorporation (due to the preferential Ga vs. In incorporation). Under this regime smooth InGaN layers can be obtained

---

[5] This fact may also be used to determine the growth rates, as in M-rich conditions the film thickness will be proportional to the nitrogen flux and in N-rich conditions proportional to the metal flux. By means of cross-sectional FE-SEM images the thickness of the grown layer can be accurately determined and by considering the growth time the actual growth rate can be established

with compositions up to 30% In. To overcome this composition limit a different approach is needed.

One very accurate way to describe the growth mechanism by MBE is presenting the growth parameters in a so-called growth diagram. In figure 5.7 (a) the growth diagram for GaN is presented [Heying 2000a]. For each point in this diagram a specific surface morphology is observed, morphologies that present similar surface properties (i.e. surface reconstruction, surface roughness and type of surface morphology) represent a regime within the diagram. In this way three growth regimes are observed:

- Ga-stable regime: characterized typically with a smooth GaN surface and Ga droplets formation
- N-stable regime: characterized typically with a rough GaN surface composed of inverted pyramid shaped pits
- Intermediate regime: characterized typically with flat GaN surface (without Ga droplets formation).

Recently our group developed a comprehensive diagram to grow (0001) InGaN alloys on GaN templates by PAMBE [Gačević 2013]. The obtained growth diagram is represented in figure 5.7 (b). The previously mentioned limitation, concerning the In incorporation (≤ ~30% In content) is clearly observed for the intermediate regime. This growth diagram was taken as the starting point after which the growth parameters were adjusted to obtain best film quality for higher In contents. In the following, the main results are presented.

All epitaxial growths were performed with a PA-MBE equipped with a radio-frequency (RF) active N_2 plasma source on commercial (0001) GaN templates, 3.3 µm thick. The growth started with an 80 nm thick GaN layer under intermediate Ga-rich conditions at a temperature of 760°C to provide a flat surface followed by an 80 nm thick InGaN layer, for which the active nitrogen flux was varied from 8.3 to 10 nm/min (6.07×10^{14} to 7.31×10^{14} atoms/cm^{2}s) by changing the RF power from 200 to 230 W. The N_2 flow was kept constant at 0.4 sccm (standard cubic centimetre per minute) by a mass flow controller. The Ga and In fluxes were 3 and 5.4 nm/min (2.19×10^{14} and 2.91×10^{14} atoms/cm^{2}s), respectively. The Ga, In, and N flux rates were calibrated by the growth rates of GaN and InN layers grown under N and Ga rich conditions [Heying 2000a]. The substrate temperature during the InGaN layer growth ranged from 460 to 540°C and were calibrated by desorption measurements of liquid In from the GaN surface with help of RHEED.

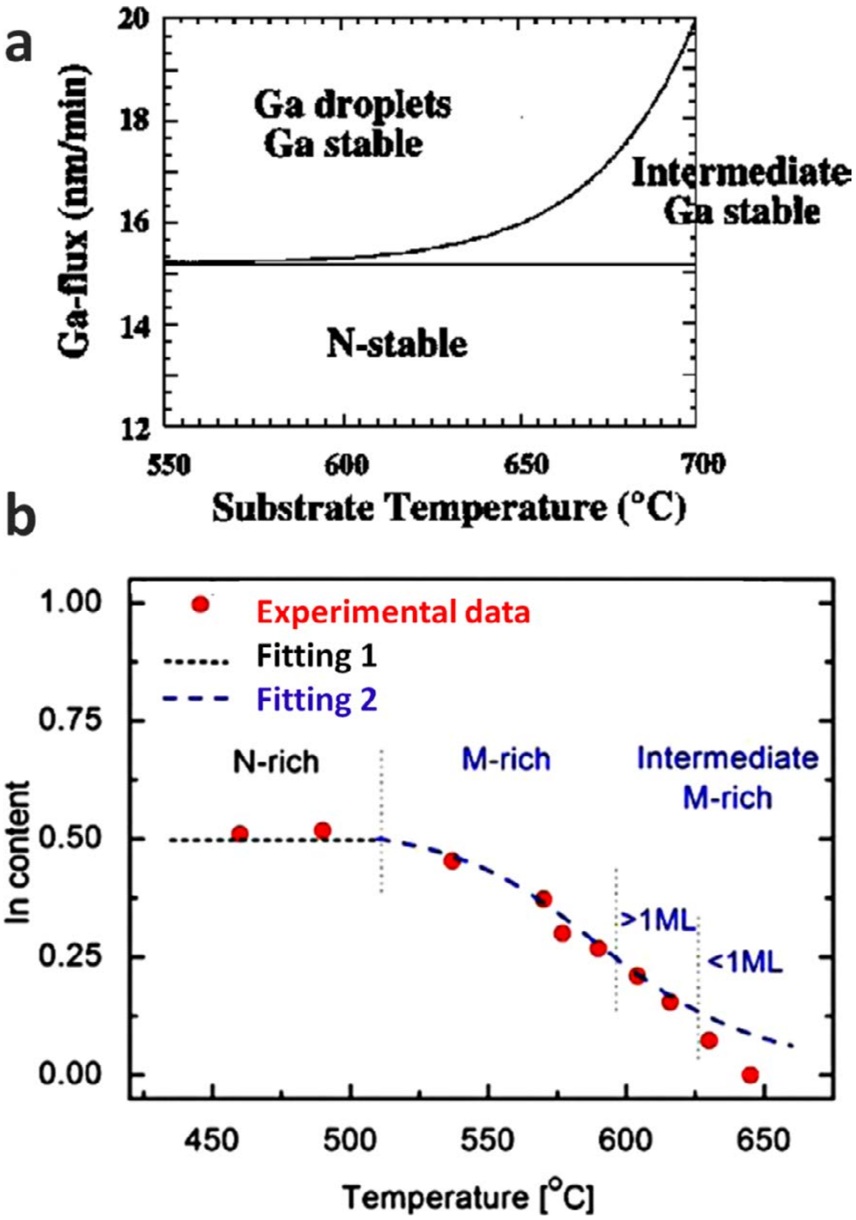

Figure 5.7: Growth diagram for (a) GaN [Heying 2000a] and (b) InGaN [Gačević 2013] both on GaN templates grown on c-plane sapphire.

The effect of the nitrogen flux on the layer morphology was checked by growing samples at two different flux values (RF power). Figure 5.8 shows AFM images of a series of six InGaN layers grown at (a, d) 460, (b, e) 500, and (c, f) 540^{o}C for (a-c) RF power of N1= 230 and (c-f) N2= 200 W. All surfaces reveal a modulated morphology. For a fixed active nitrogen flux, the average surface roughness increases with growth temperature; for a fixed growth temperature the surface roughness is higher for lower active nitrogen flux. The measured root-mean-square (rms) surface roughness increases from 0.51 nm (figure 5.8 (a)) to 3.97 nm (figure 5.8 (f)). This may suggest i) an increasing tendency to phase separation and ii) possible introduction of defects [Singh 1997, Park 2005]. The trend of i) phase separation, was also observed by HRXRD (fixed slit and mask was used ½"and 2mm respect.) with both symmetric (0002) and asymmetric (10-15) Bragg reflections ω-2θ scans. In addition ii) the possible introduction of defect was analysed by rocking curves recorded at the symmetric (0002) Bragg reflection. The average In composition and strain for the grown film was verified by means of HRXRD reciprocal space map measurements around the asymmetric (10-15) Bragg reflection.

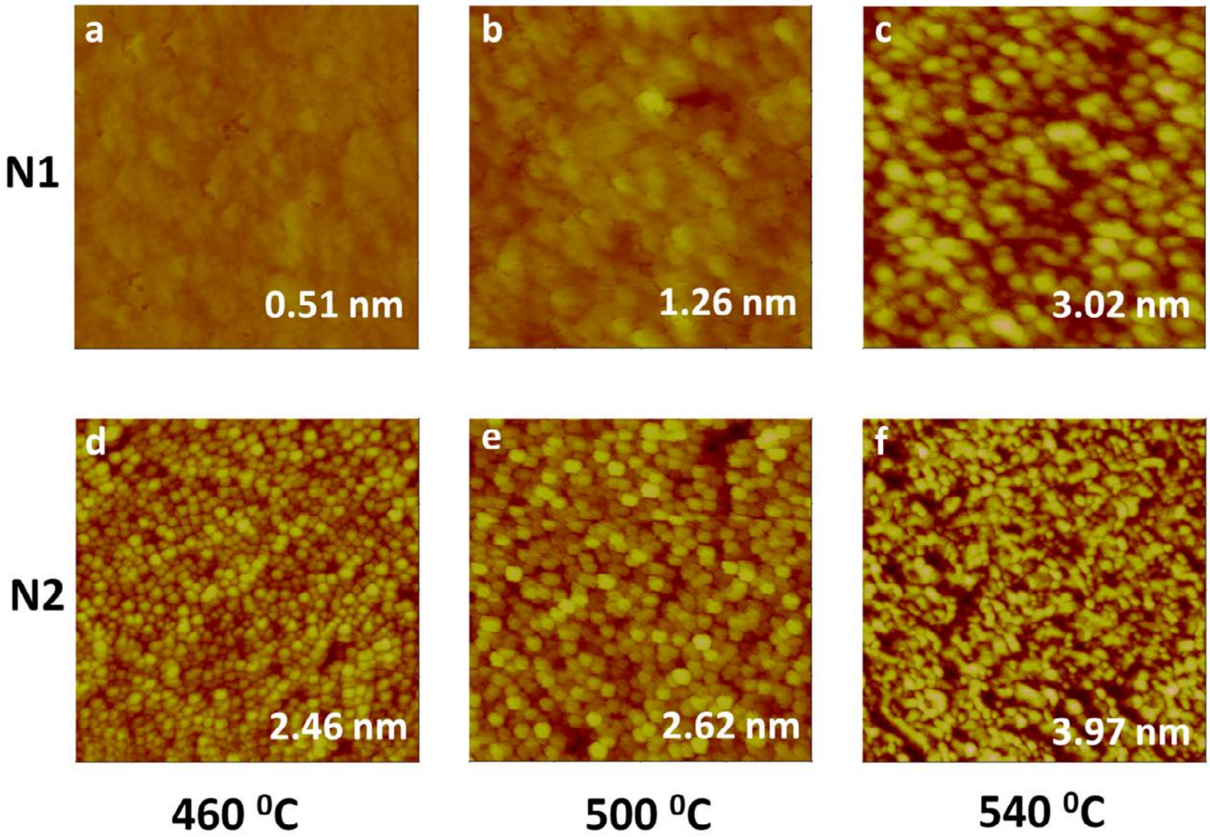

Figure 5.8: AFM images of InGaN layers grown at (a, d) 460ºC, (b, e) 500ºC, and (c, f) 540ºC for (a-c) RF power of N1= 230W and (c-f) RF power of N2= 200W. The scan fields are 1 µm × 1 µm and the full height contrast is 20 nm for all images (brightest colour corresponds to maximum value). For each AFM image its corresponding RMS value is indicated.

The grown InGaN layer is predicted to relax after a small critical height which depends on the indium content decreasing upon higher values[6]. Theory foresees thus fully relaxed

---

[6] Many models are available for the calculation of the critical height a nice overview on force balance models can be found in the work done by Jain et al. [Jain 1997] but in the case for InGaN fails to predict critical thickness above 28% In content as shown by David Holec in his thesis "Critical Thickness Calculations for $In_xG_{1-x}aN$/GaN systems" [Holec 2006] where he discusses that the hexagonal symmetry of the wurtzite structure lowers the critical thickness by about 10-20%. In his work he also shows that the energy balance model gives a

High In content InGaN layers to be grown on GaN templates. Despite obtaining a similar average composition in the ω-2θ scans (similar peak position), the full-width at half-maximum (FWHM) of the diffraction peaks broaden with increasing growth temperature, (see Table 5.2). Same is valid for the rocking curves. In figure 5.9 the symmetric ω-2θ scans and ω-scans for samples presented in figure 5.8 (a) and 5.8 (f) are presented.

Sample	ω-scan FWHM (^{o})	ω -2θ symmetric scan FWHM (^{o})	ω -2θ asymmetric scan FWHM (^{o})
(a)	0.11	0.058	0.35
(b)	0.13	0.18	0.76
(c)	0.74	Too low intensity	Too low intensity
(d)	0.31	0.070	0.35
(e)	0.37	0.079	0.66
(f)	0.43	0.087	Too low intensity

Table 5.2: FWHM values of the diffraction peaks in the symmetric and asymmetric XRD ω-2θ scans around the symmetric (0002) and asymmetric (10-15) Bragg reflections, as well as of the rocking curves, recorded around the symmetric (0002) Bragg reflection.

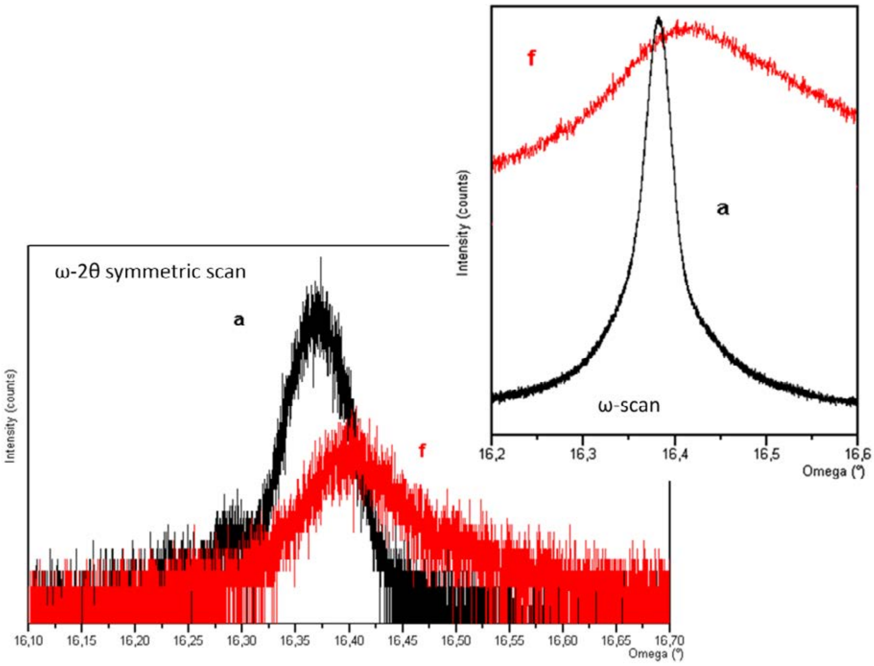

Figure 5.9: Both the symmetric ω-2θ scans around the (002) Bragg reflection and ω-scans for samples from figure 5.8 (a) and (f). The corresponding FWHM is presented in table 5.2. Both axes x, y are represented in a linear scale.

---

better approximation (as it is the only model capable of taking into account dislocation nucleation barriers) however even here for 20 % of In content a critical height as small as [4.1-4.4] nm (depending on temperature) is found.

As shown in figure 5.10 a fully strained film will show a vertical alignment with respect to the substrate (one on top of the other) on a reciprocal space map measurement. The centre point of the displayed reciprocal point corresponding to the substrate extrapolated to the origin of the reciprocal space indicates the relaxed case. By this interpretation we can consider the InGaN layer for which the RSM presented in figure 5.11 (b)) to be (nearly) fully relaxed.

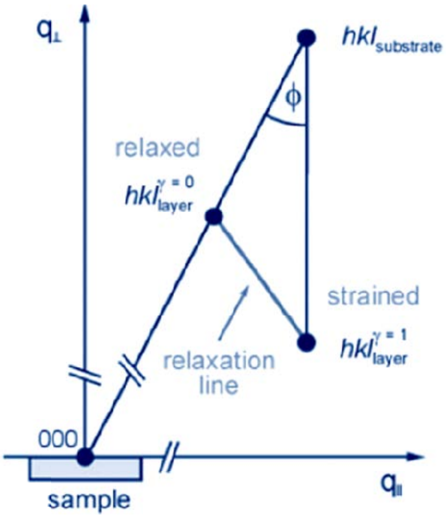

Figure 5.10: How to identify a strained or relaxed layer from the RSM [Pohl 2013].

Only the InGaN layer grown at 460°C and high nitrogen flux (N1), shown in figure 5.8 (a), has a FWHM value very close to that of the simulated spectrum of the ideal structure, as shown by the symmetric XRD ω-2θ scan (blue line) and simulated one (red line) in figure 5.11 (a). An average In composition of 54% is determined from the peak position by reciprocal space mapping around the asymmetric (10-15) Bragg reflection as shown in figure 5.11 (b).

For high quality film interfaces, in HRXRD measurements the forward diffracted beam itself fulfils the Bragg condition and shuffles intensity back to the primary direction. This round-trip period is called Pendellösung period and can be related to the film thickness, being included in most HRXRD simulation software as a way to determine film thickness. A layer thickness of 80nm is determined from the Pendellösung fringes in agreement with the thickness estimated from growth rates.

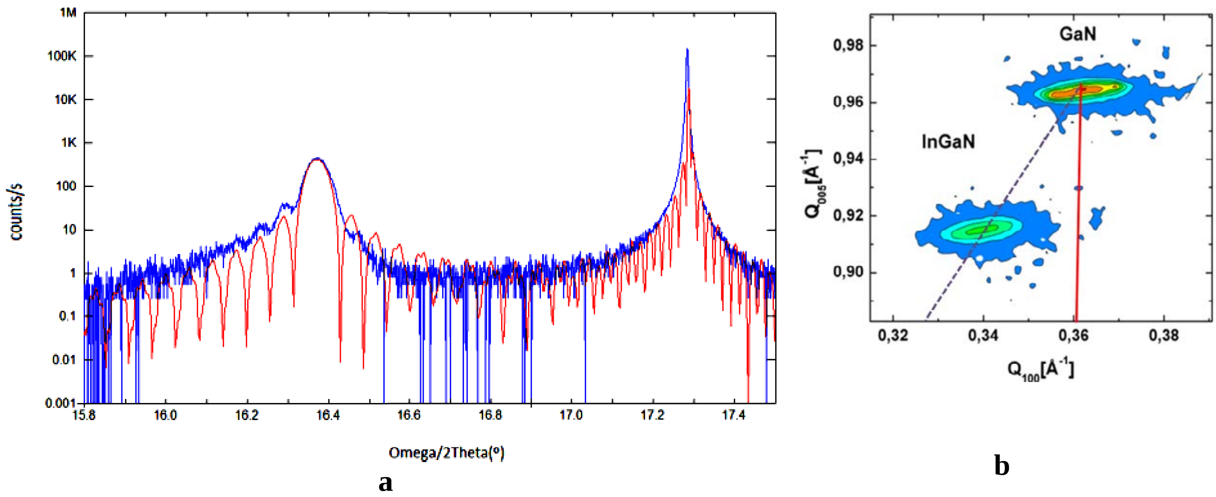

Figure 5.11: (a) High-resolution XRD ω/2θ scan (blue line) recorded around the symmetric (0002) Bragg reflection and a simulated scan (red curve) for the InGaN layer in figure 5.2 (a). (b) Reciprocal space map recorded around the asymmetric (10-15) Bragg reflection. Q_{100} and Q_{005} are the reciprocal space wave vectors. Red line is a guide to-the-eye which indicates possible positions for a fully strained layer and the purple line for the case of a fully relaxed layer in correspondence with the schematic presented in figure 5.10.

Recalling the methodology on how the ω- scan is performed, i.e the x-ray source is maintained fixed as is the detector but the sample is rocked around the Bragg peak slightly (therefore also called rocking curve) we can extract some additional information (even without explicit calculations).. In this measurement the magnitude of the wave vector (**k**) remains the same, but its orientation with respect to the sample normal changes see figure 5.12 (b). This type of scan is thus very sensitive to angular variation (distortion of the planes and therefore defects) as this will change the orientation of **k** and will cause broadening of the peak (increase in FWHM). On the other hand, for the ω-2θ scan the XRD source is fixed but the sample rotates in an angle of θ and the detector rotates thus 2θ. Here the magnitude of **k** changes and not its orientation with respect to the samples normal (see figure 5.12 (a)). This type of measurement is thus very sensitive to interplanar distance variations and therefore to phase separation and will show up as broadening of the peak (increase in FWHM).

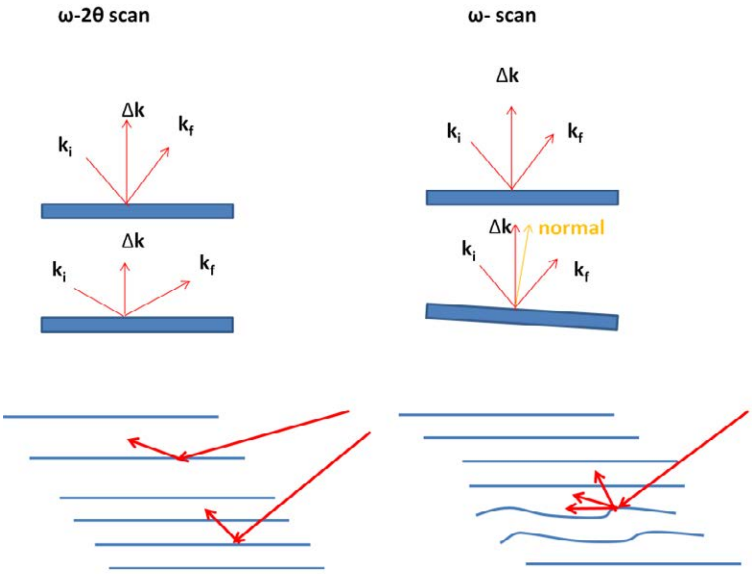

Figure 5.12: Explanation on sensitivity for both ω-2θ and ω- XRD scans.

In the table 5.2 observed broadening of the diffraction peaks (upon increase of substrate temperature for a fixed nitrogen value a-c, d-f) in both the symmetric and asymmetric XRD ω-2θ scans and the rocking curves indicates both, due to above mentioned reasons, enhanced phase separation, to which the ω-2θ scans are more sensitive, as well as introduction of dislocations, to which the rocking curves are more sensitive. Notice that this analysis is for observed trend only, considering values from table 5.2 values and no explicit calculation on density of dislocations has been performed and therefore not provided.

The smoothest InGaN film in this series of samples is also the one grown at 460°C and high active nitrogen (RF power of 230 W). This layer also exhibits PL emission at 17K. Since only high quality InGaN layers show PL emission, this finding backs the assumption that in samples grown at higher temperatures and lower active nitrogen dislocation generation may occur, thus, acting as lifetime killers and non radiative recombination centres.

In summary, from presented series of PA-MBE grown InGan layers it was observed that, good quality high-In-composition InGaN layers (above 40%) are obtained at relative low substrate temperature (460°C) together with high enough active nitrogen (RF power 230W) to avoid the formation of In droplets [Nanishi 2003b, Lliopoulos 2006, Komaki 2007]. These InGaN layers were chosen to be used as templates for InN QDs growth.

5.4.2 InN QDs

The growth of InN QDs was performed onto 80 nm thick $In_{0.54}Ga_{0.46}N$ layers by PAMBE. A schematic for the grown structure is shown in figure 5.13. InN was deposited on the InGaN templates with coverage ranging from 1 to 3 ML with at 460°C but reduced RF power to 160 W giving an active nitrogen flux of 6 nm/min (4.39×10^{14} atoms/cm^{2}s). The amount of deposited material was estimated from the input In flux and calibrated growth rate.

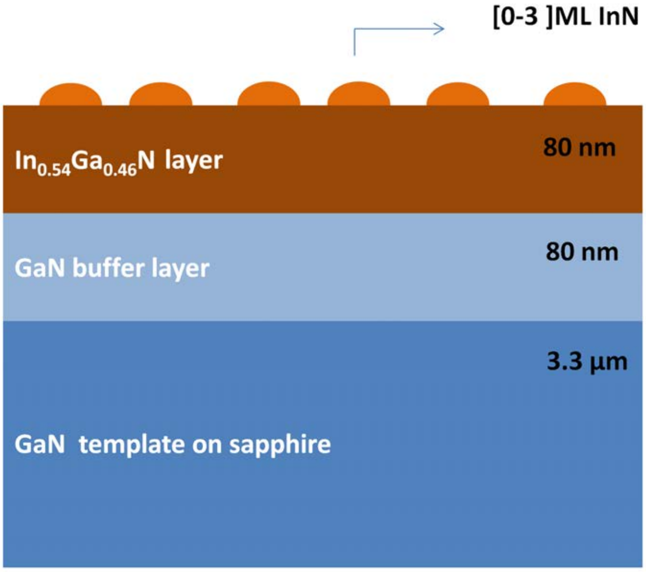

Figure 5.13: Scheme of the grown InN QDs on InGaN “templates”.

The resulting structures were analysed by AFM as shown in figure 5.14 where (a) is the bare InGaN “template” and (b) after 1 ML, (c) 2 ML, and (d) 3 ML InN grown on top. QD-like structures are clearly observed on the undulated InGaN surface for 1 and 2 ML InN deposition (figures 5.14 (b) and (c), respectively)

Though the underlying InGaN layers show a slight height variation, it remains much smaller than the height of InN QDs, as it can be seen in the topographic AFM scan shown in figure 5.14. From a statistical analysis of 8 different 1 x 1 µm^2 AFM image scans two groups of dots with different size and density can be distinguished, together with large clusters of InN QDs, as summarized in Table 5.3. This may indicate a bimodal dot size distribution accompanied by coalesced features. While the structural properties of the smaller dots do not change significantly with InN coverage, the dot density increases by almost one order of magnitude for the larger dots when the InN coverage is increased from 1 to 2 ML. No clear QD-like structures are observed for 3 ML InN deposition only InN QDs clusters in the AFM image in figure 5.14 (d) which indicates that coalescence of the dots forms an undulated compact-like film (large interconnected clusters). Thus, a very narrow InN coverage window exists to form well-defined QDs.

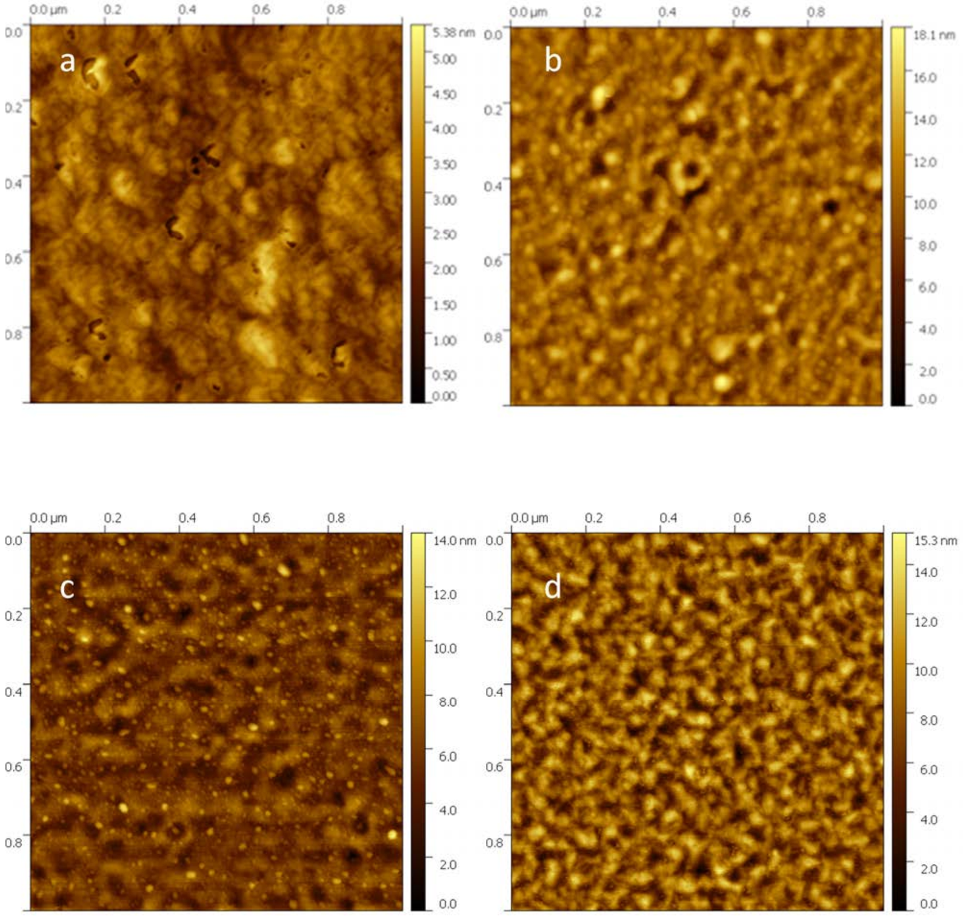

Figure 5.14: AFM images of the (a) optimized bare InGaN template for comparison; and (b) 1, (c) 2, and (d) 3 ML InN grown on top.

Sample		Larger dots	Smaller dots
1 ML InN	Diameter	20 – 30 nm	10 – 15 nm
	Height	2 – 3 nm	2 – 3 nm
	Density	2.2×10^{9} cm^{-2}	1.2×10^{10} cm^{-2}
2 ML InN	Diameter	20 – 30 nm	10 – 15 nm
	Height	2 – 3 nm	1 – 2 nm
	Density	1.5×10^{10} cm^{-2}	2.3×10^{10} cm^{-2}

Table 5.3: Statistacally obtained structural parameters of the InN QDs determined by AFM.

As mentioned before for the case of the InGaN films no In droplets are formed on the surface. Nevertheless, for the lattice mismatch present between InGaN and InN a critical layer thickness for QD formation beyond one ML is expected but at one ML of InN deposition QDs already forms. This indicates that most probably In segregation is taking place to promote the QD formation. In this same line, probable In segregation might also explain the fact that for 3 ML InN deposition already a undulated, coalesced layer is observed with larger density of InN QDs clusters.

The optical characterization, macro-photoluminescence (PL) measurements were performed at 17K and room temperature (RT). Excitation was by a 781-nm laser diode with ~3Wcm^{-2} power density. The PL was dispersed by a double monochromator and detected by a liquid-nitrogen-cooled Ge photodetector. The temperature dependent PL spectra of the 1 ML InN surface QD (SQD) sample is shown in figure 5.15 (a). For an easier comparison, the PL spectrum of the bare InGaN "template" at 17 K is also shown in the inset. The superimposed Fabry-Pérot fringes are caused by multiple reflections due to high refractive index contrast between GaN (~2.4), sandwiched between sapphire (~1.78) and air (1). The presence of pronounced fringes confirms relatively flat interfaces. The PL emission centred at higher energy (of 1.4 eV, determined from an interpolated curve through the points of half height of the fringes) stems from the InGaN "template", while the emission centred at lower energy (1.1 eV) stems from the InN SQDs. This is evident because the band centred at lower energy consistently appears in the PL from the SQD sample and is absent in the spectrum of the bare InGaN layer (the sharp feature at ~1.34 eV is a plasma line of the laser diode).

The energy corresponding to the PL emission from the InN SQDs falls within the expected range once considered the SQD size. A PL energy between 1.1 and 1.2 eV is expected considering only quantum confinement due to the SQD height. Such estimation is commonly considered [Ke 2006] as the SQD diameter is about one order of magnitude larger than the height giving a reasonable accuracy, particularly when the PL band is relatively broad due to SQD size fluctuations.

In the temperature dependent PL spectra of figure 5.15 (a), the PL intensity from the InGaN layer decreases monotonically when the temperature increases, while the PL intensity from SQDs first increases with temperature up to 40 K before it starts to decrease. This can be explained by thermally activated transfer of carriers localized at shallow traps in the InGaN layer to the SQDs before the SQD PL is also quenched [Ke 2006].

In figure 5.15 (b) the temperature dependent PL spectra is displayed for the 2 ML InN SQDs up to RT with ~3Wcm^{-2} excitation power density. No clear PL band from the InGaN layer is observed. There is only a high-energy shoulder visible at low temperature extending from 1.2 to 1.4 eV which is quenched at 180 K. Hence, energy position and temperature dependence indicate that this emission stems from the InGaN layer. The weak PL intensity from the InGaN layer with respect to the intensity of the PL of the SQDs indicates that the SQD PL originates from increase of SQDs density (1 order of magnitude for the larger and twice the amount of smaller) which, therefore capture most of the photogenerated carriers from the InGaN layer already at low temperature. Therefore, there is also no initial rise of the SQD PL intensity with temperature but a monotonic decrease.

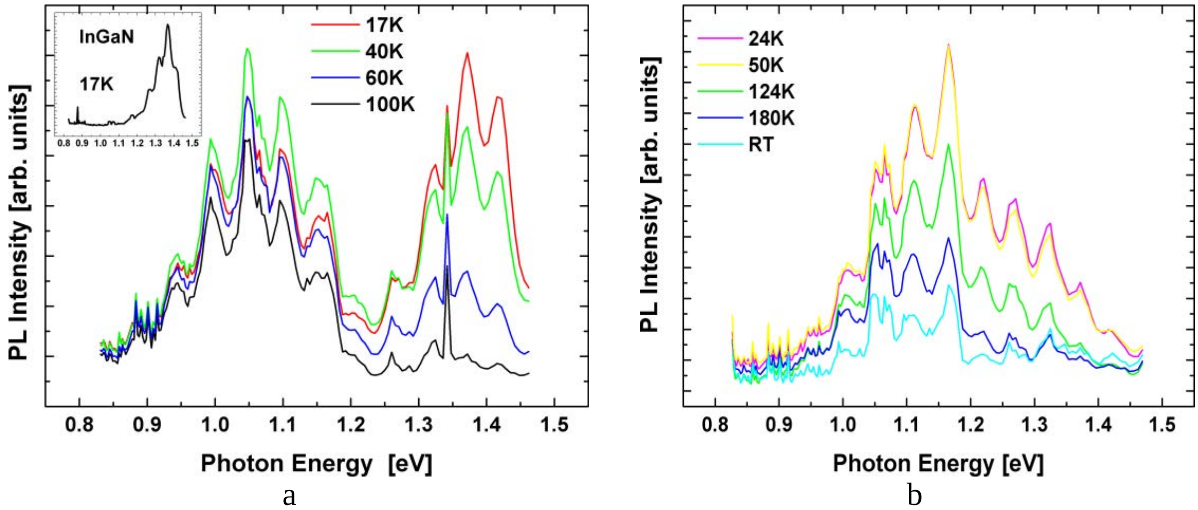

a b

Figure 5.15: Temperature dependent PL spectra of (a) 1 ML InN SQD sample. Inset: PL spectrum of the bare InGaN layer taken at 17 K; (b) 2 ML InN SQD sample.

The dominant PL SQDs behaviour was further investigated. Illustrated in figure 5.16 (a) is the Arrhenius plot of the intensity of the PL peak at 1.15 eV of the 2 ML InN SQDs as a function of temperature. The activation energy (E_a) describing the quenching of the PL intensity is derived from a fit to the expression:

$$I_{PL} = C / (1 + A \cdot e^{-E_a / k_B T}) \tag{5.2}$$

where 'k_B' is the Boltzmann constant and 'T' is the temperature. 'C' and 'A' are fitting parameters. The activation energy amounts to 23 meV. This is much smaller than the carrier confinement energy of the QDs of around 320 meV, given by the difference of the InGaN bandgap energy and InN SQD ground state energy. This indicates that defects, acting as non-radiative recombination centres are involved in the PL quenching, rather than pure thermally activated carrier transfer from the InN SQDs to the InGaN template. Still, high optical quality of the SQDs is evidenced by the linear dependence of the PL intensity on the excitation power, shown in figure 5.16 (b). Most prominently, quality also manifests by the observation of efficient PL up to RT. No PL emission is observed from the 3 ML InN sample indicating a high density of non-radiative recombination centres in the undulated InN layer and emphasizing the very narrow coverage window for obtaining high-quality InN SQDs on high-In-composition InGaN.

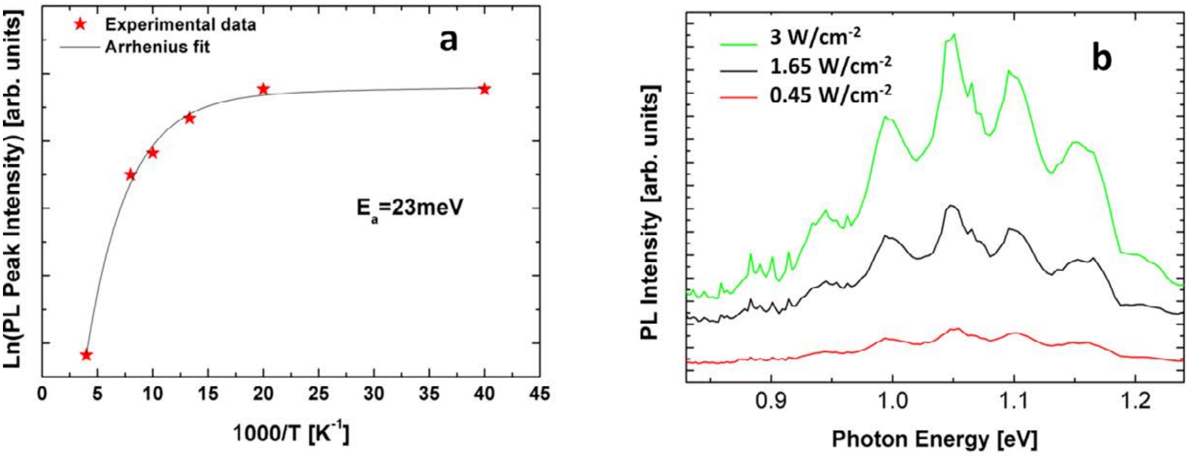

Figure 5.16: (a) Arrhenius plot of the PL intensity of the 2 ML InN SQDs versus temperature with the fitted activation energy. (b) PL spectra of the 2 ML InN SQDs as a function of excitation power measured at 17 K. Inset: Plot of the PL intensity versus excitation power.

In summary, InN QDs have been grown by PA-MBE on thick (80nm) InGaN templates with high In composition (>50%). These InGaN templates were grown on GaN/sapphire substrates under optimized conditions (low growth temperature and high nitrogen flux) in order to minimize phase separation as the defect generation. The size and density of the InN QDs can be (to some extent) tuned by the coverage amount. RT-PL at 1.5 eV was still observable from the InN SQDs.

5.5 Growth of InGaN Alloys Directly on Si(111)

A first study was realized on the direct growth of high-In composition InGaN layers on Si (111) by PAMBE without any buffer layers. The approach is to start from the knowledge acquired when growing on GaN templates, namely, low temperature to enhance In incorporation and slightly N-rich conditions. From this initial study it was found that, within a narrow window of growth conditions, micrometre sized planar areas (mesa like) are formed together with trenches and holes. Detailed structural and optical analyses reveal that the planar areas are made of InGaN with high and uniform In composition, while the trenches and holes are associated with and low-In composition InGaN and even pure GaN. Photoluminescence at low temperature is measured from the high-In composition InGaN planar areas

In general, most semiconductor devices require planar processing, thus, smooth 2D layers. On the other hand, InGaN is the choice material for a wide range of applications, particularly when grown on Si, opening the door for integrating III-nitrides with Si. The growth of InGaN layers directly on Si has been regarded as quite difficult if not impossible. Therefore, AlN or GaN, or combined buffer layers are always employed [Egawa 2005, Blake 2012]. These buffer layers, however, may behave as barriers that isolate (or at least hamper conductivity) electrically the InGaN layer from the Si substrate. Hence, advanced device designs like InGaN/Si tandem solar cells benefiting from a unique band alignment (ohmic p-Si/n-$In_{0.46}Ga_{0.54}N$ contact) theoretically predicted [Hsu 2008] cannot be achieved with buffers. Eliminating this buffer layer would also allow to make novel schemes for a possible hybrid photocathode by adding at the back part a catalyst material for example. In the case of Biosensors it is of interest for the lab-on-chip context.

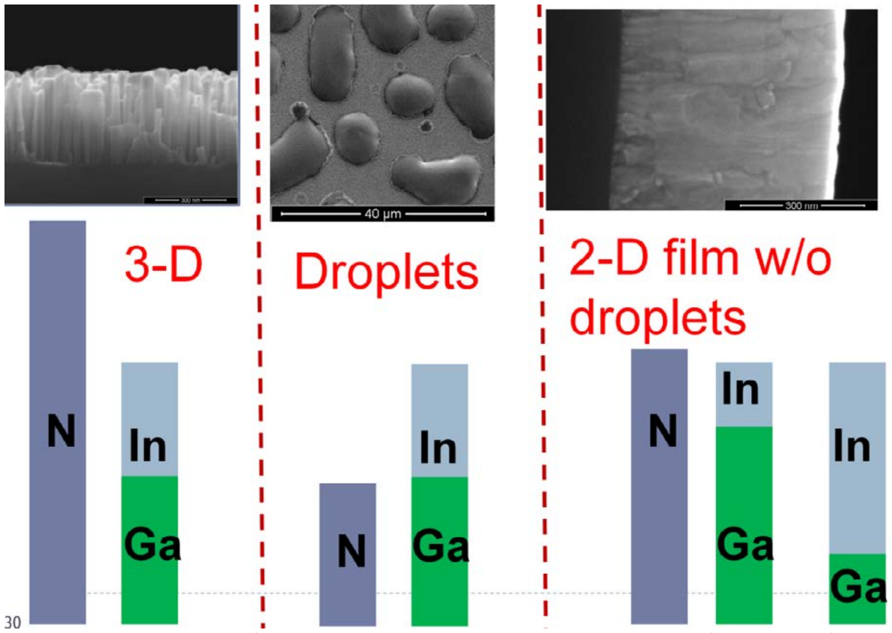

Figure 5.17: InGaN morphology for inGaN layers grown on Si111 as a function of the III/V ratio: (a) Highly nitrogen rich (nanocolumnar); (b) Metal rich (droplets), and (c) Slightly N-rich (2D homogeneous layers).

Figure 5.17 shows the morphology changes of InGaN layers grown on Si at fixed temperature, as a function of the III/V ratio. However, in a very narrow window of growth conditions, micrometre sized planar areas are formed together with trenches and holes. Such morphology is well-known from the growth of GaN on Si involving nucleation, lateral growth, coalescence, and two-dimensional film growth (a schematic drawing is presented in figure 5.18). For a limited thickness of the InGaN layer the coalescence process may not be complete, leaving trenches and holes [Riemann 2006, Cheng 2008]. SEM, HRXRD and CL imaging at RT reveal that the planar areas are made of InGaN with high and uniform In composition, while the trenches and holes are associated with low-In composition InGaN and even pure GaN. PL emission is observed from InGaN planar areas low temperature.

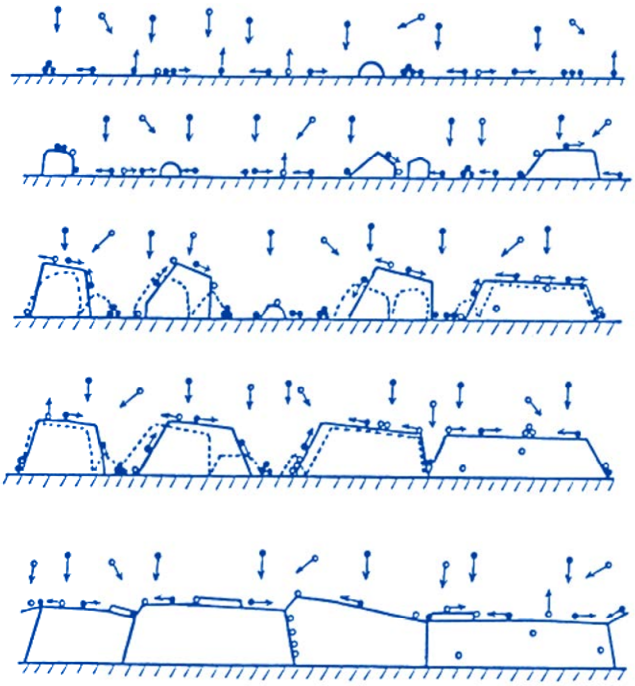

Figure 5.18: Schematics of GaN growth mechanism on Si(111) by (from top-to-bottom) nucleation, lateral growth, coalescence, and two-dimensional film growth.

In this section, all InGaN layers analysed were grown by PAMBE (MECA 2000) on Si (111) substrates without any buffer layers. After inserting the Si substrates into the MBE growth chamber, the native oxide was removed by ~20 min annealing at 850°C [Kumar 2009, 2010a]. Then an intentional SiNx layer is formed, for this the Si surface was nitrided under optimized conditions (for which best crystalline conditions were obtained), i.e an active nitrogen flux for 5 min at 850°C. This intentional nitridation increases reproducibility of the growth process[7]. Although the SiNx is insulating the obtained self limiting SiNx layer is usually observed very thin to be between 1-3 nm thick from TEM analysis and is shown to maintain the epitaxial relation between Si(111) and the nitride layer above [Nakada 2011, Kumar M. 2011]. In addition, due to the good epitaxial relationt it is not expected to be dentrimental for the electric properties. In this sense, vertical conducting schemes like adding a counter electrode directly to the back, which could be of interest for watersplitting

---

[7] This method was introduced previously to obtain high quality GaN growth on Si(111) films by other groups [Nakada 2011, Kumar M. 2011]

experiments, would in principle be possible. InGaN growth was performed at temperatures[8] of 430, 480, and 530^{o}C, keeping the In and Ga fluxes constant at 3.4 nm/min (1.83x10^{14} atoms/(cm^{2}s)) and 4.1 nm/min (3.00x10^{14} atoms/(cm^{2}s)), respectively. The InGaN growth rate was 0.45 µm h^{-1} and the average layer thickness was 450 nm. In order to perform an extensive analysis of the growth mechanisms on Si(111) (and check morphology changes) the active nitrogen flux was varied from 9.2 nm/min(6.72x10^{14} atoms/(cm^{2}s)), to values slightly above stoichiometry (9.5nm/min (6.94x10^{14} atoms/(cm^{2}s)), and 10.0 nm/min (7.31x10^{14} atoms/(cm^{2}s)), until the columnar growth regime was reached. The growth conditions for the different samples, labelled as A to E, are summarized in figure 5.19 including a scheme of the sample structure.

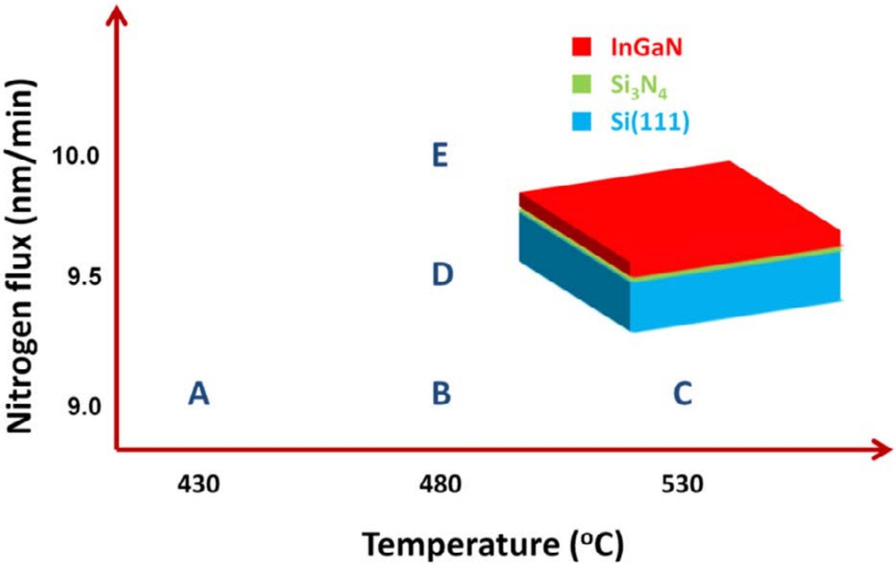

Figure 5.19: Diagram of the growth conditions of the InGaN layers (A to E). Inset: sample structure.

Figure 5.20 shows SEM images of the surface of samples A to E. Besides sample B, all InGaN layers reveal a nanostructured surface morphology with nanoscale flake, nanowall matrix (details will be presented in following section), hole, or dot-like structures. The formation of such nanostructures is well established in case of the growth of pure GaN or ZnO, however, is not desired for base layers aiming at planar device applications [Tian 2003, Yan 2009]. This is reasonably achieved only for sample B exhibiting laterally extended, micrometre sized planar areas together with trenches and holes. The initial nitridation process

---

[8] These were corrected after with respect to published values [Kumar 2013] which corresponded to 400, 450 and 500 ^{o}C (thermocouple read out) as afterwards thermocouple was changed and correctly calibrated.

used in these samples was developed to optimize the growth of GaN layers [Nakada 1998]. In the case of GaN growth, *nucleation* on the bare Si surface is difficult (if not impossible due to the low wetting properties) yielding separated crystallites. [Kumar 2010b, 2012] On SiN the *nucleation* is enhanced and layer growth becomes possible. [Wu C. 2003] The macroscopically horizontal planar regions of the InGaN layer in sample B are remarkably smooth with a root-mean-square (rms) roughness of 1.7 nm measured by AFM. These horizontal planar regions are connected to each other, being large enough to serve as barrier layers for active structures such as QWs and QDs.

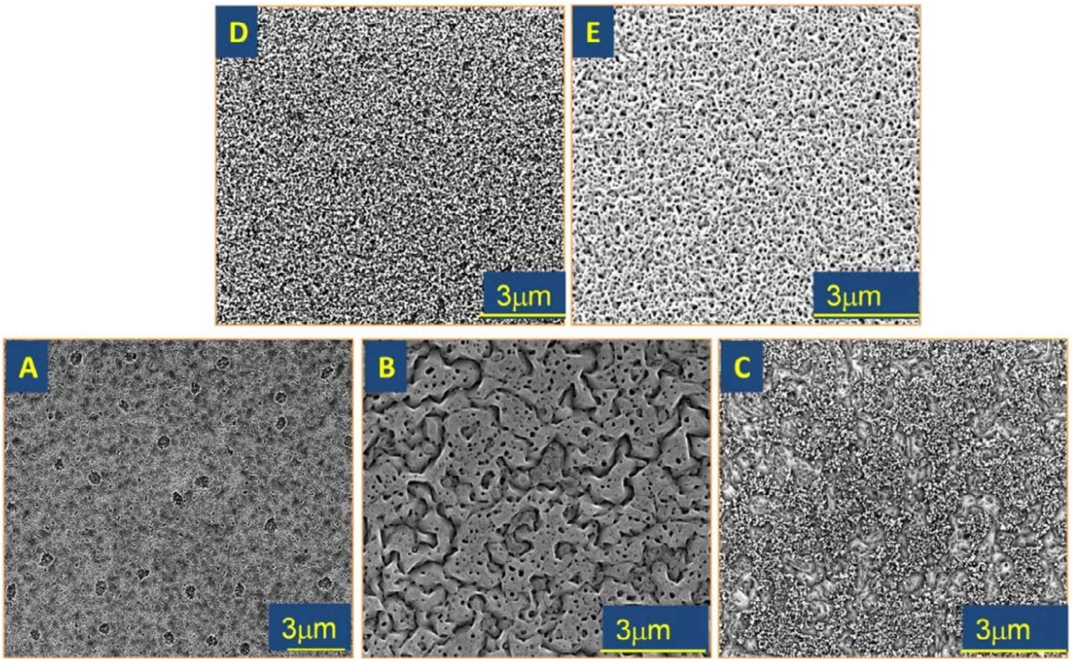

Figure 5.20: Top-view SEM images of the InGaN layers A–E grown directly on Si.

No metallic In/Ga droplets are found on the surface, evidencing that all In is incorporated in the layers with an In/Ga flux ratio close to one. Growth targeted In compositions between 40 and 50 % and both InN decomposition and In desorption should be negligible at the low growth temperatures used. Hence, InGaN layers with high In composition containing macroscopically extended horizontal planar areas can be grown on Si for active nitrogen fluxes slightly above stoichiometry and low growth temperature before the crystal quality degrades. This might be related to the initial growth stages where the low growth temperature promotes nucleation sites and the lateral growth promotes the coalescence of the islands while a low active nitrogen flux keeps the In and Ga diffusion lengths sufficiently large (as less nitrogen implies lowering the probability of recombination of metals with nitrogen) In incorporation might be different whether planar areas, trenches or holes are considered (dependence on crystal planes), however, the area ratio of the planar areas to trenches plus holes indicates that a large amount of In with the targeted amount of 40–50 % might be incorporated in the planar areas, a point that will be proven now.

Figure 5.16 shows HRXRD (fixed slit and mask was used ½”and 2mm respect.) ω-2θ scans of the samples B to E recorded in the vicinity of the GaN (0002) Bragg reflection. The layers are fully relaxed as confirmed by reciprocal space mapping. This allows determining the In composition directly from the ω-2θ scans. All layers, other than B, show a very broad reflection which is solely attributed to the sensitivity to composition variation (of the ω-2θ measurement). The measurements indicate In contents in the 45 - 0% (samples E, D and C, respectively). No InGaN diffraction is observed for sample A revealing that the InGaN layer in this sample is amorphous most likely due to a too low growth temperature. The peak at 14.22^{o} is from the Si substrate (marked in figure 5.21). Such broad reflections from the InGaN layers C to E indicate In composition variations on a micro/nanoscopic scale.

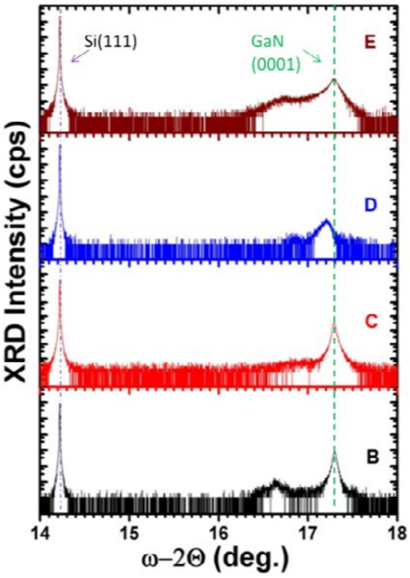

Figure 5.21: High-resolution XRD ω-2θ scans of the InGaN layers B–E recorded in the vicinity of the GaN (0002) Bragg reflection.

One way to interpret pronounced In content fluctuations is rough (faceted) InGaN morphology, which enables In incorporation through different crystal planes, in particular, (top) polar and (lateral) semipolar ones. Enhanced In incorporation on polar (vs. semipolar planes) for InGaN layers grown by PA-MBE were systematically observed by several groups (see for example: A. Das et al. [Das 2010]).

Above interpretation is in line with the two well-separated diffraction peaks observed for sample B in figure 5.21, suggesting the existence of phase separation, i.e. low In-content

InGaN with peak at 17.26° (with a FWHM of 0.14°) and another peak centred at 16.59° due to high In-content InGaN. If it is considered that the width of the HRXRD measurements is the direct measure of In-content, thus neglecting peak broadening by defects or mosaisicity, the low In-content InGaN covers (an almost) pure GaN (17.2833 °) together with In contents around 15 % and the high In-content InGaN would contain In composition ranging from 38 to 45%. This sample, as observed from the SEM image, contains all possible families of planes and therefore preferential In incorporation by the polar c-plane is highly probable to correspond to the higher In-content InGaN whilst (non-)semipolar planes for the GaN and lower In-content. The variations observed in the latter might be explained by roughness (thus variation in exposed crystallographic planes) in the trenches and holes.

Figure 5.22 (a) shows the cross-sectional SEM image of sample B. The planar areas exhibit a uniform bright contrast in the SEM image which is typical for InGaN with high In composition due its higher electrical conductivity and higher atomic number z of In compared to Ga as the secondary electron emission for high-Z materials is enhanced. Even more, underneath the trenches or holes dark stripes (darker zones in SEM image) are seen which might be associated to pure GaN and low-In composition InGaN. This is an additional hint, suggesting that In incorporation is sensitive to crystallographic planes. In this sense, an enhanced incorporation of In would occur mostly in the planar areas (0001) c-plane, leaving regions of GaN and low-In composition InGaN underneath the trenches and holes.

This hypothesis is further investigated by the CL image of an area including both trenches and holes as shown in figure 5.22 (b) recorded at room temperature at the peak emission wavelength of GaN of 365 nm (3.4 eV) and laid over the topographic top view SEM image. The electron beam voltage is 20 keV and the current is 1 µA. The bright purple, round shaped contrast in the CL image, corresponding to the emission from GaN, is located solely in the hole which appears as a dark contrast in the SEM image. No emission at room temperature is obtained from the high-In composition InGaN most likely due to defects introduced by the plastic relaxation and coalescence, similar to the case observed in some GaN layers grown on Si [Jain 2000]. As polar c-plane is enhanced upon coalescence, the In incorporation is increased in the more coalesced morphologies. Leaving thus sample B with the highest In content InGaN.

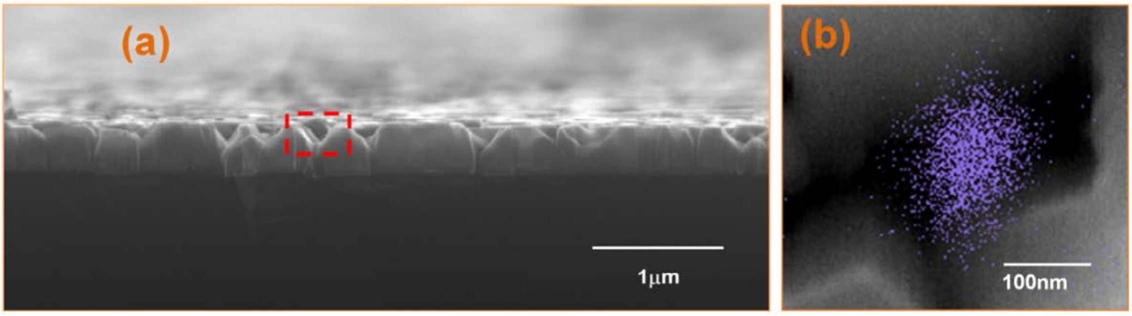

Figure 5.22: (a) Cross-sectional SEM image of the InGaN layer B. Red square indicates a zone with trenches and holes (b) CL image made from top view of a zone similar to the red square marked in (a) recorded at room temperature at the GaN peak emission wavelength of 365 nm, laid over the topographic top view SEM image.

In the following a detailed discussion regarding the correlation between growth conditions and surface morphology of samples A, C, D, and E in relation to sample B is given. In the case for which too low substrate temperature (sample A in figure 5.20) was used, the obtained grown InGaN resulted in a gently undulated (amorphous or polycrystalline) film with a large number of holes (no XRD signal). At elevated growth temperatures (sample C) the morphology is more coalesced with a dot-like (3-D structures) surface structure as seen figure 5.23. This might indicate enhanced In segregation and decomposition induced by the higher growth temperature. The formation of 3-D structure indicates the presence of locally more N-rich conditions. Despite an expected enhanced diffusivity, as more In would be available at the growth front due to the In segregation, coalescence of 3-D is enhanced creating a mixture of coalesced and individual 3-D structures. The coalesced 3-D structures form a faceted film, more-like interconnected matrix, which therefore would be expected to present less In incorporation with respect to sample B. For temperatures higher than those discussed, In incorporation decreases in the film due to a strong In desorption. For an increasing active nitrogen flux (samples D and E) a nanoscale flake or a homogenous matrix structure develops. This may indicate the transition to a columnar growth regime typical of a high active nitrogen flux. When the active N flux is decreased compared to that of sample B, (not shown) metal droplets develop on the surface. In all samples but B, all these phenomena lead to a rough surface morphology and a highly non-uniform In incorporation (broad XRD spectra).

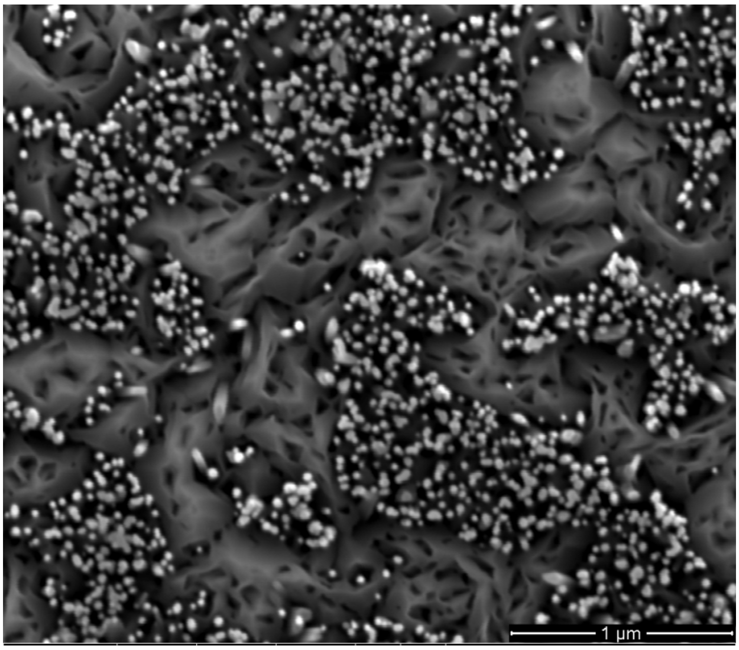

Figure 5.23: SEM Image of sample C with higher magnification 90 000X, with 20 keV

Figure 5.24 shows the PL spectrum taken at 12K from the high-In composition InGaN layer (sample B). The PL is excited by a He-Cd laser with 0.2 W/cm^2 excitation power. Considering strain free films, the two peaks at short wavelengths of 358 nm (3.46 eV) and 383 nm (3.24 eV) are most likely due to GaN-related emission (see chapter 2, value is close to F_{XA}) and low-In composition InGaN respectively. In this same line, the emission centred at a longer wavelength of 794 nm (1.57 eV) is attributed to the high-In composition InGaN. An estimated composition of 41%, taking an energy band bowing parameter ‘b’ of 3.067 eV [Heying 2000a], is in fair agreement with XRD results. As mentioned before, due the presence of defects the PL intensity of the high-In composition InGaN is much lower than that of the low-In composition InGaN and GaN. However, the mere observation of PL from the In rich regions opens space for further optical quality improvement.

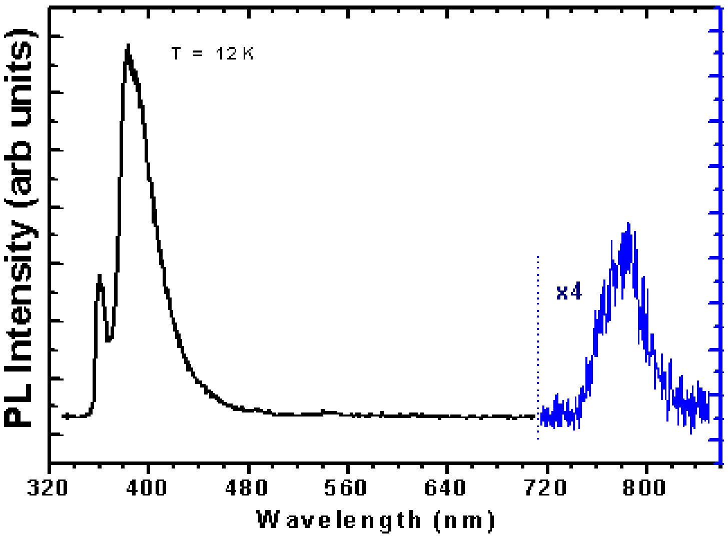

Figure 5.24: 12K PL spectrum taken from the InGaN layer of sample B

In summary, high-In composition InGaN layers have been grown directly on nitrided Si (111) substrates by PA-MBE without any buffer layer. In a very narrow window of growth conditions, centred at moderate substrate temperature and low active N flux, micrometre sized planar areas were formed together with trenches and holes. Such morphology *resembles* the well known growth of GaN on Si involving nucleation, lateral growth, coalescence, and two-dimensional film growth. SEM, XRD, and CL images revealed that the planar areas comprise an InGaN layer with high and relatively uniform In composition, while the trenches and holes are associated with GaN and low-In composition InGaN. PL emission was observed at low temperature from the high-In composition InGaN layer. After achieving the crucial step of growing micron sized planar layers of InGaN with high In composition directly on Si, fine tuning of the growth parameters in the regime of moderate growth temperature and low active nitrogen flux is now straightforward to further improve the material quality.

5.5.1 Sample used in current thesis: Fine tuning and chemically homogeneous InGaN layers

InGaN layers with micron size horizontal planar areas are generated by lateral coalescence when both In segregation and increased metal diffusion occurs. Given the fact that the micro-crystals geometry includes several planes, a dispersion of the In content is expected depending on the different In incorporation on them. In addition, the In segregation may lead to inhomogeneous In composition even considering a given crystal plane (like c-plane). One way to reduce metal diffusivity and segregation is to lower the growth temperature (e.g. 320°C in [Aseev 2015]). This, together with close to stoichiometric conditions leads to chemically uniform, compact InGaN layers (with a maximum of 33% of In content) showing a single HRXRD peak and PL emission up to RT. Nevertheless, the resulting sample morphology is still not a horizontally planar film. Improving morphology while keeping high quality and In-content of InGaN layers needs a specific temperature which balances metal diffusivity for chemical uniformity at the highest In incorporation while ensuring crystal compactness (lateral growth rate). This temperature was found to be *around* 450°C (thermocouple reading with the temperature of the silicon oxide removal from the silicon surface at 850°C taken as reference). In figure 5.25 the SEM image, PL and HRXRD spectra are shown for the optimized $In_{0.73}Ga_{0.27}N$ that will be used as template for InN QDs growth.

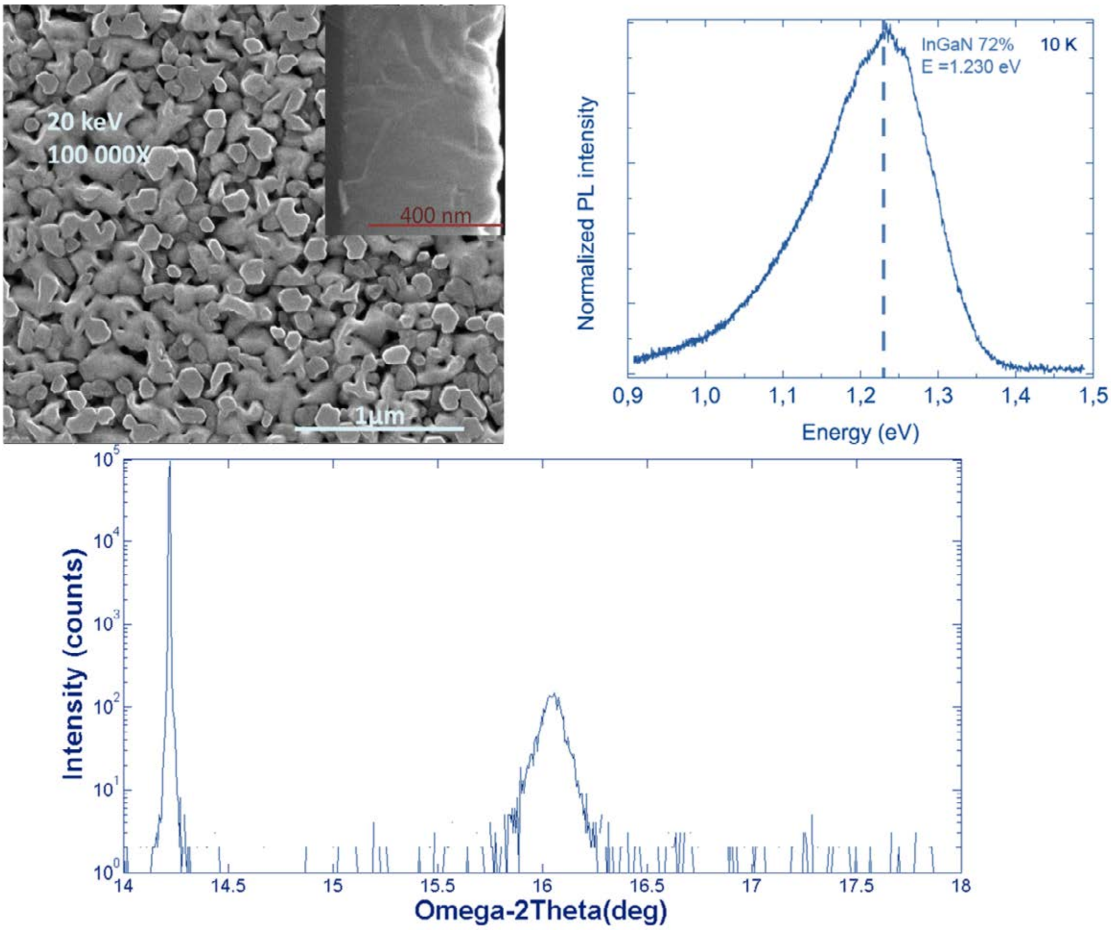

Figure 5.25: Top view SEM image with inset cross-sectional view, PL and HRXRD spectra for an optimized $In_{0.73}Ga_{0.27}N$ layer.

5.6 Spontaneous Formation of an InGaN Nanowall Matrix directly on Si

This section presents the epitaxial growth of an InGaN nanowall matrix (NWM) directly on Si by PA-MBE. Scanning electron microscopy, high-resolution X-ray diffraction, and transmission electron microscopy together with energy-dispersive X-ray analysis infer the crystalline nature of the InGaN NWM, oriented along the C-axis, with In composition ranging from pure GaN to 40%. Photoluminescence is observed up to room temperature, indicating a reasonable optical quality. The NWM is highly in-plane electrically conductive.

As shown in section 5.3 the growth of compact InGaN layers on Si without buffer layers by PA-MBE was achieved under variable growth conditions leading to different morphologies and micro/nanostructured layers. Under nitrogen-rich conditions, just below the onset of nanocolumnar regime, InGaN nanowall matrices (*NWM)* are formed [Kumar 2013]. *NWMs* are of particular interest, as they represent a laterally connected structure supporting in-plane electrical conduction together with a high surface area. They might therefore be of importance for applications such as sensors or the spontaneous surface texturing enabling enhanced light extraction and light trapping to improve light emitting diodes and solar cells [Maeng 2009, Yu L. 2012]. GaN and ZnO nanowall networks have been already reported [Maeng 2009, Yu L. 2012], though the use of InGaN alloys on Si substrates provides much more flexibility for device designs.

In this section a detailed analysis of the structural, chemical, optical, and electrical properties of InGaN NWMs is presented. Scanning electron microscopy (SEM), high-resolution X-ray diffraction (HRXRD), and transmission electron microscopy (TEM) together with energy-dispersive X-ray (EDX) analysis reveal the structure and crystalline nature of the InGaN NMW, oriented along the C-axis, with nanoscale varying In composition up to 40%. Photoluminescence (PL) is observed up to room temperature, indicating a reasonable optical quality. Current-voltage (I-V) measurements reveal that NWMs are highly in-plane electrically conductive.

The InGaN NWM has been grown on a Si (111) substrate by PA-MBE a 1¨ p-type Si(111) substrate and same surface cleaning and nitridation process as in previous presented growth was performed. The growth temperature was set to 480°C for InGaN growth[9]. The In,

---

[9] Also here temperature was corrected with respect to values presented in [Soto 2013b]

Ga, and N_2 fluxes were 1.5 nm/min (8.1×10^{13} atoms/cm^{2}s), 6.0 nm/min (4.4×10^{14} atoms/cm^{2}s) and 9.8 nm/min (7.2×10^{14} atoms/cm^{2}s), respectively, with an InGaN growth rate of 0.45 μm/h.

The surface morphology was investigated by SEM using a FEI inspect F50 microscope. The crystal structure and composition were assessed by HRXRD, selected-area electron diffraction (SAED), and EDX spectroscopy using a 5x5 nm^2 point scanning TEM (STEM) probe. The cross section and InGaN/Si interface were studied by conventional TEM (CTEM), high angle annular dark field (HAADF) imaging and high-resolution TEM (HRTEM) performed in JEOL 1200EX and JEOL-FEG 2011 microscopes. For TEM the samples were thinned to electron-transparency by mechanical grinding, polishing, and ion milling at 3 KeV with GATAN's low voltage precision ion polish system. For PL measurements a He-Cd laser with peak emission wavelength of 325 nm and excitation power of 23 mW was used as excitation source. The PL signal was dispersed by a 1-meter double monochromator and detected by a photomultiplier tube (PMT). I-V measurements were performed with a parameter analyser at room temperature. Figure 5.26 shows the top-view SEM image of the InGaN NWM. The nanowalls follow the hexagonal symmetry of the wurtzite crystal structure with main growth direction along the c-axis. Their average height is of several tens of nm and the spacing between nanowalls is in the 50 to 200 nm range.

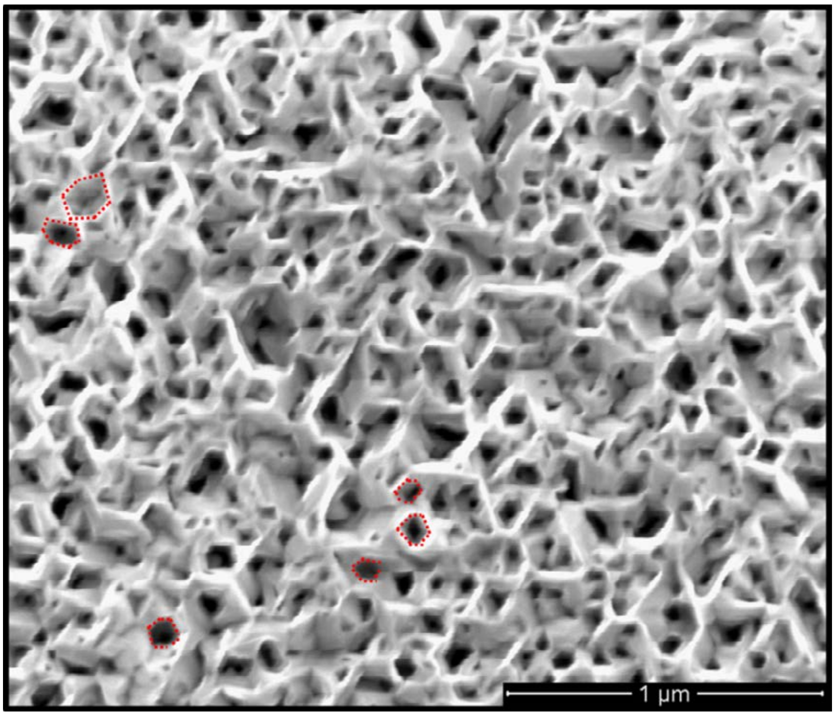

Figure 5.26: SEM top view. The red dotted lines show the hexagonal symmetry.

Figure 5.27 shows the HRXRD ω-2θ scan performed on an InGaN NWM. As seen from the SEM image in figure 5.26 a number of different crystallographic planes are present and as described in the previous section preferential In incorporation will cause a variation in observed In composition from HRXRD. Indeed, the HRXRD spectrum is very broad, and considering the film to be relaxed the In compositions can be estimated form the HRXRD ω-2θ scan with composition peaks corresponding to 1.2% and 33% indium. The selectivity for the incorporation of In due to reduced In-incorporation on the slow growing sidewalls leads to In composition fluctuations as indicated in the schematic drawing in the inset of figure 5.27. The SAED patterns such as the one shown in the inset establish the crystallographic relation being: [111]Si/[0001] InGaN along the growth direction, and $\left[1\bar{1}\bar{2}\right]Si\left[01\bar{1}0\right]InGaN$ and $\left[011\right]Si\left[2\bar{1}\bar{1}0\right]InGaN$ along the basal directions.

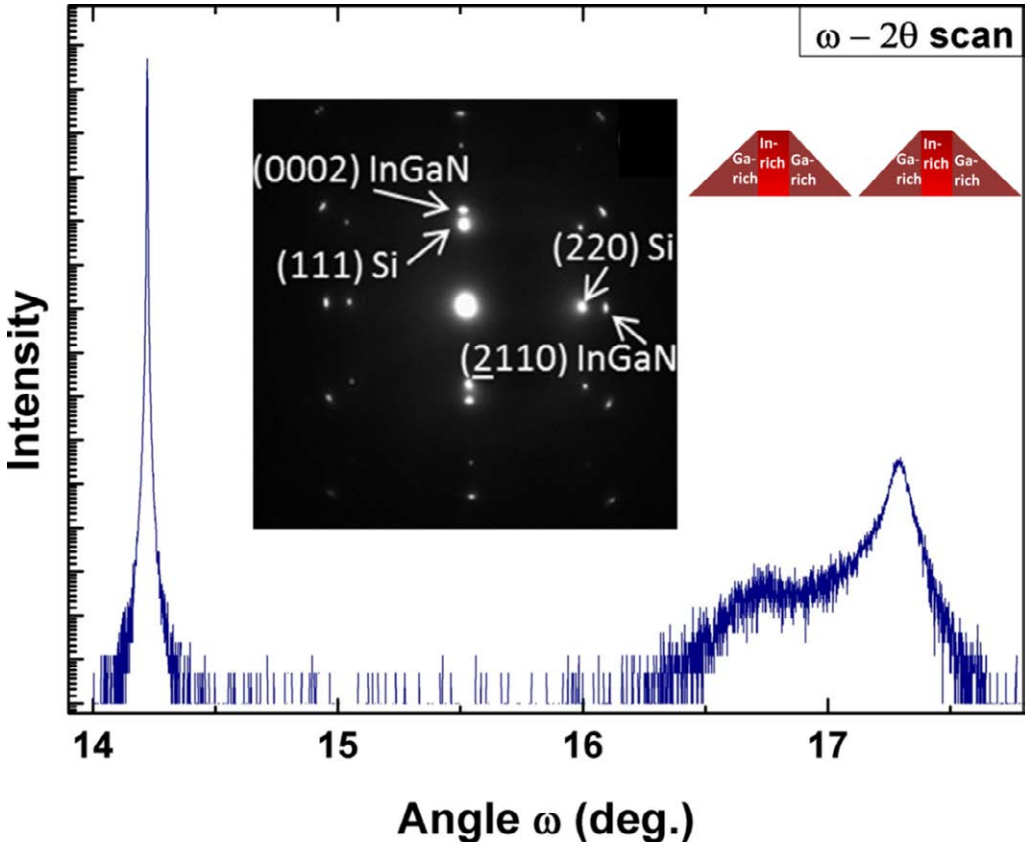

Figure 5.27: HRXRD ω-2θ scan in the vicinity of the (0002) Bragg reflection. Insets: SAED pattern viewed along the [110] and schematic drawing of the nanowalls with fluctuating In composition.

Figure 5.28 (a) shows cross-sectional TEM HAADF images that reveal an initial compact layer about 260 nm thick above which the NWM starts. The pronounced brightness fluctuations observed indicate strong fluctuations of In composition, since the brightness in the image is proportional to almost Z^2, where Z is the effective mass number of the material (more detail in chapter 3). However, the brightness in the image also depends on the thickness of the sample. This might explain the overall different contrast of the NWM compared to the compact lower layer since the NWMs are much thinner. This makes it difficult to determine the In fluctuations along the nanowalls.

The quantitative chemical analysis by EDX, on the for TEM prepared sample at different spots following the schematic drawing at the inset of figure 5.27, demonstrates that the In composition varies between 1% and 40% with a mean value of 16%, in agreement with the HRXRD measurements which measures the average composition. The typical length scale of the In composition variations, in terms of energy variation is around 50 nm. EDX also indicates that the darkest spots in the HAADF image are voids which might originate from the coalescence of nanowalls during growth, also reported in GaN NWMs [Zhong 2012]. The interface between the Si substrate and the InGaN layer (SiNx interlayer) appears sharp and very regular over the length of the sample indicating that the nitridation of the Si substrate is homogeneous along the maeasured TEM length scale. This would confirm an optimized nitridation process, in similar fashion as was first introduced and developed to grow GaN on Si by other groups[Nakada 1998, Kumar 2012]. Information about the atomic-scale structure of the Si/SiNx/InGaN interfaces is provided by HRTEM, shown in figure 4.23 (b). Also at atomic scale all interfaces are relatively smooth in the observed range by TEM. The SiNx layer appears to be non crystalline (amorphous or polycrystalline) with a thickness of about 2.5 nm. Still, above, the InGaN layer is clearly single crystalline with well visible lattice planes which, maintaining thus the epitaxial relation. The reason why an epitaxial relationship still holds is unclear and currently still subject of investigation.

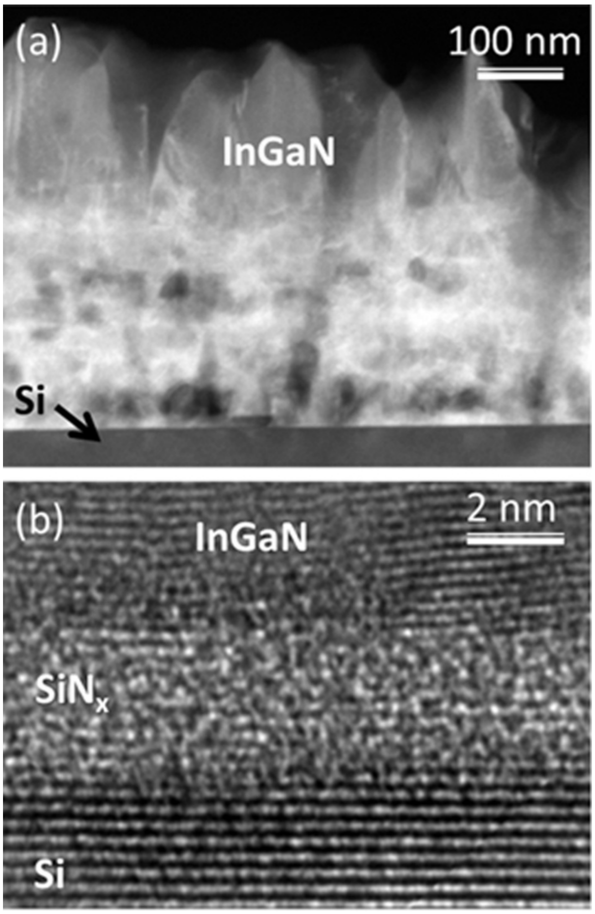

Figure 5.28: (a) TEM HAADF image and (b) HRTEM image of the InGaN/SiNx/Si.

PL emission is observed at room temperature, as shown in figure 4.29 (a). The spectrum is composed of two relatively narrow peaks in the short-wavelength range at 368 (3.37 eV) and 420 nm (2.95 eV), and one broad peak at longer wavelength of 797 nm (1.56 eV). The peak at 368 nm and the one at 420 nm is tentatively attributed to InGaN with low In composition (around 1% and 8%) [Reshchikov 2005] and GaN related emission cannot be ruled out. The peak at 797 nm most likely corresponds to InGaN with the high In composition of 41% (again assuming or measuring that the whole structure is relaxed). These composition values are inferred using an energy band bowing parameter of 3.067 eV, obtained from previous calibrations realized on structure grown on GaN templates [Soto 2013a] (notice that this bowing parameter was the only reference available during the initial investigation prior to optimized layers). These In compositions are in agreement with results from HRXRD and EDX measurements. The PL from the high-In-composition InGaN region is relatively weak, indicating the presence of defects acting as non-radiative recombination centres.

Important for electrochemical applications where the surface is in contact with the electrolyte is the high in-plane electrical conductivity of the InGaN layer. Figure 5.29 (b) shows the I-V curve measured with two Al top contacts, half a millimetre apart. The behaviour is perfectly ohmic with a low resistivity. This is related to a high intrinsic n-type electrical conductivity, commonly observed for high-In-composition InGaN (see chapter 2 for more info) and confirms the electrical connectivity of the nanowall matrix structure (connectivity clearly seen from SEM images). In a similar fashion as metal deposition on nanowires, shadow effect by metal deposition at a small angle would allow metal to be on the surface without penetrating towards the substrate. Even if it would, it would not be detrimental for the envisaged applications as the substrate (Si(111)) is not electrochemically active at the forseen operating conditions for InGaN fact tested before each electrochemical measurement.

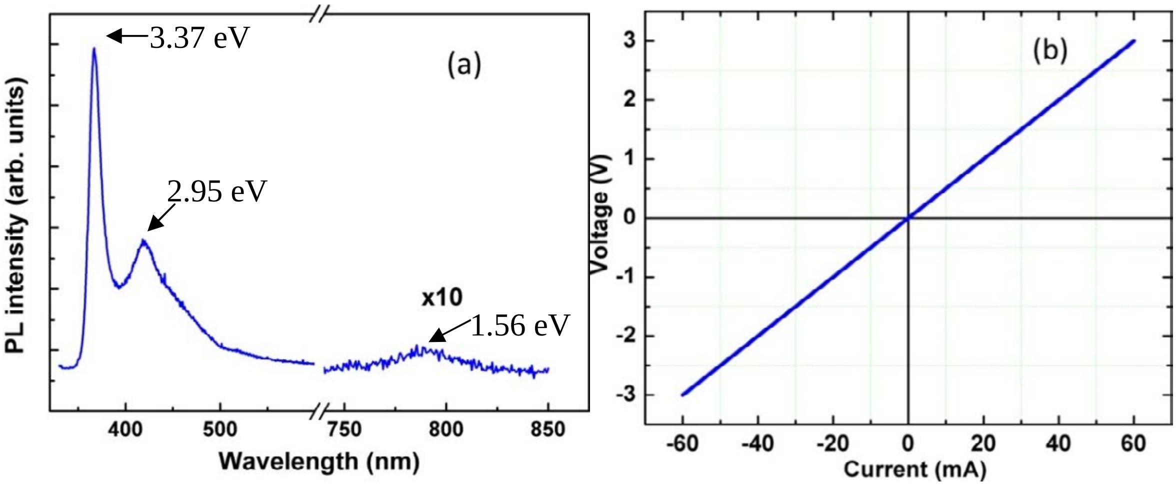

Figure 5.29: (a) RT PL spectrum and (b) I-V curve measured between two Al top contacts at room temperature.

In summary, a detailed study of the structural, chemical, optical, and electrical properties of an InGaN NWM structure grown directly on Si by PA-MBE was presented. Scanning electron microscopy, high-resolution X-ray diffraction, and transmission electron microscopy together with energy-dispersive X-ray analysis revealed the crystalline nature of the InGaN NWM, oriented along the c-axis. The preferential In incorporation by the different crystallographic planes present In composition variations low In-content InGaN (1%, 8 %) up to 40%. The NWM exhibits a high in-plane electrical conductivity, confirming its connectivity, which is important for applications such as sensors and for spontaneous surface texturing to improve the performance of light-emitting diodes and solar cells.

For the electrochemical measurements higher In content InGaN is of interest to compare with the high In-content InGaN film. The presence of the diverse crystallographic planes will allow studying the influence of the electrochemical activity of these planes. Therefore, as it was done with the InGaN layers (samples A to D), optimization aiming at higher In incorporation was realized by varying both the substrate temperature and V/III ratio several samples were grown and the best obtained in terms of highest PL was the $In_{0.6}Ga_{0.4}N$ NWMs. For this sample the growth temperature was set to 485°C and the In metal flux was increased to 14.4×10^{13} atoms s^{-1} cm^{-2}. The corresponding SEM image and LT PL is presented in figure 5.30. This sample is included in the final electrochemical characterization presented in chapter 6.

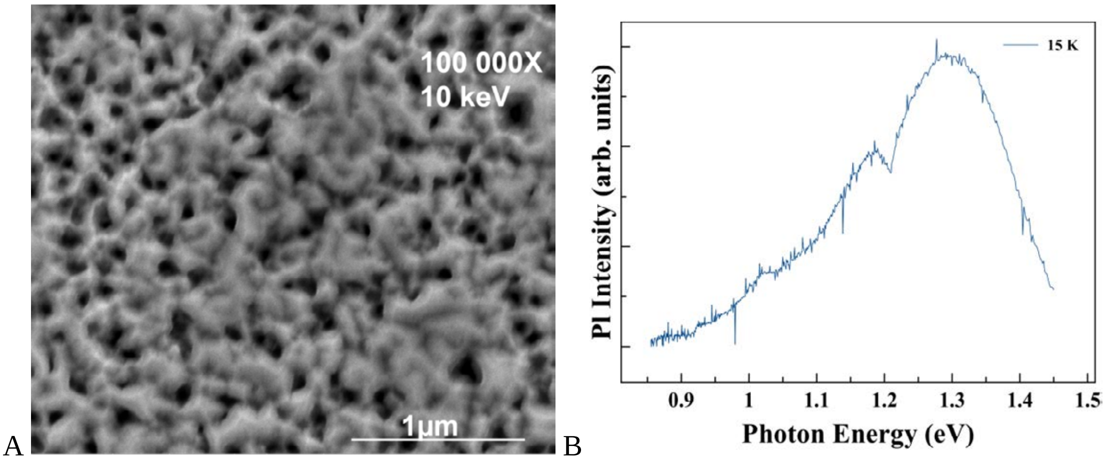

Figure 5.30: (a) SEM image and (b) PL spectrum taken at 15K of an optimized $In_{0.6}Ga_{0.4}N$ NWM.

5.7 InGaN NCs Grown on Nitrided p-type Si(111) Substrates

In order to analyze the electrochemical activity of m-planes, InGaN NCs are grown. The NCs free surfaces are characterized by free m- and c-planes. This will complete the set of different nanostructures (together with the NWMs and films) to analyze the influences of III-nitride crystallographic planes on the electrochemical activity. For this we need to obtain high In-content (close to the optimized NWM) InGaN NCs therefore best self assembled NCs will be sought. Again for this several samples were grown and first the low In- content InGaN NCs will be presented as they were obtained in the first growth series while studying the morphology changes.

It is well established that III-nitrides nanocolumnar self-assembled growth is promoted under N-rich conditions which can be reached by either increasing active nitrogen flux or increasing growth temperature aiming at reducing the actual metal flux by desorption (case of GaN). This last way may also help in In(Ga)N nanocolumns (NCs) though here the process is more complex due to the higher In desorption temperature as compared to the InN decomposition one (mushroom like geometries [Ristic 2008]), InN NCs [Grandal 2009].

Self-assembled InGaN NCs growth was performed by PA-MBE on a 1¨ p-type Si(111) Same cleaning and nitridation procedure as in previous presented growth was performed.The growth temperature was set to 580°C (above InN decomposition and at desorption onset) for sample S1 and 530°C for sample S2. The metal Ga flux was fixed at 4.41×10^{14} atoms s^{-1} cm^{-2}, while the In flux was 1.5×10^{14} atoms s^{-1} cm^{-2} for S1 and 3.1×10^{13} atoms s^{-1} cm^{-2} for S2. That is, sample S2 was grown at lower temperature and lower In flux.

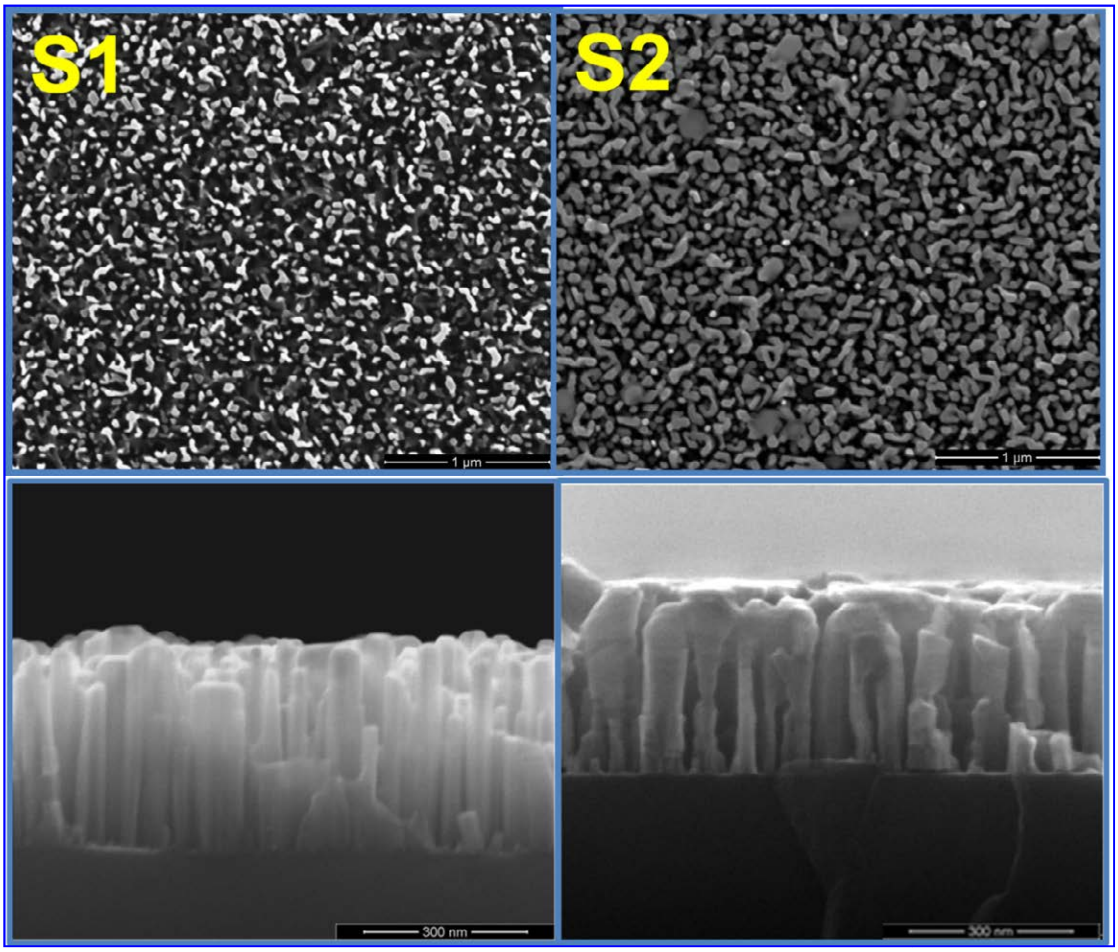

Figure 5.31: Top and cross-sectional FE-SEM images of samples S1 and S2.

Figure 5.31 presents top and cross-sectional views of SEM images that clearly show the self assembled regime and the typical coalescence of various individual NCs, more notorious in sample S2 due to a lower grow temperature (means more metal). The NCs average diameter and density were estimated to be of calculated to be 38 nm, 1.3×10^{-6} NCs /cm^2 and 152 nm, 9.8×10^{-7} NCs /cm^2 for samples S1 and S2 respectively.

HRXRD conventional ω-2 ϑ spectra (with fixed slit ½" and 2 mm mask) were recorded in the vicinity of the Si(111) Bragg reflection to compare crystalline quality (figure 5.32). Considering the obtained NCs to be relaxed, the ω-2ϑ spectra measured for S1 shows low-In composition with the peak centered at ω=17.27^o being equivalent to a 2.4% In composition. The FWHM for S1 is found to be 0.045^o indicating a good structural quality. On the other hand S2 shows a main peak at ω=17.202^o representing a 6.25% In composition. The FWHM for S2 is about 0.1239^o which is consistent with the much larger coalescence in this sample (disorder and defects created upon coalescence). Moreover, the peak for low In composition is more intense for sample S1 indicating higher crystalline quality.

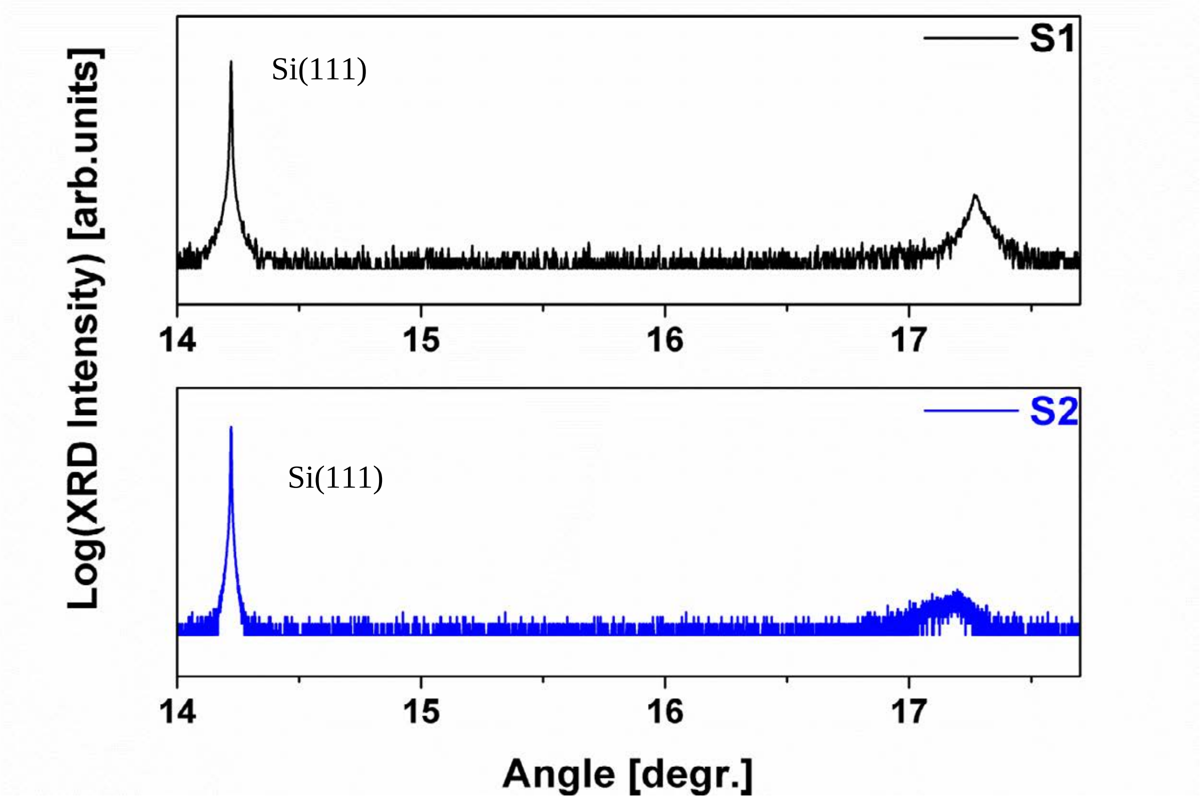

Figure 5.32: HRXRD w-2theta measurements in the vicinity of Si(111) plane for both S1 and S2 samples.

Although it might seem contradictory, that reduced In flux for S2 leads to a higher In incorporation it is the higher growth temperature (580^{o}C) used for S1 at which it is assumed that In desorption is active and that it is responsible for the lower In incorporation of S1 compared to S2. This as sample S2 was grown at 530^{o}C at which In desorption is much lower, thus leading to a higher In incorporation.

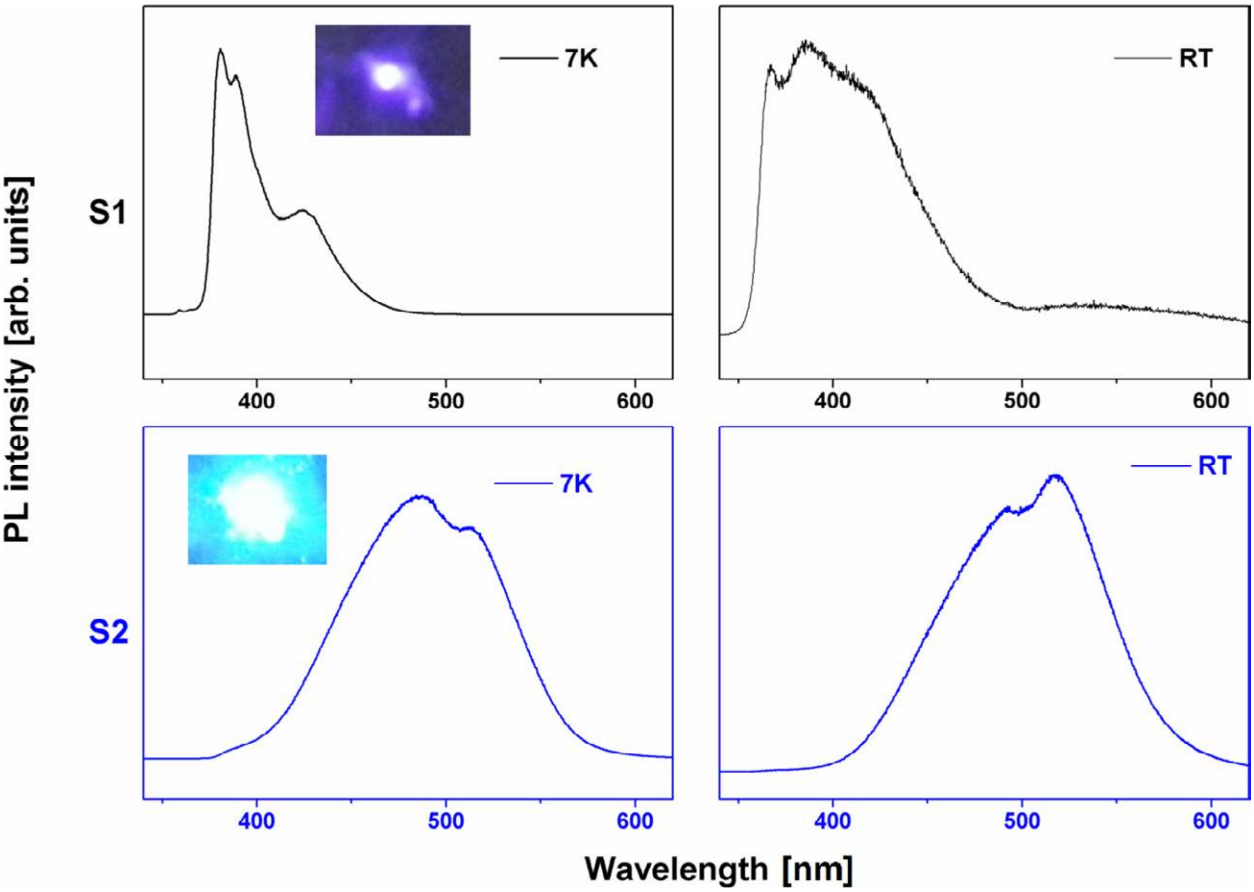

Figure 5.33: PL measurements for both sample S1 (top) and S2 (bottom). Both x, y axes are displayed in linear scales.

PL measurements were performed on both samples to determine optical performance. Figure 4.33 shows LT and RT-PL spectra where S1 shows sharp peaks close to the band edge of GaN, typical of a good quality specimen, as expected from a quite small Indium content InGaN layer. At RT the highest peak corresponds to 3.7% of In composition, with the shoulder peak maximum if due to In compostion would gives around 7.5% of In composition. The discrepancy in value compared to HRXRD, although small, is most likely due the fact that PL measures only lower energies and strongly depends on the different recombination mehchanisms (see chapter 2 for more detail) as HRXRD takes into account complete lattice considering only the lattice parameter and strain (as explained in chapter 3) its result is more general and representative. In sample S2 PL spectra, both at LT and RT, are representative of a significantly higher In composition InGaN layer. The spectrum is much broader which could be due to the higher variation in coalesced NCs similar effect to emission from varying NCs sizes. At RT, two clear peaks are seen. The two peaks could correspond to In composition of 17.9 % and 21.1% or the emission might come from radiative defects generated by the coalescence of the NCs; in addition a probable combination of both InGaN and defect emission is plausible being the later more probable. Therefore it is desired to avoid the coalescence and so the best conditions for higher In incorporation are probed.

By reducing the substrate temperature for higher In incorporation (400^{o}C) and increasing further In flux compared to S2 (In flux 11.5×10^{13} atoms s^{-1} cm^{-2} and Ga flux 5.66×10^{13} atoms s^{-1} cm^{-2}), IR emitting NCs were obtained. Specifically, the one used in this thesis for electrochemical characterization has 67% In-content and presenting main PL peak at 1.04eV, as shown in figures 5.34 and 5.35 where both a FE-SEM image and RT-PL are presented. The PL peak is still broad but here not due to the coalescence, as from the FE-SEM image clearly separated NCS are seen, but most likely due to the variation in self assembled NCs sizes.

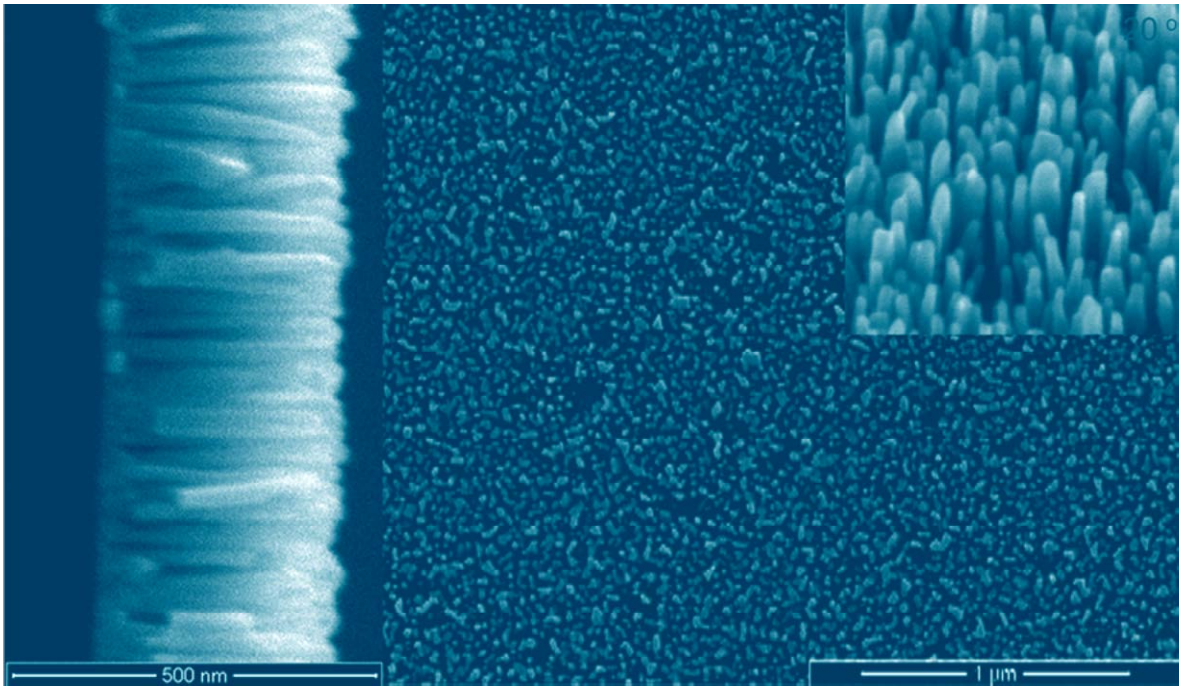

Figure 5.34: FE-SEM images both cross-sectional (at 300 000X, 5 keV) and plain view (at 100 000X, 20keV) of an optimized $In_{0.67}Ga_{0.33}N$ NCs sample. The inset shows a tilted image under a 20 degree angle (at 300.000X, 10 keV).

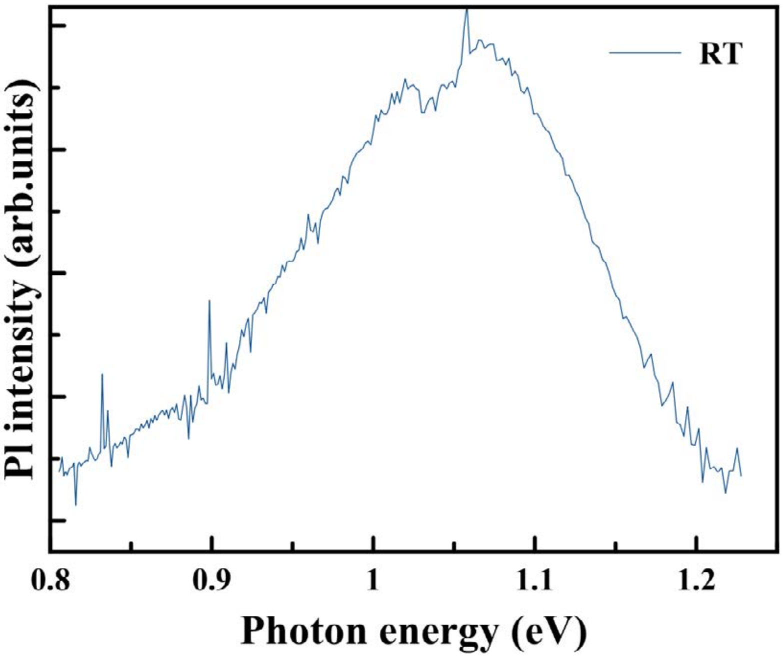

Figure 5.35: PL spectrum at RT of the optimized $In_{0.67}Ga_{0.33}N$ NCs sample.

5.8 Stranski-Krastanov InN QDs grown on InGaN/ p-type Si(111)

This section addresses the growth of InN QDs on high In-content InGaN layers grown directly on Si(111) substrates. The aim is to avoid the use of insulating buffers, like AlN, which electrically isolate the grown layers from the substrate. The choice of Si substrates will allow, in addition, a direct integration with Si technology. Furthermore, for electrochemical applications InN QDs are expected to present a catalytic impact and therefore the obtained knowledge for growth on the High In-content InGaN layers will be transferred to the high In-content NWM.

In the pursuit of high performance green LEDs, InGaN QDs have been grown on both c- and m-plane GaN [Park 2011, Yang 2012], and by selective area epitaxy applying di-block[10] copolymer lithography [Liu G. 2011]. InGaN QDs on GaN have been obtained by both molecular beam epitaxy (MBE) and metal organic vapor phase epitaxy (MOVPE) by

---

[10] Block copolymers (BCPs) are macromolecular materials comprised of two or more chemically different polymeric segments. As a result of their segmented structures BCPs have a propensity to phase-separate and order themselves into a range of complex morphologies on the nanoscale. By changing the temperature the ordering can be controlled and a posterior etching can transfer the ordered morphology to underlying template.

either direct island formation (Volmer-Weber, VW growth mode) or wetting layer followed by island formation (Stranski-Krastanov, SK growth mode) [Damilano 1999, Adelmann 2000, Kruse 2012, Zhao 2012].

Near-infrared PL emission was reported for InN QDs on GaN with size dependent peak energy, blue shifting from 0.78 to 1.07 eV when the QD height was reduced from 32.4 to 6.5 nm [Ke 2006], as discussed in chapter 2. In addition, in section 5.2, the growth conditions for InN QDs on high-In-content InGaN layers by PA-MBE, with good optical properties, have been discussed. As for most of previous studies, these QD structures were grown on GaN templates. This limits device design flexibility due to the insulating behaviour of sapphire. Hence, the direct growth on Si substrates is the ultimate goal, allowing for novel device designs, such as InGaN/Si tandem solar cells and vertical contact schemes at much lower cost and for the direct integration with existing Si technology. Along this line, the growth of thick and uniform high-In-content InGaN layers on Si was shown (section 5.3) producing films with micron-sized atomically flat In-rich regions [Kumar 2013] and more recently by reduction of growth temperature undulated, chemically uniform InGaN layers [Aseev 2013] with high optical quality were obtained.

This section will deal with the growth of InN surface QDs (SQDs) on the above mentioned optimized $In_{0.73}Ga_{0.27}N$ layers (section 5.3) grown directly on Si(111) by PA-MBE. AFM and TEM data reveal uniformly distributed SQDs with diameters ranging from 10 to 40 nm and a relatively low density of $\sim 7\times10^{9}$ cm^{-2}. Therefore, due to the smaller size and in consequence stronger confinement any detected emission originated from SQDs would be expected to be blueshifted compared to results from Ke et al. [Ke 2006]. AFM measurements also show SQD heights of 2-4 nm. The formation of a thin (0.9 nm) and uniform two-dimensional InN wetting layer proves the SK growth mode. Near-field scanning optical microscopy (NSOM) measurements show spatially uniform emission from the InGaN layer and a distinct and spatially well localized emission from single SQDs in the near-infrared.

All samples were grown in a PA-MBE on a 1¨ Si(111) wafers. The substrate was previously cleaned and intentionally nitrided following the method introduced in previous growth. Growth temperature was set to 450°C for InGaN growth with the Ga, In, and active N_2 fluxes of 8.1×10^{13}, 4.4×10^{14}, and 7.2×10^{14} atoms/cm^{2}s, respectively. The growth time was one hour resulting in a 450 nm thick and compact InGaN layer. For the InN SQDs growth, the same In and N fluxes were maintained and no growth interruption was considered. The growth time for the SQDs was 10 seconds (~3 monolayers). Notice that this growth rate is on the higher limit used for arsenide systems (0.3 ML/s compared to 0.15ML/s as is used for InAs QDs on thin GaAs by for example by J.X.Chen et al. [Chen J. 2002], where they explicitly show thath low growth rate gives low density QDs whereas high growth rates gives small sized QDs with a large density. The growth rate employed was close to the one used by J. Brown et al [Brown 2004].

The SQDs surface morphology was investigated by AFM in tapping mode in air. For the TEM investigations the samples were prepared in cross-sectional orientations and thinned to electron transparency by mechanical grinding, polishing, and ion milling at 3 keV with a Gatan low-voltage precision ion polishing system. The high-resolution TEM (HRTEM) results were collected in a JEOL2010 FEG microscope operated at 20 keV. The optical properties were studied using a home built low-temperature NSOM operating at 10K inside a high vacuum chamber, described in detail elsewhere [Behme 1997]. The sample was excited by a 543-nm He–Ne laser. The laser light was coupled into an uncoated, single mode near-field fiber probe from Nanonics resulting in a laser power in the fiber of 3.9 µW. The PL from the sample was collected through the same fiber, providing a spatial resolution of about 150 nm [Intonti 2001]. The signal was dispersed in an imaging monochromator and recorded with a liquid-nitrogen-cooled InGaAs (OMA V) detector.

Figure 5.36(a) shows a 1x1 μm^2 AFM image of the InGaN and SQDs surface morphology. The InGaN surface comprises 100-200 nm wide plateaus where uniformly distributed InN SQDs were grown. The development of these plateaus, ideally suited for QD formation, proceeds just at the onset of the columnar regime that fully dominates at higher active nitrogen fluxes, though the present InGaN layer is still compact. A three-dimensional AFM image with enlarged magnification of one of the plateaus with a single SQD on top is presented in figure 5.36 (b). The corresponding AFM line scan across the InN SQD is depicted in figure 5.36 (c). By averaging over line scans recorded on a large number of different individual SQDs, SQD diameters ranging from 10 to 40 nm and heights of 2-4 nm can be estimated. The average density of the SQDs, deduced from AFM, is 7×10^9 QDs cm^{-2}.

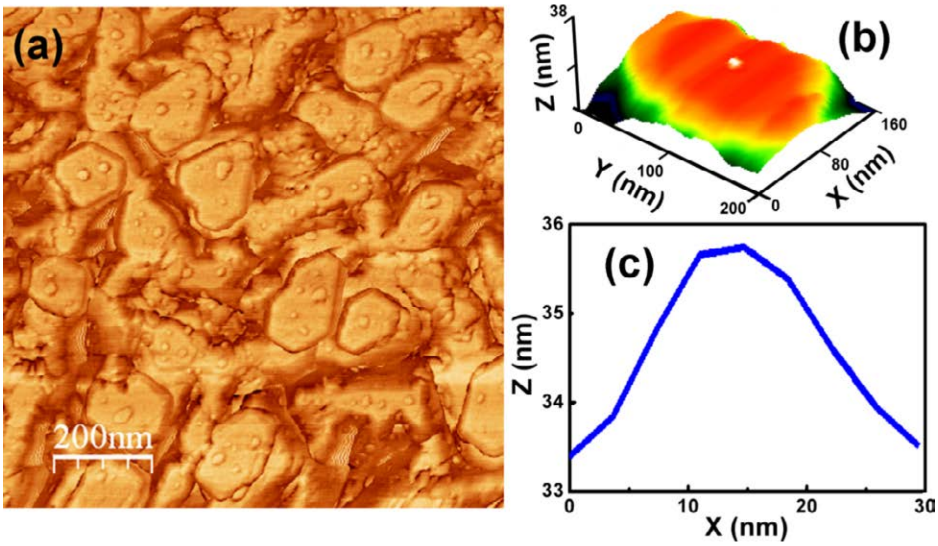

Figure 5.36: (a) 1 µm × 1 µm AFM image of the InN SQD/$In_{0.73}Ga_{0.27}N$ layer sample surface. (b) Three-dimensional AFM image with enlarged magnification. (c) AFM line scan across the SQD.

A detailed atomic-scale structural analysis is provided by the cross-sectional HRTEM image of a single SQD, shown in figure 5.37. The SQD, indicated by the blue line is 3 nm high and has a base width of 10 nm. The continuous two-dimensional InN wetting layer underneath the QD, indicated by the red lines, is about 0.9 nm thick. The observed crystal structure of the wetting layer indicates it to be cubic, whereas the crystal structure of the InGaN layer and lower SQD portion is clearly hexagonal or, in the SQD case, a mixture of cubic and hexagonal phases. This implies a change of the stacking sequence upon initiation of the InN growth, while the successive relaxation by SQDs formation results in the introduction of stacking faults, i.e., a mixing of the initial hexagonal structure of the InGaN layer and the cubic structure of the thin InN wetting layer. The origin of the observed cubic structure for the InN wetting layer is not clear, possible causes might be related to the abrupt increase of the group V/III flux ratio when switching to InN growth (closing of the Ga shutter) [Zhang 2007] or the high compressive strain in the InN layer as a Polarity change or an initial stacking fault at this growth phase (due to the wetting layer small dimension it is difficult to determine). Although oxidation of InN is seen to occur in a two step process with an intermediate step where amorphous In_2O_3 is formed [Sarantopoulou 2006]. Recent investigations of long-term oxidization of hcp-InN lattices grown on GaN/sapphire substrates indicate a phase transformation of hcp-InN to an alloy phase of fcc-InN (InN Zb) and fcc-In_2O_3, (InN-Zb/In_2O_3), after exposing the films for 36 months at ambient conditions [González 2009]. Altough this process could explain observed results, it is an extremely slow process and as the sample was characterized in much shorter period of time it seems a less possible reason.

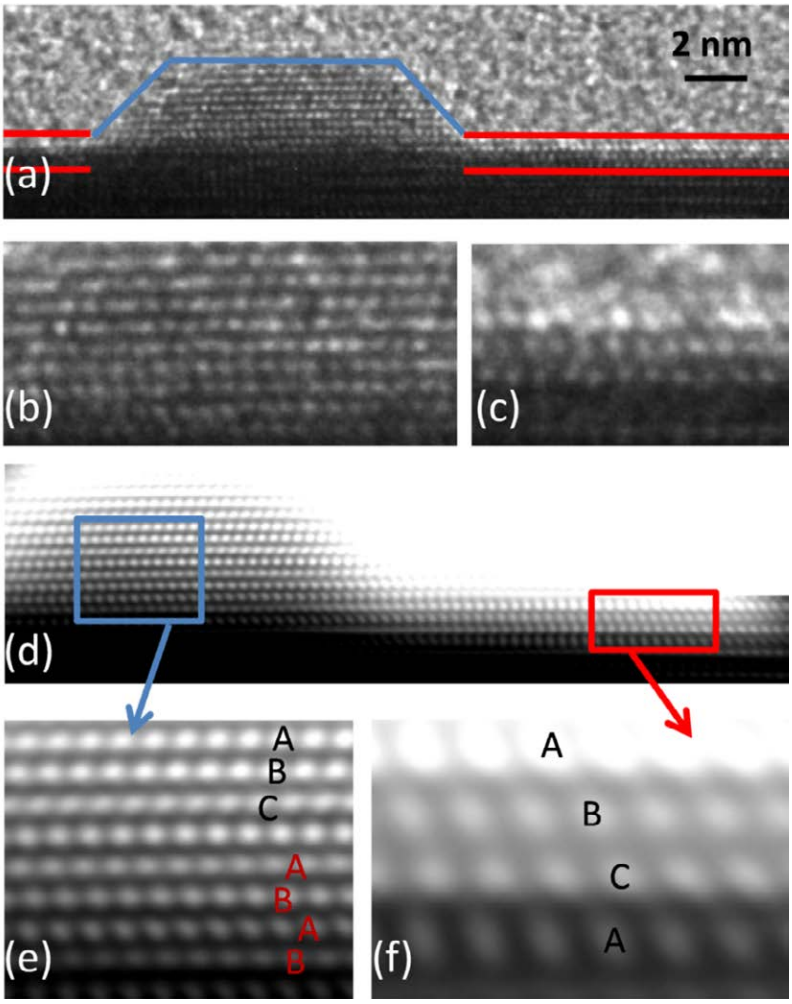

Figure 5.37: HRTEM image of an InN SQD/$In_{0.73}Ga_{0.27}N$ layer directly grown on Si(111) taken along the (11-20**)**

Pointing out the SK growth mode as the most probable growth mode, the formation of a wetting layer in the SK mode can be attributed to the moderate lattice mismatch of the InN/ $In_{0.73}Ga_{0.27}N$ heterostructure, quite close to the InAs/GaAs system, which is the most widely studied SK model system. An even lower lattice mismatch easily results in an undulated surface instead of QDs nucleation, while larger lattice mismatch favors the VW growth mode.

Figure 5.38 (a) shows a PL spectrum obtained by the SNOM set-up and taken at an arbitrary position of the sample surface. This broad PL spectrum with peak energy at 1.23 eV is due to emission from the InGaN layer, as confirmed by reference spectra of samples without InN SQDs. At selected positions on the sample, the emergence of narrow PL peaks in the energy range from 0.95 to 1.10 eV is observed. These peaks are tentatively attributed to the emission from SQDs. A representative PL spectrum from SQDs is shown in figure 5.33 (b) with a peak width of 15 meV. These assignments SQD emissions are directly confirmed by spatial maps of the PL intensity. It is necessary to highlight that statistical measurements on TEM prepared sample of punctual EDX showed no In/Ga intermixing for the QDs and that the higher confinement compared with the results of Ke et al. [Ke 2006] are in line with observed emission peaks for the SQDs. However as the analyzed QDS is just a small portion of the total density of QDs the possibility of having some InGaN QDs cannot be ruled out 100%.

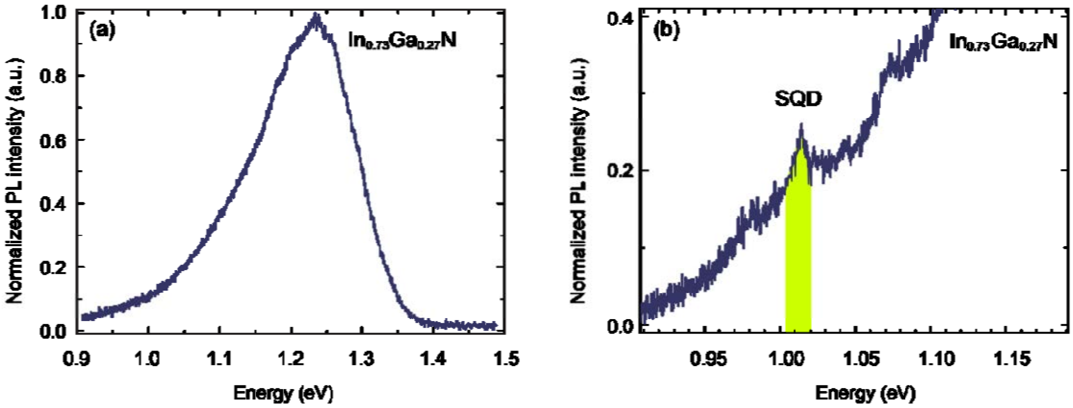

Figure 5.38: (a) Near-field PL spectrum taken at an arbitrarily chosen sample position. (b) Selected near-field PL spectrum showing distinct emission peaks from SQDs on the low energy tail of the InGaN emission. Noticethere are several SQDS emission and the yellow marked is the one presented in measurement presented in text.

In figure 5.39 (a) a spatial map of the PL intensity related to the InGaN layer is shown, tuned at the energy of 1.19 eV, far from the SQDs expected energy range, revealing a spatially uniform emission intensity. The near-field integrated PL intensity map, from 1.00 to 1.08 eV, shown in figure 5.39 (b), reveals several well localized emission spots. The density of optically active (detected) SQDs is smaller than the SQD density deduced from AFM, indicating that not all SQDs are optically active. Also, emission spots may come from a bunch of SQDs. However, the probability that all of them have exactly same size and emit at exactly same energy, is less likely. Instead a bunch of well-defined narrow peaks would show over probed energy range if, coming from a bunch of SQDs. The PL peak presented in figure 5.38 (b) stems from the localized emission center in the area indicated by the white square in figure 5.39 (b). The corresponding near-field PL intensity map of a possible single SQD with enlarged magnification is presented in figure 5.39 (c) for the PL intensity integrated from 1.005 to 1.020 eV (figure 5.38 (b), yellow shadowed area). Evidently, single SQD emission is spatially and spectrally well resolved. The PL peak width for the single SQDs of 15 meV is wider than that of the highest purity single QDs of several μeV. This is typical for SQDs due to the nearby presence of charged surface states. Temporal variations in the charge distribution within these states give rise to fluctuating electric fields in the confined SQDs and thus to a line broadening in continuous wave PL measurements. InN has the highest density of charged surface states among all semiconductors and such line broadening effects are, therefore, particularly pronounced. This is in line with the reported 3-meV peak width for single InAs/GaAs SQDs [Selçuk 2010] and the 9-meV peak width for single InGaN SQDs with 20 – 25% In content [Robinson 2005]. Most useful, this sensitivity of the energy states of SQDs to the charge environment with the highest surface state density for InN SQDs is at the heart for highly sensitive sensing applications.

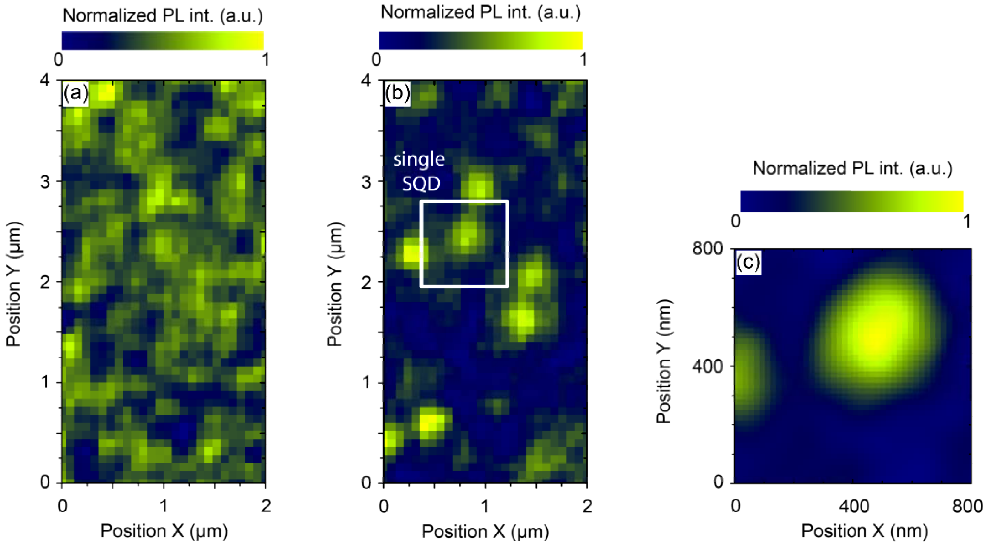

Figure 5.39: Near-field map of the PL intensity acquired at 10 K for: (a) InGaN layer at energy 1.19 eV far from the expected energy range of the SQDs; (b) from, as appears (single maximum peak is observed), an individual SQDs integrated over the energy range of 1.00-1.08 eV, and (c) a most probable single SQD (again because a single maximum can be observed) with enlarged magnification integrated from 1.005-1.020 eV.

In summary, InN SQDs have been grown on high-In-content $In_{0.73}Ga_{0.27}N$ layers previously grown on Si(111) by PA-MBE. AFM and TEM data revealed uniformly distributed SQDs with diameters from 10 to 40 nm, heights from 2 to 4 nm, and a rather low density of $\sim 7\times10^{9}$ cm^{-2}. The SK growth mode was evidenced by the presence of a thin wetting layer below the SQDs. Near-field scanning PL measurements showed uniform emission from the InGaN layer and distinct and spatially well localized emission from single SQDs in the near-infrared spectral range. Such achievements have high potential for telecommunication and highly efficient sensing devices.

For electrochemical applications it is interesting to see the role of InN QDs. Therefore, not only growth of InN QDs on the high In-content film with higher density of c-polar planes is of interest but also on structures exposing non polar planes as is the case for the NWM. For this reason, a similar approach was used to grow InN QDs on top of the optimized NWM structures. After the growth of the NWM at 485^{o}C the temperature was reduced to 450^{o}C and InN was deposited using the same parameters as those for optimized SQDs formation previously mentioned. Due to the NWM complex morphology, it is difficult to characterize these InN QDs by AFM. Instead, a high quality FE-SEM image allows in this case identifying, after careful inspection, features that could represent the InN SQDs. Figure 5.40 shows FE-SEM pictures where some of the mentioned features, observed all over the sample, are indicated by red arrows. The final proof of SQDs formation will be derived from their electrochemical performance, analyzed in section when probing the electrochemical activity of the diverse crystal planes.

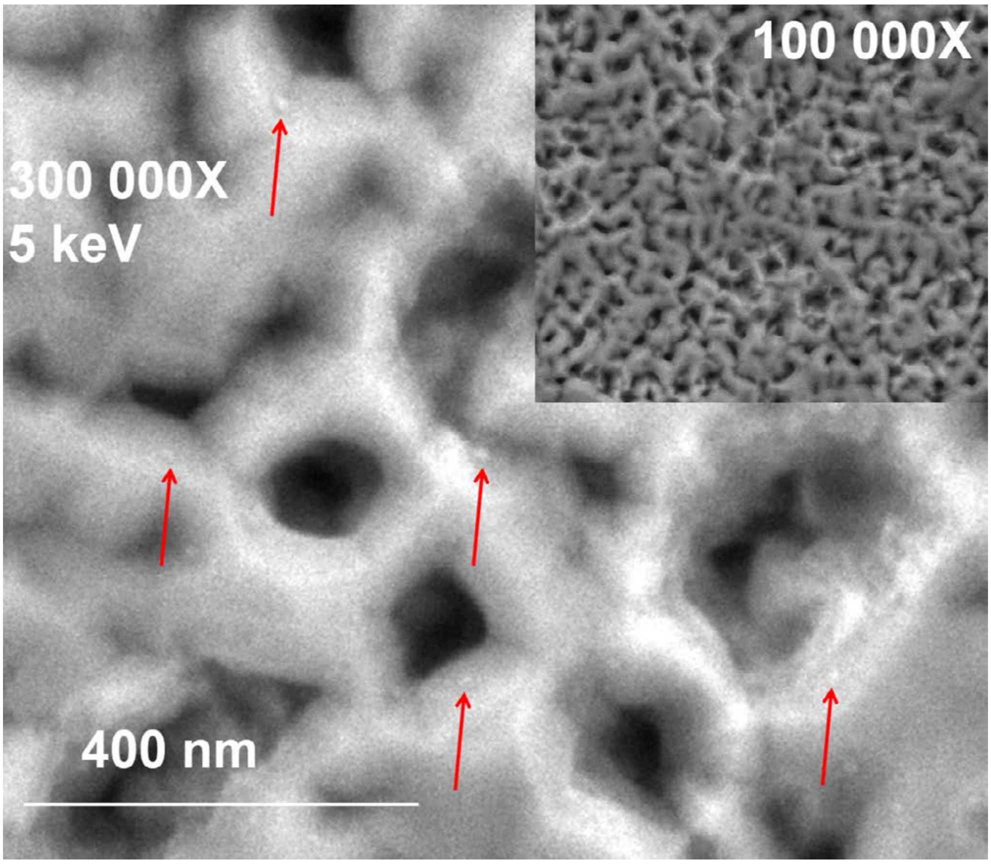

Figure 5.40: FE-SEM image of a NWM structure with features pointed out by the red arrows which could correspond to the InN QDs.

CHAPTER 6

APPLICATIONS

In the following chapter both, water splitting and bio-sensing applications are shown based on selected, optimized structures presented in chapter 5. The main behaviour parameters introduced in chapter 4 are achieved and the device performance is analyzed.

6.1 Applications to Bio-sensing: Glucose and cholesterol biosensors

In this section the selected structures are those presented in section 5.4 which involve high In-content InGaN layers grow on GaN templates. Samples were prepared for potentiometric measurements. The potentiometric measurement technique here is chosen due to the simple 2 –electrode configuration needed and as it has been proven to be suitable for measuring low concentration in tiny sample volumes. Howver, compared to amperometric measurements the observed sensitivity is generally inferior [Grieshaber 2008]. As the high In-content InGaN is anion selective [Alvi2013b] in a similar manner as to InN [Lu2007][Lu2008], good linearity and fast response is expected. Both proof of concept of III-nitride based biosensors for glucose as cholesterol is presented and discussed, but, due to their similar nature in sample preparation and measurements, just one will be explicitly shown with optimized procedure.

The first step in sample preparation is to deposit aluminium (Al) ohmic contacts on the InGaN surface, verifying the ohmic behaviour between top-to-top contacts separated half a millimetre apart with a parametric analyzer. In figure 6.1 the observed ohmic behaviour is presented together with AFM data for sample with (figure 6.1 (a,c)), and without InN QDs (figure 6.1 (b,d)). These contacts are then protected by epoxy to avoid interfering in the potentiometric measurements when immersed in the electrolyte.

In order to measure the analyte of interest, a biological recognition element is needed, being in this case the enzymes glucose oxidase (GODx), for glucose detection, and cholesterol oxidase, for cholesterol detection (ChOx).

The GODx elaboration was done by preparing 10 mg/ml GOD in a phosphate buffer saline (PBS) solution with a pH value of 7.4 and stirring for 24h. The sample was then dipped in 5ml of this solution and dried in air for 2h for electrostatic immobilization. All glucose biosensors were stored at 4ºC in dry conditions when not in use. Different glucose concentration solutions were used, ranging from 1×10^{-5} M to 1×10^{-2} M.

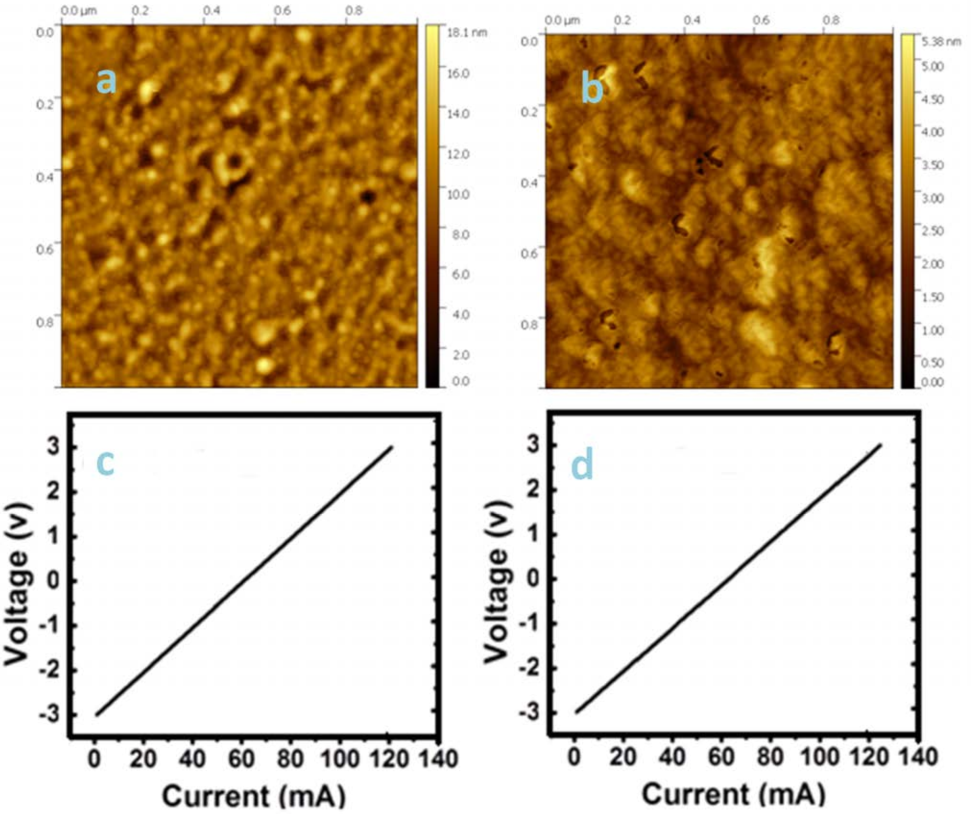

Figure 6.1: 1×1 um^2 AFM image of: (a) InN QDs on InGaN layer grown on a GaN template and (b) the bare InGaN layer. Full height contrast is 10 nm (brightest corresponds to the highest spot); (c, d) the current- voltage curves measured between two top-to top Al contacts. The indicated resistance is the slope of the graph. The high native n-type behaviour of the InGaN layer surface is responsible for the ohmic behaviour.

The chemicals used for the glucose sensing experiment were GOD type GO3A from Aspergillus niger, 360 U/mg (BBI enzymes (UK) Ltd.) where one U is the enzyme activity which oxidizes one µM cholesterol per minute under the essay at room temperature and a pH of 7 and Nafion (5 wt. %), glutaraldehyde (50% solution), bovine serum albumin (BSA98%), and d-(þ)-glucose (99.5%) from Sigma–Aldrich. A phosphate buffered, 10mM solution (PBS) from Na_2HPO_4 and KH_2PO_4 (Sigma–Aldrich) was prepared with sodium chloride having concentration of 0.134mM. The pH value of the PBS solution was adjusted to 7.4.

For biosensor fabrication, the immobilization of the cholesterol oxidase (ChOx) enzyme was carried out electrostatically by dipping the electrodes into 50 µL of enzyme solution for 20 min and then drying in air for 2 h.

For cholesterol sensing the chemicals used were ChOx with a concentration of 25 U/mg from Sigma Aldrich (Stockholm, Sweden). The ChOx stock solution was prepared by dilution with tris–HCl (1×10^{-2} M). Cholesterol powder (Sigma), Triton X-100 (Sigma

Aldrich), and phosphate buffered saline (PBS) tablets (Medicago, Québec, Canada) were used for preparation of the nutrient cholesterol solutions with different concentrations ranging from 1×10^{-6} M to 1×10^{-3} M. As cholesterol powder is insoluble in water, a PBS solution which contained 1% of Triton X-100 was added as solvent (PBST). The cholesterol solution was prepared by dissolving 500 mg of standard cholesterol in isopropanol, Triton X-100 and phosphate buffer (pH of 7.0) by stirring at 65 °C until the solution was clear and colourless. The isopropanol, Triton X-100, phosphate buffer ratio was 10:4:86 by weight.

Before measurements, the above mentioned enzymes were further immobilized on the sample surface and protected to avoid undesired interference with the analytes present in the electrolyte. Protection was done by covering the enzymes with a Nafion membrane (of 0.5% Nafion). The additional immobilization was realized by adding a small amount, 3µl aqueous solution with 2.5% of glutaraldehyde, which interlinks enzymes and immobilize them on the surface.

Figure 6.2 shows a schematic of the cholesterol detection mechanism. The ChOx is in principle a bi-functional catalyst able to oxidize the cholesterol (5-cholesten-3β-ol) attached to the electrode surface to a temporary intermediate 5-cholesten-3-one with the reduction of molecular oxygen to hydrogen peroxide (H_2O_2) and additionally catalyzes the isomerization of the steroid (with a trans A:B ring junction) to 4-cholesten- 3-one, as shown in figure 6.2. This electrochemical reaction is responsible for the charge transfer near the surface of the working- and reference electrodes to produce the electrochemical cell voltage. In the experimental process the enzyme activity is 0.35 UmL^{-1}.

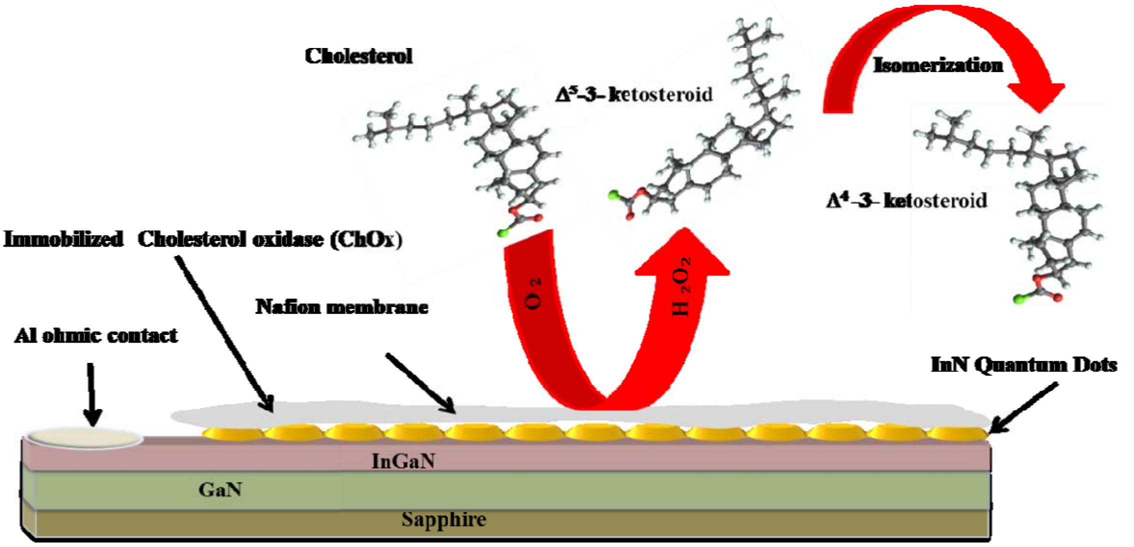

Figure 6.2: Sample preparation for cholesterol detection and sensing mechanism.

The measurement scheme to detect glucose is shown in figure 6.3. The enzyme of choice, the glucose oxidase (GOD), catalyzes the oxidation process of glucose at the anode producing glucose acid. In the process H_2O_2 and β-glucolactone are also produced (the last typically found as food additive with E575code). The working electrode is immersed in a glucose solution and the potential is externally recorded for different glucose concentrations. A silver chloride reference electrode (Ag/AgCl) is added to establish a relative potential to be compared to other biosensors. For cholesterol, sensing and recording process is exactly the same.

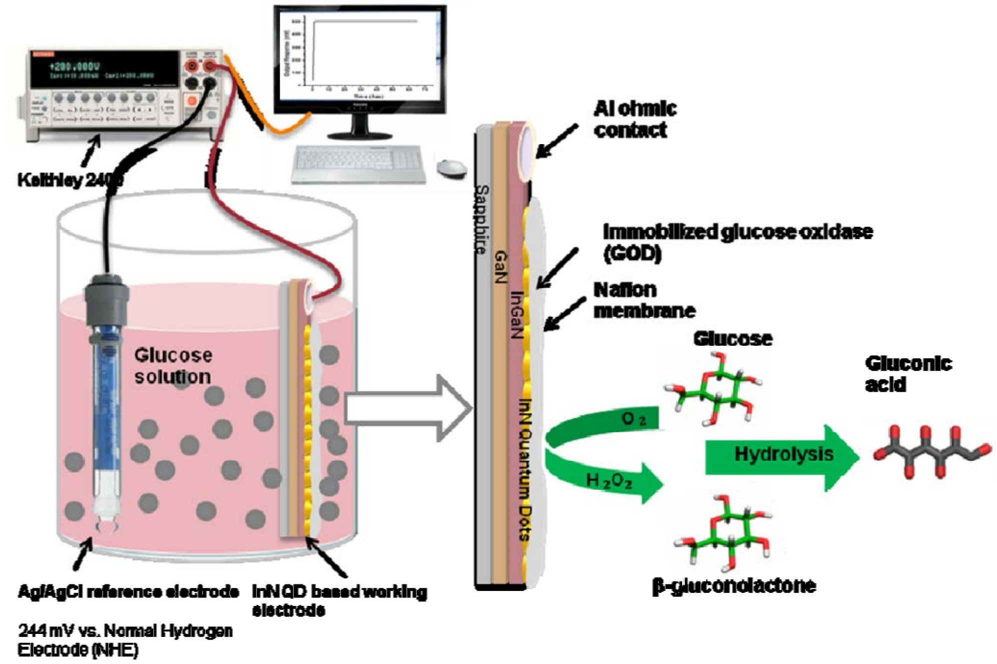

Figure 6.3: Schematic for glucose detection mechanism**.**

The potentiometric measurements were performed using functionalized InN QDs, InN thin films, and InGaN layers as working electrode and a Ag/AgCl reference electrode (Metrohm Nordic, 3MKCl, Bromma, Sweden) and recorded by a computer controlled Keithley 2400 meter (Keithley Instruments, Inc., Cleveland, OH, USA).

As mentioned before, the working electrode was, either bare InGaN or InGaN with 2 ML and 3 ML InN coverage producing QDs. Their 1x1 μm^2 AFM images are shown in figure 6.4 (a-c) and a schematic drawing of the complete structure in figure 6.4 (d). The maximum height contrast corresponding to the brightest spot is 5 nm.

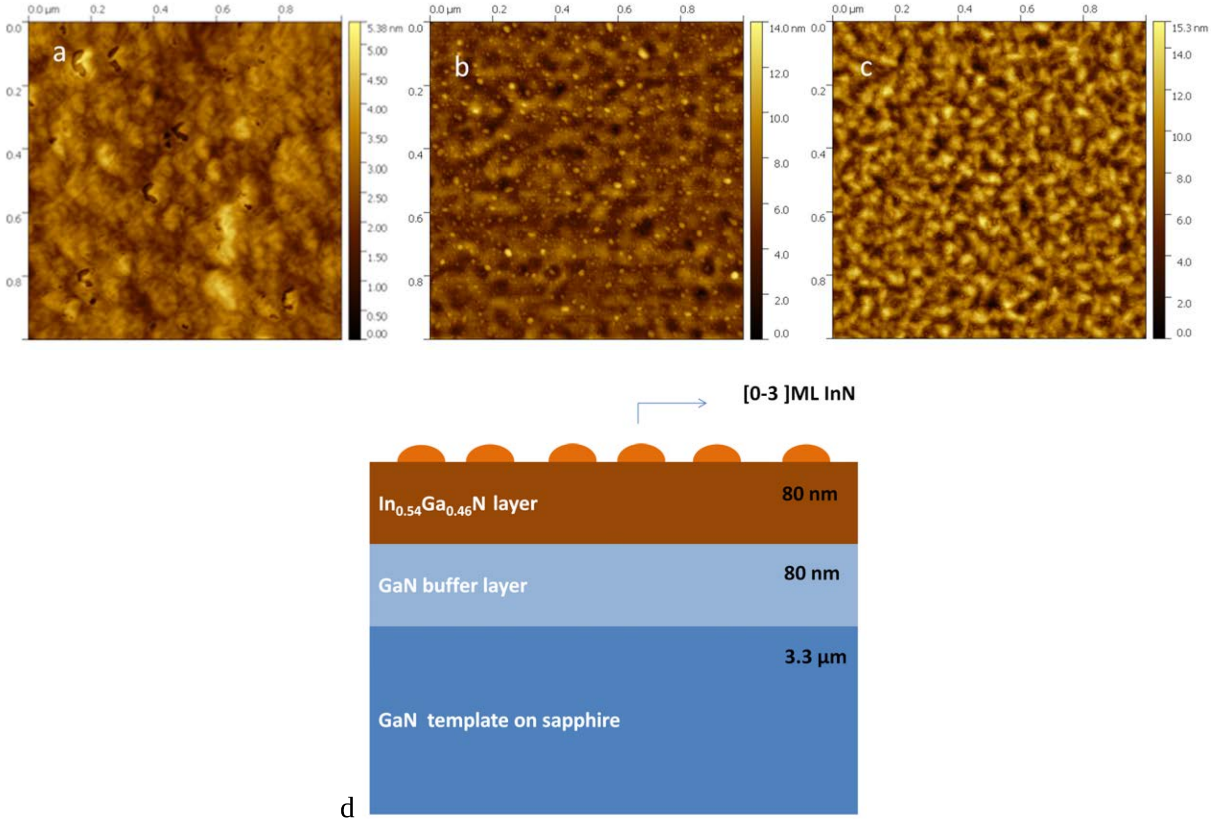

Figure 6.4: 1x1 µm^2 AFM images of: (a) bare InGaN layer, (b) InN QDs (2 ML), and (c) InN thin film (3ML). Full height contrast (brightest highest) is 5 nm for all images. (d) Presents a schematic drawing of the sample nominal structure.

The PEC electrochemical potential (electromotive force, EMF) is limited if the redox reaction is only governed by the available redox species and no catalyst is used. In that case the maximum expected EMF is given by the Nernst equation, electrochemical systems obeying this equation are said to have a nernstian behavior:

$$EMF = E_0 - \frac{RT}{nF}\ln\left(\frac{[red]}{[ox]}\right)$$

$$25^0 C \rightarrow \frac{RT}{F} = 59.2\,mV \qquad (6.1)$$

In where n is the amount of electron transferred in the reaction, F is the Faraday constant (96,500 C mol^{-1}), R is the universal gas constant (R = 8.314 472(15) J K^{-1} mol^{-1}) and E_0 is the initial cell potential.

Before continuing with the in depth EMF analysis, both response time and stability measurements for all considered layers were studied. As a result, it was found that the InGaN layer is unstable and that even the InN thin film is not stable over the whole measured time period, the signal starting to decay slowly. Therefore only one EFM plot is presented in figure 6.5 for InN thin film (cholesterol sensing) and for InGaN films (glucose sensing). As it can be seen in figure 6.5 the InN QDs/InGaN samples show a very fast response (<2s) for glucose detection and even faster for cholesterol sensing, being quite stable over the measured time interval.

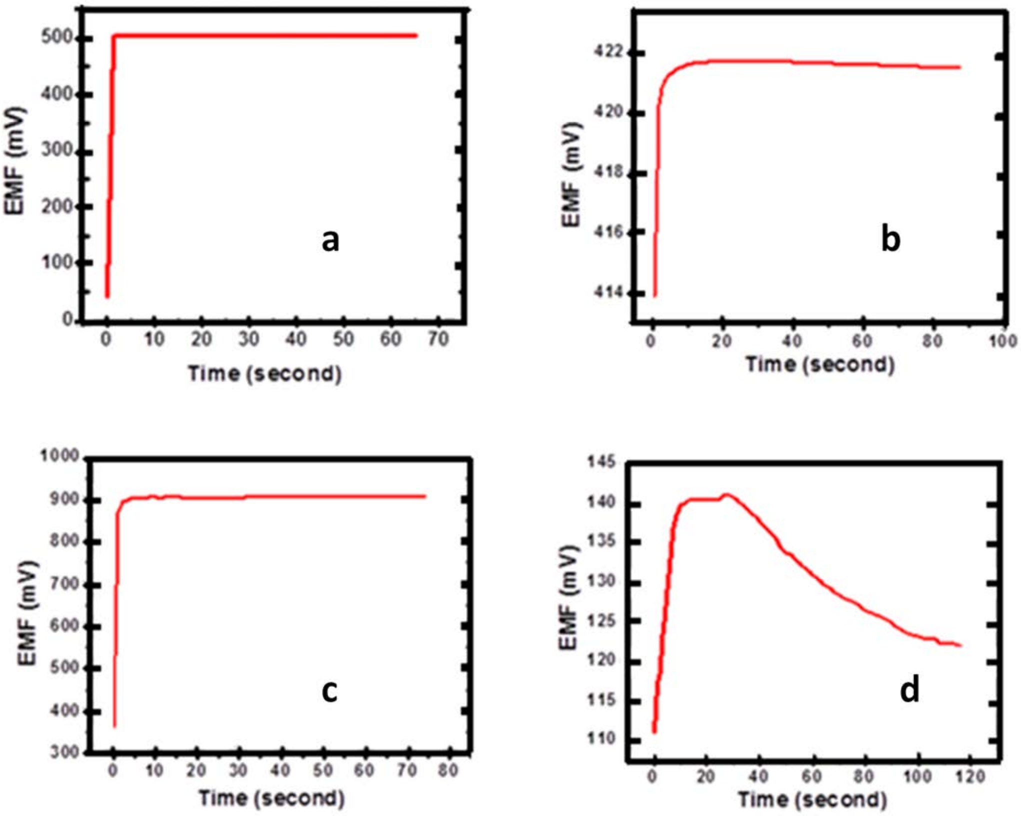

Figure 6.5: Biosensor response time and stability: (a) InN QDs/for 500 µM glucose concentration, (b) InN thin film for 500 µM cholesterol concentration, (c) InN QDs for 500 µM cholesterol concentration, (d) bare InGaN layer for 1mM glucose concentration.

The variation of the EMF values upon analyte concentration was verified to be non *nernstian* for samples with InN QDs, meaning that the sensibility is much higher than the maximum expected from the Nernst equation, however still varying linearly, implying that a catalyst effect is present. The linearity and sensibility responses for InN QDs in both glucose and cholesterol cases, and for the InN thin film for cholesterol are presented in figure 6.6. It can be seen that the InN QDs sensibility is above 79 mV/decade for glucose and above 84 mV/decade for cholesterol. On the other hand, the InN thin film response obeys the *nernstian* equation having average value around 46 mV/decade with some of the dispersed values reaching even the maximum expected value of 52.9 mV/decade.

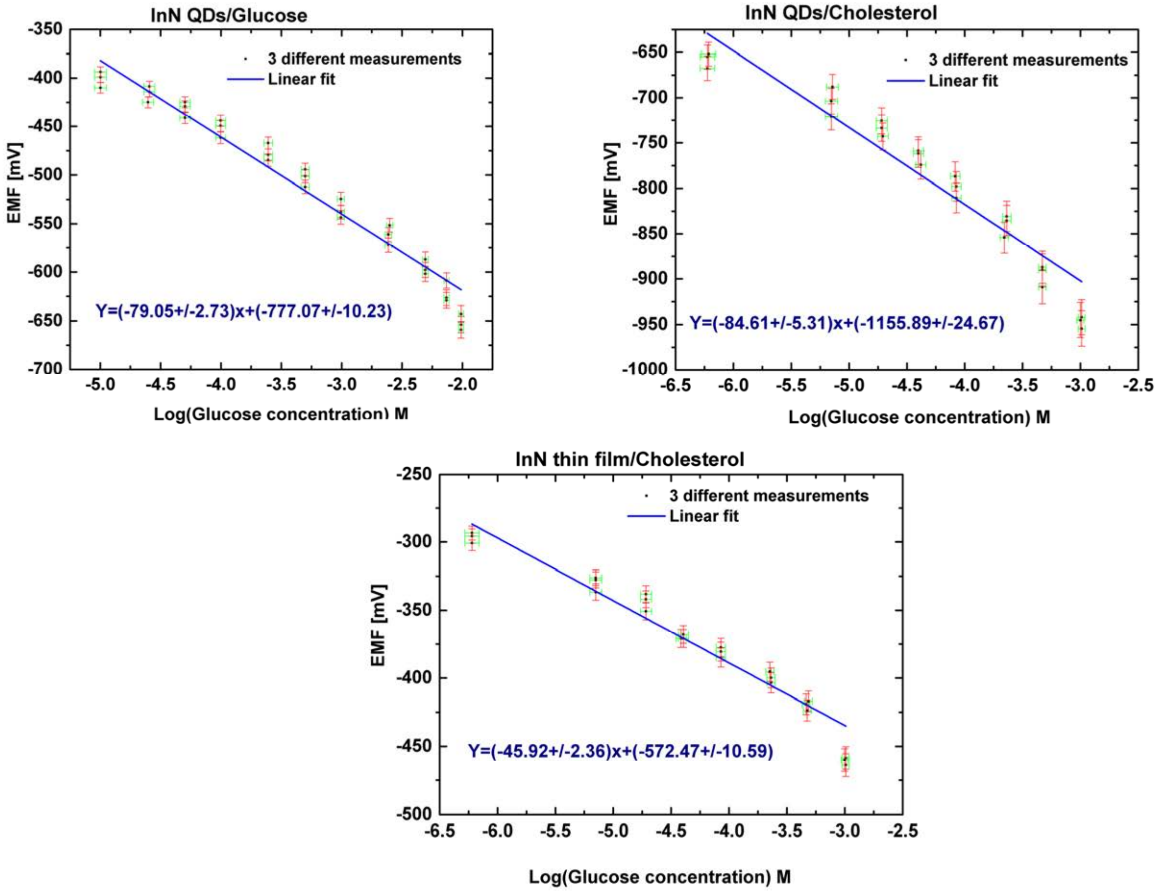

Figure 6.6: Biosensor sensibility

The selectivity of the InN QDs/InGaN based biosensor response was inspected by adding typical interfering elements present in the blood. There exist a large variety and only two were chosen for present study namely uric acid and ascorbic acid. The *normal* (standard levels) concentration in blood for uric acid lies between 3-5.5 mg/dl (0.17-0.3 mmol/l) [Web arthritiscare] and for ascorbic between 0.6-2 mg/dl (0.02-0.11 mmol/l) [Web Mayo Clinic] therefore being present in less than 10% compared to glucose levels in blood. For this reason in the case of glucose sensing, elements such as Uric Acid (50µM) and Ascorbic Acid (50µM) were added to the 500µM glucose solution. The results are presented in figure 6.7 (a). From these results we see the effectiveness of the enzyme (selectively oxidizing glucose) as only a very small perturbation is observed which is rapidly stabilized. In addition the long term storage stability of the glucose biosensor was tested by repeated experiments over a time period of fourteen consecutive days with a 500 µM glucose solution (same glucose biosensor). As shown in figure 6.7 (b), a stable EMF output was measured.

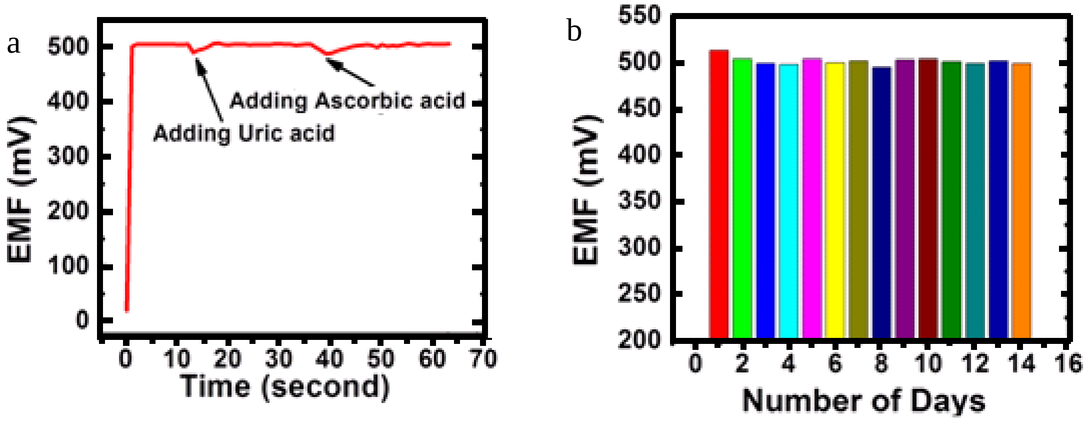

Figure 6.7: Selectivity and long term storage stability of the InN QDs/glucose biosensor. (a) Selectivity analyzed when 50µM of both Uric Acid and Ascorbic Acid were added to the 500µM glucose solution and (b) Long term storage stability of InN QDs glucose sensors over a period of 14 days.

A similar excellent long term storage stability was observed for InN QDs cholesterol biosensors, as shown in figure 6.8 (a), for a period of 10 days. The storage conditions between each measurement were the following: temperature was 4ºC and ambient was at dry conditions in both cases. Temperature stability data shown in figure 6.8 (b) reveal that the enzyme activity decreases below and above 40°C (peak) leading to a decrease of the EMF output. Hence, the temperature has to be carefully controlled during cholesterol sensing measurements. Notice that this is exclusively related to the intrinsic properties of the enzyme and not to the electrode material properties.

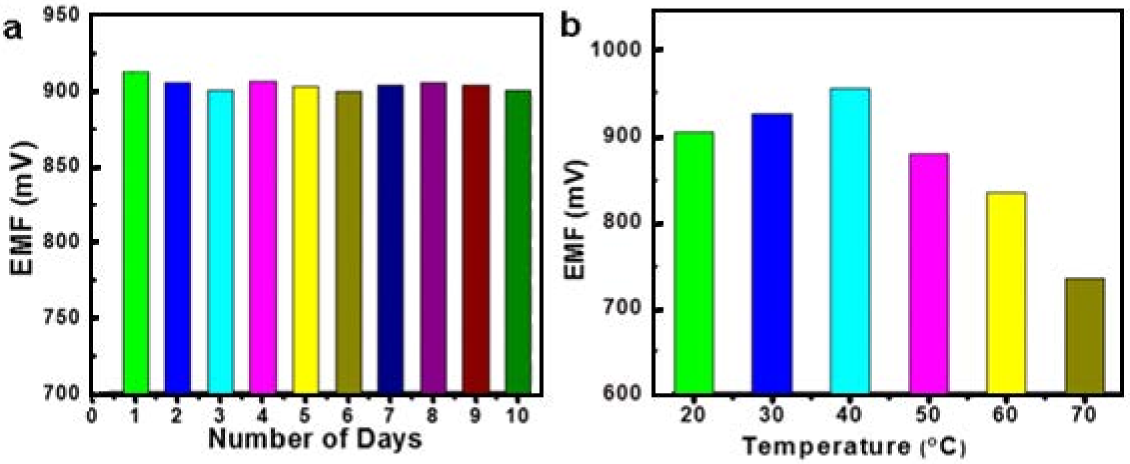

Figure 6.8: (a) Long term storage stability of InN QDs cholesterol sensors over a 10 days period measured in a 500 µM cholesterol solution, (b) EMF temperature stability of InN QDs cholesterol sensors in a 500 µM cholesterol solution

The best way to emphasize these results is to compare with other biosensors. For this purpose, table 6.1 offers a comparison with other well-known glucose biosensors while table

6.2 gives a summary of cholesterol biosensors in terms of response time and sensibility, demonstrating the superior performance of our InN QDs/InGaN biosensor.

Electrode matrix	Detection techniques	Sensitivity/detection limit	Response time(s)	Reference
ZnO nanotube	Potentiometric	69.12 mV/decade/0.5×10^{-6} M to 12×10^{-3} M	~4	[1]
Si–SiO2–Si	Potentiometric	12 mV/decade in humanurine	90	[2]
SnO_2 film enzymatic	Potentiometric	50±2 ΔmV ΔpC^{-1}/-	~300	[3]
InN QDs/InGaN	Potentiometric	80.0 ±4.6 mV/decade /1×10^{-5} to 1×10^{-2} M	<2	[4]

Table 6.1: Comparison with other electrochemical glucose biosensors.

Electrode matrix	Detection techniques	Sensitivity/detection limit	Response time(s)	Reference
ZnO nanorods	Potentiometric	35.2 mV/decade/0.001–10 mM	10	[5]
ZnO nanowalls	Potentiometric	53 mV/decade/10−6–10−3 M	5	[6]
InN QDs/InGaN	Potentiometric	97.0 ± 5.4 mV/decade /1×10^{-6}– 1×10^{-3} M	<2	[7]

Table 6.2: Comparison with other electrochemical cholesterol biosensors.

To summarize glucose biosensor was fabricated based on functionalized InN QDs with glucose oxidase. This biosensor utilizes the substantial advantages of a high surface charge density and low-dimensionality of the InN QDs for high sensitivity and fast response. The sensitivity, reusability, and selectivity were investigated over a large glucose concentration range, from 1×10^{-5} to 1×10^{-2} M. The glucose biosensor presented an excellent sensitivity slope of (79.05 ±2.73) mV/decade with a fast response of 2 sec.

A second potentiometric biosensor for cholesterol, also based on functionalized InN QDs was fabricated. The sensitivity, selectivity, and long term storage stability over a large cholesterol concentration range, from 1×10^{-6} – 1×10^{-3} M, were investigated. The biosensor had an excellent sensitivity slope of (84.61 ± 5.31) mV/decade with a fast response of 2 sec. The performances of these InN QDs biosensors were compared with those of an InN thin film. The sensitivity of the InN QDs biosensor was twice that of the InN thin film one; the EMF was three times larger; and the response time was five times shorter. The response of a biosensor based on a bare InGaN layer was not stable. Therefore, the results are first indication that the superior (bio-) sensing properties of the InN QDs/InGaN biosensor may be attributed to their unique surface properties, presented in chapter 2 and discussed in chapter 4. The high sensitivity, rapid response time, good selectivity, and excellent reusability reveal that both glucose and cholesterol biosensors have great potential for clinical diagnosis.

6.2 Water splitting

Photoelectrochemical water splitting by a spontaneously formed In-rich InGaN nanowall matrix was investigated, combining the material of choice with the advantages of surface texturing for light harvesting by light scattering. The current density of the InGaN-nanowall photoelectrode at zero voltage versus the Ag/AgCl reference electrode is 3.4 mA cm^{-2} *with an incident-photon-to-current-conversion efficiency (IPCE) of 16% under 350 nm laser power density of 0.075* Wcm^{-2}*. In comparison, the current density for a planar InGaN-layer-photoelectrode is 2 mA* cm^{-2} *with an IPCE of 9% at zero voltage. The* H_2 *generation rates at zero applied voltage versus the Pt counter electrode per illuminated area were 2.8 and 1.61* μ *mol* $h^{-1}\cdot cm^{-2}$ *for the InGaN nanowalls and InGaN planar layer, respectively, revealing a 57% enhancement for nanowalls.*

6.2.1 Photoelectrochemical water splitting and hydrogen generation by a spontaneously formed InGaN nanowall network

Solar energy driven photo-electrochemical (PEC) water splitting to generate H_2 is a clean, renewable approach for sustainable energy provision. [Van de Krol 2008, Kudo 2009, van Dorp 2009, Maeda 2010, Tachibana 2012] Semiconductor nano-structures have been studied extensively in recent years for PEC cells due to their distinctive properties and promising superior PEC performance [Goodey 2007, Peng 2008, Boettcher 2010, 2011, Chen Z. 2011, Sun 2011, Alireza 2013]. The main requirement of the PEC industry is to find semiconductor materials with the capability of efficient and cost effective conversion of sunlight to H_2 by splitting water [Turner 1999, Weisz 2004, Crabtree 2004]. GaInP has been reported as an attractive PEC electrode material but it has unacceptably high corrosion rates and suffers from poor stability [Nozik 1996, Khaselev 1998]. In comparison, TiO_2 has high corrosion resistance but it has large bandgap energy of 3.2 eV allowing only for absorption of 3% of solar radiation [Nozik 1996]. Recently, GaN has been considered as a promising PEC electrode material, but also has too large bandgap energy [Waki 2007, Wang 2011, Hwang

2012, Hwang J. 2013, Benton 2013]. Therefore, and as discussed in previous chapter considering the general requirements for efficient PEC water splitting, InGaN appears to be ideal with a tunable bandgap energy matching the solar spectrum, a large absorption coefficient, high carrier mobility, and good corrosion resistance. However, up to now there are only very few reports on the feasibility of solar water splitting using InGaN alloys [Fujii 2005, Li J. 2008]. Regarding the In optimum composition, between 40% and 50% balances a wide enough bandgap to maintain a sufficiently large over-potential against the redox potential of water ($V_{redox} = 1.23V$), while being low enough for efficient absorption of solar radiation. Moreover, as pointed out in chapter 2 and 5 the unique surface properties together with the quantum nature of the QDS are likely to facilitate the oxidation process of O_2^-, i.e., the acceptance of electrons.

In addition, various InGaN-based nanostructures have been reported, including nanowalls, nanoflakes, and nanowires with the potential to enhance the redox reaction due to enhanced light absorption by light scattering and enlarged surface area [Aprile 2008]. In particular, nanowall structures are proposed as promising materials considering the requirements of PEC cells [Su 2011, Zhou 2010,2012]. In this chapter the enhanced PEC water splitting and H_2 generation using an InGaN-nanowall photoelectrode with In composition up to 40% is experimentally demonstrated. The InGaN-nanowall photoelectrode exhibits a significantly larger current density, higher IPCE value, and higher H_2 generation rate in comparison to planar InGaN-layer photoelectrodes with similar In composition.

The growth process, structural, and optical properties of the InGaN nanowalls and planar InGaN layers have been introduced in the previous chapter 3. As a reminder, growth was performed by plasma assisted molecular beam epitaxy (PA-MBE) at 450 ^{o}C under slightly N-rich conditions on both Si (111) and (0001) GaN/sapphire substrates with 40% to 50% In composition. The bandgap energy of the InGaN nanowall structure and that of the InGaN layer is 1.4 eV, determined from PL measurements, implying absorption up to near-infrared wavelengths. In figure 6.9 a schematic of the structures is presented.

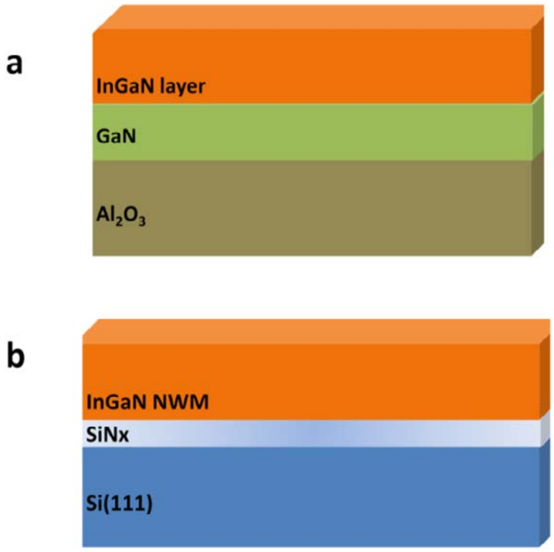

Figure 6.9: Layer structure of the samples used (a) High In-content InGaN layer on GaN templates and (b) InGaN NWM on Si(111).

As it was done for the biosensors, Al contacts were deposited on the InGaN nanowalls and InGaN layer with excellent ohmic behavior due to the high residual n-type conductivity typical of high- In-composition InGaN layers. PEC characterization was performed in a 0.5 mol·l^{-1} HBr (pH 3.0) electrolyte solution using a customized three-electrode electrochemical cell configuration as reactor. The samples were diced in rectangular pieces. Light irradiation was provided by a 350 nm laser with a power density of 0.075 Wcm^{-2} relative to a total illuminated area of 0.175 cm^2. An external voltage was applied to the InGaN nanowalls and InGaN layer working electrodes versus the Pt counter electrode and the voltage between the working electrodes and the Ag/AgCl reference electrode was monitored. The photocurrent was measured with a standard computer controlled chrono-amperometric setup built up of a Keithley 2000 Multimeter and a Keithley 2400 Source meter. Hydrogen and oxygen were collected by a sampling loop and analyzed separately by a gas chromatography (GC) analyzer (China GC 2000), which was equipped with a TCD (thermal conductive detector) and a 3.5 m long molecular 5Å sieve packed column to determine the hydrogen and oxygen concentrations. Figures 6.10(a) and 6.10(b) show the top-view SEM images of the InGaN nanowalls and InGaN layer morphology. The NWM properties were presented in chapter 5. Figure 6.10(c) shows a photograph of the experimental PEC cell setup where the formation of H_2 bubbles is clearly observed during the experiment (in the figure it is indicated where they were formed but picture resolution is not enough for them to be clearly seen) on the Pt counter electrode during illumination.

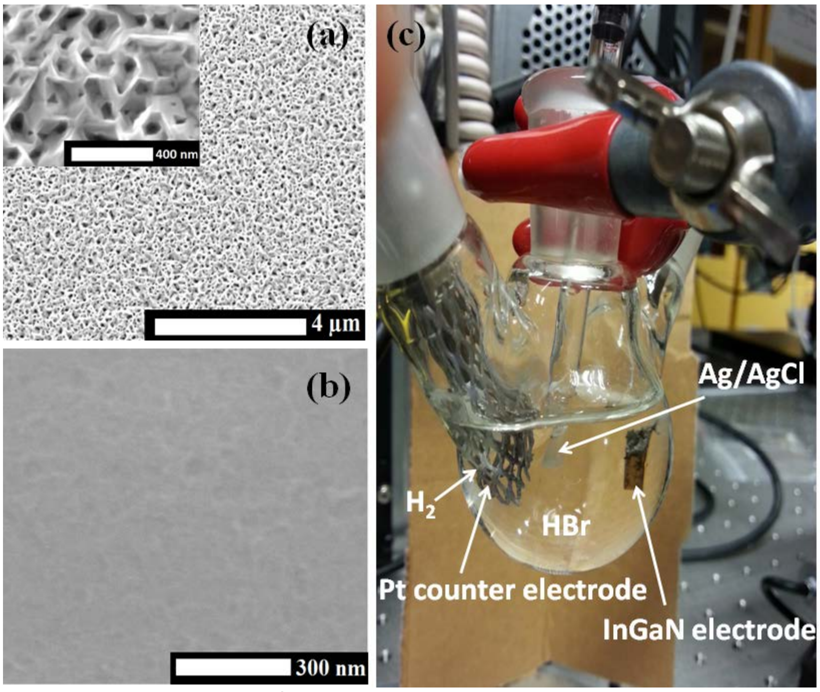

Figure 6.10: Plan-view SEM images of: (a) InGaN nanowalls and (b) planar InGaN layer. The inset in (a) shows the nanowall structure with enhanced magnification. (c) Photograph of the experimental PEC cell setup.

In figure 6.11 the measured current density as a function of the voltage versus the Ag/AgCl reference electrode is plotted for the InGaN-nanowalls and the InGaN- layer photoelectrodes under dark and illumination conditions. In the dark, the current densities are negligibly small. Under illumination, the onset voltages, at which the photocurrent density shows a rapid rise, are approximately -0.35 V for both electrodes. The photocurrent density is about 70% larger for the InGaN nanowalls compared to that for the InGaN layer. The photocurrent densities measured for zero voltage are 3.4000 ± 0.0018 mA·cm^{-2} for the InGaN nanowalls and 2.0000±0.0013 mA·cm^{-2} for the InGaN layer, confirming the enhanced PEC properties of the InGaN nanowalls due to superior light absorption [Li H. 2007, Zhou 2012] and much higher surface area [Maiolo 2008] compared to the planar InGaN layer.

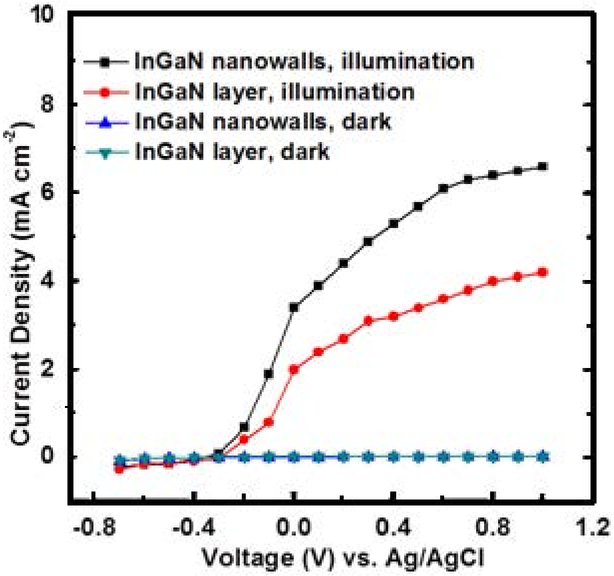

Figure 6.11: Current density as a function of voltage versus the Ag/AgCl reference electrode in a 0.5 mol·l-1 HBr electrolyte solution for InGaN-nanowalls and InGaN-layer photoelectrodes in the dark and under 350 nm laser illumination with 0.075 W/cm^2 excitation power density. The measurements are performed using a three-electrode configuration.

Figure 6.12 shows the IPCE evolution (defined as the percentage of electrons taking part in the redox reaction with respect to the number of incident monochromatic photons) for InGaN-nanowalls and InGaN-layer photoelectrodes as a function of voltage versus the Ag/AgCl reference electrode, given by equation 4.19 presented previously.

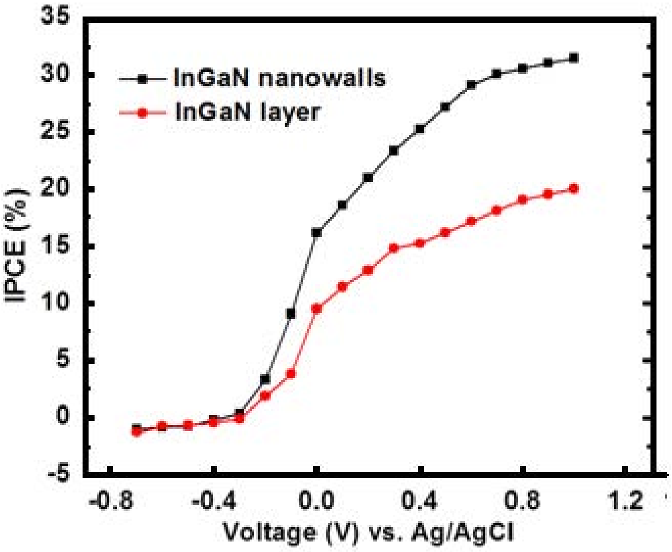

Figure 6.12: IPCE of InGaN-nanowalls and InGaN-layer photoelectrodes under 350 nm laser illumination with 0.075 W·cm^{-2} excitation power density as a function of voltage versus the Ag/AgCl reference electrode in 0.5 mol·L^{-1} HBr electrolyte solution. The measurements are performed using a three-electrode configuration.

The IPCE is seen to increase faster and towards higher values for the case of InGaN nanowalls compared to the InGaN layer. For both cases when realizing the experiment, H_2 gas generation is clearly observed on the Pt counter electrode during illumination.

Figure 6.13 shows the hydrogen and oxygen amount generated in a two electrode setup and the evolution versus the reaction time. The total amount of H_2 and O_2 generated after 8 h irradiation is 22.4 μmol and 7.92 μmol for the InGaN nanowalls, and 12.88 μmol and 4.64 μmol for the InGaN layers, respectively. This unambiguously evidences the splitting of water into H_2 and O_2 gases. The strongly enhanced performance of the nanowalls is attributed to the large surface area and higher absorption. However, the yield of hydrogen obtained is almost three times (2.83) that of the oxygen yield while pure splitting of water would provide a yield of 2:1. This means that some hydrogen is generated through the redox reaction of the HBr electrolyte. It is clear that the role of the electrolyte in water splitting, not widely considered so far, needs careful attention in the future. Nevertheless, the data reveal that the photocurrent and H_2/O_2 generation are very stable over time, confirming the good chemical stability of the InGaN layers and InGaN nanowalls as photoelectrodes.

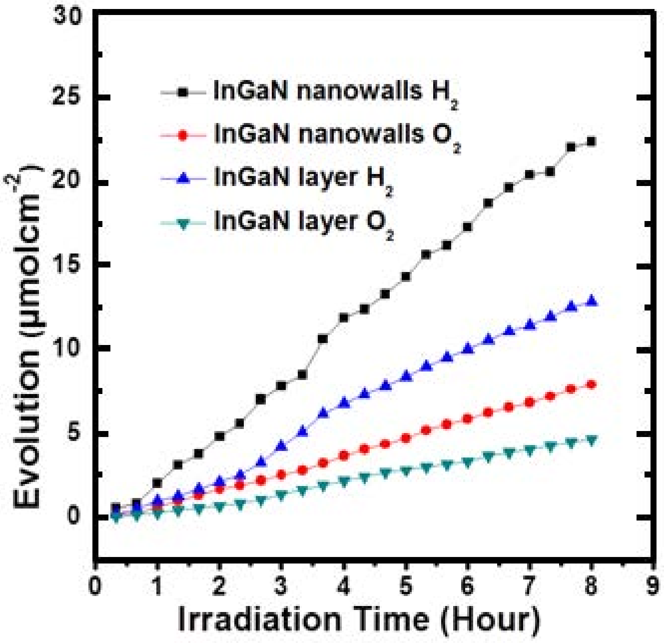

Figure 6.13: H_2 and O_2 evolution vs. Reaction time per illuminated area at zero applied voltage versus the Pt counter electrode for the InGaN-nanowalls and InGaN-layer-photoelectrodes in 0.5 mol·l^{-1} HBr electrolyte solution. The measurements are performed in a two-electrode configuration.

To summarize, more efficient PEC water splitting and H_2 generation is achieved with InGaN nanowall photoelectrodes in comparison with a planar InGaN layer one. This was attributed to increased light absorption by light scattering and the larger surface area of the nanowalls structure together with the excellent PEC properties of InGaN. The InGaN-nanowalls-PEC cell exhibits enhanced photocurrent density, high IPCE, and a large H_2 generation rate.

6.2.2 InN/InGaN quantum dot photoelectrode: Efficient hydrogen generation by water splitting at zero voltage

Light to hydrogen conversion via water splitting is of immense interest as a clean, storable, and renewable energy source [Van de Krol 2008, Kudo 2009, van Dorp 2009, Maeda 2010, Tachibana 2012] but efficient materials need to be found. InGaN alloys have properties ideally suited and it has been demonstrated that InN QDs more than double the PEC water splitting efficiency of an $In_{0.54}Ga_{0.46}N$ layer photoelectrode. The InN QDs /$In_{0.54}Ga_{0.46}N$ photoelectrode reveals a maximum IPCE of 56% at a wavelength of 600 nm with a hydrogen generation rate of 133 µmol h^{-1} cm^{-2} at zero voltage under illumination of a 1000 W Xenon arc lamp. The bare $In_{0.54}Ga_{0.46}N$-layer photoelectrode delivers a much lower IPCE (24%) with a hydrogen generation rate of 59 µmol $h^{-1}cm^{-2}$.

As presented in chapter 5, a growth process was established that complies with the PEC water splitting requirements and even more InN QDs were possible to be grown on top on InGaN layers. In this section the performances of these structures, as PEC water splitting systems, will be analized. So far there are only a few reports on the feasibility of water splitting using InGaN alloys, either theoretically considering the bands energy alignments [Moses 2010], or experimentally [Li J. 2008, Fujii 2005]. The main challenge being the growth of high-quality InGaN layers with high In content while avoiding the formation of a large density of surface pits and phase separation [Srinivasan 2003, Stringfellow 2010]. The modification of the surface properties by depositing InN QDs to enhance the redox reaction is a powerful aspect that has been exploited.

Although a detailed description was given in Chapter 4, an overview of the main growth conditions is given here. The growth of InGaN layers and InN QDs was performed with the same recipe as that shown in section 5.1, used to develop bio sensors, namely, at 460ºC under slightly N-rich conditions [Soto 2013a] on 3.3 micron thick GaN templates (figure 5.6 (d)). The growth started with an 80nm thick GaN layer at 760ºC followed by an 80 nm thick InGaN layer at 460ºC. Finally one monolayer InN was grown on the InGaN layer for QD formation. The obtained QDs height, diameter, density were 2-3 nm, 20-30 nm, and 2.2×10^{9} cm^{-2}, respectively, on the gently undulated InGaN layer. AFM images of the InN

QDs and the bare InGaN layer were taken in tapping mode. The optical properties were characterized by CL spectroscopy at room temperature.

Al electrical contacts were deposited on the InN QDs and bare InGaN layer to perform I-V measurements with a parameter analyzer (PA). The contacts showed excellent ohmic behaviour due to the high n-type conductivity typical of high-In-content (54%) InGaN layers. The samples were diced in rectangular pieces with an active area of 0.175cm^2. The contact areas and electrode wires were covered with insulating glue. The PEC characterizations were performed in a pH 3 H_2SO_4 solution with 0.5M Na_2SO_4 salt as electrolyte using a customized three-electrode electrochemical cell with the InN/InGaN QDs and InGaN layer working electrodes, an Ag/AgCl reference electrode from Metrohm (3M KCl), and a Pt counter electrode (2cm x 4 cm).

Sample was illuminated with white light from a 1000W Xe arc lamp with ~100 mWcm^{-2} power density (typical power density for solar simulating setup). For spectrally resolved measurements, several band-pass filters with peak wavelengths between 360 and 750 nm were used. The incident power density was measured by a power meter for each filter and varied between 93 and 98 mWcm^{-2}.

A 0 to1.0 V voltage was applied to the InN QDs and InGaN layer working electrodes versus the Ag/AgCl reference electrode. The photocurrent was measured with a standard computer controlled chrono-amperometric setup built up of a Keithley 2000 Multimeter and a Keithley 2400 Source meter. The IPCE was determined from the measured photocurrent density and wavelength dependent incident power density according to equation 4.19 (IPCE).

The measure of the PEC hydrogen and oxygen generation and of the time dependent photocurrent density were carried out in a two electrode configuration with zero externally applied voltage. The PEC was kept at18 ± 2ºC in thermostatic water bath. Hydrogen and oxygen were collected by a sampling loop and analyzed separately by a GC analyzer (China GC2000) equipped with a TCD (thermal conductive detector) and a 3.5 m long molecular 5Å sieve packed column to determine the hydrogen and oxygen generation rates.

The analyzed sample with QDs corresponds to the 1ML InN QDs grown on the GaN templates in figure 6.14(a) a three-dimensional AFM image of selected QDs is shown. Figure 6.14 (b) displays the CL spectrum taken at room temperature of the InN/InGaN QDs sample, with the emission spanning from 500 nm (2.5eV) to 800nm (1.5eV) most likely due to variations of the In content and less likely however possible, due to QDs observed sizes, QDS size dispersion. The PL spectrum taken at low temperature and previously shown at chapter 5, in figure 5.15 (a), is red shifted compared to presented RT CL spectrum most probably due to carrier localization in higher-In-content regions (Stokes shift) while RT PL measurements provide a better measure of the bandgap energy when carriers become thermally delocalized. The PEC cell photograph is shown in figure 6.14 (c)

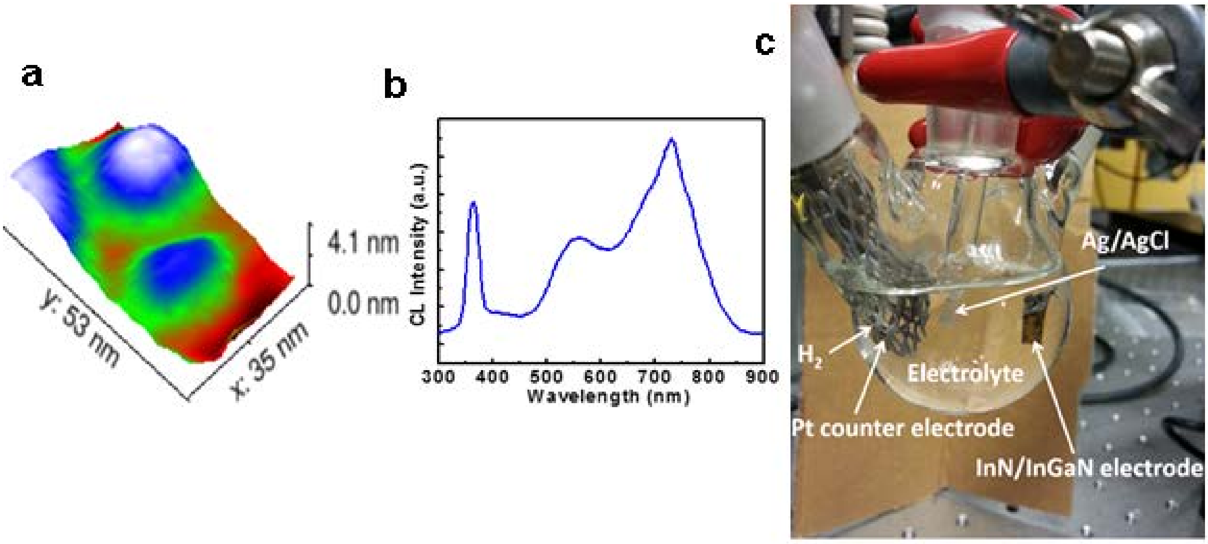

Figure 6.14: (a) Three-dimensional AFM image of the InN/InGaN QDs. (b) CL spectrum of the InGaN/InN QDs at room temperature. (c) Photograph of the PEC cell setup.

Figure 6.15 shows the evolution of the current density as a function of voltage versus the Ag/AgCl reference electrode for the InN/InGaN QDs and InGaN layer in the dark and under illumination with white light (Xe arc lamp with ~100 mWcm^{-2} power density). The current density in the dark is negligibly small. Remarkably, under illumination the photocurrent density for the InN/InGaN QDs is more than twice higher than that for the InGaN layer. Onset voltages, at which the photocurrent density shows a rapid rise (extrapolating the rising curves to zero), of -0.3 and -0.2 V for the InN/InGaN QDs and InGaN layer are found respectively. The photocurrent density at zero voltage versus the Ag/AgCl reference electrode is 12.7000±0.60697 mAcm^{-2} for the InN/InGaN QDs and 5.0000±0.0024 mAcm^{-2} for the InGaN layer, evidencing the superior PEC properties of the InN/InGaN QDs.

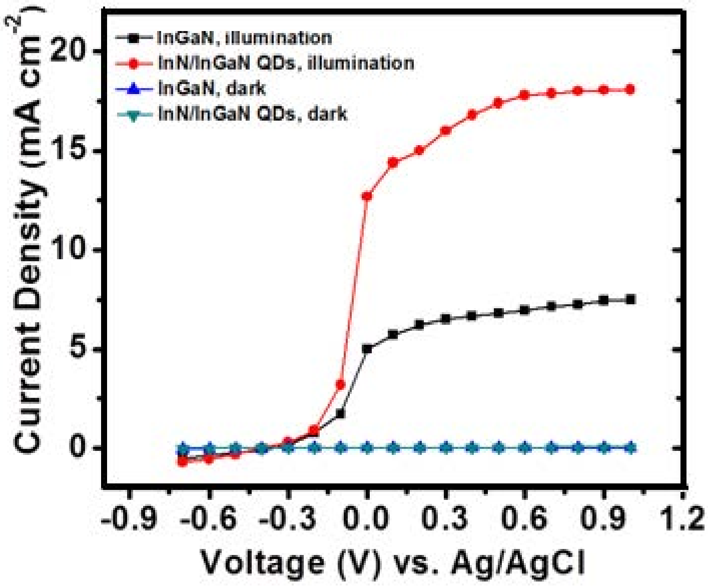

Figure 6.15: Current density evolution as a function of voltage versus the Ag/AgCl reference electrode for the InN/InGaN QDs and InGaN layer photoelectrodes in the dark and under white light illumination.

The PEC water splitting is essentially a redox reaction, as that described in the previous chapter for biosensors. The difference lies in the absence of a specific analyte of interest and that, instead of a potential applied by a potentiostat to start the reaction, direct sunlight, or, as in this case, a white light source is used. The astonishing PEC properties of InN/InGaN QDs can be attributed to the enhanced redox reaction (induced by the presence of InN QDs) by effectively promoting electron transfer as explained in chapters 2 and 4. It facilitates the oxidation of O_2^- ions (oxygen-producing half reaction), i.e., the transfer of electrons to the working electrode (attraction of opposite charges) compensated by the attraction/repulsion of photogenerated holes/electrons in the InGaN layer to maintain a stationary charge distribution. This charge balancing opposes the downward band-bending present towards the surface, due to the net positive surface charge which screens the electron accumulation present below the surface. This electron accumulation would normally generate an energy barrier for electron transport from the surface to the current collector and for hole transfer to the electrolyte. However, due to the high, easily degenerate electron occupation of the InGaN conduction band [Bailey 2008], photogenerated electrons move at the Fermi energy and the band-bending zone is so narrow that the photogenerated holes tunnel to the surface, similar to the ohmic contact formation to the InGaN layer and generally to n^+ or p^+ semiconductors. This is displayed in figure 6.16.

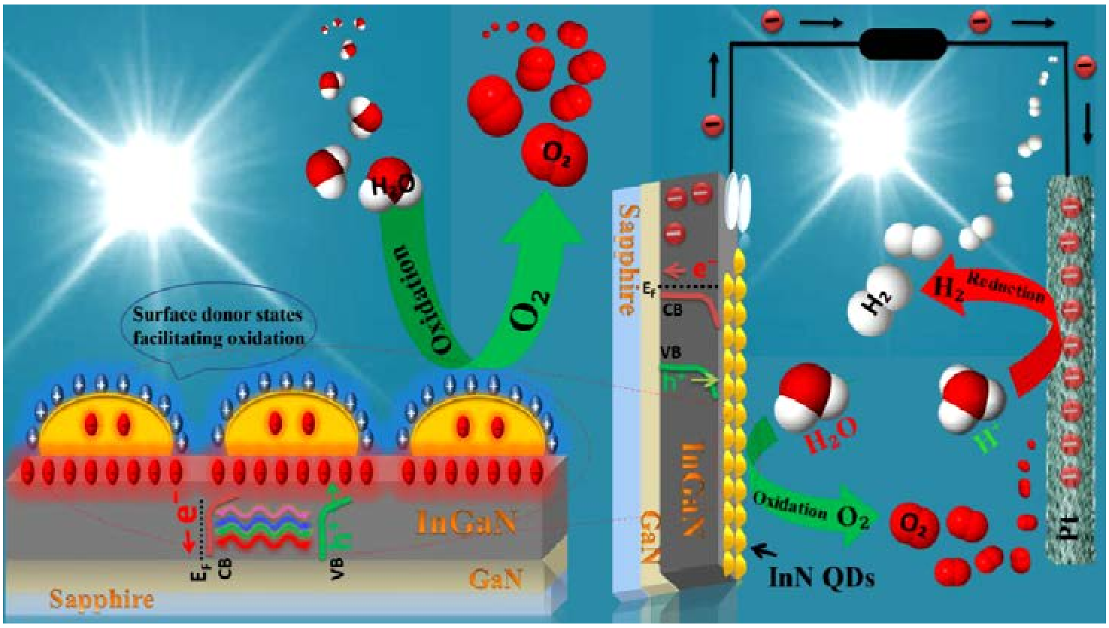

Figure 6.16: Scheme of the photocatalytic water splitting reaction.

Thus, the operation of the InN/InGaN QDs differs from that of other n-type semiconductor photoanodes, where there is a typical upward band bending at the surface and where an electron depletion region is present. Besides, providing a high positive surface charge attracting more efficiently anions, the InN QDs are not participating in the PEC redox reaction due to the too low bandgap energy, while the bandgap energy of the InGaN layer is high enough to drive the redox reaction in the presence of photogenerated electrons and holes under illumination. The same unique property of InN/InGaNQDs, to promote oxidation, has been identified by the superior performance of InN/InGaN-QDs-based potentiometric biosensors [Alvi 2012, 2013].

In addition, the zero-dimensional electronic property of the QDs plays an important role for the observed modulated surface charge distribution, as discussed in chapter 5: for InGaN thin films the positive surface charge effectively screens the surface electron (2DEG). However, when InN QDs are present, the 2DEG charge at the QDs positions is not completely screened leaving a charge modulated surface. The screening becomes less effective as QDs cannot accommodate as many electrons as a flat surface, due to the Pauli Exclusion Principle. This unscreening at the InN QDs site creates a local positive charge which actively attracts electrons. Notably, graphene also acts and is used as an electron acceptor and transporter to enhance the PEC activity comparably [Ng 2010, Hwang 2012, Hou 2012, Kim 2012, Lin 2012, Song P. 2012, Benton 2013, Zhang K. 2013]. A scheme of the PEC cell operation is shown in figure 6.16.

The IPCE as function of wavelength, from 360 to750 nm, is shown in figure 6.17 at 0.0, 0.5, and 1.0V applied voltage versus the Ag/AgCl reference electrode for the InN/InGaN-QDs and InGaN layer photoelectrodes, and the GaN substrate. The IPCE between 450 and 750nm arises clearly from the InGaN layer, since within this wavelength range there is no response from the GaN substrate out ruling any contribution of the GaN template towards the water splitting process. The IPCE increases rapidly for voltages above -0.3V and IPCE values for InN/InGaN QDs are higher by a factor of 2.3 than those for the InGaN layer. At zero voltage the maximum IPCE values for the InN/InGaN QDs and InGaN layer are 55% and 24%, respectively, while at 0.5V the maximum IPCE values for the InN/InGaN QDs and InGaN layer are 67% and 30%, respectively. The maximum IPCE values for the InN/InGaN QDs and InGaN layer are 77% and 35% at 1.0V. Such high values are obtained for a relatively thin (80nm) InGaN layer. This is made possible by the exceptionally high absorption coefficient of III- nitrides (about 10 times that of III-Arsenides) which is a notable advantage regarding growth time, materials consumption and, therefore, cost.

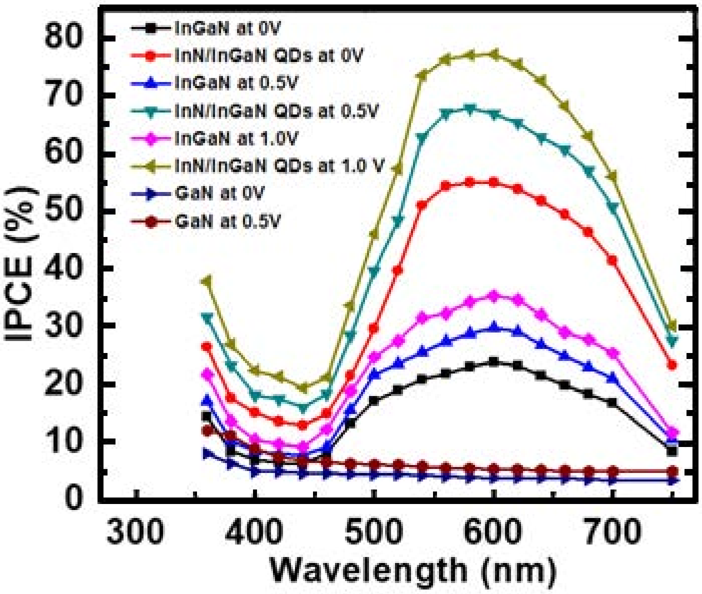

Figure 6.17: IPCE spectra of the InN/InGaN QDs, InGaN layer, and GaN template used as photoelectrodes as a function of wavelength at 0.0, 0.5, and 1.0 V external voltage.

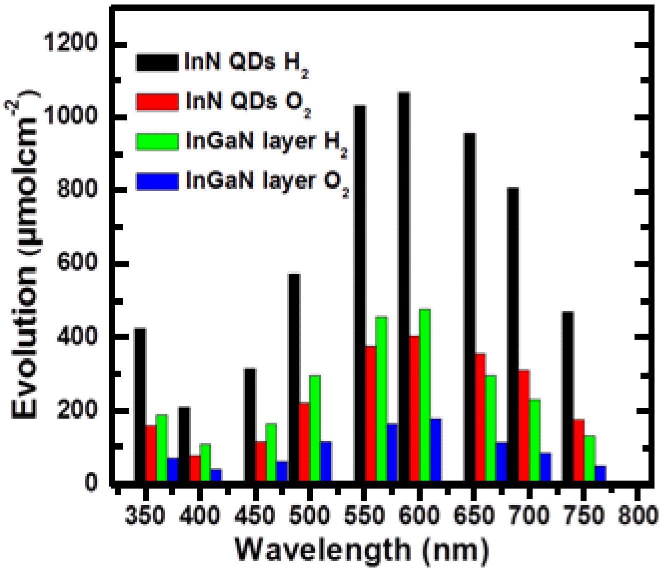

Figure 6.18: Hydrogen and oxygen evolution after 8 h illumination (per illuminated area) as function of wavelength at zero applied voltage.

The evolution of the amount of hydrogen and oxygen generated, as function of the wavelength (from 360 to 750 nm) at zero applied voltage, is shown in figure 6.18. The maximum amount of hydrogen and oxygen generated after 8 hours irradiation is 1067 and 404 µmol cm^{-2} for the InN/InGaN QDs, and 477 and 180 µmol cm^{-2} for the InGaN layer, respectively. The yield of hydrogen is about 2.6 times that of oxygen while pure water splitting would provide a yield of hydrogen to oxygen of 2:1. This implies that some hydrogen is generated by the redox reaction of the electrolyte, H_2SO_4 in this case, and as previously stated this is an issue still open for investigation. Importantly, the photocurrent, and hydrogen and oxygen generation are very stable over time, a direct indication of the good chemical stability of the InN/InGaN QDs and InGaN layer.

The transient photocurrent for InN/InGaN-QDs and InGaN layer photoelectrodes, measured under white light illumination with 30 sec. On/off cycles, is displayed in figure 6.19 (a). The InN/InGaN QDs photoelectrode exhibits very good photo-switching performance and stability, three times faster than that of the InGaN layer photoelectrode. Furthermore, the current density for the InN/InGaN-QDs photoelectrode, measured during 10 hours at zero applied voltage, under white light illumination, is very stable (figure 6.19 (b)). Figure 6.19 (c) shows the theoretical and experimental values of amount of hydrogen produced at zero applied voltage under white light illumination per active area during 8 h for the InN/InGaN-QDs-photoelectrode. Quantitatively the hydrogen generation as function of time is determined from Faraday's law of electrolysis, introduced in the previous chapter by equation 5.20. From which the theoretically deduced and experimentally measured hydrogen generation rates per active area amount to 86 µmol·h^{-1}·cm^{-2} and 81 µmol·h^{-1}·cm^{-2}, respectively. The Faradaic efficiency (which refers to the ratio of theoretically predicted amount of H_2 divided by the measured amount in a certain time period) is about 94%.

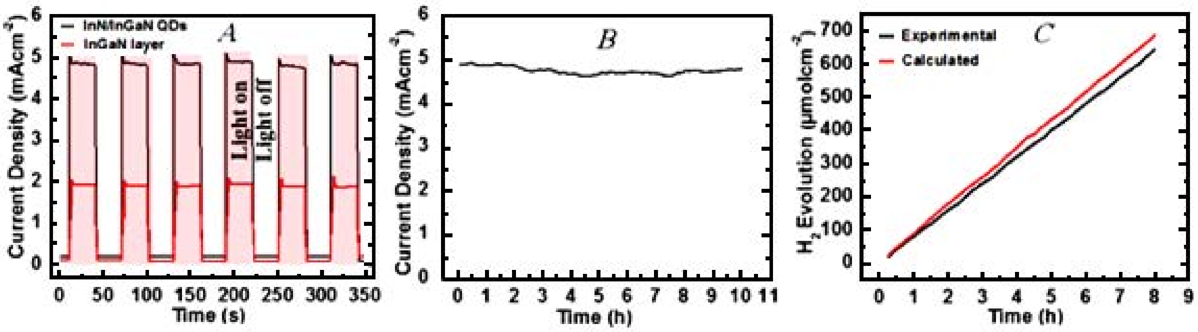

Figure 6.19: (a) Current densities as function of time at zero externally applied voltage versus the Pt counter electrode under white light illumination with 30 s light on/off cycles for the InN/ InGaN-QDs and InGaN-layer-photoelectrodes. (b) Current density measured during 10 h at zero applied voltage under white light illumination for an InN/InGaN QDs photoelectrode. (c) The theoretical and experimental amount of hydrogen generated during 8 h at zero applied voltage under white light illumination for the InN/InGaN QDs photoelectrode.

To summarize, a PEC cell using InN/InGaN QDs photoelectrodes been demonstrated, exhibiting excellent photocurrent density, high IPCE values, good switching performance, stability, and a large hydrogen generation rate, significantly higher than that obtained when using a bare InGaN layer photoelectrode. Presented InN/InGaN-QDs-PEC cell has full potential to compete and even outperform other reported PEC cells.

A real comparison between presented results for the InN /InGaN-QDs electrode and the previous NWM cannot be done; mainly due to the fact that both excitation light and used electrolyte differed. Nevertheless the amount of Hydrogen obtained at 360 nm is much higher for the InN/InGaN-QDs (~420.0 µmol cm^{-2}) than the NWM based photo-anode obtained at 350 nm (~22.4 µmol cm^{-2}). To clarify the possible origin of the difference, further studies are required.

6.3 Electrochemical analysis

6.3.1 Electrocatalytic oxidation enhancement at the surface of InGaN films and nanostructures grown directly on Si(111)

In the following an extensive electrochemical is presented for a series of structures grown on Si(111) by the recipes shown in chapter 3. The growth temperatures, V-III flux ratios, and In and Ga fluxes, as are In-content and bandgap listed in Table 6.3.

Sample	Growth temperature [ºC]	V-III flux ratio	In flux [10^{13}atoms/ (s cm)]	Ga flux [10^{13}atoms/ (s cm)]	In content (%)	E_g (eV)
M1	450	1.3	3.32	52.1	6	3.09
M2	400	1.37	18.4	34.2	35	1.89
M3	450	1.58	33.3	12.3	73	0.94
M4	450	1.69	37.5	5.11	88	0.76
M5	485	2	21.6	14.4	60	1.18
M6	400	4.2	11.5	5.66	67	1.04

Table 6.3: Growth temperatures, V-III flux ratios, In and Ga fluxes, In contents and bandgap energies for samples M1 to M6.

Samples M1-M4, grown under slightly N-rich conditions with V-III flux ratio around 1.5 are compact InGaN layers with increasing In content, distinct c-plane island structure (seen in the SEM images in figure 6.20 (a-d)), and ~450 nm thickness. For sample M5, the V-III flux ratio was increased to 2 and the growth temperature to 485^{o}C. For sample M6 the V-III flux ratio was further increased to 4 and the growth temperature was decreased to 400^{o}C. Sample M5 (SEM image in figure 6.20 (e)) exhibits a nanowall network and sample M6 (plan-view and cross-sectional SEM images in figure 6.20 (f)) nanocolumns. In addition, two samples were grown in same conditions as M3 and M5 with InN QDs on top. The QDs were formed by supplying the In flux of M3 for 10 seconds for sample ‘M3 plus InN QDs’ and after In flux adjustment for sample ‘M5 plus InN QDs’.

For electrochemical measurements silver paste contacts were deposited. The contacts are ohmic for the higher In. For all electrodes, the contacts were placed on the surface at the edge of the samples, not in contact with the electrolyte. For the nanocolumnar sample this implies a contact with the p-Si substrate which is also in contact with the electrolyte. Independent measurements, however, showed that the p-Si substrate is not electrochemically active. Further, the contact between In-rich InGaN and p-Si is ohmic [Aseev 2015], guaranteeing a valid measurement of the electrochemical properties also for the NCs. The fixed sample area exposed to the electrolyte was 7.5 mm^2. The electrocatalytic properties of the InGaN samples were probed with the potassium hexacyanoferrate (II) / potassium hexacyanoferrate (III) redox couple with 5 mM equimolar concentration and 0.1 M KCl in aqueous solution. This specific redox couple is chosen as it has a fast electron transfer rate and has a negative charge (anion) for which as seen by previous experiments (water splitting) presented electrodes are very sensitive to as selective. In all CV measurements a scan rate of 25 mVs^{-1} was used. The electrode potential was scanned first from positive to negative voltages and then back over ranges to fully develop the characteristic shapes without scanning towards highly positive or negative voltages to avoid other reactions.

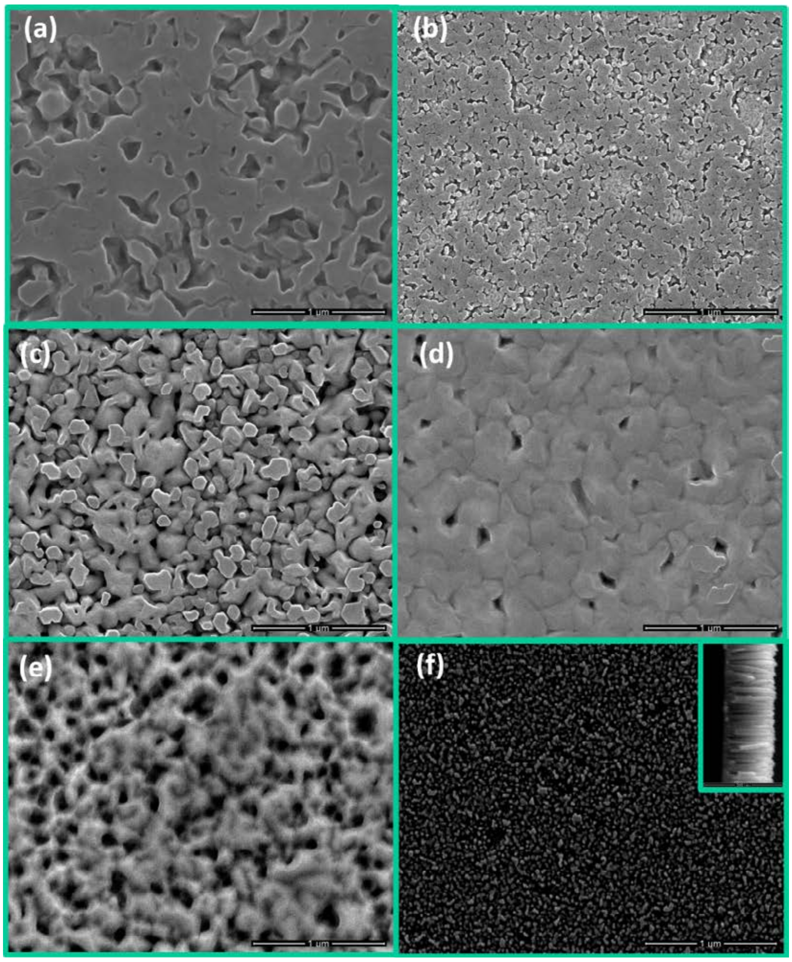

Figure 6.20: (a)-(f) Plan-view SEM images of samples M1-M6. The inset in (f) shows the cross-section of sample M6.

Figure 6.21 (a)-(d), shows the CV measurements for samples M1-M4. Sample M1 does not show clear anodic or pronounced cathodic current peaks, which could be ascribed to the wide InGaN bandgap and higher ohmic resistance, shifting the anodic and cathodic peaks to potential values not recorded in this experiment. As it can be observed, the anodic peak became better developed and shifted to less positive electrode potential values as the In content increased (samples M2 to M4), most clear for samples M2 to M3; less evident for samples M3 to M4. Samples M3 and M4 both likely already exhibit an InN like surface due to In surface accumulation/segregation during growth for the high In contents. On the other hand, a cathodic current peak develops for samples M2 and M3 and then becomes strongly suppressed for sample M4. This shows the enhancement of catalytic oxidation activity or anion selectivity with increase of the In content which is attributed to the presence of the intrinsic positively charged surface donors with increasing density. This is also in line with the symmetric CV curve for sample M2, *i.e.*, quasi-reversible oxidation and reduction which is more like for metallic electrodes: The density of surface donors decreases with decreasing In content. Below around 40% In content the surface states move from the conduction band into the bandgap and, hence, change from donor-like to acceptor-like, causing a transition from electron accumulation to electron depletion [Bailey 2008]. Therefore, M2 behaves like a common highly-doped n-type semiconductor similar to metals.

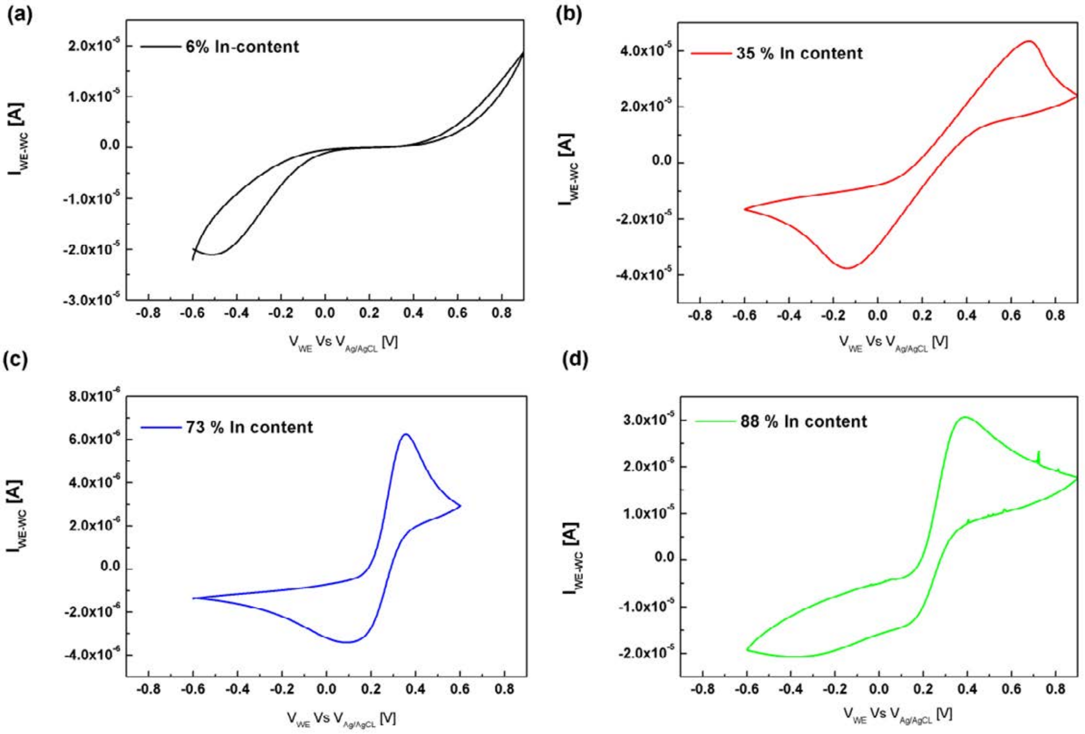

Figure 6.21: (a)-(d) Cyclic voltagrams for the c-plane InGaN layers M1 to M4 with increasing In content in 0.1 M KCl solution containing 5 mM $K_3[Fe(CN)_6]/K_4[Fe(CN)_6]$ (1:1). Scan rate: 25 mVs^{-1}.

The reduced overall current for sample M3 already indicates the major electrochemical activity of the c-plane due to the highest density of surface donors because its portion is lowest for this sample as is seen in the SEM image in figure 6.20 (c). This will become very clear when discussing the nanowall network and nanocolumns with surfaces intentionally inclined towards the c-plane of reduced or no electrocatalytic activity.

Figure 6.22 (a,b) depicts the cyclic voltagrams of the nanowall network and nanocolumns of samples M5 and M6. The electrode potentials of their anodic current peaks are consistent with those of samples M2 to M4 for the In contents between 60 and 70% together with the quasi-reversible oxidation and reduction for these In contents. The anodic and cathodic peak currents are smallest for the nanowall network, exhibiting the smallest portion of active c-plane of all samples. These results together with the ones from figure 6.21 show that the electrode potential of the anodic current peak is mainly given by the In content, i.e., the density of positively charged surface donors while the peak current itself is governed by the area of active c-plane – consistently referring back to the low current for sample M3.

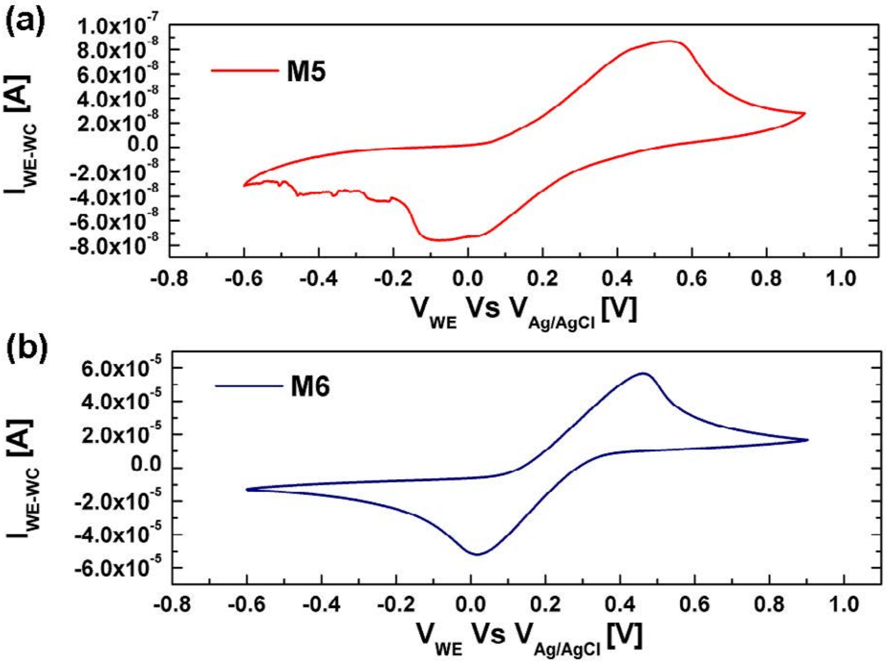

Figure 6.22: Cyclic voltagrams for the (a) nanowall network M5 and (b) nanocolumns M6 in 0.1M KCl solution containing 5 mM $K_3[Fe(CN)_6]/K_4[Fe(CN)_6]$ (1:1). Scan rate: 25 mVs^{-1}.

For the nanocolumns, the portion of active c-plane on top is still relatively high and the accordingly high current might be supported by the generally high crystal quality of nanocolumns where dislocations are eliminated when reaching the sidewalls. Notably, the current is comparable to that of samples M2 and M4 despite the large surface area of the m-plane sidewalls and the electrode potential of the anodic current peak agrees with that of the c-plane InGaN layers. This leaves the conclusion that the m-planes are not or negligibly participating in the electrochemical reaction which is attributed to the absence or low density of surface donors requiring larger electrode potentials.

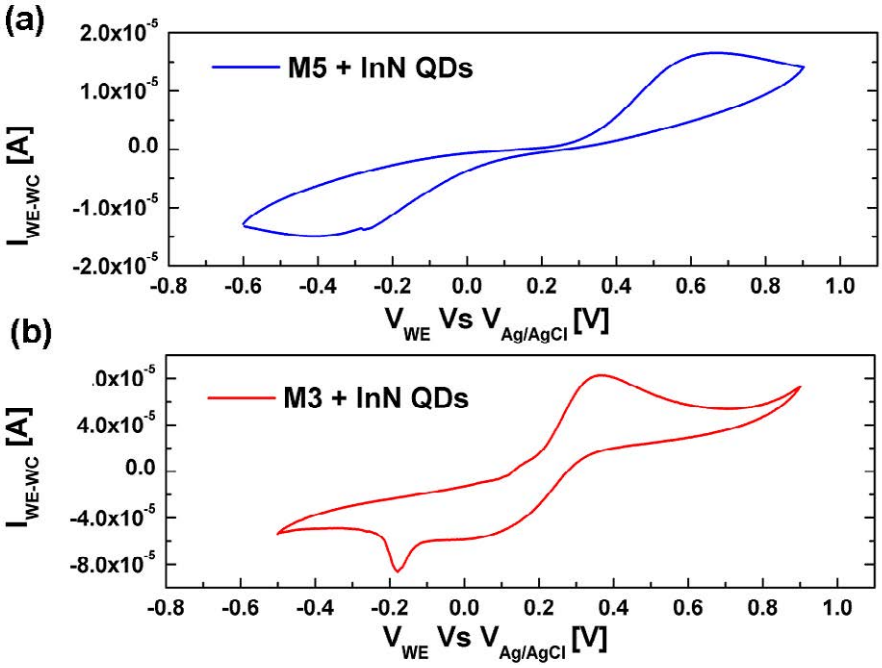

Figure 6.23: Cyclic voltagrams for the (a) nanowall network M5 plus InN QDs and (b) c-plane InGaN layer M3 plus InN QDs in 0.1M KCl solution containing 5mM $K_3[Fe(CN)_6]/K_4[Fe(CN)_6]$ (1:1). Scan rate: 25 mVs^{-1}.

Finally, the effects of the InN QDs for the nanowall network, sample ‘M5 plus InN QDs’, and for the c-plane InGaN layer with 73% In content, sample ‘M3 plus InN QDs’ are shown in figure 6.23 (a,b). There is a clear enhancement of the overall currents indicating that the QDs act as active sites; notice the different current scale in the graphs. For the nanowall network, however, the electrode potentials of the anodic and cathodic current peaks are strongly enlarged. This suggests that the QDs activate the semi-polar sidewalls of the nanowall network with large surface area, having, however, a lower density of positively charged surface donors, requiring the larger electrode potentials. The anodic peak current of sample ‘M3 plus QDs’ is most strongly enhanced staying at the low electrode potential while the cathodic current peak is suppressed. The anodic peak current of sample M3 is the highest among all investigated samples. All results together, this confirms that the combination of the highest surface donor density for c-plane InN with the zero-dimensional QD electronic properties is leading to the strongest increase of catalytic oxidation activity or anion selectivity as observed in the biosensor and water splitting experiments [Alvi 2012, 2015].

In summary, a pronounced electrocatalytic oxidation enhancement has been shown at the surface of InGaN films and nanostructures directly grown on Si(111) by PA MBE with increasing In content and proximity of surface and nanostructure sidewalls to the c-plane. This was attributed to the corresponding increase of the density of positively charged surface donors promoting the electron transfer. Most pronounced is the enhancement by functionalization of c-plane In-rich InGaN layers with InN QDs, attributed to the highest density of surface donors together with the zero-dimensional electronic QD properties inducing uncompensated surface charge. These results are of extreme importance for further boosting the excellent efficiency of InN/InGaN QDs based biosensors and water-splitting and other activated electrochemical processes, finding an optimum balance between catalytic efficiency driving the reaction and surface area increasing the amount.

CHAPTER 7

CONCLUSIONS

7.1 Conclusions

The most significant results obtained throughout this thesis are summarized and briefly commented below.

A comprehensive study by MBE growth of InN QDs on High In-.content InGaN on commercial GaN templates showed that optical active InN QDs are obtained for 1 and 2 ML InN coverage. Presented results are first of their kind on High In-content InGaN.

Fabricated InN QDs/InGaN based *potentiometric* biosensors, for glucose as for cholesterol, presented high sensibility and stability together with fast response (among fastest) compared to other semiconductors/metal oxides materials.

InN QDs/InGaN photoande used for water splitting showed that Hydrogen generation occurred not only with high efficiency, compared to bare InGaN layer, but in addition was shown to occur even at zero applied overpotential. Care has to be taken when selecting electrolyte as it is seen to contribute to the redox process.

Their good performance in both biosensing (Glucose and Cholesterol biosensor) and water splitting applications are direct proof that their unique, quantum and intrinsic, material properties directly influences the electrochemical activity of the high In-content InGaN material. Local variations, by the presence of InN QDs, in screening of the 2-DEG present directly below the high In-content InGaN surface, is thought to give rise to a non uniform surface charge distribution which would effectively enhance the electron capture mechanism by the electrode, i.e the oxidation process.

The know-how was successfully transferred to the cheap and widely known/used Si(111) substrate. Growth was optimized, in terms of In-content and crystal quality, for both nanowall network and InGaN layers. Indication of island formation with wetting layer, thus possible SK growth of InN QDs, on high In-content InGaN/Si(111) was demonstrated for the first time.

Hydrogen generation by the Nanowall network showed good efficiency, compared to InGaN films grown on GaN templates, and without the need of any external overpotential.

An extensive study on the electrocatalytic properties done by cyclic voltammetry and a redox probe (potassium hexacyanoferrate (II) / potassium hexacyanoferrate (III)) for both film and nanostructures showed that an increase of In-content correlates with an enhancement in the oxidation process (reduced oxidation potential) occurring at the III-nitride electrode. This is consistent with the increase of positive donor states that is expected upon increase of In content, being therefore assigned as the main responsible for observed results. The amount of polar (c-) planes, which varies among used nanostructures, is reflected in the obtained current intensity (oxidation peak) value. The presence of InN QDs is seen in the nanostructures to electrochemically activate non-polar planes increasing overall current intensity. In the case of InGaN layers it also enhances the oxidation process, having thus a catalytic effect. Therefore the performance of InGaN films in electrochemical applications demands an optimization in both In-content as amount of polar (c-) plane and InN QDs can be used a catalyst for the oxidation process occurring at the anode.

In summary, it is shown that InN QDs on high In-content InGaN can be grown both on sapphire and Si and that they present exceptional performance as glucose and cholesterol bio sensors as for H_2 production by electrochemical water splitting.

7.2 Future Outlook

In the presented thesis several critical points were studied, from growth optimization to electrochemical optimization. In terms of direct growth on Silicon by MBE there still is a lot of room for investigation especially for ordered growth. In general, capping and stacking of quantum dots has to be explored to improve the luminensce efficiency and quality of surface dots, required for optoelectronic applications. Doping of the layers for optical applications would also be of great importance.

From an electrochemical point of view a balance for the electrochemical active sites (In content) and morphology (crystal planes) needs to be found as this would considerably increase the efficiency for water-splitting. Applications as optical biosensors and ion selective field transistor should be explored as the observed photoluminescence and anion selectivity shows great potential for this.

REFERENCES

References on alphabetic order

Adelmann 2000	C. Adelmann, J. Simon, G. Feuillet, N. T. Pelekanos, B. Daudin, and G. Fishman, *Appl. Phys. Lett*. **76**, 1570 (2000)
Aharoni 2000	A. Aharoni (2000), *Introduction to the theory of ferromagnetism* (2nd ed.). New York, Oxford University Press Inc.
Akasaki 1989	I. Akasaki, H. Amano. Y. Koide, K. Hiramatsu and N. Sawaki, *J. Cryst. Growth.* **98**, 209 (1989)
Akasaki 1991	I. Akasaki, H. Amano, M. Kito, and K. Hiramatsu, *J. Lumin.* **666**, 48-49, (1991)
Alireza 2013	K. Alireza, S. Ke, J. Yi, C. Chulmin, J. Huisu, Z. Yuchun, M. Kristian, N. Perry, J. Sungho, Y. J. Gun and W. Deli, *Nano Lett*. **13** (7), 3017–3022 (2013)
Alvi 2012	N. H. Alvi, P. E. D. Soto Rodriguez, V. J. Gómez, Praveen Kumar, G. Amin et al. *Appl. Phys. Lett.* **101**, 153110 (2012)
Alvi 2013	N. H. Alvi, V. J. Gómez, P. E. D. Soto Rodríguez, P. Kumar, S. Zaman, M. Willander and R. Nötzel, *Sensors* **13**, 13917-13927 (2013)
Alvi 2013b	N. H. Alvi, P. E. D. Soto Rodríguez, V. J. Gómez, P. Kumar, M. Willander and R. Nötzel, *Appl. Phys. Express* **6**, 115201 (2013)
Alvi 2015	N. H. Alvi, P. E. D Soto Rodriguez, P. Aseev, V. J. Gómez, A. H. Alvi, W. Hassan, M. Willander, and R. Nötzel. *Nano Energy*, **13**, 291-297 (2015)
Amano 1986	H. Amano, N. Sawaki, I. Akasaki and Y. Toyoda, *Appl. Phys. Lett.* **48**, 353 (1986)
Amano 1989	H. Amano, M. Kito, K. Hiramatsu, and I. Akasaki, *Jpn. J. Appl. Phys.* **28**, L2112 (1989)
Ambacher 1998	O. Ambacher, *J. Phys. D: Appl. Phys.* **31**, 2653–2710 (1998)
Aprile 2008	C. Aprile, A. Corma, and H. Garcia, *Phys. Chem. Chem. Phys.* **10**, 769-783 (2008)
Aseev 2013	P. Aseev, P. E. D. Soto Rodriguez, P. Kumar, V. J. Gómez, N. H. Alvi, J. M. Mánuel, F. M. Morales, J. J. Jiménez, R. García, E. Calleja, and R. Nötzel, *Appl. Phys. Express* **6**, 115503 (2013)
Aseev 2015	P. Aseev; P. E. D. Soto Rodriguez; V. J. Gómez; N.H. Alvi; J. M. Mánuel; F. M. Morales; J. J. Jiménez; R. García; A. Senichev; C. Lienau; E. Calleja; R. Nötzel. *Appl. Phys. Lett.*, **106**, 072102 (2015)
Bailey 2008	L. R. Bailey, T. D. Veal, P. D. C. King, C. F. McConville, J. Pereiro, J. Grandal, M. A. Sánchez-García, E. Muñoz and E. Calleja, *J. Appl. Phys.* **104**, 113716 (2008)
Bae 2016	H. Bae, E. Kim,J. Park, S. Kang, K. Fujii, S. H. Lee,d, H. Lee and J. Ha, *J. Electrochem. Soc.*, **163** (3) H213-H217 (2016); DOI: 10.1149/2.0831603jes
Bard 2001	A.J. Bard, L.R. Faulkner (2001). *Electrochemical Methods*. 2nd Ed. John Wiley and Sons Ltd., New York

Basu 2007	A. K. Basu, P. Chattopadhyay, U. Roychoudhuri and R. Chakraborty, *Bioelectrochemistry* **70**, 375–379 (2007)
Behme 1997	G. Behme, A. Richter, M. Süptitz, and Ch. Lienau, *Rev. Sci. Instrum.* **68**, 3458 (1997)
Benton 2013	J. Benton, J. Bai and T. Wang, *Appl. Phys. Lett.* **102**, 173905-1–173905-4 (2013)
Berezkin 1989	V. G. Berezkin, *Chem. Rev* **89** (2), pp. 279-285 (1989)
Bernardini 1997	F. Bernardini, V. Fiorentini, and D. Vanderbilt, *Phys. Rev. B.* **56**, R10024 (1997)
Bhattacharya 1997	P. Bhattacharya (1997). *Semiconductor optoelectronic devices* (2nd ed.). Upper Saddle River, NJ: Prentice Hall Inc. Pp. 46-49.
Blake 2012	A. H. Blake, D. Caselli, C. Durot, J. Mueller, E. Parra, J. Gilgen, A. Boley, D. J. Smith, I. S. T. Tsong, J. C. Roberts, E. Piner, K. Linthicum, J. W. Cook, D. D. Koleske Jr., M. H. Crawford, and A. J. Fischer, *J. Appl. Phys.***111**, 033107 (2012).
Boettcher 2010	S. W. Boettcher, J. M. Spurgeon, M. C. Putnam, E. L. Warren, D. B. Turner-Evans, M. D. Kelzenberg, J. R. Maiolo, H. A. Atwater and N. S. Lewis, *Science* **327**, 185–187 (2010)
Boettcher 2011	S. W. Boettcher, E. L. Warren, M. C. Putnam, E. A. Santori, D. Turner-Evans, M. D. Kelzenberg, M. G. Walter, J. R. McKone, B. S. Brunschwig, H. A. Atwater and N. S. Lewis, *J. Am. Chem. Soc.* **133**, 1216–1219 (2011)
Boo 2011	B. H. Boo, D.E. Kang, *J Korean Phys. Soc*. **59**, (5) (2011)
Brown 2004	J. Brown, F. Wu, P.M Petroff and J. S. Speck "GaN quantum dot density control by rf-plasma molecular beam epitaxy" Appl. Phys. Lett. (5) 84 (2004) DOI: 10.1063/1.1645333
Butcher 2005	K. S. A. Butcher and T. L. Tansley, *Superlattices Microstruct.* **38**, 1–37 (2005)
Chang 2010	Y. L. Chang, Z. Mi, F. Li, *Adv. Funct. Mater*. **20**, 4146-4151 (2010)
Chao 2006	C. K. Chao, H. S. Cchang, T. M. Hsu, C.N Hsiao, C. C. Kei, S. Y. Kuo, and J. I Chyi, *Nanotechnology* **17**, 3930 (2006)
Chen 2001	P. P. Chen, Z. L. Miao and W. Lu, *J. Cryst. Growth* **227**, 108 (2001)
Chen C. 2006	C. F. Chen, C. L. Wu, and S. Gwo, *Appl. Phys. Lett.* **89**, 252109 (2006)
Chen J. 2002	J. X. Chen, A. Markus, A. Fiore, U. Oesterle, R. P. Stanley, J. F. Carlin, R. Houdré, M. Ilegems, L. Lazzarini, L. Nasi, M. T. Todaro, E. Piscopiello, R. Cingolani, M. Catalano, J. Katcki, and J. Ratajczak, *J. Appl. Phys*. **91**,6710 (2002)
Chen **Z.** 2011	Z. Chen, D. Cummins, B.N. Reinecke, E. Clark, M. K. Sunkara, T. F. Jaramillo, *Nano Lett.* **11**, 4168–4175 (2011)
Cheng 2008	K. Cheng, M. Leys, S. Degroote, M. Germain, and G. Borghs, *Appl. Phys. Lett.* **92**, 192111 (2008).
Chichibu 1996	S. Chichibu, T. Azuhata, T. Sota, and S. Nakamura, *Appl. Phys. Lett.* **69**, 4188 (1996)

Cimalla 2007	V. Cimalla, B. Pradarutti, G. Matthäus, C. Brückner, S. Riehem ann, G. Notni, S. Nolte, A. Tünnermann, V. Lebedev, and O. Ambacher, *Phys. Status Solidi (B)* **244**, 1829 (2007)
Coelho 2010	B. Coelho, A. C. Oliveira, and A. Mendes, *Energ. Environ. Sci.* **3** (10), 1398-1405 (2010)
Condon 1928	E. Condon, *Phys. Rev*. **32**, 858-872 (1928)
Crabtree 2004	G. W. Crabtree, M. S. Dresselhaus, and M. V. Buchanan, *Phys. Today* **57** (12), 39 (2004)
Damilano 1999	B. Damilano, N. Grandjean, S. Dalmasso, and J. Massies, *Appl. Phys. Lett*. **75**, 3751 (1999)
Das 2010	A. Das, S. Magalhaes, Y. Kotsar, P.K. Kandaswamy, B. Gayral, K. Lorenz, E. Alves, P. Ruterana and E. Monroy, *Appl. Phys. Lett.* **96**, 181907 (2010)
Davies 1998	J. H. Davies (1998), The physics of low-dimensional semiconductors: An introduction, Cambridge University Press, New York
Davydov 2002	V. Y. Davydov, A. A. Klochikhin, R. P. Seisyan, V. V. Emtsev, S. V. Ivanov, F. Bechstedt, J. Furtmuller, H. Harima, A. V. Mudyri, J. Aderhold, O. Semchinova, and J. Graul, *Phys. Status Solidi (B)* **229**(3), R1-R3 (2002)
Deerinck 2008	T. J. Deerinck, *Toxicol Pathol.* **36**, 112-116 (2008)
Dhand 2007	C. Dhand, S. P. Singh, S. K. Arya, M. Datta and B. D. Malhotr, *Anal. Chim. Acta* **602**, 244–251 (2007)
Dhand 2008	C. Dhand, S. K. Arya, M. Datta, and B. D. Malhotra, *Anal. Biochem.* **383**, 194-199 (2008)
Diels-Alder	*The Diels-Alder Reaction*, Department of Chemistry, Michigan State University, https://www2.chemistry.msu.edu/faculty/reusch/VirtTxtJml/enrgtop.htm
Dingle 1971	R. Dingle, K. L. Shakleek, R. F. Leheny and R. B. Zetterstrom, *Appl. Phys. Lett.* **19**, 5 (1971)
Dogonadze 1965	R. R. Dogonadze, A. M. Kuznetsov and A. A. Chernenko, *Russ. Chem. Rev.* **34** 858 (1965)
Dreybrodt 1993	J. Dreybrodt, A. Forchel, and J. P. Reithmaier, *Phys. Rev. B* **48**, 14741(R) (1993)
Egawa 2005	T. Egawa, B. Zhang, and H. Ishikawa, *IEEE Elect. Devices Lett.* **26**, 169 (2005).
Farrow 1996	R. F. C. Farrow (1996), *Molecular Beam Epitaxy: Applications to Key Materials*, Materials Science and Process Technology, William Andrew.
Fenger 2009	J. Fenger, *Atmos. Environ.* **43** (1), 13-22 (2009)
Finken 2015	M. Finken, A. Wille, B. Reuters, M. Heuken, H. Kalisch and A. Vescan, *Phys. Status Solidi B* **252**, (5), 895–899(2015); DOI 10.1002/pssb.201451576
Föll	H. Föll, “Recombination and Luminescence”, *Semiconductors I*. Retrieved from www.tf.uni-kiel.de/matwis/amat/semi_en/kap_5/backbone/r5_1_2.html
Franck 1925	J. Franck, *Trans. Faraday Soc.* **21**, 536-542 (1925)

Fujii 2005	K. Fujii, K. Kusakabe and K. Ohkawa, *Jpn. J. Appl. Phys.* **44**, 7433–7435 (2005)
Gačević 2013	Ž. Gačević, V. J. Gómez, N. García Lepetit, P. E. D. Soto Rodríguez, A. Bengoechea, S. Fernández-Garrido, R. Nötzel and E. Calleja, *J. Cryst. Growth*, **364**, 123–127 (2013)
Gallinat 2007	C. S. Gallinat, G. Koblmüller, J. S. Brown, and J. S. Speck, *J. Appl. Phys.* **102**, 064907 (2007)
Gerrischer 1983	H. Gerrischer and W. Elardst, *Appl. Phys. Lett*. **43** 393 (1983)
Gfroerer 2000	T. H. Gfroerer (2000) *Photoluminiscence in analysis of surfaces and interfaces*. In Enclopedia of Analytical Chemistry. Ed. R.A. Meyers. Pp. 9209-9231. John Wiley and Sons Ltd., Chichester.
Gileadi1975	E. Gileadi, E. Kirowa-Eisner, and J. Penciner (1975), *Interfacial Electrochemistry: An Experimental Approach*. Addison-Wesley Publishing Company
González 2009	González D, Lozano JG, Herrera M, Browning ND, Ruffenach S, Briot O, Garcia G: *J Appl Phys* **105**:013527 (2009)
Goodey 2007	A.P. Goodey, S. M. Eichfeld, K. K. Lew, J. M. Redwing and T. E. Mallouk, *J. Am. Chem. Soc.* **129**, 12344–12345 (2007)
Grandal 2009	J.Grandal, M.A. Sánchez-García , E. Calleja , S. Lazic, E. Gallardo, J. M. Calleja, E. Luna , A. Trampert, M. Niebelschutz, V. Cimalla, O. Ambacher (2009). *'InN nanocolumns* (Book Chapter)' ,Ed. Taylor and Francis Group: Indium Nitride and related alloys, 599-615
Grandjean 2007	N. Grandjean M. Ilegems, *Proceedings of the IEEE* **95**, 9, 1853-1865 (2007)
Grieshaber 2008	D. Grieshaber, R. MacKenzie, J. Vörös and E. Reimhult, *Sensors* **8**, 1400-1458 (2008)
Haddad 200**3**	D. B. Haddad, H. Dai, R. Naik, C. Morgan, V. M. Naik, J. S. Thakur, G. W. Auner, L. E. Wenger, H. Lu, W. J. Schaff, *Mater. Res. Soc. Symp. Proc.* **798**, Y12.7 (2003)
Hauswald 2014	C. Hauswald, P. Corfdir, J. K. Zettler, V. M. Kaganer, K. K. Sabelfeld, S. Fernández-Garrido, T. Flissikowski, V. Consonni, T. Gotschke, H. T. Grahn, L. Geelhaar, and O. Brandt, *Phys. Rev. B* **90**, 165304 (2014)
Heying 1996	B. Heying, X. H. Wu, S. Keller, Y. Li, D. Kapolnek, B. P. Keller, S. P. DenBaars, and J. S. Speck, *Appl. Phys. Lett.* **68**, 643 (1996)
Heying 2000a	B. Heying, R. Averbeck, L. F. Chen, E. Haus, H. Riechert, and J. S. Speck, *J. Appl. Phys*. **88**, 1855 (2000)
Heying 2000b	B. Heying, I. Smorchkova, C. Poblenz, C. Elsass, P. Fini, S. Den Baars, U. Mishra, and J. Speck, *Appl. Phys. Lett.* **77**, 2885-2887 (2000)
Higashiwaki 2004	M. Higashiwaki and T. Matsui, *J. Cryst. Growth* **162**, 269 (2004)
Ho 1996	I. Ho, G.B. Stringfellow, *Appl. Phys. Lett.* **69**, 2701 (1996)

Hoffmann 1996	A. Hoffman (1996). *Festkörperprobleme 36: Optical properties GaN*. In R. Helbig (Ed.), *Advances in Solid State Physics*. Springer Berlin Heidelberg. Pp. 33-56
Hoffmann 1998	A. Hoffmann, L. Eckey, H. Siegleand A. Kaschner, J. Christen, F. Bertram, and Q. K. K. Liu. *Acta. Phys. Pol. A* **94**,125 (1998)
Hofmann 2006	T. Hofmann, T. Chavdarov, V. Darakchieva, H. Lu, W. J. Schaff, and M. Schubert, *Phys. Status Solidi C* **3**, 1854 (2006)
Holec 2006	D. Holec (2006), *Critical Thickness Calculations for InxG1-xaN/GaN systems*, Selwyn College, University of Cambridge (2006)
Hooper 2004	S. E. Hooper, M. Kauer, V. Bousquet, K. Johnson, J. M. Barnes, et al., *Electron. Lett.* **40**, 33–34 (2004)
Hou 2012	Y. Hou, F. Zuo, A. Dagg and P. Feng, *Nano Lett.* **12**, 6464–6473 (2012)
Hovel 1972	H. J. Hovel, and J. J. Cuomo, *Appl. Phys. Lett.* **20**, 71 (1972)
Hovington 1997	P. Hovington, D. Drouin, and R. Gauvin. *Scanning*, **19** (1), 1–14 (1997).
Hsu 2008	L. Hsu and W. Walukiewicz, *J. Appl. Phys*. **104**, 024507 (2008).
Hwang 2012	Y. J. Hwang, C. H. Wu, C. Hahn, H. E. Jeong and P.D. Yang, *Nano Lett.* **12**, 1678–1682 (2012)
Hwang **J.** 2013	J. S. Hwang, T. Y. Liu, S. Chattopadhyay, G. M. Hsu, A. M. Basilio, H. W. Chen, Y. K. Hsu, W. H. Tu, Y. G. Lin, K. H. Chen, C. C. Li, S. B. Wang, H. Y. Chen, and L. C. Chen, *Nanotechnology* **24**, 055401 (2013)
Intonti 2001	F. Intonti, V. Emiliani, C. Lienau, T. Elsaesser, R. Nötzel, and K. Ploog, *Phys. Rev. B* **63**, 075313 (2001)
Inushima 2001	T. Inushima, V. V. Mamutin, V. A. Vekshin, S. V. Ivanov, T. Sakon, M. Motokawa, and S. Ohoya, *J. Cryst. Growth* **227-228**, 481-485 (2001)
Israr 2010	M. Q. Israr, J. R. Sadaf, M. H. Asif, O. Nur, M. Willander and B. Danielsson, *Thin Solid Films* **519**, 1106–1109 (2010)
Israr 2011	M. Q. Israr, J.R. Sadaf, O. Nur, M. Willander, S. Salman and B. Danielsson, *Appl. Phys. Lett.* **98**, 253705:1–253705:3 (2011)
Jacob 2007	K. T. Jacob, Shubhra Raj, and L. Rannesh, *Int. J. Mater. Res.* **98** (9), 776-779 (2007)
Jain 1997	Jain, S. C., Harker, A. H., and Cowley, R. A., Misfit strain and misfit dislocations in lattice mismatched epitaxial layers and other systems, Phil. Mag. A 75, June 1997, pp. 1461–1515.
Jain 2000	S. C. Jain, M. Willander, J. Narayan, and R. V. Overstraeten, *J. Appl. Phys*. **87**, 965 (2000)
Jamieson 2007	T. Jamieson, R. Bakhshi, D. Petrova, R. Pocock, M. Imani, and A. M. Seifalian, *Biomaterials* **28**, 4717–4732 (2007)
Jones 2011	J. Jones (2011), *An Introduction to Nanotechnology*, Agilent Technologies www.agilent.com/labs/features/2011_101_nano.html

Juodkazytė 2014 J. Juodkazytė, B. Šebeka, I. Savickaja , A. Kadys, E. Jelmakas, T. Grinys, S. Juodkazis, K. Juodkazis, and T. Malinauskas, Solar Energy Materials & Solar Cells **130**, 36–41 (2014)

Juza 1938 R. Juza and H. Hahn, *Z. Anorg. Alleg. Chem.* **239**, 282 (1938)

Kane 1957 E. Kane, *J. Phys. Chem. Solids* **1**, 249-261 (1957)

Kane 2014 M. H. Kane and N. Arefin (2013) Chapter 4: *Gallium nitride (GaN) on silicon substrates for LEDs*. In Jian-Jang Huang, Hao-Chung Kuo, and Shyh-Chiang Shen, *Nitride Semiconductor Light-Emitting Diodes (LEDs)*: Materials, Technologies and Applications.

Kapolnek 1995 D. Kapolnek, X. H. Wu, B. Heying, S. Keller, B. P. Keller, U. K. Mishra, S. P. DenBaars, and J. S. Speck, *Appl. Phys. Lett.* **67**, 1541 (1995)

Ke 2006 W. C. Ke, C. P. Fu, C. Y. Chen, L. Lee, C. S. Ku, W. C. Chou, W.-H. Chang, M. C. Lee, W. K. Chen, W. J. Lin, and Y. C. Cheng, *Appl. Phys. Lett.* **88**, 191913 (2006)

Khaselev 1998 O. Khaselev and J. Turner, *J. Electrochem. Soc.* **145**, 3335 (1998)

Kim 2012 J. Y. Kim, J. W. Jang, D. H. Youn, J. Y. Kim, E. S. Kim and J. S. Lee, *RSC Adv.* **2** 9415–9422 (2012)

King 2007 P. D. C. King, T. D. Veal, C. F. McConville, F. Fuchs, J. Furthmuller, F. Bechstedt, P. Schley, R. Goldhahn, J. Schoermann, D.J. As, K. Lischka, D. Muto, H. Naoi, Y. Nanishi, H. Lu and W. J. Schaff, *Appl. Phys. Lett.* **91**, 092101 (2007)

King 2008a P. D. C. King, T. D. Veal, P. H. Jefferson, S. A. Hatfield, L. F. J. Piper, C. F. McConville, F. Fuchs, J. Furthmüller, F. Bechstedt, H. Lu, and W. J. Schaff. *Phys. Rev. B* **77**, 045316 (2008)

King 2008b P. D. C. King, T. D. Veal, A. Adikimenakis, H. Lu, L. R. Bailey, E. Iliopoulos, A. Georgakilas, W. J. Schaff, and C. F. McConville, *Appl. Phys. Lett.* **92**, 172105 (2008)

King 2009 P. D. C. King, T. D. Veal, and C. F. McConville. *J. Phys. Cond. Matt.* **21**, 174201, (2009)

Kirste 2015 R. Kirste, N. Rohrbaugh, I. Bryan, Z. Bryan, R. Collazo, and A. Ivanisevic, “Electronic Biosensors Based on III-Nitride Semiconductors“, *Annu. Rev. Anal. Chem*, 8:8.1–8.21 (2015)

Kittel 1956 C. Kittel (1956). *Introduction to Solid State Physics* (2nd ed.). New York: John Wiley and Sons, Inc.

Knübel 2010 A. Knübel, V. M. Polyakov, L. Kirste, and R. Aidam, *Appl. Phys. Lett.* **96**, 082106 (2010)

Komaki 2007 H. Komaki, R. Katayama, K. Onabe, M. Ozeki, and T. Ikari, *J. Cryst. Growth* **305**, 12 (2007).

Korotcenkov 2011 G. Korotcenkov (2011). *Chemical Sensors Fundamentals of Sensing Materials*, Vol. 3. New York: Momentum Press.

Kruse 2012	C. Kruse, S. Figge, and D. Hummel (2012). *Growth of II-VI and III-nitride quantum-dot microcavitity systems*, in: F. Jahnke, Optics with Semiconductor Nanostructures, Woodhead publishing Limited, Cambridge, pp. 447.
Kryliouk 2005	O. Kryliouk, H. J. Park, H. T. Wang, B. S. Kang, T. J. Anderson, F. Ren, and S. J. Pearton, *J. Vac. Sci. Technol. B* **23**, 1891 (2005)
Kucharski 2009	R. Kucharski, M. Rudziński, M. Zając, R. Doradziński, J. Garczyński, L. Sierzputowski, R. Kudrawiec, J. Serafińczuk, W. Strupiński, and R. Dwiliński, *Appl. Phys. Lett.* **95**, 131119 (2009)
Kudo 2009	A. Kudo and Y. Miseki, *Chem. Soc. Rev.* **38**, 253–278 (2009)
Kumar 2009	P. Kumar, M. Kumar, B. R. Mehta, S.M. Shivaprasad, *Appl. Surf. Sci*. **256**, 480 (2009).
Kumar 2010a	P. Kumar, M. Kumar and S. M. Shivaprasad, *Appl. Phys. Lett*. **97**, 122105 (2010)
Kumar 2010b	P. Kumar, K. Jithes, and S. M. Shivaprasad, *Appl. Phys. Lett*. **97**, 221913 (2010).
Kumar 2012	P. Kumar, M. Tuteja, M. Kesaria, U. V. Waghmare and S. M. Shivaprasad, *Appl. Phys. Lett*. **101** 131605 (2012).
Kumar 2013	P. Kumar, P. E. D. Soto Rodriguez, V. J. Gómez, N. H. Alvi, E. Calleja, and R. Nötzel, *Appl. Phys. Express* **6**, 035501 (2013).
Kumar **A.** 2000	A. Kumar, R. Malhotra, B.D. Malhotra, S. K. Grover, A. Kumar, R. Malhotra, B. D. Malhotra and S. K. Grover, *Anal. Chim. Acta* **14**, 43–50 (2000)
Kumar **M.** 2011	M. Kumar, M.K. Rajpalke, B. Roul, T. N. Bhat, N. Sinha, A.T. Kalghatgi and S. B. Krupanidhi, *Applied Surface Science* **257** (6) 2107-2110 (2011)
Kung 1995	P. Kung, A. Saxler, X. Zhang, D. Walker, T. C. Wang, I. Ferguson, and M. Razeghi, *Appl. Phys. Lett.* **66**, 2958 (1995)
Lauterbach 2012	M. A. Lauterbach, *Optical Nanoscopy* **1** (8) (2012)
Lefebvre 2011	P. Lefebvre, S. Fernández-Garrido, J. Grandal, J. Ristíc, M. A. Sánchez-García, and E. Calleja, *Appl. Phys. Lett.* **98**, 083104 (2011)
Lester 1995	S. D. Lester, F. A Ponce, M. G. Craford, and D. A. Steigerwald, *Appl. Phys. Lett.* **66**, 1249−1251 (1995)
Leszczynski 1999	M. Leszczynski, P. Prystawko, and S. Porowski (1999). *Epitaxy of III-N layers on GaN substrates*, in J. H. Edgar, S. Strite, I. Akasaki, H. Amano, C. Wetzel, *Gallium Nitride and Related Semiconductors*. EMIS Data Review Series 23. London, INSPEC, The Institution of Electrical Engineers.
Li 2005	S. X. Li, K. M. Yu, J. Wu, R. E. Jones, W. Walukiewicz, J. W. Ager, W. Shan, E. E. Haller, Hai Lu, and William J. Schaff. *Phys. Rev. B.* **71**, 161201, (2005)
Li H. 2007	H. Li, Z. Bian, J. Zhu, D. Zhang, G. Li, Y. Huo, H. Li, and Y. Lu, *J. Am. Chem. Soc.* **129**, 8406 (2007)
Li J. 2008	J. Li, J. Y. Lin and H. X. Jiang, *Appl. Phys. Lett.* **93**, 162107 (2008)
Lim 2008	W. Lim, J. S. Wright, B. P. Gila, S. J. Pearton, F. Ren, W. T. Lai, L. C. Ch en, M. S. Hu, and K. H. Chen, *Appl. Phys. Lett.* **93**, 202109 (2008)

Lin 2012	Y. G. Lin, C. K. Lin, J. T. Miller, Y.K. Hsu, Y. C. Chen, L. C. Chen and K. H. Chen, *RSC Adv*. **2**, 11258–11262 (2012)
Linhart 2010	W. M. Linhart, T. D. Veal, P. D. C. King, G. Koblmüller, C. S. Gallinat, J. S. Speck, and C. F. McConville, *Appl. Phys. Lett.* **97**, 112103 (2010)
Linhart 2012	W.M. Linhart, Ö. Tuna, T.D. Veal, J.J. Mudd, C. Giesen, M. Heuken and C.F. McConville, *Phys. Status Solidi (C)* **9** (3-4), 662-665 (2012)
Liu 1997	X. Q. Liu, W. Lu, W. L. Xu, Y. M. Mu, X. S. Chen, Z. H. Ma, S. C. Shen, Y. Fu and M. Willander, *Phys. Lett. A* **225** (1), 175 (1997)
Liu G. 2011	G. Liu, H. Zhao, J. Zhang, J. Park, L. Mawst, and N. Tansu, *Nanoscale Res. Lett*. **6**, 342 (2011)
Lliopoulos 2006	E. Lliopoulos, A. Georgakilas, E. Dimakis, A. Adikimenakis, K. Tsagaraki, M. Androulidaki, and N. T. Pelekanos, *Phys. Stat. Sol.* (A) **203**, 102 (2006).
Lu 2007	Y. S. Lu, C. C. Huang, J. A. Yeh, C. F. Chen, and S. Gwo, *Appl. Phys. Lett.* **91**, 202109 (2007)
Lu 2008	Y. S. Lu, C. L. Ho, J. A. Yeh, H. W. Lin, and S. Gwo, *Appl. Phys. Lett.* **92**, 212102 (2008)
Lu 2009	Y. S. Lu, Y. H. Chang, Y. L. Hong, H. M. Lee, S. Gwo, and J. A. Yeh, *Appl. Phys. Lett.* **95**, 102104 (2009)
Lu H. 1997	H. Lu, M. Thothathiri, Z.Wu and I. Bhat, *J. Electron. Mater*. **26**, 281 (1997)
Lu H. 2000	H. Lu, W.J. Schaff, J. Hwang, H. Wu, W. Yeo, A. Pharkya, L.F. Eastman, *Appl. Phys. Lett.* **77** (2000) 2548
Lu H. 2004	H. Lu, W. J. Schaff, L. F. Eastman, *J. Appl. Phys.* **96**, 3577 (2004)
Luo 2008	W. Luo, B. Liu, Z. Li, Z.Xie, D. Chen, Z. Zou and R. Zhang, *Appl. Phys. Lett.* **92**, 262110 (2008); DOI: 10.1063/1.2955828
Ludwig 2006	P. Ludwig, A.V. Filinov, M. Bonitz, H. Stolz, *Phys. Stat. Sol. B* **243** 10, 2363–2366 (2006)
Luque 1997	A. Luque and A. Martí, *Phys. Rev. Lett*. **78** (26), 5014–5017 (1997)
MacChesney 1970	J. MacChesney, P. M. Bridenbaugh, and P. B. O'Connor, *Mater. Res. Bull.* **5**, 783 (1970)
Maeda 2010	K. Maeda andK. Domen, *J. Phys. Chem. Lett*. **1**, 2655–2661 (2010)
Maeng 2009 ,	J. Maeng, G. Jo, M. Choe, W. Park, M. K. Kwon, S. J. Park, and T. Lee, Thin *Solid Films* **518**, pp. 865, (2009).
Magonov 1996	S. N. Magonov, M.-H. Whangbo (1996). *Surface Analysis with STM and AFM,* New York, VHC Publishers.
Mahboob 2004a	I. Mahboob, T.D. Veal, C.F. McConville, H. Lu and W.J. Schaff, *Phys. Rev. Lett.* **92**, 036804 (2004)
Mahboob 2004b	I. Mahboob, T. D. Veal, L. F. J. Piper, C. F. McConville, H. Lu, W. J. Schaff, J. Furthmüller and F. Bechstedt, *Phys. Rev. B* **69**, 201307 (2004)
Maiolo 2008	J. R. Maiolo, H. A. Atwater, and N. S. Lewis, *J. Phys. Chem. C* **112**, 6194 (2008)
Marasina 1977	L. A. Marasina, I. G. Pichugin, and M. Tlaczala, *Krist. Tech.* **12**, 541 (1977)

Marcus 1965	R. A. Marcus, *J. Chem. Phyus.* **43**, 679 (1965)
Miao 2000	Z. L. Miao, P. P. Chen, W. Lu, W. L. Xu, Z. F. Li, W. Y. Cai, G. L. Shi, and S. C. Shen, *Phys. Lett. A* **273** (4), 271 (2000),
Miao 2005	Z. L. Miao, Y. W. Zhang, S. J. Chua, Y. H. Chye, P. Chen, and S. Tripathy, *Appl. Phys. Lett.* **86**, 031914 (2005)
Michler 2009	P. Michler (Ed.) (2009). *Single Semiconductor Quantum Dots*. Springer-Verlag Berlin Heidelberg.
Milla 2014a	M. J. Milla, J. M. Ulloa, and A Guzmán, *Nanotechnology* **25** (44), 445501 (2014)
Milla 2014b	M. J. Milla, J. M. Ulloa, and Á. Guzmán, *ACS Appl. Mater. Interfaces* **6** (9), 6191–6195. (2014)
Miyajima 2001	T. Miyajima, H. Yoshida, K. Yanashima, T. Yamaguchi, T. Asatsuma, K. Funato, S. Hashimoto, H. Nakajima, M. Ozawa, T. Kobayashi, S. Tomiya, T. Asano, S. Uchida, S. Kijima, T. Tojyo, T. Hino, and M. Ikeda, *Mater. Sci. Eng. B* **82**, 248 (2001)
Moison 1990	J. M. Moison, K. Elcess, F. Houzay, J. Y. Marzin, J. M. Gerard, F. Barthe, and M. Bensoussan, *Phys. Rev. B.* **41**, 12945 (1990)
Monemar 1997	B. Monemar, J.P. Bergman, and I. A. Buyanova (1997). *Optical Properties of GaN and Related Materials*. In S. J. Pearton (Ed.), *GaN and Related Materials*. New York: Gordon and Breach Publishers.
Morales 2009	F.M. Morales, D. González, J.G. Lozano, R. García, S. Hauguth-Frank, B. Levedev, B. Cimalla and O. Ambacher, *Acta Material A* **57**, 5681-5692 (2009).
Moses 2010	P. G. Moses and C. G. Van de Walle, *Appl. Phys. Lett.* **96**, 021908 (2010)
Nagatomo 1989	T. Nagatomo, T. Kuboyama, H. Minamino, and O. Omoto, *Jpn. J. Appl. Phys.* **28**, L1334 (1989)
Nakada 1998	Y. Nakada, I. Aksenov, and H. Okumura, Appl. Phys. Lett. 73, 82 (1998)
Nakamura 1991a	S. Nakamura, *Jpn. J. Appl. Phys.* **30**(10A), L1705 (1991)
Nakamura 1991b	S. Nakamura, Y. Harada and M. Seno, *Appl. Phys. Lett.* **58**, 2021 (1991)
Nakamura 1991c	S. Nakamura, T. Mukai, and M. Senoh, *Jpn. J. Appl. Phys.* **30**, L1998. (1991)
Nakamura 1992a	S. Nakamura, T. Mukai, M. Senoh and N. Iwasa, *Jpn. J. Appl. Phys.* **31**, L139 (1992)
Nakamura 1992b	S. Nakamura, N. Iwasa, M. Senoh, and T. Mukai, *Jpn. J. Appl. Phys.* **31**, 1258 (1992)
Nakamura 1996	S. Nakamura, M. Senoh, S. Nagahama, N. Iwasa, T. Yamada, T. Matsushita, H. Kiyoku and Y. Sugimoto, *Jpn. J. Appl. Phys.* **35**, L74 (1996)
Nanishi 2003a	Y. Nanishi, Y. Saito, and T. Yamaguchi, *J. Appl. Phys.* **42**, 2549 (2003)
Nanishi 2003**b**	Y. Nanishi, Y. Saito, T. Yamaguchi, M. Hori, F. Matsuda, T. Araki, A. Suzuki, and T. Miyajima, *Phys. Stat. Sol*. (A) **200**, 202 (2003).
Nath 2011	D. N. Nath, E. Gür, S. A. Ringel and S. Rajan, “growth model for plasma-asisted molecular beam epitaxy”, *J. Vac. Sci. Technol. B* **29** (2) (2011)

Newbury 1976	D. E. Newbury, and H. Yakowitz (1976), Studies of the Distribution of Signals in the SEM/EPMA by Monte Carlo Electron Trajectory Calculations. In: K. F. J. Heinrich, D. E. Newbury, and H. Yakowitz (Ed.) Electron Probe Microanalysis and Scanning Electron Microscopy, NBS Special Publications. Washington. Pp. 15–44.
Ng 2010	Y. H. Ng, A. Iwase, A. Kudo and R. Amal, *J. Phys. Chem. Lett.* **1** (17), 2607–2612 (2010)
Nobel Media	Nobel Media AB (2014). “*Shuji Nakamura – Facts*”. Nobelprize.org. www.nobelprize.org/nobel_prizes/physics/laureates/2014/nakamura-facts.html
Nozik 1996	A.J. Nozik and R. Memming, *J. Phys. Chem.* **100**, 13061 (1996)
Park 2005	I. K. Park, M. K. Kwon, S. H. Baek, Y. W. Ok, T. Y. Seong, S. J. Park, Y. S. Kim, Y. T. Moon, and D. J. Kim, *Appl. Phys. Lett.* **87**, 061906 (2005).
Park 2011	I. K. Park and S. J. Park, *Appl. Phys. Express* **4**, 042102 (2011)
Pastor-Moreno 2002	G. Pastor-Moreno (2002). Chapter 4 of *Electrochemical Applications of CVD Diamond*. Retrived from: http://www.chm.bris.ac.uk/pt/diamond/gustavothesis/chapter4.htm
Peng 2008	K. Peng, X. Wang and S. T. Lee, *Appl. Phys. Lett.* **92**, 163103 (2008)
Pohl 2013	Udo W. Pohl, Epitaxy of Semiconductors: Introduction to Physical Principles Springer Science & Business Media (2013)
Polyakov 2006	V. M. Polyakov, and F. Schwierz, *Appl. Phys. Lett.* **88**, 032101 (2006)
Popovici 2000	G. Popovici, and H. Morkoc (2000). In: S. J. Pearton (Ed.), *GaN and Related Materials II*. Netherlands: Gordon and Breach Science, p. 93.
Prystawko 1999	P. Prystawko, M. Leszczynski, A Sliwinski, H. Teisseyre, T. Suski, M. Bockowski, S. Porowski, J. Domagala, C. Kirchner, A. Pelzmann, M. Schauler, and M. Kamp. *J. Cryst. Growth* **198/199** (part 2),1061 (1999)
Raghavan 1999	V. Raghavan, K. Ramanathan, P. V. Sundaram and B. Danielsson, *Clin. Chim. Acta* **289**, 145–158 (1999)
Reshchikov 2005	M.A. Reshchikov and H. Morkoç, *J. Appl. Phys*. **97**, 061301 (2005).
Riemann 2006	T. Riemann, T. Hempel, J. Christen, P. Veit, R. Clos, A. Dadgar, A. Krost, U. Haboeck, and A. Hoffmann, *J. Appl. Phys*. **99**, 123518 (2006).
Rinke 2008	P. Rinke, M. Winkelnkemper, A. Qteish, D. Bimberg, J. Neugebauer, and M. Scheffler, *Phys. Rev. B* **77**, 075202 (2008)
Ristic 2008	J. Ristic, E. Calleja, S.Fernández-Garrido, L. Cerutti, A.Trampert, U. Jahn, K.H. Ploog, *Journal of Crystal Growth* **310**, 4035 (2008)
Robinson 2005 183	J. Robinson, J. Rice, K. Lee, J. Na, R. Taylor, D. Hasko, R. Oliver, M. Kappers, C. Humphreys, and G. Briggs, *Appl. Phys. Lett*. **86**, 2013103 (2005).
Ryou 2009	J.H. Ryou, P.D. Yoder, J. Liu, Z. Lochner, H. Kim, S. Choi, H.J. Kim, R.D. Dupuis *Selected Topics in Quantum Electronics*, IEEE **15** 4 1080-1091 (2009)
Saito 2002	Y. Saito, T. Yamaguchi, H. Kanazawa, K. Kano, T. Araki, Y. Nanishi, N. Teraguchi, A. Suzuki, *J. Cryst. Growth* **237** (2002) 1017

Sarantopoulou 2006	E. Sarantopoulou, Z. Kollia, G. Dražic, S. Kobe and N. Spyropoulos Antonakakis, *Nanoscale Research Letters* **6**:387 (2006)
Schleife 2009	A. Schleife, F. Fuchs, C. Rödl, J. Furthmüller, and F. Bechstedt, *Appl. Phys. Lett.* **94**, 012104 (2009)
Scholz 2009	F. Scholz (2009). *Compound semiconductors*: *Physics, technology and device concepts* (lecture notes). Retrieved from: http://www-opto.e-technik.uni-ulm.de/lehre/cs/
Scholz 2012	F. Scholz *Semicond. Sci. Technol.* **27**, 024002 (2012)
Selçuk 2010	E. Selçuk, G. J. Hamhuis, and R. Nötzel, *AIP Conf. Proc.* **1199**, 535 (2010)
Shen 1990	H. Shen, M. Dutta, L.Fotiadis, P. G. Newman, R. P. Moerkirk, and W. H. Chang, *Appl. Phys. Lett.* **57**, 2118 (1990)
Shimizu 1994	M. Shimizu, K. Hiramatsu and N. Sawaki, *J. Cryst. Growth* **145**, 209 (1994)
Simmonds 2012	P. J. Simmonds and M. L. Lee, *J. Appl. Phys*. **112**, 054313 (2012)
Singh 1997	R. Singh, D. Doppalapudi, T. D. Moustakas, and L. T. Romano, *Appl. Phys. Lett.* **70**, 1089 (1997).
Sofikiti 2009a	N. Sofikiti, N. Chaniotakis, J. Grandal, M. Utrera, M. A. Sanchez-Garcia, E. Calleja, E. Iliopoulos, and A. Georgakilas, *Appl. Phys. Lett.* **95**, 113701 (2009)
Sofikiti 2009b	N. Sofikiti, G. Tsiakatouras, E. Iliopoulos, A. Georgakilas, and N. Chaniotakis, *J. Mater. Sci. Eng* **3**, 28-39 (2009)
Sofikiti 2010	N. Sofikiti, N. Chaniotakis, J. Grandal, M. Utrera, M. A. Sánchez-García, and E. Calleja, *Mater. Lett*, **64**, 1332-1335 (2010)
Song **P.** 2012	P. Song, X. Zhang, M. Sun, X. Cui, Y. Lin, *Nanoscale* **4**, 1800–1804 (2012)
Soto 2013a	P. E. D. Soto Rodríguez, V. J. Gómez, P. Kumar, E. Calleja and R. Nötzel, *Appl. Phys. Lett.* **102**, 131909 (2013)
Soto 2013b	P. E. D. Soto Rodríguez, P. Kumar, V. J. Gómez, N. H. Alvi, J. M. Manuel, F. M. Morales, J. J. Jiménez, R. García, E. Calleja and R. Nötzel, *Appl. Phys. Lett.* **102**, 173105 (2013).
Srinivasan 2003	S. Srinivasan, L. Geng, R. Liu and F. A. Ponce, *Appl. Phys. Lett.* **83**, 5187 (2003)
Stringfellow 2010	G. B. Stringfellow, *J. Cryst. Growth* **312**, 735–874 (2010)
Su 2011	J. Su, X. Feng, J. D. Sloppy, L. Guo, and C. A. Grimes, *Nano Lett.* **11** (1), 203 (2011)
Sun 2011	J. Sun, C. Liu, P. Yang, *J. Am. Chem. Soc.* **133** (48), 19306–19309 (2011)
Suris 1996	R. A. Suris (1996). *Prospects for quantum dot structures applications in electronics and optoelectronics*. In S. Luryi, J. Xu, and A. Zaslavsky (Ed.) Future Trends in Microelectronics. Springer Netherland. Pp.197-208.
Synge 1928	E. H. Synge, *Philos. Mag. Ser. 7*, **6**, 35, 356-362 (1928).
Tachibana 2012	Y. Tachibana, L. Vayssieres and J.R. Durrant, *Nat. Photonics* **6**, 511–518 (2012)
Tansley 1986	T. L. Tansley, and C. P. Foley, *J. Appl. Phys.* **59**, 3241 (1986)

Tartakovskii 2012	A. Tartakovskii (Ed.) (2012), Quantum dots: optics, electron transport and future applications, Cambridge
Tian 2003	Z. R. Tian, J. A. Voigt, J. Liu, B. Mckenzie, M. J. Mcdermott, M. A. Rodriguez, H. Konishi, and H. Xu, *Nature Materials* **2**, 821 (2003).
Tian **J.** 2013	J. Tian, and G. Cao, *Nano Reviews*. **4**, (2013)
Turner 1999	J. A. Turner, *Science* **285**, 687 (1999)
Tverberg 2012	G. Tverberg, “An Economic Theory of Limited Oil Supply” (2012) http://ourfiniteworld.com/2012/10/25/an-economic-theory-of-limited-oil-supply/
Vainshtein 1964	B.K Vainshtein (1964), *Structure analysis by electron diffraction*, Oxford, New York, Pergamon Press.
Van de Krol 2008	R. van de Krol, Y. Liang and J. Schoonman, *J. Mater. Chem.* **18**, 2311–2320 (2008)
Van de Walle 2003	C. G. Van deWalle and J. Neugebauer, *Nature* (London) **423**, 626 (2003)
Van de Walle 2007	C. G. Van de Walle and D. Sefev, *J. Appl. Phys.* **101**, 081704 (2007)
van Dorp 2009	D.H. van Dorp, N. Hijnen, M. Di Vece and J. J. Kelly, Angew. *Chem.—Int. Ed.* **48**, 6085–6088 (2009)
Veal 2006	T. D. Veal, P. H. Jefferson, L. F. J. Piper, C. F. McConville, T. B. Joyce, P. R. Chalker, L. Considine, H. Lu, and W. J. Schaff, *Appl. Phys. Lett.* **89**, 202110 (2006)
Vegard 1921	L. Vegard, *Z. Phys.* **5**, 17-26 (1921)
Vegard 1928	L. Vegard, *Z. Krist.* **67**, 239 (1928)
Vurgaftman 2003	I. Vurgaftman and J. R. Meyer, *J. Appl. Phys.* **94**, 3675 (2003)
Waki 2007	I. Waki, D. Cohen, R. Lal, U. Mishra, S. P. Den-Baars and S. Nakamura, *Appl. Phys. Lett.* **91**, 093519 (2007)
Waltereit 2000	P. Waltereit, O. Brandt, A. Trampert, H. T. Grahn, J. Menniger, M. Ramsteiner, M. Reiche, K. H. Ploog, *Nature* **406**, 865-868 (2000)
Walukiewicz 1987	W. Walukiewicz, *J. Vac. Sci. Technol. B* **5**, 1062 (1987)
Walukiewicz 1989	W. Walukiewizc, *Appl. Phys. Lett.* **54**, 2094 (1989)
Walukiewicz 2001	W. Walukiewicz, *Physica B* **302-303**, 123–134, (2001)
Wang 2011	D. F. Wang, A. Pierre, M. G. Kibria, K. Cui, X. G. Han, K. H. Bevan, H. Guo, S. Paradis, A. R. Hakima and Z. T. Mi, *Nano Lett.* **11**, 2353–2357 (2011)
Warwick	N.A., *Atomic Force Microscopy* (AFM), Department of Physics, Warwick, www2.warwick.ac.uk/fac/sci/physics/current/postgraduate/regs/mpags/ex5/techniques/structural/afm/
Web 2014	Transparency Market Research, *GaN Semiconductor Devices Market* (2014) www.transparencymarketresearch.com/gallium-nitride.html
Web arthritiscare	High Fructose Corn Syrup & Gout (Published 2010, retrived 2016) www.arthritiscare.com/-new--gout---high-fructose-corn-syrup.html
Web Earth	Global Education Project ‘Earth’: *World Energy Supply* www.theglobaleducationproject.org/earth/energy-supply.php

Web Mayo Clinic	Mayo Clinic: Mayo Medical Laboratories. (retrived 2016) ://www.mayomedicallaboratories.com/test-catalog/Overview/60296.
Web TUK	N.A., *Molecular beam epitaxy* (MBE), AG Magnetismus Fachbereich Physik, Technishe Universitat Kaiserslautern www.physik.uni-kl.de/hillebrands/research/methods/molecular-beam-epitaxy
Wei 2003	S.H. Wei, X. Nie, I. G. Batyrev, and S. B. Zhang, *Phys. Rev. B* **67**, 165209 (2003)
Weisz 2004	P. Weisz, *Phys. Today* **57**(7), 47 (2004)
West	P. West and A. Ross, *An Introduction to Atomic Force Microscopy Modes*. Retrieved on 2007 from: www.pacificnano.com/afm_modes_single.html
Wilke 2008	I. Wilke, R. Ascazubi, H. Lu, and W. J. Schaff, *Appl. Phys. Lett.* **93**, 221113 (2008)
Wu 2002	J. Wu, W. Walukiewicz, W. Shan, K. M. Yu, J. W. Ager III, E. E. Haller, H. Lu, and W. J. Schaff, *Phys. Rev. B* **66** (20), 201403 (2002)
Wu 2003	J. Wu, W. Walukiewicz, W. Shan, K. M.Yu, J. W. Ager, S. X. Li, E. E. Haller, H. Lu and W. J. Schaff, *J. Appl. Phys.* **94**, 4457 (2003)
Wu 2009	J. Wu, *J. Appl. Phys.* **106**, 011101 (2009)
Wu C. 2003	C. L. Wu, J. C. Wang, M. H. Chan, T. T. Chen, and S. Gwo, *Appl. Phys. Lett.* **83**, 4530 (2003).
Wu C. 2009	C. L. Wu, H. M. Lee, C. T. Kuo, C.H. Chen and S. Gwo, *Phys. Rev. Lett.* **101**, 106803 (2009)
Xia 1993	H. Xia, Q. Xia, and A. L. Ruoff, *Phys. Rev. B* **47** (19), 12925 (1993)
Yam 2008	F. K. Yam, and Z. Hassan, *Superlattices Microstruct*. **43**, 1-23 (2008).
Yan 2009	R. Yan, D. Gargas, and P. Yang, *Nature Photonics* **3**, 569 (2009).
Yang 2012	X. Yang, M. Arita, S. Kako, and Y. Arakawa, *Phys. Status Solidi (C)* **9**, 613 (2012)
Yoshimoto 1991	N. Yoshimoto, T. Matsuoka, T. Sasaki, and A. Katsu, *Appl. Phys. Lett.* **59**, 2251 (1991)
Yu 1999	P. Y. Yu and M. Cardona (1999). Fundamentals of Semiconductors: Physics and Materials Properties. Springer-Verlag, Berlin
Yu **L.** 2012	L. M. Yu, X. H. Fan, J. Y. Shui, L. Cao and W. Yan, *Mater. Lett*. **68**, 423 (2012).
Zhang 2007	C. G. Zhang, L. F. Bian, W. D. Chen, and C. C. Hsu, *J. Cryst. Growth*. **299**, 268 (2007)
Zhang **K.** 2013	K. Zhang, X. Shi, J. K. Kim, J. S. Lee, J. H. Park, *Nanoscale* **5**, 1939–1944 (2013)
Zhao 2012	W. Zhao, L. Wang, J. Wang, W. Lv, Z. Hao, and Y. Luo, *Phys. Status Solidi* (A) **209**, 1096 (2012)
Zhong 2012	A. Zhong and K. Hane, *Nanoscale Res. Lett*. **7**, 686 (2012).
Zhou 2010	M. Zhou, S. Zhang, Y. Sun, C. Wu, M. Wang, and Y. Xie, *Chem. Asian J.* **5**, 2515 (2010)

Zhou 2012 M. Zhou, J. Bao, M. Tao, R. Zhu, Y. Zeng, Z. Wei, and Y. Xie, *Chem. Commun.* **48**, 3439 (2012)

References table 6.1

[1] S. M. U Ali, M. Kashif, Z. H. Ibupoto, M. Fakhar-e-Alam, U. Hashim, and M. Willander, *Micro & Nano Letters* **6**, 609 (2011).

[2] A. S. Poghossian, *Sens. Actuat. B Chem.* **44**, 361 (1997).

[3] F. Kormos, L. Szira´ki and I. Tarsiche, *Lab. Robotics Autom.* **12**, 291 (2000).

[4] N. H. Alvi, P. E. D. Soto Rodriguez, V. J. Gómez, Praveen Kumar, G. Amin et al. *Appl. Phys. Lett.* **101**, 153110 (2012).

References table 6.2

[5] M. Q. Israr, J. R. Sadaf, M. H. Asif, O. Nur, M. Willander and B. Danielsson, *Thin Solid Films*, **519**, 1106–1109 (2010).

[6] M. Q. Israr, J.R. Sadaf, O. Nur, M. Willander, S. Salman and B. Danielsson, *Appl. Phys. Lett.* **98**, 253705:1–253705:3 (2011).

[7] N. H. Alvi, V. J. Gómez, P. E. D. Soto Rodríguez, P. Kumar, S. Zaman, M. Willander and R. Nötzel, *Sensors* **13**, 13917-13927 (2013).

APPENDIX 1

Three subdivisions of BSFs can be identified (see figure A1), where intrinsic BSFs are formed by the change from one hcp lattice to another one, i.e. from AB to BC or AC stacking, while extrinsic BSFs are formed through the insertion of an extrinsic layer, i.e. a C layer in an AB sequence:

- Intrinsic I1 BSFs: These involve one breach of the WZ stacking (ABABAB…) where the third-nearest neighbour should be the same. They exhibit a stacking sequence of ABABCBCBC…
- Intrinsic I2 BSFs: Introduces two changes along the WZ stacking sequence presenting the stacking sequence ABABCACAC…
- Extrinsic E BSFs: These involve three breaches of the WZ stacking and have the stacking sequence ABABCABAB…

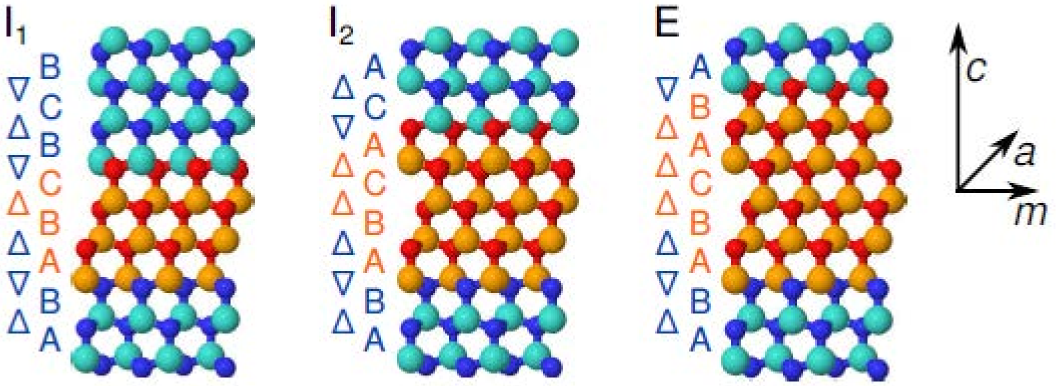

Figure A1: Stacking sequences for the intrinsic I1 and I2 as well as the extrinsic E stacking fault. The layers for which the ZB stacking sequence is interupted are highlighted, while alongside the breaches to the wurtzite stacking rule are highlighted.

APPENDIX 2

The problem of an electron confined in a QW with bended bands, (a consequence of externally applied electric field) can be successfully treated by the application of perturbation theory. For that, two different confining potentials are considered. First the electron in: (i) infinite rectangular potential well is treated (unperturbated system). Second, the electron in: (ii) infinite triangular potential well is considered. The unperturbed system (the case of an infinite potential well, see figure A3.1) has well-known exact solutions:

The electron in infinite rectangular potential

- Eigenvalues (Energy levels) for this system are:

$$\varepsilon_n = n^2 \frac{\pi^2 \hbar^2}{2m^*_{e,hh} d^2} \quad n = 1, 2, 3.... \tag{A2.1}$$

- Eigenfunctions (wavefunctions) of the Hamiltonian are either even or odd:

$$\begin{aligned} \varphi_{n_{even}}(x) &= \sqrt{\frac{2}{d}} \cos\left[\frac{n\pi}{d} x\right], n = 1, 3, 5, ... \\ \varphi_{n_{odd}}(x) &= \sqrt{\frac{2}{d}} \sin\left[\frac{n\pi}{d} x\right], n = 2, 4, 6, .. \end{aligned} \tag{A2.2}$$

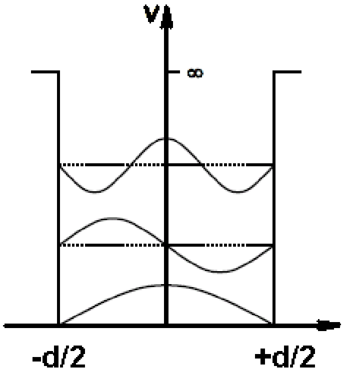

Figure A2.1: Schematic of an infinite potential well with width d.

The electron in infinite triangular potential The triangular potential has analytic form:

$$V = e \cdot x \cdot E_z \tag{A2.3}$$

The perturbation theory states that the solutions (i.e. eigenvalues and eigenfunctions) of a perturbed system can be well approximated by the following analytic expressions:

$$E_n = \varepsilon_n + \int_{-\infty}^{\infty} \varphi_z^*(z) \varphi_k(z) dz + \sum\nolimits_{k,k \neq n} \frac{\left| \langle \varphi_k | V | \varphi_n \rangle \right|^2}{\varepsilon_n - \varepsilon_k} + ... \tag{A2.4}$$

$$\Psi_n = \varphi_n + \sum_{k,k\neq n} \frac{V_{nk}^*}{\varepsilon_n - \varepsilon_k} \varphi_k + \ldots \tag{A2.5}$$

$$\left| \langle \varphi_k | V | \varphi_n \rangle \right| = \int_{-\infty}^{\infty} \varphi_k^*(z)\, \mathrm{V}\, \varphi_n(z) dz \tag{A2.6}$$

Where ε_n and φ_n are eigen values and eigenfunctions of the unperturbed system (system (i)), while E_n and Ψ_n are those of the perturbed system (system (ii)).

For n=1, the first order correction has an odd function (x) as integrand, odd function times an even function ($\cos^2$) equals odd function, to be evaluated over symmetric integral limits and therefore the integrand cancels itself out:

$$E_1 = V_{11} = \frac{2}{d} eE_z \int_{-d/2}^{d/2} x \cos^2 \left[\frac{\pi}{d} x \right] dx = 0 \tag{A2.7}$$

The second order correction is different to zero only when the integrand of is an even function:

$$\left| \langle \varphi_k | V | \varphi_1 \rangle \right| = \frac{2}{d} eE_z \int_{-d/2}^{d/2} \sin \left[\frac{k\pi}{d} x \right] x \cos \left[\frac{\pi}{d} x \right] dx, k = 2,4,6,.. \tag{A2.8}$$

That means that for all even values of k it is non-zero. Taking k=2 the equation reads:

$$\left| \langle \varphi_2 | V | \varphi_1 \rangle \right| = \frac{2}{d} eE_z \int_{-d/2}^{d/2} \sin \left[\frac{2\pi}{d} x \right] \mathrm{x} \cos \left[\frac{\pi}{d} x \right] dx = \frac{16}{9\pi^2} eE_z d \tag{A2.9}$$

Here we used integration by parts and the following identiy:

$$\int \sin(au) \cos(\mathrm{b}u)\, \mathrm{du} = -\frac{\cos\left[(a-b)u\right]}{2(a-b)} - \frac{\cos\left[(a+b)u\right]}{2(a+b)} + C$$

Considering the fact that the relative energy difference between the second and the first energy levels is 4 ($\varepsilon_2 = 4 \cdot \varepsilon_1$), the second energy correction is then:

$$E_1^{(2)} = -\frac{\left| \langle \varphi_2 | V | \varphi_1 \rangle \right|}{\varepsilon_2 - \varepsilon_1} = -\frac{\left| \langle \varphi_2 | V | \varphi_1 \rangle \right|}{3\varepsilon_1} = -\frac{1}{3} \left(\frac{16}{9} \right)^2 \frac{e^2 E_z^2 d^2}{\varepsilon_1 \pi^4} \tag{A2.10}$$

the first eigenvalue for the potential well is, thus:

$$\varepsilon_1 = \frac{\pi^2 \hbar^2}{2 \cdot m_e^* d^2} \tag{A2.11}$$

Yielding finally:

$$E_1^{(2)} = -24 \left(\frac{2}{3\pi} \right)^6 \frac{e^2 E_z^2 d^4}{\hbar^2} \tag{A2.12}$$